



# Kent Academic Repository

**Almoteriy, Mohammed (2020) *System and Circuit Models for Microwave Antennas and Communication Channels*. Doctor of Philosophy (PhD) thesis, University of Kent,.**

## Downloaded from

<https://kar.kent.ac.uk/80039/> The University of Kent's Academic Repository KAR

## The version of record is available from

## This document version

UNSPECIFIED

## DOI for this version

## Licence for this version

UNSPECIFIED

## Additional information

## Versions of research works

### Versions of Record

If this version is the version of record, it is the same as the published version available on the publisher's web site. Cite as the published version.

### Author Accepted Manuscripts

If this document is identified as the Author Accepted Manuscript it is the version after peer review but before type setting, copy editing or publisher branding. Cite as Surname, Initial. (Year) 'Title of article'. To be published in *Title of Journal*, Volume and issue numbers [peer-reviewed accepted version]. Available at: DOI or URL (Accessed: date).

## Enquiries

If you have questions about this document contact [ResearchSupport@kent.ac.uk](mailto:ResearchSupport@kent.ac.uk). Please include the URL of the record in KAR. If you believe that your, or a third party's rights have been compromised through this document please see our [Take Down policy](https://www.kent.ac.uk/guides/kar-the-kent-academic-repository#policies) (available from <https://www.kent.ac.uk/guides/kar-the-kent-academic-repository#policies>).

# **System and Circuit Models for Microwave Antennas and Communication Channels**

A Thesis Submitted to the University  
of Kent

For the Degree of DOCTOR OF  
PHILOSOPHY

In ELECTRONICS ENGINEERING

By  
Mohammed Almoteriy

January, 2020

## Abstract

Antenna characterisation for modern communication systems involves obtaining the reflection coefficient ( $S_{11}$ ) using a three-dimensional (3D) electromagnetic (EM) simulator and conducting experimental verification using a network analyser. The gain and radiation patterns are then obtained at certain frequencies from the simulation or measurement. These parameters are insufficient to completely characterise the antenna as a two-port network, however, because radiation pattern simulation and measurements require a large number of frequencies. The conventional design also does not provide essential antenna parameters such as  $S_{11}$  phase and the complex transfer parameter,  $S_{21}$ . These parameters are important in digital communication systems (DCSs), which are typically simulated and studied in the time domain. The aim of this thesis is to derive circuit and system models for antennas and to then use these derivations in different applications. These derivations are useful for characterising antennas in point-to-point (P2P) and domestic applications. Initially, wideband Vivaldi and narrowband patch antennas are characterised in this work using three techniques: (1) deriving an equivalent circuit model (ECM), (2) processing the measurements between two identical antennas in an anechoic chamber, and (3) applying the Hilbert transform to the amplitude of  $S_{21}$ . These techniques are then used to obtain the  $S_{21}$  of the antenna. The  $S_{21}$  values obtained through these techniques are then compared to verify their validity and to show their difference when realising a low  $S_{11}$  in the conventional design. The ECM is also derived to characterise the antenna behaviour in the frequency domain.

The thesis also presents the characterisation of antennas and channels from only one  $S_{21}$  measurement in a multipath channel, which will allow designers to obtain the  $S_{21}$  of an antenna without using an anechoic chamber. The antenna and channel responses in the time domain are separated from the time response, which is derived from the antenna's frequency measurement. The procedure is then validated using wideband and narrowband antennas to establish measurement limitations in multipath channels.

The antenna's frequency response can be characterised in terms of effective aperture and gain. This characterisation is important in P2P communications, as the

frequency response can vary due to changes in the radiation pattern in the physical channel. This thesis presents a process to investigate the frequency response of a wideband antenna to identify the best orientation of the antenna for P2P communications. During this process, the antenna's effective aperture and gain are predicted for each orientation. The frequency-variant radiation pattern is ascertained from the  $S_{21}$  phase obtained from the ECM for the antenna. For each orientation, the  $S_{21}$  phase is analysed based on the linear, minimum, and all-pass phase components, which then enables the derivation of an ECM. The process is validated using a non-minimum-phase monopole ultra-wideband (UWB) antenna.

An antenna is also modelled as a system to predict its effects when used in a DCS. A time-domain system model is derived to enable estimation of the antenna effects in a DCS. The results show that antennas cause symbol scattering and contribute to the error vector magnitude (EVM) and the bit error rate (BER). The technique is applied to different types of antennas with varying orientations and environments and with added noise.

The modelling of an inverse antenna system to de-embed the antenna is also presented in this work for P2P communications to characterise channels and to compensate for antenna effects within DCSs. A stable inverse antenna system is derived for a Vivaldi antenna to be applied to the measurements within two different office environments to characterise the two channels. The technique is also applied to a commercial antenna to improve system performance and to reduce the BER caused by the antenna in DCSs. The results show that the inverse antenna system can be useful for several applications in DCSs. Finally, an antenna's total radiated power from measurements in a reverberation chamber built with aluminium walls is computed using an empirical equation, which enables the prediction of antenna losses and antenna characterisation for domestic applications.

## **Acknowledgements**

Thanks to Allah for giving me the strength to finish my research and thesis.

I would like to express my sincere gratitude to Professor Mohamed Sobhy for his patience, motivation and continuous support of my PhD study and related research for setting such high standards. It has been a great honour to work with him and to receive his invaluable, expert advice. My warm thanks also go to Professor John Bachelor for his guidance, recommendations, insights and ideas during my PhD research. I am happy to have worked with such highly professional academics.

In addition to my supervisors, I would like to thank specialist workshop technician Mr Simon Jakes for his accurate and speedy antenna fabrication. Thanks also go to student learning advisor Dr Matthew Copping who has supported and guided me to achieve high quality academic writing. I would also like to thank the members of the School of Engineering and Digital Arts in the University of Kent for their support, both academically and emotionally.

Special warm thanks go to my mother Habibah Almutari for her continuous, unconditional love and to my father Abdulrahman for his guidance and support throughout my life. My loving thanks also go to my wife Widad for her patience and support in the UK and to my kids Rimas, Meshari, Sultan and little Ghada. Thanks also to my sisters and brothers for always keeping me motivated. Without this support from my family, I would never have been able to achieve my goals.

Finally, I would like to thank the Saudi Government for awarding me a Doctoral Scholarship, which provided me with the necessary financial assistance to complete my degree.

## CONTENTS

Abstract .....	i
Acknowledgements .....	iii
List of Figures .....	vii
List of Tables.....	x
Abbreviations .....	xi
CHAPTER 1: INTRODUCTION .....	1
1.1 Overview and Motivations.....	1
1.2 Antenna Characterisation.....	2
1.3 Minimum and Non-Minimum Antenna Phase.....	5
1.4 Antenna Gain .....	5
1.5 Antenna Effects in Digital Systems .....	6
1.6 Channel Characterisation .....	6
1.7 Research Objectives and Contributions .....	7
1.8 Methodology and Design Steps .....	9
1.9 Measurement Techniques .....	10
1.10 Software and Measurement Facilities .....	12
1.11 Analysis.....	12
1.12 Publication List .....	13
1.13 Organisation of the Thesis .....	14
CHAPTER 2: LITERATURE REVIEW .....	17
2.1 Introduction.....	17
2.2 Antennas as Two-Port Networks .....	17
2.3 Antenna Phase.....	26
2.4 Antenna Effects in DCSs .....	32
2.5 Channel Models .....	35
CHAPTER 3: NARROW AND WIDEBAND ANTENNA CHARACTERISATION AS TWO-PORT NETWORKS.....	41
3.1 Introduction.....	41
3.2 Antenna Characterisation Methodology .....	43
3.3 Vivaldi Antenna Design.....	46
3.4 ECM for Vivaldi Antennas .....	49
3.5 $S_{21}$ Measurement between Two Identical Antennas.....	51
3.6 The Hilbert Transform .....	52

3.7 Results and Discussion .....	52
3.8 Summary .....	66
<b>CHAPTER 4: ANTENNA MODELLING TECHNIQUE FOR DIGITAL COMMUNICATION SYSTEMS .....</b>	<b>68</b>
4.1 Introduction.....	68
4.2 Antenna Measurements.....	69
4.3 ECM for the Commercial Antenna .....	70
4.4 Characterisation of the Commercial Antenna .....	72
4.5 Antenna System Model.....	73
4.6 Antenna Simulation in a DCS.....	77
4.7 Experimental Setup for Antennas in a DCS.....	80
4.8 Experimental Verification of the Simulations.....	83
4.9 Summary .....	86
<b>CHAPTER 5: CHARACTERISATION OF NON-MINIMUM-PHASE WIDEBAND ANTENNAS FOR POINT-TO-POINT COMMUNICATIONS.....</b>	<b>88</b>
5.1 Introduction.....	88
5.2 Mathematical Formulation .....	89
5.3 Monopole UWB Antenna Design .....	91
5.4 ECM for a Monopole UWB Antenna .....	93
5.5 Results and Discussion .....	94
5.6 Summary .....	107
<b>CHAPTER 6: INVERSE ANTENNA SYSTEMS AND THEIR APPLICATIONS IN DIGITAL COMMUNICATION .....</b>	<b>109</b>
6.1 Introduction.....	109
6.2 Methodology for Deriving Inverse Antenna Systems.....	111
6.3 Measuring and Modelling the Vivaldi Antenna.....	112
6.4 Measuring and Modelling the Channel.....	119
6.5 Antenna and Channel Performance in a DCS .....	122
6.6 Summary .....	129
<b>CHAPTER 7: DETERMINING TOTAL RADIATED ANTENNA POWER FROM REVERBERATION CHAMBER MEASUREMENTS .....</b>	<b>131</b>
7.1 Introduction.....	131
7.2 Mathematical Formulation.....	132
7.3 Reverberation Chamber Cavity.....	135
7.4 Measuring Antennas in the Cavity.....	139
7.5 Empirically Modelling Cavity Losses in Reverberation Chambers.....	142

7.6	Summary .....	146
<b>CHAPTER 8: CONCLUSIONS AND FUTURE WORK.....</b>		<b>148</b>
8.1	Conclusions.....	148
8.2	Future Work.....	155
<b>REFERENCES.....</b>		<b>157</b>

## List of Figures

Figure 2.1. An ECM for a narrowband antenna. ....	19
Figure 2.2. An ECM for a broadband microstrip-fed antenna.....	20
Figure 2.3. ECM for a button antenna. ....	23
Figure 2.4. Horn antenna transfer function measurement (dB) for three identical antennas [2]. ....	28
Figure 2.5. Measured Horn antenna $S_{21}$ and the Hilbert transform phase [2].....	28
Figure 2.6. Measured Horn antenna phase on-axis with linear phase removed and the Hilbert transfer phase from its amplitude [4].....	30
Figure 3.1. Method for obtaining $S_{21}^a$ , which provides the total radiated power.....	44
Figure 3.2. Vivaldi antenna parameters.....	47
Figure 3.3. Vivaldi antenna geometry: (a) top view and (b) cross-sectional side view.....	48
Figure 3.4. Comparison of $S_{11}$ from CST and measurement. ....	49
Figure 3.5. Radiation pattern gain at (a) 3.5 GHz and (b) 6.3 GHz. ....	49
Figure 3.6. ECM for a Vivaldi antenna. ....	50
Figure 3.7. $S_{11}$ of the Vivaldi antenna from measurement and ECM. ....	50
Figure 3.8. Photograph of the Vivaldi antenna measurement along with endfire direction in the anechoic chamber. ....	51
Figure 3.9. Measurement of $S_{21}^b$ between two Vivaldi antennas in an anechoic chamber. ....	51
Figure 3.10. Comparison of the amplitude of $S_{21}^a$ and $S_{21}$ of the Vivaldi antenna.....	53
Figure 3.11. Comparison of the phase of $S_{21}^a$ and $S_{21}$ of the Vivaldi antenna.....	53
Figure 3.12. Comparison of group delay between the Vivaldi antenna $S_{21}$ and the minimum phase from the Hilbert transform. ....	54
Figure 3.13. Impulse response of the Vivaldi antenna $S_{21}$ . ....	55
Figure 3.14. Measurement of $S_{21}^b$ between two antennas in a channel (communication link). ....	55
Figure 3.15. Antenna and channel characterisation flowchart. ....	56
Figure 3.16. Schematic of a typical laboratory environment.....	58
Figure 3.17. $S_{21}^b$ measurement of the Vivaldi antenna in the laboratory environment after de-embedding the direct path.....	58
Figure 3.18. Impulse response of the $S_{21}^b$ measurement of the Vivaldi antenna after de-embedding the direct path.....	59
Figure 3.19. $S_{21}$ of the Vivaldi antenna from the measurement in the anechoic chamber and the procedure.....	60
Figure 3.20. Frequency response of the multipath channel. ....	60
Figure 3.21. Patch antenna geometry (all dimensions in mm). ....	62
Figure 3.22. ECM for the patch antenna. ....	62
Figure 3.23. $S_{11}$ of the patch antenna from EM simulation, measurement, and ECM.....	62
Figure 3.24. The input resistance and reactance of the patch antenna from EM simulation and ECM.....	63
Figure 3.25. Comparison of the amplitude of $S_{21}^a$ and $S_{21}$ of the patch antenna. ....	64
Figure 3.26. Comparison of the phase of $S_{21}^a$ and $S_{21}$ of the patch antenna. ....	64
Figure 3.27. Impulse response of the $S_{21}^b$ measurement of the patch antenna in the laboratory environment after de-embedding the direct path.....	65
Figure 3.28. $S_{21}$ of the patch antenna from measurements in the anechoic chamber and the procedure. ....	65
Figure 4.1. Photographs of two characterised antennas: (a) Vivaldi and (b) commercial dual-band. ..	69
Figure 4.2. Commercial dual-band antenna structure and ECM topology (all dimensions in mm). ....	70
Figure 4.3. ECM for the commercial dual-band antenna. ....	71
Figure 4.4. Comparison of $S_{11}$ from measurements and from ECM: commercial antenna. ....	71
Figure 4.5. Amplitude of $S_{21}^a$ and $S_{21}$ of the commercial antenna. ....	72

Figure 4.6. $S_{21}$ and $S_{21}^a$ phases from the measurement and the ECM.....	73
Figure 4.7. Impulse response of the $S_{21}^b$ FIR model for (a) commercial and (b) Vivaldi antennas.....	74
Figure 4.8. Complete antenna system model with four FIR models in SIMULINK. ....	75
Figure 4.9. Frequency response of the commercial antenna: (a) system model and (b) $S_{21}^b$ measurement. ....	76
Figure 4.10. Frequency response of the Vivaldi antenna: (a) system model and (b) $S_{21}^b$ measurement. .	76
Figure 4.11. Flow chart to predict antenna effects in a DCS.....	77
Figure 4.12. Antenna with free-space channel in a DCS. ....	78
Figure 4.13. Output constellation diagrams based on the commercial antenna system model at carrier frequencies of (a) 2 GHz and (b) 6 GHz. ....	79
Figure 4.14. Output constellation diagrams based on the Vivaldi antenna system model at carrier frequencies of (a) 3.5 GHz and (b) 6.3 GHz. ....	80
Figure 4.15. Experimental setup: (a) BTB connection and (b) antennas.....	82
Figure 4.16. Photograph of the experiment setup.....	82
Figure 4.17. Output constellation at 2 GHz without antenna from (a) simulation and (b) experimentation. ....	83
Figure 4.18. Output constellation at 2 GHz with the commercial antenna from (a) simulation and (b) experimentation. ....	84
Figure 4.19. Signal captured in the oscilloscope at 2 GHz from (a) BTB connection and (b) wireless channel with commercial antenna. ....	84
Figure 4.20. Output constellation at 3.5 GHz with the Vivaldi antenna from (a) simulation and (b) experimentation. ....	85
Figure 5.1. Phase components of $S_{21}$ . ....	91
Figure 5.2. $S_{11}$ from simulation and measurement, and inset antenna structure (all dimensions in mm). 92	
Figure 5.3. Radiation pattern gain at (a) 4 GHz and (b) 7 GHz. ....	92
Figure 5.4. Current distribution at (a) 4 GHz and (b) 7 GHz.....	93
Figure 5.5. ECM for the monopole UWB antenna. ....	94
Figure 5.6. $S_{11}$ of the UWB antenna from measurement and ECM.....	94
Figure 5.7. Antennas at (a) broadside and (b) second orientation (aligning the main beam at 7 GHz). ....	95
Figure 5.8. Comparison of $S_{21}^b$ between simulation and measurement in the broadside direction. ....	95
Figure 5.9. Comparison of $S_{21}^a$ and $S_{21}$ at two orientations. ....	97
Figure 5.10. Effective aperture of the UWB antenna at two orientations. ....	98
Figure 5.11. Gain of the antenna at two orientations from the proposed process.....	98
Figure 5.12. Phase of $S_{21}$ from ECM and measurements with two orientations. ....	99
Figure 5.13. Minimum-phase component and antenna $S_{21}$ phase after removing the linear component in the broadside orientation. ....	100
Figure 5.14. Minimum-phase component and antenna $S_{21}$ phase after removing the linear component in the second orientation. ....	101
Figure 5.15. Group delay of antenna $S_{21}$ from broadside and second orientation measurements.....	102
Figure 5.16. Impulse responses of the $S_{21}^b$ FIR model for monopole at (a) broadside and (b) second orientation. ....	103
Figure 5.17. Frequency response in broadside: (a) antenna system and (b) $S_{21}^b$ measurement.....	104
Figure 5.18. Frequency response in second orientation: (a) antenna system and (b) $S_{21}^b$ measurement. ....	104
Figure 5.19. DCS with antennas at two orientations.....	105
Figure 5.20. Constellation diagram at 3.5 GHz for (a) broadside and (b) second orientation. ....	105
Figure 5.21. Constellation diagram at 6 GHz for (a) broadside and (b) second orientation. ....	106

Figure 6.1. Antenna structure and $S_{11}$ from simulation and measurement (all dimensions in mm). ..	113
Figure 6.2. $S_{21}$ of the Vivaldi antenna and the antenna's IIR model. ....	114
Figure 6.3. Poles and zeros of the IIR model in the s-domain using Method I for (a) antenna $S_{21}$ and (b) minimum-phase model. ....	115
Figure 6.4. Minimum-phase $S_{21}$ IIR model from the two methods. ....	116
Figure 6.5. Difference in group delay between the antenna $S_{21}$ and the two minimum-phase models. .	116
Figure 6.6. Derivation of a channel-transfer function for P2P using an inverse antenna system. ....	117
Figure 6.7. Stable inverse system of the Vivaldi antenna from the two methods. ....	118
Figure 6.8. IIR model from Method I and the model's inverse system, with both models' convolutions. ....	118
Figure 6.9. Vivaldi antenna $S_{21}$ and the inverse system, with the systems' convolutions. ....	119
Figure 6.10. Schematic of the environment in (a) Office1 and (b) Office2. ....	120
Figure 6.11. Measurements of $S_{21b}$ between the two Vivaldi antennas at 100-cm distance in (a) Office1 and (b) Office2. ....	120
Figure 6.12. Deconvolved channel-transfer function of Office1 at two distances. ....	121
Figure 6.13. Deconvolved channel-transfer function of Office2 at two distances. ....	122
Figure 6.14. DCS with Vivaldi antenna and channel. ....	123
Figure 6.15. Constellation diagram from Vivaldi antenna measurements in an anechoic chamber with distances of (a) 1 m and (b) 3 m. ....	124
Figure 6.16. Constellation diagram with a 1-m distance based on a Vivaldi antenna and a channel model in (a) Office1 and (b) Office2. ....	125
Figure 6.17. Constellation diagram with 1-m distance based on the channel model after de-embedding the antenna in (a) Office1 and (b) Office2. ....	125
Figure 6.18. Impulse response of the antenna $S_{21}$ in (a) commercial antenna and (b) inverse antenna effects. ....	127
Figure 6.19. Constellation diagram at carrier frequency of 2 GHz (a) after commercial antenna system and (b) with inverse time response system. ....	128
Figure 6.20. Constellation diagram at carrier frequency of 6 GHz (a) after commercial antenna system and (b) with inverse time response system. ....	128
Figure 7.1. Rectangular cavity design as a function of the reverberation chamber. ....	134
Figure 7.2. Photograph of the cube cavity used as a reverberation chamber. ....	136
Figure 7.3. Skin depth of the aluminium. ....	137
Figure 7.4. Surface resistivity of the aluminium. ....	137
Figure 7.5. Quality factor of the cube cavity from the aluminium walls. ....	138
Figure 7.6. Reverberation chamber constant of the cube cavity. ....	138
Figure 7.7. Measurement of $S_{11}^{RC}$ in the reverberation chamber. ....	139
Figure 7.8. Vivaldi antenna $S_{21}^{RC}$ measurements in the reverberation chamber with different orientations. ....	140
Figure 7.9. Commercial antenna $S_{21}^{RC}$ measurement in the reverberation chamber with different orientations. ....	141
Figure 7.10. UWB antenna $S_{21}^{RC}$ measurement in the reverberation chamber with different orientations. ....	142
Figure 7.11. Vivaldi antenna $S_{21}^a$ obtained from (a) $S_{11}^{RC}$ and (b) $S_{21}^{RC}$ measurement in the reverberation chamber. ....	144
Figure 7.12. Commercial antenna $S_{21}^a$ obtained from (a) $S_{11}^{RC}$ and (b) $S_{21}^{RC}$ measurement in the reverberation chamber. ....	144
Figure 7.13. Monopole UWB antenna $S_{21}^a$ obtained from (a) $S_{11}^{RC}$ and (b) $S_{21}^{RC}$ measurement in the reverberation chamber. ....	145

## List of Tables

Table 2.1: Recent research in deriving ECMs for different antennas.....	22
Table 3.1: Impulse response from Vivaldi antenna and channels. ....	57
Table 4.1: Comparison of EVM and BER with different carrier frequencies without adding noise. ...	80
Table 4.2: Experimental parameters.....	82
Table 4.3: Values of the attenuators used in the experiments. ....	83
Table 4.4: Comparison of EVM (%) between simulation and measurement after adding noise.....	85
Table 5.1: Gain in dB (broadside orientation).....	98
Table 5.2: DCS parameters. ....	107
Table 6.1. EVM and BER in different channels with a 1-m distance.....	126
Table 6.2. EVM and BER values in a DCS with an inverse antenna in the broadside orientation.....	128
Table 7.1. Cube-cavity properties of aluminium walls. ....	136

## Abbreviations

3D	Three-Dimensional
ADS	Advanced Design System®
AWG	Arbitrary Waveform Generator
AWR	Applied Wave Research
BER	Bit Error Rate
BTB	Back-to-Back
CPW	Coplanar Waveguide
CST	Computer Simulation Technology
CRLH	Composite Right/Left-Handed
DCS	Digital Communication System
ECM	Equivalent Circuit Model
EIRP	Effective Isotropic Radiated Power
EM	Electromagnetic
EVM	Error Vector Magnitude
FCC	Federal Communications Commission (US)
FFT	Fast Fourier Transform
FIR	Finite Impulse Response
HFSS	High Frequency Structure Simulator
IF	Intermediate Frequency
IFFT	Inverse Fast Fourier Transform
IIR	Infinite Impulse Response
LHS	Left-Hand Side
LoS	Line-of-Sight
LPDA	Log-Periodic Dipole Array
LTI	Linear Time-Invariant
MIMO	Multiple-Input-Multiple-Output
MWO	Microwave Office®
NLoS	Non-Line of Sight
OFDM	Orthogonal Frequency Division Multiplexing
P2P	Point-to-Point
PSK	Phase Shift Keying
QAM	Quadrature Amplitude Modulation

RF	Radio Frequency
RFID	Radio-Frequency Identification
RHS	Right-Hand Side
RLC	Resistor (R), Inductor (L), and Capacitor (C)
Rx	Receiving
S1P	One-Port <i>S</i> -Parameter
S2P	Two-Port <i>S</i> -Parameter
<i>S</i> -parameters	Scattering Parameters
SNR	Signal-to-Noise Ratio
TEM	Transverse Electromagnetic
TOSM	Through-Open-Short-Match
Tx	Transmitting
UWB	Ultra-Wideband
VSS	Visual System Simulator®
Wi-Fi	Wireless Fidelity

# CHAPTER 1: INTRODUCTION

## 1.1 Overview and Motivations

Understanding antenna effects in wireless systems has become an important part of achieving accurate system performance. Modern communication standards use digital modulations that can be affected by the antenna and the channel, which in turn influence the performance of the digital communication systems (DCSs). Errors in transmission might be caused by multipath channels, non-linearity in the radio frequency (RF) components, added noise in the channel, or by properties of the antenna such as non-linear transmission-phase response or rippling in the frequency response, both of which produce additional components in the time-domain response. These effects increase the symbol scattering of the systems and result in performance degradation. Thus, characterisation of the antenna and channel effects must be performed to understand the cause of the symbol scattering and to obtain optimum performance from the antenna. This characterisation also helps to identify sophisticated antenna structures to minimise the effect of the antenna in the DCS and to predict the effects of the channel.

Antennas are analogue dynamic systems whose equivalent circuits contain integrators, differentiators, and delay elements. These elements cause symbol scattering, which increases the bit error rate (BER) in DCSs. Most designers in the field aim to have non-dispersive wideband antennas and, ideally, for having a linear transmission phase across the frequency band in the direction of the physical channel [1], all of which can affect the DCS.

The main objective of this research is to propose techniques and experimental procedures for identifying those antenna properties in both the frequency and time domains that cause symbol scattering. Different antennas express time-varying delays in their impulse responses. In the time domain, the mean group delay indicates the rate change of the transmission phase with respect to the frequency. The signals will travel with different delays, and these delays then cause dispersion to the signal. This situation requires the derivation of a system model for an antenna to be included in a DCS in order to predict the antenna effects as dynamical dispersive systems. This

derivation will enable designers to understand the limitation of using an antenna in the multipath channel in a DCS and also to create better DCSs by choosing the optimum antenna design.

## 1.2 Antenna Characterisation

A conventional antenna design procedure starts by designing the antenna for a low-input scattering parameter ( $S_{11}$ ), following which the radiation pattern, antenna gain, effective aperture, and polarisation are obtained for certain frequencies of operation. These steps do not provide the performance of the antenna with respect to its physical orientation, which is an important factor to consider in point-to-point (P2P) communication applications and those cases of frequency-selective antenna transmission where the direction of the main beam is a function of frequency. Knowing the  $S_{11}$  value alone allows the total radiated power to be determined but provides no insight into the beam direction or its frequency dependence. It is important to distinguish between the total radiated power and the radiated power in the direction of the physical channel. Total radiated power in any direction is a function of frequency, angular direction (azimuth and elevation), and distance. The conventional procedure to obtain the frequency response in terms of effective aperture and gain requires measurement or simulation of the radiation pattern at a large number of frequencies, which is often impractical. A procedure is thus required to design P2P antennas and to predict performance in DCSs.

Antennas are typically characterised in P2P and domestic applications. P2P communications can be applied to different settings, such as in the use of two base stations and in satellite and military applications. The antenna parameters obtained from conventional designs are insufficient to completely characterise the antenna as a two-port network. This procedure also fails to provide essential antenna parameters such as the  $S_{11}$  phase and the complex transfer parameter ( $S_{21}$ ). Including the amplitude and the phase of the scattering parameters ( $S$ -parameters) can improve the accuracy of modulated transmission simulations. These parameters are important factors in DCSs, which are typically simulated and studied in the time domain. Characterisation of the antennas is usually performed in P2P communications, where the power is radiated in

a certain direction, whereas in domestic or office environments an alternative method is required to provide the total power transmitted by the antenna.

Accurate antenna characterisation is essential to derive circuit and system models. An accurately characterised circuit model will match the measured  $S_{11}$  in both phase and amplitude and will enable calculation of the total radiated power as well as the radiation resistance. This characterisation, which is useful especially if the antenna is to be used in domestic or office environments, tells designers about antenna behaviours such as frequency-variant radiation patterns and antennas' resonant structures. The system model enables the antenna simulation within the DCS simulation to predict the antenna effects in a DCS. The use of antenna responses in the frequency and time domains allows for an accurate representation of the antenna in wideband systems. Although several different methods have been proposed for obtaining the  $S_{21}$ , an accurate  $S_{21}$  for P2P communications can be obtained by conducting measurements in an anechoic chamber in the frequency domain [2]-[4]. The data from the  $S$ -parameter measurement can then be used to evaluate the time-domain response. The time and frequency responses can be computed, respectively, using the inverse fast Fourier transform (IFFT) and the fast Fourier transform (FFT) methods.

Measurements in an anechoic chamber yield the power radiated in P2P, whereas measurements in a reverberation chamber provide the total radiated power in all directions by an antenna [5]. The directivity of the two antennas is the difference between the two environmental measurements [6]. Measurements in a reverberation chamber can be used for domestic applications. Different circuit and system models for antennas are required because of this difference between P2P and domestic communications. These models and the antenna characterisation can then be used in various applications.

### *1.2.1 Equivalent Circuit Model for Antennas*

Representing an antenna as a two-port equivalent circuit will help designers relate the frequency response of the antenna to its physical structure. Equivalent circuit models

(ECMs) can be derived from the amplitude and phase of  $S_{11}$  or from the complex input impedance ( $Z_{11}$ ). The radiation resistance is typically identified at the second port, and the radiated power is the power dissipated within that resistance. Researchers have recently shown interest [7]-[15] in the development of accurate ECMs for antennas operated within microwave bands, but their focus has mainly been on the amplitude response of  $S_{11}$ , without considering the phase [7]-[15], which means that the electromagnetic (EM) structure of the antenna is not represented by circuit elements. Such circuits also fail to provide the phase of  $S_{21}$ , which results in inaccuracies in modelling the antenna  $S_{21}$ . Including the phase as well as the amplitude of  $S_{11}$  preserves information about antenna parameters and properties such as  $Z_{11}$  and  $S_{21}$  as well as the behaviour of the antenna as a resonant structure and the antenna's frequency-invariant radiation pattern.

### *1.2.2 Antenna System Model*

Modelling the antenna as a system allows for antenna simulation in an end-to-end wireless channel link, which then allows designers to analyse the effect of antennas in DCS simulation software [16]-[18]. Antenna models can be derived from either an infinite impulse response (IIR) or a finite impulse response (FIR) to confirm the compatibility of the antenna within the DCS simulation. Measuring the full set of four  $S$ -parameters using two identical antennas in an anechoic chamber for P2P communications increases the antenna modelling accuracy [2]-[4]. Including the amplitude and phase of the full  $S$ -parameters is important for deriving an accurate system. One aim of the current study is to derive a time-domain system model from the antenna's frequency-domain measurement. This technique will enable designers to predict the effects of an antenna on the modulated signal (16-QAM and 64-QAM) in a DCS and to characterise the symbol scattering that occurs. IIR system models will also be developed to derive an inverse antenna system for characterising channels for P2P communications by de-embedding the two antennas from the measurements conducted within multipath channels. Deriving a time-domain FIR system model for an antenna is discussed further in Chapter 4, while the inverse antenna system is discussed in Chapter 6.

### 1.3 Minimum and Non-Minimum Antenna Phase

Antennas can be categorised into minimum and non-minimum phase [2], [3], [19]. The phase of  $S_{21}$  is related to the path of energy transmission across the antenna's ECM [4]. Therefore, the minimum phase of  $S_{21}$  can occur only if one path exists through the network. For instance, a ladder network has minimum phase because it has a single path for energy transfer. Research shows that not all antennas provide a minimum phase [2], [3], [19]. Well-known minimum-phase examples include the horn and Vivaldi designs, both of which are minimum phase only at their principal axes [4], [20]. A minimum-phase antenna will have a frequency-invariant radiation pattern and a non-resonant structure over the band on its principal axis. To the best of my knowledge, no comprehensive studies have yet been conducted to determine the transmission-phase response in the performance of non-minimum-phase antennas.

### 1.4 Antenna Gain

Conventional gain measurements are often conducted in an anechoic chamber using calibrated reference antennas with a fixed distance in the far field. This setup requires time and effort, however, and building and maintaining the chamber is relatively costly. Anechoic chambers are rarely installed for these reasons. Hirano, Hirokawa, and Ando [21] proposed a technique to obtain the gain by taking the measurements in an anechoic chamber over two sets of distances. However, the accuracy of the distances, and the replacement of calibrated reference antennas by using conventional designs, may affect the accuracy of the gain measurements. In addition, most calibrated reference antennas have changeable phase centres over the frequency axis, and the measurements are usually taken from the aperture of the horn [22]. This situation also decreases the accuracy of the distance measurement, resulting in inaccuracies in gain measurements. Instead, by taking one  $S$ -parameter measurement with one distance, the accuracy will be increased, thus yielding precise gain measurements over the frequency axis. The present study will also predict the frequency response without having to resort to using an anechoic chamber, which enables the determination of the gain and the group delay.

## **1.5 Antenna Effects in Digital Systems**

The purpose of the antenna system model is to determine the compatibility of the antenna within the DCS simulation in order to predict antenna effects in a DCS. Symbol scattering in DCSs can be caused by antennas [16]-[18]. Modelling antennas and channels in the time domain improves the accuracy of modulated transmission simulations. Antenna effects are usually included in the total effects from the two antennas and the channel. The effects of the antenna on the modulated signal need to be studied in both the frequency and time domains. Doing so also allows designers to improve antenna designs for robust DCS performance. While previous studies [16]-[18] have found that some antenna behaviours distort the signal at certain frequencies in the operating range, the effects of antennas at different orientations need to be analysed in terms of the symbol scattering that occurs due to the radiation pattern. The effects of the antenna and channel should also be examined separately in a DCS. Error vector magnitude (EVM) and BER are commonly accepted metrics when characterising symbol scattering and examining system performance.

## **1.6 Channel Characterisation**

Antenna effects are included in the total effects from the measurement obtained between the two antennas in a channel. As a result, de-embedding the antenna from the  $S$ -parameter measurements is another aim of the present study. This step allows for identifying the responses in the time and frequency domains of both the antenna and the channel; it also allows for an analysis of the channel in addition to characterisation of the antenna. This technique allows for the channel's separation from the antenna measurement in a channel.

The impulse response of an antenna is related to the electric field surrounding the antenna [23]. Research has shown that the effect of the antenna impulse response was neglected in the standard interpretation of the impulse response of the wideband wireless channel in earlier studies [23], [24], such as in the popular Saleh-Valenzuela model [25]. The hypothesis of having several independent multipath components in a wideband wireless channel model has also shown that the impulse response for each multipath manifests the antenna impulse response [24], [26]. One prominent drawback

in statistical models that characterise the impulse response of the ultra-wideband (UWB) channel is that the designers of such models assume that the antennas do not affect the channel response and that the antennas will not cause any signal distortion. The channel response due to the antenna essentially depends on the antenna's time response and the transmission phase, which in turn depend on antenna structure and radiation patterns.

Multipath-channel modelling, which is conventionally obtained from the measurements between two antennas, assumes that the antennas do not cause signal distortion. This situation indicates that the antenna response is embedded within the channel. The antenna's inverse response is necessary to de-embed the antenna from the channel. A technique is required to de-embed antennas from measurements taken between two antennas and to predict channel effects only, especially in DCSs. Such a technique will enable designers to derive inverse systems for different antennas to be used in various applications in DCSs, as will be discussed in Chapter 6.

## **1.7 Research Objectives and Contributions**

The purpose of the present research is to identify the antenna properties and channel characteristics, in both the frequency and time domains, that cause symbol scattering. Such identification will be done by characterising different antennas and multipath channels and by deriving circuit and system models for the antennas. Calculating the frequency response of the transmission between two antennas in a specific direction is required in P2P communications. Conventional antenna design methods are unsuitable for P2P communications, since by realising a low  $S_{11}$ , they only provide the total radiated power. A novel procedure hence is required to design and predict the performance of P2P antennas in DCSs. This characterisation procedure will then be used for different applications.

### *1.7.1 Objectives*

The main aims of this research are to:

1. characterise different antennas in P2P communications and office environments;

2. derive accurate circuit models to show the total radiated power and to characterise antenna behaviour;
3. develop system models from the  $S$ -parameter measurements, to be included in a DCS;
4. predict the effects of the antenna in a DCS;
5. design antennas with minimum transmission phase to simplify the equalisation of  $S_{21}$  and to achieve minimal effects in DCSs;
6. derive inverse antenna systems for different applications in DCSs for P2P communications, such as for characterising stationary multipath channel-transfer functions and for compensating for antenna effects in DCSs to reduce the BER.

### 1.7.2 Contributions

The main contributions produced from this study's characterisations, and from the models that are derived and used in different applications, are the ability to:

- extract the impulse response of transmit-receive antennas from a multipath channel using only one  $S$ -parameter measurement in the channel;
- obtain the frequency response of an antenna without requiring access to an anechoic chamber;
- undertake comprehensive studies to determine the transmission-phase response in the performance of non-minimum-phase antennas;
- characterise the antenna's frequency response in terms of effective aperture and gain;
- predict the antenna effects in DCSs by including the antenna system model in a DCS;
- derive a stationary multipath channel-transfer function by using an inverse antenna model;
- predict different channel effects in DCSs;
- calculate the antenna losses from the measurement in a reverberation chamber.

## 1.8 Methodology and Design Steps

Different types of antennas are designed in this thesis for a microwave frequency range by first obtaining the  $S_{11}$  value from an EM simulator. Those results are then compared with the results from the measurements acquired by using a network analyser. An ECM is then derived based on each physical antenna structure in order to characterise the antenna behaviour and to obtain the total radiated power. The  $S$ -parameters are measured in an anechoic chamber to obtain the frequency response of each antenna and to compute the impulse response in the time domain. Comprehensive studies are also conducted to determine the transmission-phase response in the performance of the antennas.

For this characterisation procedure, two different transmission  $S$ -parameters are used for each antenna. These parameters can be defined as follows:

- $S_{21}^a$  provides the total power transmitted by the antenna in all directions and is used to characterise antennas in domestic or office environments.
- $S_{21}^b$  provides the power radiated in a certain direction for P2P communications. This can be measured in an anechoic chamber to eliminate the multipath components.

Following this characterisation, either the  $s$ -domain linear time invariant (LTI) IIR model or the FIR can be derived for each  $S$ -parameter. The effect of each antenna on the simulation of a DCS can then be predicted. Lastly, stationary multipath channel-transfer functions are extracted from the antenna's system measurements by de-embedding the transmitting (Tx) and receiving (Rx) antenna system models from the global transfer function of a radio link in a desired channel for P2P communication.

This research uses different techniques and methods to characterise different types of antennas, including Vivaldi, patch, commercial dual-band, and monopole UWB antennas. Five techniques are applied to characterise the antennas, including the Hilbert transform method, equivalent circuit modelling, anechoic chamber measurement, reverberation chamber measurement, and the time-domain technique.

The steps followed to characterise and model the antenna and channel for different applications are as follows:

1. Measure the four  $S$ -parameters of a channel consisting of two identical antennas in an anechoic chamber.
2. Analyse the antenna-transmission phase based on the linear, minimum, and all-pass phase components. This analysis enables the derivation of an ECM and the antenna's behaviour characterisation.
3. Develop a lumped/distributed ECM for each antenna. This is the 'circuit model'.
4. Calculate the time-domain response and digital filter equivalent for each  $S$ -parameter.
5. Develop a time-domain model for the whole antenna. This is the 'system model'.
6. Use the system model to study the effect of the antenna in a DCS.
7. Derive an inverse antenna system to generate stationary multipath channel-transfer functions and to compensate for the antenna effects in a DCS.
8. Predict the effects of various channel models from the measurements in different office environments in a DCS.
9. Compute the total radiated power from the measurement in a reverberation chamber to identify the antenna losses.

## **1.9 Measurement Techniques**

Several measurement techniques are typically used to characterise antennas. Measurements conducted in an anechoic chamber are used to characterise antennas in P2P communications, whereas measurements conducted in reverberation chambers yield the total radiated power, which can be used to characterise antennas in domestic applications. Measurements in an anechoic chamber provide the power radiated in a certain direction, whereas measurements in a reverberation chamber provide an antenna's total radiated power in all directions. Knowing the radiation patterns of an antenna is important for antenna characterisation, especially in terms of the channel that is used. Zhao, Hu, and Chen [6] examined an antenna's power received between measurements in an anechoic chamber and a reverberation chamber. The relationship

between the two different environments was found to be the directivity of the Tx and Rx antennas and was verified using the power received in the anechoic chamber and the average power received in the reverberation chamber.

To characterise a channel in general, measurements must be conducted in a reverberation chamber, since such measurements provide the antenna's total radiated power, which will radiate in all directions, especially in office environments. Measurements conducted in office environments take on the properties of the antennas and their channel characteristics, which depends on the antenna's radiation pattern. To characterise the effects of a channel, the measurements must be done in an office environment.

### *1.9.1 Anechoic Chambers*

Measurements taken in an anechoic chamber provide the power radiated in certain directions. Such chambers are used for P2P communications. Anechoic chambers are built with absorbers on all side walls, the floor, and the ceiling and are equipped with expensive RF components.

### *1.9.2 Reverberation Chambers*

Conducting measurements in a reverberation chamber provides the total radiated power and is used for domestic applications. A reverberation chamber is a room with minimal absorption of EM energy. In this work, a medium-size cube cavity of  $1 \text{ m}^3$  with aluminium walls was built for the antenna measurements inside the reverberation chamber of the cube. The reverberation chamber was designed from metallic walls so that the measurements could be done inside the cube cavity. Some losses occurred due to the skin depth of the material used in the wall. This step is required to compensate for cavity losses to obtain the total radiated power by the antenna and to identify any losses due to the antenna itself.

### *1.9.3 Office Environments*

Measurements conducted in an office environment will mix the antenna properties with the channel characteristics. The total radiated power by the antenna travels in all directions and produces multipath components in the time-domain response. The

multipath components in fact manifest the antenna-impulse response that is used in the measurement. Hence, the antenna properties must be de-embedded from the channel measurement in order to accurately characterise stationary multipath channel-transfer functions.

## 1.10 Software and Measurement Facilities

Several simulations and measurements were carried out in an antenna lab to execute this research. Various software components were used, as follows:

- MATLAB, including SIMULINK, for system models and signal processing and general computing
- Advanced Design System® (ADS) software for circuit simulation
- Computer Simulation Technology (CST) Microwave Studio Suite® for antenna layout simulation
- an anechoic chamber for the antenna measurements in the free-space channel
- a reverberation chamber for the antenna measurements to yield the total radiated power
- different office environments for the antenna measurements within multipath channels
- an engineering lab, including a network analyser with calibrated equipment
- symbol-scattering equipment, including an arbitrary waveform generator (Tektronix AWG7122C), an oscilloscope (Tektronix DPO72304DX), two broadband RF amplifiers, and various attenuators with different values

## 1.11 Analysis

The antenna and multipath channels developed in this work were analysed in several ways. These methods included:

- comparing the simulated circuit and system models with measurement data;
- matching the frequency-domain response;
- comparing the experimental results with the simulation results;
- applying the Hilbert transform to obtain the minimum phase of the  $S_{21}$ ;
- using plot pole-zero diagrams in the  $s$ -domain to identify the antenna phase and stability of the antenna's system model;

- computing the impulse response of the antenna system;
- applying IFFT-FFT to convert the antenna's frequency responses into time-domain responses, and vice versa;
- calculating the group delay and dispersion, which are related to the antenna phase; the phase then affects the symbol scattering in DCSs.

## 1.12 Publication List

- [1] M. Almoteriy, M. Sobhy and J. Batchelor, "Antenna Characterization as a Two Port Network," at the 2016 Loughborough Antennas & Propagation Conference (LAPC 2016), November 2016.
- [2] M. Almoteriy, M. Sobhy and J. Batchelor, "Antenna Characterisation and Channel Effects on Digital Systems," at the 2017 Loughborough Antennas & Propagation Conference (LAPC 2017), November 2017.
- [3] M. Almoteriy, M. Sobhy and J. Batchelor, "Derivation of Circuit and System Models for Microwave Antennas." School Research Conference 2018, Poster, School of Engineering and Digital Arts, University of Kent.
- [4] M. Almoteriy, M. Sobhy and J. Batchelor, "Establishing the Limits of Antenna Measurement in Fading Channels," at the European Conference on Antennas and Propagation (EuCAP 2018), London, in April 2018.
- [5] M. Almoteriy, M. Sobhy and J. Batchelor, "Antenna Modelling Technique for Digital Communication Systems," at the 15th International Conference on Synthesis, Modeling, Analysis and Simulation Methods and Applications to Circuit Design (SMACD 2018) in July 2018.
- [6] M. Almoteriy, M. Sobhy and J. Batchelor, "Characterisation of Wideband Antennas for Point-to-Point Communications," published in IEEE Transaction on Antennas and Propagation, September 2018.
- [7] M. Almoteriy, M. Sobhy, J. Batchelor, S. Noor, and N. Gomes, "Antenna Simulation and Effects in Digital Communication Systems," at the 2018 Loughborough Antennas & Propagation Conference (LAPC 2018), November 2018.

- [8] M. Almotery, M. Sobhy and J. Batchelor, “Inverse Antenna Systems and Their Applications in Digital Communication,” submitted in IET Microwave Antennas & Propagation journal, October 2019.

### **1.13 Organisation of the Thesis**

This thesis, which presents simulation, measurement, and experimental results, is divided into eight chapters. Chapter 1 has provided an introduction in which conventional antenna design has been shown to be insufficient for completely characterising an antenna as a two-port network. The chapter has also shown the impracticality of conventional design method for characterising antennas in domestic and P2P communication applications. This characterisation is required in order to include an antenna and a channel in DCSs.

Chapter 2 provides a literature review of previous work in antenna modelling as two-port networks. The chapter also highlights how the phase of  $S_{11}$  and the transmission phase  $S_{21}$  have thus far been largely ignored in antenna characterisation. The parameters obtained from conventional antenna designs are insufficient for characterising an antenna as a two-port network in order to be included in DCS simulation. Recent studies in the literature on antennas’ two-port ECMs show that most ECMs only match the amplitude of  $S_{11}$ , without the phase being considered. The literature also shows that minimum-phase antennas exhibit specific directionality and that not all antennas have a minimum phase. Minimum-phase examples include horn and Vivaldi antennas. Research also shows that antennas cause symbol scattering in DCSs.

The characterisation of wideband Vivaldi and narrowband patch antennas is investigated in Chapter 3. The antennas are characterised by (1) deriving an ECM, (2) processing the measurements between two identical antennas in an anechoic chamber, and (3) applying the Hilbert transform to the amplitude of antenna  $S_{21}$ . The  $S_{21}$  results from these three techniques are then compared and discussed. Chapter 3 also includes an explanation of how antennas and channels can be characterised from only one S-parameter measurement in a multipath channel. Doing so will allow designers to

obtain the frequency response of the antenna without using an anechoic chamber, which will then enable them to determine the gain and the group delay of the antenna.

Chapter 4 demonstrates the modelling of an antenna so that its effects can be predicted when the antenna is used in a DCS. This technique is applied to commercial dual-band and Vivaldi antennas. An ECM is derived for the commercial antenna to characterise its behaviour and to compute the total radiated power in the frequency domain. A time-domain FIR system model is then derived to enable the estimation of the antenna's effects in a DCS. Symbol-scattering experiments are also performed in an anechoic chamber and then verified using a DCS simulation model. The experiments and simulations confirm the same effects from each antenna type in the DCS. The equivalent noise caused by the RF components is also considered in the simulation. As Chapter 4 will show, the symbol scattering and the change in EVM are dependent on the type of antenna that is employed.

Chapter 5 presents a characterisation of a non-minimum-phase antenna, which is especially important in P2P communications, since the frequency response can vary due to changes in the radiation pattern in the physical channel. The Friis equation is modified in terms of total radiated power and radiated power in a certain direction. The effective aperture and gain are then derived for identical antennas with respect to the frequency axis. This chapter also presents a process for investigating the frequency response of a wideband antenna to identify the best orientation of the antenna for P2P communications. The process allows for predicting the antenna's effective aperture and gain for each orientation. The technique is validated by using a non-minimum-phase monopole UWB antenna. An ECM for the UWB antenna is derived to obtain the total radiated power and to study the antenna's behaviour. The frequency-variant radiation pattern is ascertained from the  $S_{21}$  phase obtained from the ECM. The  $S_{21}$  phase is then analysed based on the linear, minimum, and all-pass phase components. This analysis then enables the derivation of an ECM. Finally, the various antenna effects in a DCS with different orientations are examined.

Chapter 6 demonstrates a new approach to modelling an inverse antenna system for two different antennas for P2P communications and then applying them in various applications in DCSs. Two applications are described: through characterising

the multipath channels and by compensating for the antenna effects in a DCS. A stable inverse system is derived for a minimum-phase Vivaldi antenna to characterise the stationary multipath channel-transfer functions in the frequency domain. The inverse model is achieved by eliminating the linear-phase component using two methods: by applying the Hilbert transform and by shifting the zeros of the antenna IIR system model to the left-hand side (LHS) of the  $s$ -plane. The inverse system is then applied to the measurement within two different office environments for characterising different multipath office channels. The antenna effects and various office-channel conditions are also investigated in a DCS. Another application of an inverse antenna system was applied to compensate for antenna effects as a way of reducing the BER in the DCS and improving system performance. The two different antennas examined in the chapter were selected because Vivaldi antennas exhibit few effects in digital systems when different channels are characterised, while an inexpensive commercial antenna was used because such antennas do have effects in digital systems.

Chapter 7 presents a technique for obtaining the total radiated antenna power from the antenna measurements in a reverberation chamber. A medium-size cavity with aluminium walls was built as a reverberation chamber for measuring the different antennas within the chamber. In general, these measurements are useful for characterising antennas in domestic applications, as measurements conducted in a reverberation chamber show the total radiated power. An empirical equation is then derived for compensating the cavity losses due to the walls using a Vivaldi antenna. Such an antenna is used for calibration purposes because it is lossless. The cavity is used as the standard to compute the total antenna effects for different antennas and to identify any losses caused by the antenna itself.

Chapter 8 concludes the thesis and discusses relevant future work in antenna and channel characterisation that will enhance other research in this field.

## CHAPTER 2: LITERATURE REVIEW

### 2.1 Introduction

Chapter 2 presents a discussion of relevant research related to the scope of this thesis. The intention of the present work is to provide insights into established methods and relatively recent contributions to antenna characterisations as two-port networks as well as noting the drawbacks of such networks in antenna modelling. Most studies in the literature focus on ECMs for different antennas and examine antenna-transmission phases. Conventional antenna designs have been shown to be insufficient for completely characterising an antenna as a two-port network. This chapter describes previous work in antenna and channel characterisation and the state-of-the-art technologies available to analyse modern digital systems, especially in regard to antenna characteristics.

### 2.2 Antennas as Two-Port Networks

Three main categories of two-port antennas are typically discussed in the literature: (1) antenna ECMs, (2) antenna models that allow for self-tuning (in the case of  $Z_{11}$  models) and mutual ( $Z_{21}$ ) impedances such as arrays and radio-frequency identification (RFID) systems, and (3) those two-port antenna models that control the matching of antennas by the use of RF circuitry designs.

#### 2.2.1 *Antenna Equivalent Circuits*

Two-port ECMs can be used to model antennas. Several recent works have focussed on the development of accurate ECMs for antennas that operate within microwave bands. The focus of these studies has mainly been on the amplitude response of  $S_{11}$ , however, without considering the phase [7]-[15]. Neglecting the phase does not yield an accurate representation of  $S_{21}$ .

The key to deriving the ECM of an antenna is to calculate the  $S$ -parameters, along with the limiting bandwidth and the achievable matching  $S_{11}$  in both amplitude

and phase. Two approaches are commonly described in the literature for synthesising the ECM of antennas: physical models and mathematical models. Physical models are related to the physical design of an antenna and are based on selecting a circuit topology, where the circuit components can be related directly to the EM structure of the antenna. Most mathematical models, in contrast, are based on curve fitting to match the  $S_{11}$  impedance bandwidth. The circuit elements derived in mathematical models cannot be related to the EM structure of the antenna (unlike in the physical model) and hence lack any physical meaning. An ECM may contain a combination of lumped and/or distributed components. Lumped elements usually consist of inductors, capacitors, and resistors, so several types of complex two-port network models can be used to characterise and model antenna performance.

As the following brief overview of recent studies in the literature on the ECMs of antennas shows, most ECMs only match the amplitude of the  $S_{11}$ , without the phase being considered.

In [7]-[15], [17], [18], ECMs were derived for a variety of antennas. In [8]-[10], the researchers focussed on microstrip antennas, which are printed onto circuit boards and have two physical dimensions. Moradikordalivand *et al.* [8] derived an ECM for a broadband microstrip-fed antenna based on the ‘stepped cut four corners’ technique from a single mode to a broadband mode in the frequency range 0.5–3 GHz. The ECM for an antenna with a single model for a narrowband frequency was derived as shown in Figure 2.1. The ECM for a broadband microstrip-fed antenna was then derived by starting from the ECM of a narrowband antenna, as shown in Figure 2.2. The authors noted reasonable agreement in the amplitude of  $S_{11}$  between the ECMs and the antenna simulation.

Lin and Chung [9] represented a compact microstrip antenna excited by a T-shape resonator by using a second-order Chebyshev bandpass filter in the frequency range 4.4–5.6 GHz. The complex input impedance of the Chebyshev circuit and the U-shape patch antenna were matched by calculating the element values of the prototype Chebyshev filter response. The amplitudes of the  $S_{11}$  values obtained from the measurement and the Chebyshev circuit were also found to be reasonably matched [9]. Kufa, Raida, and Mateu [10] proposed an approach for a filtering planar antenna

design to be modelled using an ECM with a single port. A three-element patch antenna array was represented by the ECM, where each patch antenna in the planar array was represented by a parallel RLC circuit, which is a circuit consisting of a resistor (R), an inductor (L), and a capacitor (C) connected in parallel. The amplitude values of  $S_{11}$  from the layout simulation using CST and from the ECM were nearly matched within the frequency range 4–8 GHz. Subsequently, this ECM, the frequency response of which resembled that of a band-pass filter, was transformed into its prototype low-pass equivalent.

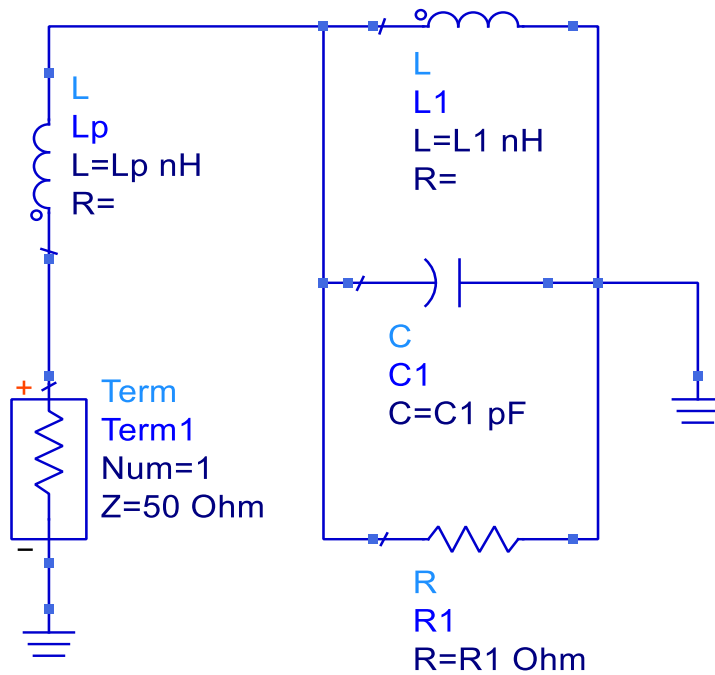


Figure 2.1. An ECM for a narrowband antenna.

Research on the ECMs of UWB antennas has shown that a few common techniques may be used to represent different UWB antennas [7], [11], [12]. Heong, Chakrabarty, and Hock [11] derived an ECM for an ultra-wideband rectangular-printed disc monopole antenna with an etched slot by comparing only the amplitude of  $S_{11}$ . The resistors and inductors in the ECM represented the surface resistance and inductance values of the patch antenna. The authors compared the amplitude of  $S_{11}$  by changing the slot width and the element values in the ECM in the frequency range 1–12 GHz. The results of the  $S_{11}$  amplitude from the antenna simulation and the ECMs were found to be quite similar, with only a slight shift in the resonance frequency [11]. Guo *et al.*

[12] derived a complicated ECM of an ultra-wideband antenna with a frequency range of 2.8–14 GHz by adding lumped elements to an initial RLC circuit to match the response of the complex input impedance from the antenna simulation. Wang, Jiang, and Li [7] derived an ECM for an ultra-wideband antenna with a triple-frequency rejection band. The notches were represented by series RLC circuit elements at rejection frequencies of 2.92 GHz, 4.06 GHz, and 5.28 GHz. The amplitude values only of  $S_{11}$  from the full wave simulation and from the ECM were compared and were found to nearly match.

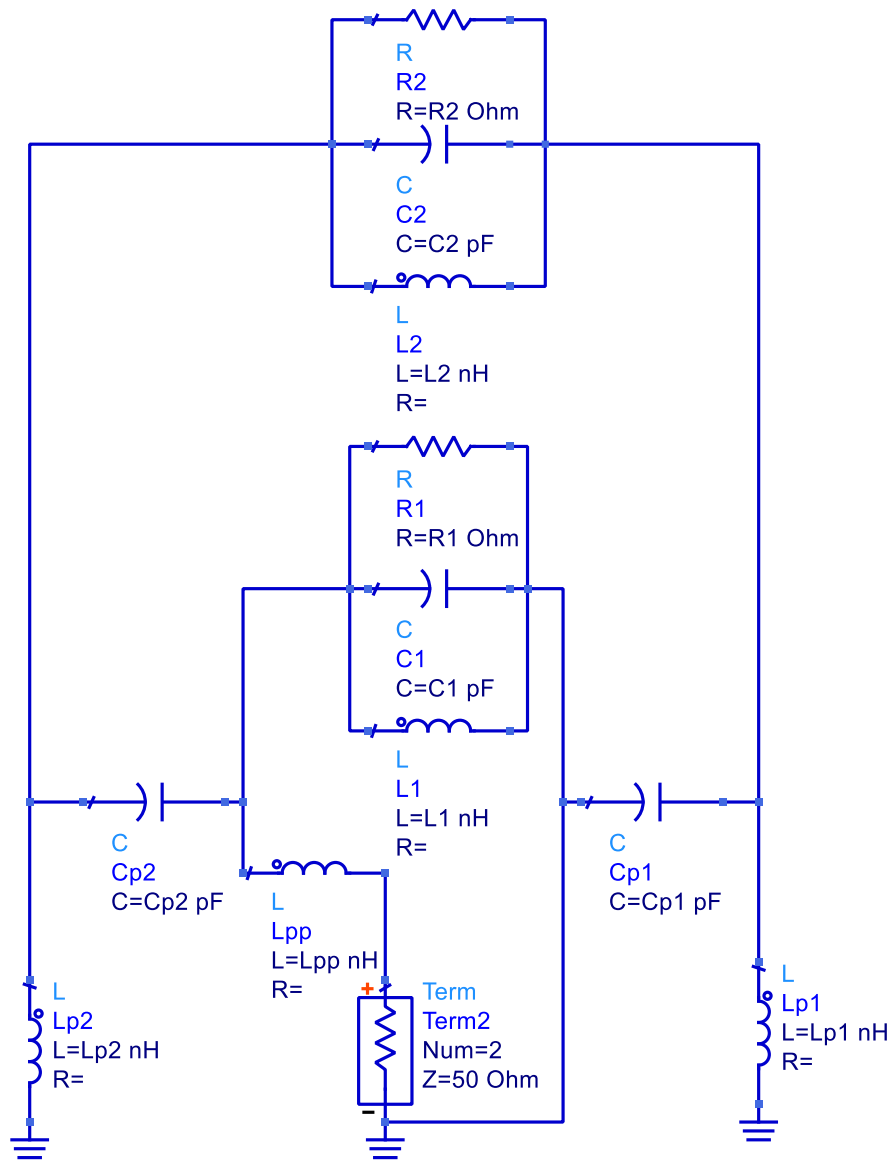


Figure 2.2. An ECM for a broadband microstrip-fed antenna.

Research has also been conducted on other types of antennas, such as dipoles, feed horns, and various types of bowtie antennas. Li *et al.* [13] proposed a novel Gauss filter technique to derive an ECM for a dipole antenna. The ECM was derived by applying the technique of characteristic modes. In their study, each mode represented the radiation mode of the antenna, which had a band-pass filter response. Then, the two band-pass filters were combined in parallel to represent the dipole antenna. The amplitude of  $S_{11}$  and the input impedance between the antenna simulation and the ECM were well matched within the frequency range 30–300 MHz.

An approach has also been developed to derive the ECM of a terahertz feed-horn antenna in the band 1.2–1.3 THz [14]. The results of determining the amplitude value of  $S_{11}$  from an antenna simulation and an ECM were found to be reasonably matched in the band. Moulay, Abri, and Abri Badaoui [15] derived ECMs for mono-band, dual-band, and quad-band bowtie antennas. The amplitude of  $S_{11}$  was provided from the ECM as well as from the three different full-wave antenna simulations: exploitation CST, the High Frequency Structure Simulator (HFSS), and Momentum. The results of the amplitude values of  $S_{11}$  from all antenna layouts simulated by adopting CST, HFSS, and Momentum were compared with the results from the ECM and were found to be reasonably matched [15].

Sobhy, Sanz-Izquierdo, and Batchelor conducted two studies in which they derived an ECM for a wearable button antenna where the amplitude and phase values of  $S_{11}$  matched the values from the antenna simulation in CST software [17], [18]. This matching was achieved in the response of the  $S_{11}$  value between the ECM and the full-wave simulation with a frequency range 1–7 GHz. Three choices of ECM were available, allowing for negative values, positive values, and a combination of lumped and distributed circuit elements [17]. Good agreement was noted in the input current values between the three choices of ECMs. Furthermore, the authors extended their work from [17] in [18] by explaining the technique of deriving circuit and system models for a wearable button antenna. The radiation resistance, power, and voltage-transfer function were calculated (respectively) after deriving the ECM, as shown in Figure 2.3. These values were then used to derive system models for Tx and Rx antennas. In general, designers can use the ECM to relate the antenna response to the structure of the antenna in terms of the antenna's dimensions. The authors of [18]

derived the ECM based on the  $S_{11}$  of the wearable button antenna, which can be used for wireless fidelity (Wi-Fi) and Bluetooth applications [27]. The authors identified the radiation resistance in the ECM and computed the  $S_{21}$ . This  $S_{21}$  value from the ECM then provided the total radiated power, which in general helps to characterise antennas in domestic applications.

Table 2.1 summarises the works that have achieved ECMs from different resources. Note that matching the amplitude and phase of  $S_{11}$  and computing the radiation resistance and  $S_{21}$  from ECM have only been done for a wearable button antenna [17], [18].

Table 2.1: Recent research in deriving ECMs for different antennas.

Antenna type	Amplitude of $S_{11}$	Phase of $S_{11}$	Complex of $Z_{in}$ or $Y_{in}$	Radiation resistance	$S_{21}$ calculated	Reference number
Triple-frequency rejection band UWB (2017)	√					[7]
Broadband modified rectangular microstrip-fed monopole (2014)	√					[8]
Compact filtering microstrip (2011)	√		√			[9]
Three-element patch antenna array (2014)	√					[10]
UWB rectangular printed disc monopole (2012)	√					[11]
UWB antenna (2010)			√			[12]
Dipole antenna (2015)	√		√			[13]
Terahertz feed horn (2015)	√					[14]
Bowtie antennas (2015)	√					[15]
Button antenna (2006 & 2007)	√	√		√	√	[17], [18]

Rogers, Aberle, and Auckland [28] also derived an ECM by replacing the resistor with a transformer and considering the efficiency. A planar inverted F antenna was represented as a two-port network ECM in the frequency range 800–900 MHz [28]. The ECM comprised a simple series RLC circuit, where the radiation resistance was replaced by a transformer. An amplifier or attenuator block was added to the ECM to model the directivity of the antenna. This model was developed to observe the effect of the antenna in a wireless link by using efficiency measurements. Two methods were used to measure the efficiency: the spherical near-field Satimo range technique and the Wheeler cap technique. The measurements from using the different methods were found to agree along the frequency axis. The total efficiency, which yields the amplitude of the antenna's  $S_{21}$  value, was obtained and was used to evaluate the band-pass and band-reject responses of the antenna. The  $S_{21}$  phase was not discussed in [28], however.

Zhao *et al.* conducted a study of an antenna's power received between measurements in an anechoic chamber and a reverberation chamber [6]. The relationship between the two different environments was found to be the directivity of the Tx and Rx antennas and was verified using the power received in the anechoic chamber and the average power received in the reverberation chamber.

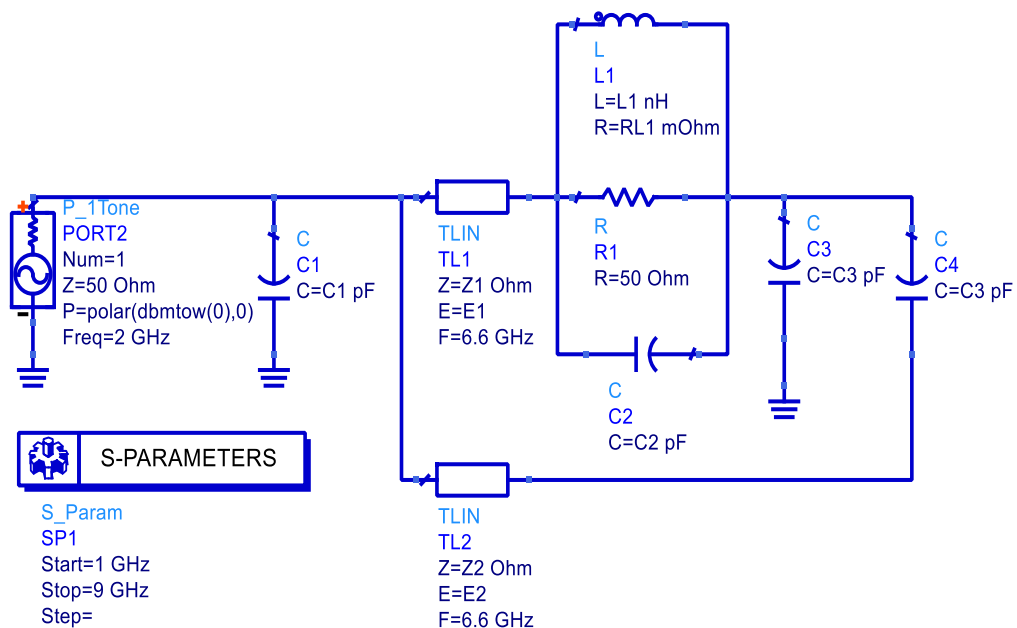


Figure 2.3. ECM for a button antenna.

### 2.2.2 *Antenna Mutual Impedance*

Antennas may also be modelled as two-port networks that are able to control the  $Z_{11}$  and  $Z_{21}$  values; examples include arrays and RFID systems [29]-[31]. Tseng and Chung designed and characterised a two-port aperture-coupled microstrip antenna in their study [29]. The two ports were the feeding and coupling microstrip lines, respectively, both on the same layer and running parallel to each other. The radiating patch was separated from the feeding/coupling layer by a ground plane with two rectangular apertures, one above each microstrip. The principle of operation followed in their study [29] is as follows. An electromagnetic field from the feeding line was coupled onto the radiating patch via the aperture on the ground plane, and a part of this field was coupled back into the coupling line via the second aperture. Stubs were used on the feeding and coupling lines to tune the coupled power and the antenna resonance. The antenna was used to design an oscillator circuit, where this antenna structure was used both as a radiating element and as a feedback resonator [29].

Piazza, Michele, and Dandekar [30] built a leaky-wave antenna, which uses a guided structure, by using composite right/left-handed (CRLH) materials for a line loaded with two varactor diodes with two inputs. This step was taken to achieve the same gain and matching impedance between the two ports of the array. High-radiation-pattern configurability for multiple-input-multiple-output (MIMO) communication systems was also attained. While the two papers discussed above ([29] and [30]) focussed on characterising two-port antennas – as well as their coupling, which controls the mutual impedances between the two ports – our goal in the present work is to model and characterise a one-port wideband antenna.

Caizzone, DiGiampaolo, and Marrocco described a novel pole-zero synthesis and analysis technique to characterise the phase response of the backscatter between an RFID reader and a tag [31]. The proposed system consisted of an RFID reader, a tag, and a sensor. The analysis itself was based on the mutual impedance coupling between the tag and the sensor. Essentially, a change in a physical environment (such as in temperature or chemistry) will affect the load impedance of the sensor, which in turn changes the impedance of the tag due to the mutual coupling. As a consequence, any backscatter phase and amplitude changes can be computed. The backscatter

amplitude and the change in backscatter phase were parameterised as mathematical equations [31], which were defined as the phase response and the amplitude response. Intuitively, while the amplitude-response equation is a mathematical representation of the communication range between the tag and the reader, the phase-response equation represents the change in backscatter phase. These functions depend on the load impedance (i.e. sensor impedance) as well as other fixed parameters, which, when arranged into a mathematical formulation, contain the poles and zeros of the system. Then, since the complex load impedance of the sensor depends on the derived amplitude and phase-response equations, by plotting their contours (as isolines) over the complex  $Z_L$  plane, a nomogram may be obtained. The above contours can be used for properly constraining the poles and zeroes to obtain desired communication ranges and phase resolution/span.

Lastly, Caizzone and colleagues carried out a geometrical synthesis of the two-port RFID antenna in the same study [31]. This procedure can offer a design methodology for an RFID-reader antenna. But because the design is based on the mutual impedance between the RFID sensor and the RFID tag and is specific to the design of RFID sensors or RFID-reader antennas only, it cannot be used as a general guide for other antenna models.

### 2.2.3 *Antenna Matching*

Antenna models can also be used in RF circuit designs for the purpose of matching [32]. Aberle proposed a method to derive an ECM for an antenna based on the simulated or measured complex input impedance and the radiation efficiency [32]. In this model, the radiation resistance of the antenna was replaced by a transformer with a specific turns ratio, which was used to couple the two-port ECM of the antenna into the external environment. This ECM was valid only for a single frequency and a narrowband antenna and did not represent the physical structure of the antenna. The author did not provide any matched data between the ECM and the antenna simulation. In the same study, Aberle also presented a technique to couple the simulated  $S$ -parameter data as a two-port network, which was obtained from the antenna simulation for an external match [32]. This technique was demonstrated using a narrowband monopole antenna. This antenna was coupled to both passive and active

(non-Foster) matching circuits. While the passive circuit kept the overall response narrowband, the active matching circuit delivered a broadband response. The use of active circuits entails the use of DC power, however, thus making the technique unsuitable for energy-constrained environments.

From the above summaries, ECMs for antennas are essentially complex two-port networks with lumped components and distributed elements. Understanding the electromagnetic structures involved allows for an analysis of the electrical performance of the ECM. The power radiated from the radiation resistance and the transmission phase will be studied in the present work. This investigation will help designers to study antenna behaviours such as resonance structures and frequency-variant radiation patterns. This derivation will also be used to evaluate the performance in both the frequency and time domains in order to characterise an antenna for both P2P and domestic applications.

### **2.3 Antenna Phase**

Several studies on antenna phases have compared the measured phase with the minimum phase, which is typically obtained by utilising the Hilbert transform method [2], [3], [19], [20]. Studies have also shown that antenna equalisation corresponds to particular angles of rotation in circularly polarised antennas [4], [20]. Several techniques have also addressed the differential time delays in Tx-Rx UWB antenna systems and have employed the Hilbert transform method [3].

Antennas are generally categorised into minimum-phase and non-minimum-phase antennas [2], [3], [19]. Researchers have shown that double-ridged horn antennas and Vivaldi antennas are minimum-phase antennas [19], [4]. Mathematically, the minimum phase of the antenna's  $S_{21}$  value has all zeros in the LHS of the  $s$ -plane [33]. From the physical perspective, the  $S_{21}$  phase is related to the path of energy transmission through the antenna-equivalent network [4]. The minimum-phase transfer function hence can be used in a network only when it has a single path for energy transmission through the network [4]. For instance, the transfer function of any ladder network or coaxial cable transverse electromagnetic (TEM)

system has a minimum phase, because the equivalent network has been proven to have only one path of transmission.

Using the fractional Hilbert transform technique, Foltz *et al.* [20] mathematically derived and validated by measurements that the rotation of the Tx antenna in the line-of-sight (LoS) axis will change the  $S_{21}$  phase equally to the angle of rotation, although they found the  $S_{21}$  measurement of a quad-ridged horn to be minimum phase only at a particular rotational angle on the principal axis. McLean, Foltz, and Sutton found the minimum-phase  $S_{21}$  only on the principal axis in the E- and H-planes for a double-ridged horn antenna in their study [4]. This finding implies that the antenna can be equalised only for those particular angles of rotation that correspond to the minimum phase, but this also means that an additional phase is added to the  $S_{21}$  phase at certain frequencies over the frequency range when the measurements are taken in directions other than in the principle axis. Hence, the  $S_{21}$  phase must be analysed using minimum- and non-minimum-phase antennas with different orientations in the frequency axis.

In another study, Foltz *et al.* [2] compared the measured phase of the antenna's  $S_{21}$  with the minimum phase, which they obtained by applying the Hilbert transform method to the measured amplitude to identify the compensating distance between the two antennas. Firstly, the amplitude of the  $S_{21}$  was measured in an anechoic chamber for three horn antennas as they were identical, as shown in Figure 2.4. It can be noticed that the horn antenna is radiated in the principal axis over the whole band from 1-18 GHz. The measured  $S_{21}$  phase was then obtained from the measurement and compared with that obtained by applying the Hilbert transform method, as illustrated in Figure 2.5. The minimum transmission phase indicates that the radiated power in the direction of the principal-axis continued to radiate over the entire band. The  $S_{21}$  phase has three components: (1) a 90-degree phase (due to the  $j\omega$  factor), (2) a phase that is twice the  $S_{21}$  value, and (3) the exponential free-space phase. This minimum phase was compared with the measured phase to identify the error in distance for an ultra-wideband antenna [2]. In this case, when the distance was corrected for this error, the measured  $S_{21}$  phase was found to be minimum phase. The experiment started with the assumption of a nominal value of distance of 3.4096 m between two identical double-ridged horn UWB antennas in an anechoic chamber. This step was taken to

measure the  $S_{21}$  amplitude and phase with a frequency range of 1.0–18.0 GHz. Using the Hilbert transform, the minimum phase of the  $S_{21}$  was obtained [2] from the magnitude of  $S_{21}$ . In general, the difference between the measured and minimum phase is due to the linear-phase component. Foltz *et al.* used the linear phase to obtain a corrected distance of 19.5 mm at each end [2]. The measurement was then repeated using this corrected distance. The measured and minimum phases were found to match, meaning that the measured phase did not have a linear-phase component. In general, the corrected distance, which is due to the effective distance from the edge of the antenna to the phase centre [34], produces an additional linear phase, which then causes a constant time delay. This method can only be applied to minimum phase antennas such as horn and Vivaldi.

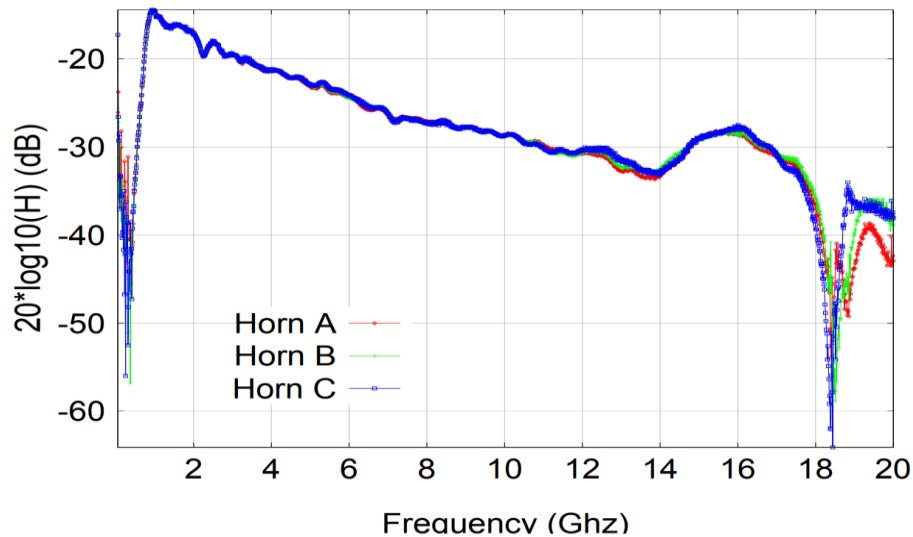


Figure 2.4. Horn antenna transfer function measurement (dB) for three identical antennas [2].

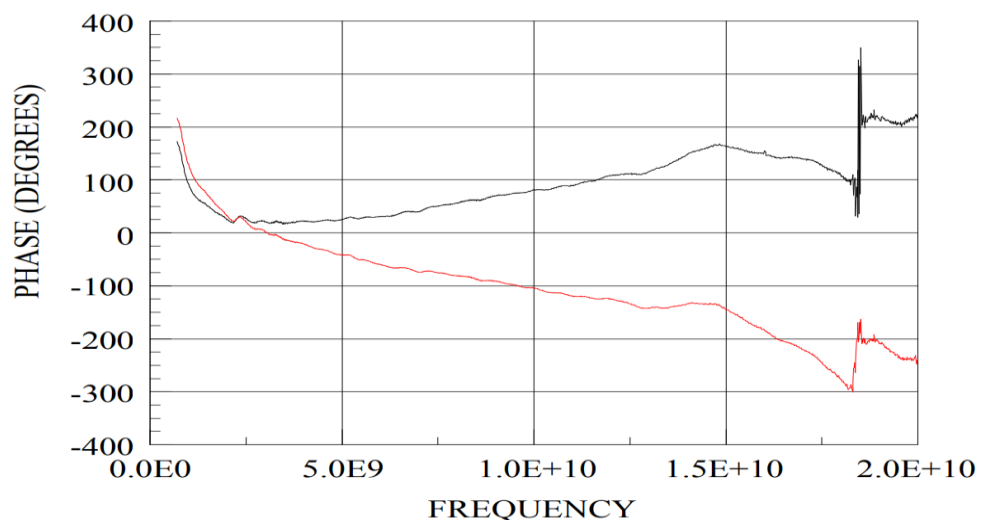


Figure 2.5. Measured Horn antenna  $S_{21}$  phase and the Hilbert transform phase [2].

Researchers have revealed that not all antennas can yield a minimum-phase transfer function, including double-ridged horn antennas and Vivaldi antennas [19]. Similarly, the log-periodic dipole array (LPDA) is not a minimum-phase antenna. The  $S_{21}$  of LPDA antennas can be separated into three components: (1) minimum phase, (2) all-pass function, and (3) linear phase with a constant time delay, which is obtained from the exponential factor. Researchers have obtained the antenna-impulse response from three LPDAs with different numbers of elements, all of which have shown ringing characteristics in the antenna [19]. The ringing in the impulse response can be attributed only to the all-pass characteristic of the  $S_{21}$ , however, and not to the minimum phase. This all-pass characteristic can be directly related to existing paths for the transmission of energy. Because LPDAs are not minimum-phase antennas, broadband-equalisation schemes are limited. For this reason, complex circuits must be used to increase the equalisation bandwidth.

McLean *et al.* [4] used a broadband double-ridged horn in an anechoic chamber to measure the  $S_{21}$  values both on- and off-axis. The results were compared with the minimum phase that was obtained from the  $S_{21}$  amplitude using the Hilbert transform. The authors noted agreement between the measured phase on-axis and the minimum phase obtained from the Hilbert transform, as shown in Figure 2.6. The measurement was repeated at 45 degrees off the axis in the E-plane to show the deviation from the minimum phase. (In general, deviation from the minimum phase of an antenna's  $S_{21}$  values varies only slightly from 0–60 degrees on the principal axis, but after 60 degrees, variations in the phase of the antenna transfer function can be substantial.) The authors noted that in the H-plane, measurements conducted on minimum-phase deviations were much higher off the principal axis as compared to the E-plane [4]. Thus the deviation from the minimum phase was verified to be much greater for directions off-axis in the H-plane than in the E-plane. The above behaviour was postulated to be due to the diffraction in the front edges of the horn [4]. The authors further posited that because the electric field was parallel to the horn antenna's walls perpendicular to the H-plane, the diffracted fields from the front edges of these walls were much greater than the diffracted fields from the front edges of the horn antenna's walls perpendicular to the E-plane. The authors thus proved that the minimum-phase  $S_{21}$  can be found only in the principal axes for this antenna [4].

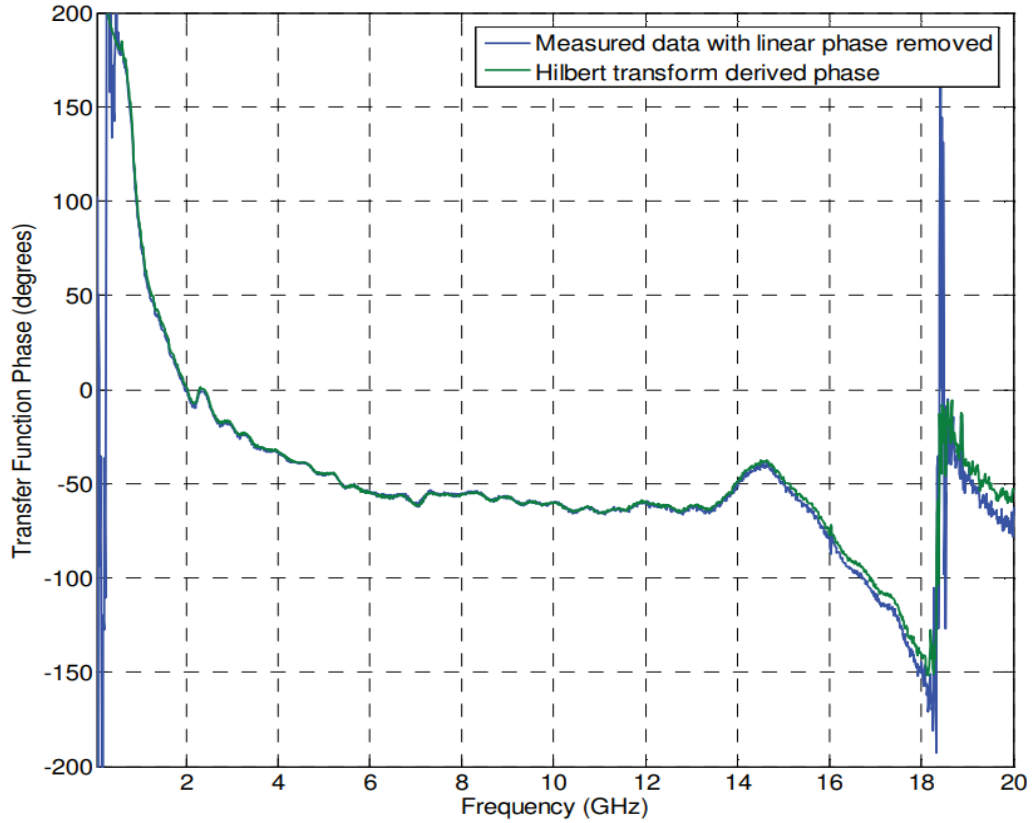


Figure 2.6. Measured Horn antenna phase on-axis with linear phase removed and the Hilbert transfer phase from its amplitude [4].

Port-to-port transmission  $S_{21}$  values have also been analysed using two circularly polarised broadband antennas, especially the behaviour of the antennas when the Tx antenna is rotated [20]. Using the fractional Hilbert transform technique, Foltz *et al.* mathematically derived and validated by measurements that the rotation of the Tx antenna in the LoS axis will change the  $S_{21}$  phase equally to the angle of rotation [20]. The  $S_{21}$  of a circularly polarised antenna cannot be minimum phase, however, except at a particular rotational angle, or by adding  $n * 180^{\circ}$  to that angle (i.e. at an integral multiple of that angle). This setup implies that the antenna can be equalised only for those particular angles of rotation that correspond to the minimum phase. The authors thus proved that antenna equalisation always depends on those particular angles of rotation that correspond to the minimum-phase condition [20]. This technique was applied to a broadband circularly polarised two-ridged horn antenna system. The difference of the measured  $S_{21}$  phase was confirmed to be nearly equal to the rotational angle of the principal axis. By comparing the measured phase with the minimum phase – which was obtained from the measured amplitude at different

rotational angles – the authors also observed that the minimum-phase condition of  $S_{21}$  occurred only at a rotational angle of 198 degrees [20].

In another study, McLean *et al.* examined time-delay patterns for UWB antennas [3]. The authors applied several techniques to analytically compute the differential time delay of two UWB Tx-Rx antenna systems, including (1) the differential time delay that has maximum correlation with a particular template function, which in turn can be derived from the radiated field or antenna  $S_{21}$ ; (2) the linear phase obtained from the  $S_{21}$ ; and (3) the time delay based on the Tx-Rx waveforms.

The Hilbert transform method is typically used to extract the minimum-phase component without any associated components. The Hilbert transform is thus the best tool for obtaining the minimum phase of the transfer function. McLean *et al.* plotted the analytically obtained differential time delays from the above-described methods versus the off-boresight angles in the E- and H-planes [3]. They noted that, because computing the time delay in the presence of noise is difficult, minimum-phase extraction from the Hilbert transform is the most accurate in terms of time-delay estimation [3]. In the ideal case of the antenna not distorting a pulse, the differential time delay computed from correlation with a template function and from the Hilbert transform will be equivalent.

In summary, antennas can be categorised into minimum-phase and non-minimum-phase antennas. Minimum-phase antennas have both minimum-phase and linear-phase components [6]. The minimum phase represents the amplitude of the frequency response of the antenna, while the linear phase causes a constant time delay due to the effective length of the antenna's phase centre. The non-minimum phase has three components: minimum, linear, and all-pass. The all-pass component, which is an additional phase at certain frequency ranges, does not exist in the principal axes of minimum-phase antennas, such as horn and Vivaldi antennas. When the antenna has a minimum transmission phase, the antenna has a frequency-invariant radiation pattern and can be used for directive antennas for P2P communications. The all-pass component will cause large variations in the antenna's group delay, which in turn will cause symbol scattering in DCSs.

## 2.4 Antenna Effects in DCSs

Several previous studies have examined the effect of the antenna in DCS simulations [16]-[18]. As discussed in the previous section, Sobhy *et al.* have shown how to represent a system model from the voltage transfer function across the radiation resistance of the ECM of a button antenna [17], [18]. The purpose of the antenna system model is to make the antenna simulation compatible with DCS simulation and to predict the effect of the antenna in a DCS. The radiated power and the  $S_{21}$  of the antenna are calculated from the ECM to derive a complete system model for Tx and Rx antennas. The authors used two methods to derive the system model from the ECM of the antenna. The first was by using an infinite impulse response (IIR) filter structure, while the second used topological analysis for the ECM to derive a system model. In this type of analysis, the elements of the physical structure from the ECM can be identified. Knowing the  $S_{11}$  is sufficient to obtain the voltage-transfer function in the ECM, which the authors used to derive Tx and Rx system models in order to simulate the models in a DCS [18]. This step helps in predicting the effect of the antennas in such DCSs and in calculating the BER. This method was applied to a wearable button antenna to derive the system models for both Tx and Rx antennas derived from the  $S_{21}$  obtained from the ECM [18]. In general, these system models are developed as an LTI system in the  $s$ -domain as the ratio of two polynomials by using the IIR filter method. This setup also helps to secure the stability of the system. These system models are sixth-order  $s$ -domain ratio polynomials in the numerator and denominator.

Following the derivation of the system model, Sobhy *et al.* conducted a study in which they simulated a model in a DCS to predict the effect of the antenna in the DCS and to calculate the BER [17]. The system model of a button antenna which was derived from the antenna ECM was represented in an  $s$ -plane function as the ratio of two polynomials. The model was then simulated in SIMULINK using a complete DCS with a carrier frequency of 2.4 GHz and 8-PSK (phase shift keying) modulation. The effect of the antenna on the 8-PSK-modulated signal was studied, and the BER of the DCS was calculated. Based on a comparison between the constellation diagram before and after antenna usage, the antenna was shown to have caused the symbol scattering found in the constellation diagrams. The receiver was able to recover the symbols, however, and the BER then became zero.

Sobhy *et al.* have also derived a system model using the IIR filter technique [18]. The model was simulated as a Tx antenna in a 64-QAM (quadrature amplitude modulation) DCS. A constellation diagram showed that the antenna caused symbol scattering in the transmission signal, and spikes and distortions were visible in the phase and amplitude in the time domain. For the Rx antenna, the  $S_{21}$  value of the Tx antenna between two identical antennas was shown to be the same as that of the Rx antenna, except for the scaling factor that was incorporated in the system's amplifier and automatic gain control. Sobhy *et al.* also simulated Tx and Rx antennas within a complete DCS with two channels, at 2.4 GHz and 5 GHz [18]. The authors found the symbol scattering for the 2.4 GHz channel to be more notable than for the 5 GHz channel. This poorer performance was due to the transmission phase being non-linear, at 2.4 GHz. In addition, the  $|S_{21}|^2$  value represents the power-transfer ratio, which represents the total transmitted power to the power available from the source.

Prakoso *et al.* described another method by which an antenna may be represented as a two-port network [16]. In general, the load power in the two-port network of an antenna is the same as the effective isotropic radiated power (EIRP) [35]. The EIRP for a given direction is defined as the net power accepted by a transmitting antenna multiplied by the gain of the antenna [35]. The total radiated power by an antenna is the same as the accepted power for a lossless antenna, which indicates that the antenna efficiency is 100%. By applying the EIRP and the two-port network with general source and load impedance, Prakoso *et al.* determined the values for the  $S$ -parameters in the Tx and Rx modes [16]. In the Tx mode,  $S_{21}$  was calculated by using the gain and  $S_{11}$ , while  $S_{12}$  and  $S_{22}$  were considered to be arbitrary. In general in the Rx mode,  $S_{22}$  is equal to  $S_{11}$  in both amplitude and phase, whereas  $S_{12}$  should be zero. Therefore, a two-port  $S$ -parameter (S2P) file block in a simulator cannot be used to represent the antenna in the bidirectional mode. This was proven from simulations in OptiSystem, because the receiving mode requires the  $S_{12}$  value to be zero [16]. Prakoso *et al.* [16] applied the method to the button antenna that Sobhy *et al.* described in their study [18] for validation. The circuit model and system model were simulated in Microwave Office (MWO) and the Visual System Simulator (VSS), which are part of the Applied Wave Research (AWR) company's design environment [16]. The results from this method were then compared with the results from the original

reference design of the button antenna described in Sobhy *et al.*'s work [18] to confirm their validity. Next, using this two-port-network method, the group delays of the button antenna in the Tx, Rx, and Tx-Rx modes were obtained as a function of frequency using AWR software [16]. In general, knowing the group delay value enables evaluation of the distortion introduced by the antenna in wireless systems. The authors showed that the group delay in the Tx-Rx mode was double that of the Tx or Rx modes, as predicted [16].

Prakoso *et al.* also calculated the EVM values with and without AWG noise and compared these values for the Tx and Tx-Rx modes via a system simulation using VSS software [16]. The authors observed that without AWG noise, the EVM only depended on the antenna distortion and that the distortion introduced by the antenna was related to the group delay. Therefore, flat  $S_{21}$  and a good  $S_{11}$  (gain and input impedance bandwidth) will result in low EVM, whereas large variations in  $S_{21}$  and poor  $S_{11}$  (or low input impedance bandwidth) along with a poor gain will result in high EVM values. For example, the EVM values at 2.4 GHz and 5 GHz were found to be 0.613% and 0.054%, respectively [16]. From the simulations, the EVM values in the Tx-Rx modes without AWG noise were found to be twice those of the Tx modes, again confirming the validity of this two-port-network method [16]-[18].

Lastly, according to Prakoso *et al.*, only OptiSystem software features a bidirectional S2P file block [16]. The authors simulated a system in the antenna Tx and Rx modes with frequency ranges of 1–3 GHz and 3–9 GHz for the Tx and Rx modes, respectively. The authors showed the symbol scattering in the constellation diagrams, and they observed that the EVM values using unidirectional and bidirectional S2P in OptiSystem were similar. As noted earlier, this finding proves that the two-port-network model described in Prakoso *et al.*'s work [16] can be used in bidirectional S2P file blocks, but only for different frequencies. That is, antennas in the Tx and Rx modes have different  $S$ -parameters and hence are not inherently bidirectional.

Investigators have concluded that antennas in DCS simulations cause symbol scattering [16]-[18]. This scattering occurs because of the large variations in group delay, which depend on the antenna's  $S_{21}$  transmission phase [36]. In turn, this result

occurs because the transmission phase is non-linear. A non-linear transmission phase indicates that the antenna has a frequency-variant radiation pattern and that the direction of the radiated power has changed to a different direction in the frequency response [37]-[40]. The current study aims to predict the effects of different antennas on the modulated signal in a DCS in different orientations as well as different environments and with added noise. Doing so will also help to describe the symbol scattering due to the signal distortion caused by the antennas.

## 2.5 Channel Models

The UWB covers the FCC-approved (US Federal Communications Commission) bandwidth 3.1–10.6 GHz. Two measurement techniques are used for UWB channel modelling: the time-domain and frequency-domain methods [41]. In the time-domain method, a short pulse is sent, and the samples from the pulse through the channel are recorded in the receiver after being captured by the antenna. The measurement of the complex response of the channel using a vector network analyser yields the channel response in the frequency domain, and the impulse response of the channel can be computed from the antenna's frequency measurement using the IFFT.

Matin *et al.* modelled an ultra-wideband channel to demonstrate the scattering effects with a non-line-of-sight (NLOS) path in an industrial environment [42]. The UWB channel was described in terms of a discrete time impulse response, as follows [42]:

$$h(t) = \sum_{l=0}^L \sum_{k=0}^K \alpha_{k,l} \delta(t - T_l - \tau_{k,l}) \quad (2.1)$$

where  $l$  and  $k_l$  are the number of clusters and the multipath components (rays) in each cluster (respectively),  $\alpha_{k,l}$  is the multipath gain coefficient of the  $k$  multipath,  $T_l$  is the arrival time of the first multipath component of the  $l$  cluster, and  $\tau_{k,l}$  is the delay of the  $k$  multipath component in the  $l$  cluster to the first arrival time  $T_l$ .

Unlike conventional channels, UWB channels require careful measurement for modelling because at ultra-wide bandwidths, the channel tends to generate a clustered impulse response in the time domain. The power-delay profile of such channels

consists of several multipath components that can be further associated into a set of clusters. Each cluster has a constant ‘cluster’ delay spread. The set of multipaths within a cluster is also separated by a ‘multipath’ delay spread. The duration of these delay spreads and the power of every multipath component depend on the bandwidth of the channel as well as the fading environment.

Statistical channel models are generally derived from measurements between Tx and Rx antennas in multipath channels. The statistical channels are modelled in three data-analysis steps, as shown in Figure 2.7 [43]. The modelling begins by using a channel-sounding technique to obtain the channel-impulse response and then applying algorithms to estimate the channel parameters before modelling the statistics channel. The channel sounding includes the use of tools for calibration and configuration for the measurements to obtain the channel-impulse response. The result from the channel-impulse response can be used and then processed and analysed to obtain channel parameters such as path delay and path loss to model the statistical channel model. Channel sounding, which includes measurement between Tx and Rx antennas, is essential for modelling the statistical channel. As these models indicate, the antenna response in the channel-sounding step is embedded with the channel response. An inverse antenna system must be derived to de-embed the antenna from the global transfer function of a radio link. Both the antenna system and its inverse system must be stable to achieve cascading and a stable convolution.

One technique used in [44] to characterise the multipath channel is channel sounding, which is used to evaluate the radio environment for wireless systems. Channel sounding provides information on the impulse response of the channel and is used, along with a synchronised clock between the transmitter and receiver. Tx and Rx antennas are included in the transmitter and receiver, respectively. The transmitter consists of a vector-signal generator with a modulation scheme and an upconverter. The measured signal is transmitted over a channel to the receiver. The signal is then received and passed to a downconverter and a receiver for recovering. This step is taken to obtain the channel-impulse response in the time domain, although the impulse responses are included in the responses of the two antennas, along with the channel characteristics. The power-delay profile, multipath components, RMS delay spread and arrival time can be calculated from the channel-impulse response.

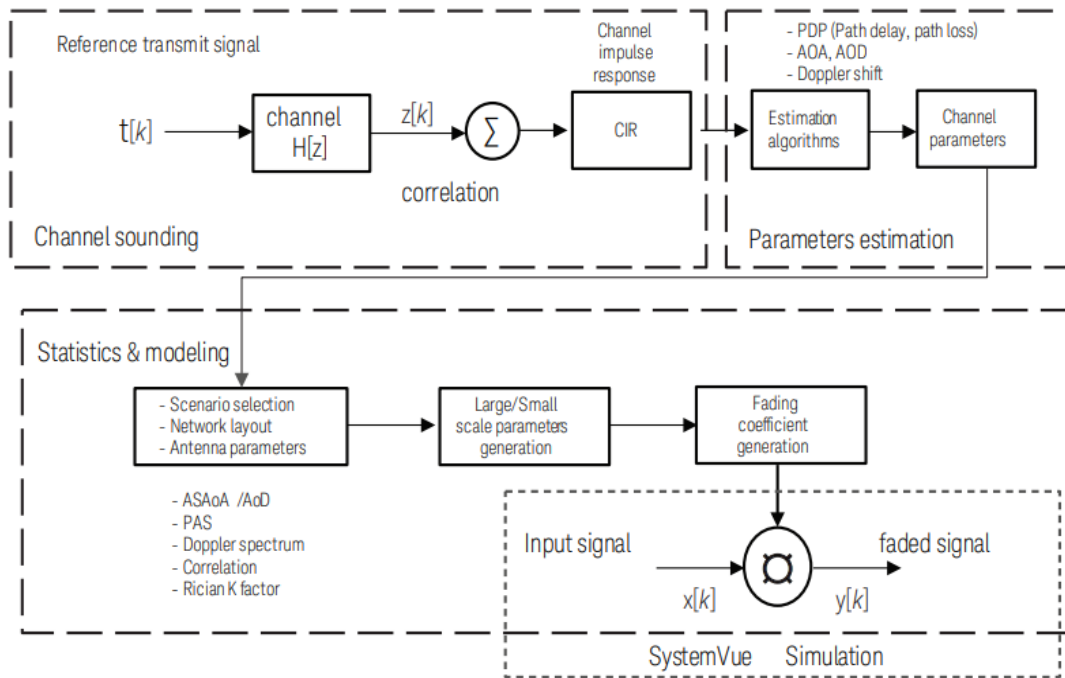


Figure 2.7. Steps for characterising and modelling a channel, starting with channel-sounding measurements, parameter estimation and modelling of a statistical channel [43].

The Saleh-Valenzuela model is a popular statistical channel model for describing UWB channels [25]. The development of the model was based on a number of channel measurements in multipath channels. The channel measurements include multipath components and the components' arrival times within clusters. In their study [25], Molisch, Foerster, and Pendergrass took the measurements between the two antennas in different locations in an environment, and the effects of the two antennas were included with the channel. The measurements between the Tx and Rx antennas in a multipath channel were found to reflect the responses of the two antennas with the multipath channel [24]. In general, both multipath channels and antennas cause symbol scattering in DCSs.

Sipal, Allen, and Edwards [23] argue that assumptions about the clusters in the Saleh-Valenzuela model are incorrect because the model's authors overlooked the distortion caused by antennas and assumed that the antennas would not cause any effects on the channel. The impulse responses of Tx and Rx antennas are typically convolved with a channel impulse response. This postulation was validated through simulation and measurements in the free-space channel in an anechoic chamber [23]. The impulse responses of an antenna in the free-space channel from the measurement and the simulation were found to be almost the same. These impulse responses showed

that the ringing of the antenna-impulse response did not show a Dirac impulse, as the simulation and the measurement had in the free-space channel [23]. The authors also found that the impulse response of an antenna varies with changed antenna sizes. Therefore, distortion in the channel can also be caused by the antenna [23]. The manifestation of the impulse response of the antenna in each cluster within a free-space channel indicates that there is only one multipath component, which appears as the convolution of the impulse response of Tx and Rx antennas with the free-space channel. Clusters with several multipath components manifest the impulse response of the antenna. The impulse response of the antenna hence is embedded in all multipath components in the channel response, and the effects of the impulse response of the antenna are generally disregarded. A technique is required to extract the antenna from the global transfer function of a radio link for modelling the multipath channel for P2P communications.

The work that Sipal *et al.* described in [24] extended their work in [23], where measurements were conducted in a laboratory environment. The authors showed that the clusters in the Saleh-Valenzuela model manifest the impulse response of the Tx and Rx antennas [24]. This manifestation typically occurs because of the wideband antenna type that is selected and because of changes in the radiation pattern of an antenna. The authors measured the antenna in the time domain in a laboratory environment to manifest the antenna-impulse response in the multipath components from the reflected metallic scatter and ceiling reflection [24]. The first multipath was found to represent the direct path, and the multipath reflected in the horizontal plane manifested the direct path apart from the sign, whereas the multipath component reflected from the ceiling was different due to the radiation pattern of the antenna and the channel condition.

The channel-sounding technique is used in Chapter 4 with integer inputs and with only a free-space channel in an anechoic chamber to predict different antenna effects in a DCS with a 16-QAM OFDM modulation scheme. This technique is used to compare the antenna effects with the effects from using the antenna system model (including in a DCS). The proposed technique is used to model the frequency antenna measurement using  $S$ -parameters, either with a free-space channel or with a multipath channel. These models can then be included in a DCS simulation using SIMULINK

software to predict the antenna and channel effects separately. Obtaining the channel-transfer function also helps to characterise the channel conditions and to improve the performance of the digital system.

McLean *et al.* [4] also interpreted the minimum phase by studying multipath propagation. The channel will affect the minimum-phase transfer function in such a way so as to produce zeros in the right-hand side (RHS) of the  $s$ -plane. But multipath interference does not always destroy the minimum-phase transfer function of the antenna, which has motivated the design and fabrication in the present work of a minimum-phase antenna to characterise the antenna's  $S_{21}$  values and to characterise multipath channels using minimum-phase antenna measurements.

Duroc *et al.* developed theoretical models to represent an ultra-wideband antenna system that could be used to derive a multipath channel model [45]. They also developed experimental techniques for a sample UWB patch antenna. The authors discuss three types of theoretical models for the UWB antenna system. The first is an electromagnetic model, which uses incident and radiated fields associated with incident open-circuit voltages and excitation currents, respectively. The second is a circuit model, which represents the Tx-channel-Rx UWB radio link as a transfer function derived from each antenna ECMs. The third is system modelling, where an LoS far-field UWB radio link model is developed based on system-transfer functions. From the measured  $S_{21}$  values in an anechoic chamber, the authors then derived equations for the UWB Tx, channel, and Rx transfer functions [45]. The LoS far-field radio link was also modelled in an anechoic chamber [45].

In the present research, the LoS far-field radio link measurements will be extended to characterise a wideband multipath channel in different office environments for P2P communications. This derivation can be achieved by using a minimum-phase antenna, since the stability of the antenna can be ensured when the inverse of the antenna system is obtained to extract the multipath channel-transfer function from the antenna measurements. This derivation helps in modelling the multipath channel for office environments by using the inverse of the antenna system model that is derived from the measurement in the free-space channel. Then, from the global transfer function of a radio link and the inverse of a minimum-phase antenna

system model, the unknown multipath channel-transfer function can be obtained in a wideband radio link. In this way, the channel will be independent of a particular antenna and can be used to predict the channel and antenna effects separately in a DCS for P2P communications. Doing so also helps in deriving an inverse antenna system for inexpensive antennas, which typically cause symbol scattering in DCSs to compensate for the antenna effects.

In summary, an antenna can be represented as a two-port network. This representation is based on the antenna type, including the structure and the application. Those antennas with a one-port network that are used in transmitting and receiving in DCSs are typically designed and fabricated so that they can be characterised and modelled to be included in a DCS. Inverse antenna systems are also generally derived to de-embed the antenna from the  $S$ -parameter measurements for P2P communications to characterise the multipath channels in different environments.

## CHAPTER 3: NARROW AND WIDEBAND ANTENNA CHARACTERISATION AS TWO-PORT NETWORKS

### 3.1 Introduction

Antenna engineers conventionally design antennas using simulations and measurements to obtain a low  $S_{11}$ . The radiation patterns and gain are then obtained at discrete frequencies. However, this procedure does not predict the correct performance of the antenna with respect to the physical orientation. The  $S_{11}$  yields the total radiated power, not the power radiated in the physical channel. P2P communication requires the calculation of the frequency response of the transmission between two antennas in a specific direction. Conventional methods of designing antennas to realise a low  $S_{11}$  only provide the total radiated power and are unsuitable for P2P communication. A procedure is required to design P2P antennas and to predict their performance in DCSs in particular.  $S$ -parameters can be measured in an anechoic chamber between two identical antennas [2]-[4], which enables designers to predict the correct frequency response in the direction of the channel. The frequency and time responses of an antenna can then be computed from  $S$ -parameter measurements.

Conventionally, antennas are measured in costly anechoic chambers, where  $S_{21}$  measurements are undertaken by using two identical antennas with a fixed distance in the far field. Since doing so requires a relatively large amount of time, space, effort, and cost for building and maintaining an anechoic chamber, such factors often prohibit these chambers from being installed. Measurements of  $S_{21}$  outside of an anechoic chamber mix the properties of the antennas with the channel characteristics. The impulse response of the complex  $S_{21}$  measurement in a multipath channel will have many components, which represent the two antennas as well as the channel impulses. Each ray in the time-domain response represents one path component [24], [26] and depends on various phenomena, such as reflection, diffraction, and scattering. The ray that represents the impulse response of the direct path is a result of the time response of both the Tx and Rx antennas.

Several theoretical models have been developed to represent wideband antenna systems in a free-space channel that can be used to derive antenna and channel models [45], [46]. In these models, LoS far-field UWB radio link models have been developed based on the  $S_{21}$  value. Characterisation of the multipath channel has not been modelled in detail, however, where the channel would be incorporated along with the antennas. Hirano *et al.* proposed a technique to obtain the gain by taking  $S_{21}$  measurements over two sets of distances in an anechoic chamber [21].

The aim in this chapter, in addition to characterising an antenna in an anechoic chamber, is to extract the antenna response from the  $S_{21}$  measurement outside of an anechoic chamber in order to separate the impulse responses and to determine the frequency responses for the antenna and the channel. This step will also allow for channel analysis and antenna characterisation. Determining the frequency response of the antenna also enables the determination of the gain and group delay.

In this chapter, the characterisation procedure is applied to a wideband Vivaldi antenna and a narrowband patch antenna to examine and test three techniques. These techniques were used to obtain the  $S_{21}$  of the antenna and to show the difference between the conventional approach in only realising a low  $S_{11}$  and the new approach of calculating the antenna response in a specific direction. The Vivaldi antenna is a minimum-phase, coplanar, wideband antenna with high gain. In the present work, the antenna was designed and simulated in a three-dimensional (3D) EM simulator to obtain the  $S_{11}$  value as well as the radiation pattern at discrete frequencies. Then, to verify the simulation modelling,  $S_{11}$  was compared with the measurement obtained using a network analyser. Three techniques were applied to characterise the antenna and to obtain the two different  $S_{21}^a$  and  $S_{21}$  values. First, an ECM was derived that had the same  $S_{11}$  in amplitude and phase as the measurement. Next, the port-to-port  $S_{21}^b$  value between the two identical antennas was measured in an anechoic chamber to obtain the antenna's  $S_{21}$ . The Hilbert transform was then applied to derive the minimum phase of  $S_{21}$  from its amplitude. The chapter then presents a comparison of the amplitude and phase of  $S_{21}$  obtained through these techniques.

This chapter also introduces a procedure to characterise a Vivaldi antenna and a channel with multipath components in the frequency and time domains. The  $S_{21}^b$

value was then measured between two identical antennas in a typical laboratory environment with added reflectors. The impulse responses in the time domain of the antennas and channel were subsequently obtained. The antenna  $S_{21}$  was then determined from the procedure and compared with the  $S_{21}$  obtained from the measurements in an anechoic chamber. The time response of the multipath channel was then extracted from the  $S_{21}^b$  measurement and was also presented in the frequency domain. Finally, the procedure was applied to a narrowband patch antenna to establish the limitation due to the long ringing that occurs in the time domain.

### 3.2 Antenna Characterisation Methodology

S-parameters characterise the electrical behaviour of two-port networks at specific frequency ranges. These ranges represent the voltage ratios of the waves. For the port-to-port  $S_{21}$  between the Tx and Rx antennas, the frequency response of the  $S_{21}$  depends on the orientations of both antennas. As a result, there are two different transfer scattering parameters,  $S_{21}^a$  and  $S_{21}^b$ :

- $|S_{21}^a|^2$  is the power transfer ratio, representing the total transmitted power (radiated power in all directions) for each antenna to the power available from the source.  $S_{21}^a$  can be calculated from  $S_{11}$  for a lossless antenna, from the antenna ECM, or from antenna simulation.
- $|S_{21}^b|^2$  is the power transfer ratio, representing the measured  $S_{21}$  between the Tx and Rx antennas and their physical channels over distance  $d$ . For identical antennas, the  $S_{21}$  for each antenna can be calculated from the  $S_{21}^b$  after de-embedding the free-space channel and dividing by two in dB and radians for the amplitude and phase, respectively. The  $S_{21}$  value of each antenna represents the directional dependency of  $S_{21}^a$ .

For a lossless network, the amplitude of the  $S_{21}^a$  can be calculated from the amplitude of  $S_{11}$  [47]:

$$|S_{21}^a| = \sqrt{1 - |S_{11}|^2} \quad (3.1)$$

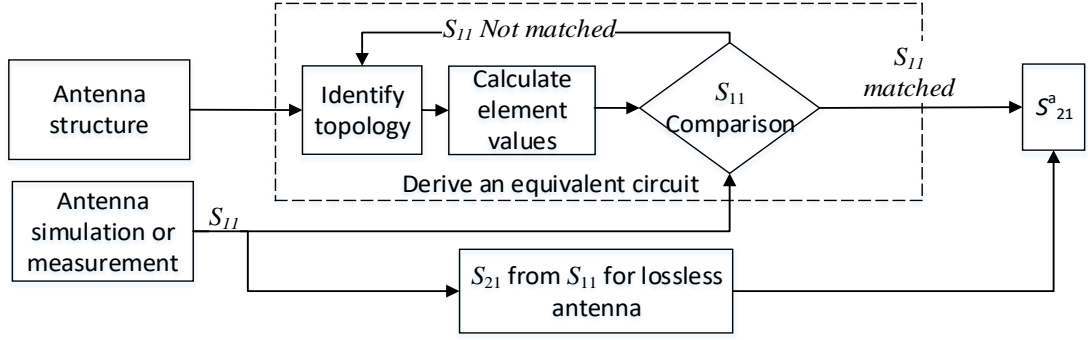


Figure 3.1. Method for obtaining  $S_{21}^a$ , which provides the total radiated power.

The flowchart in Figure 3.1 shows the steps for deriving an ECM and obtaining  $S_{21}^a$ . This calculation yields the total radiated power of the antenna. The second port provides the radiation resistance of the antenna. Initially, the layout structure is simulated to obtain the  $S_{11}$  amplitude and phase. Next, the  $S_{11}$  value is compared with that of the measurement. The antenna ECM is then derived by identifying the topology of the circuit and calculating the element values to represent the antenna as a two-port network, which must be matched with the  $S_{11}$  in both amplitude and phase. The topology is identified based on the structure of the antenna, whereas the circuit-element values are computed by using an iterative optimisation process to match the  $S_{11}$ . The voltage-transfer function can be calculated from the simulator as the ratio of the voltage ( $V_r$ ) across the radiation resistance ( $R_r$ ) and the source voltage ( $V_s$ ). The  $S_{21}^a$  in the amplitude and phase of the ECM can then be computed by [18]:

$$S_{21}^a = \frac{2V_r}{V_s} \sqrt{\frac{R_s}{R_r}} \quad (3.2)$$

where  $R_s$  is the input resistance. Lastly, the  $S_{21}^a$  value obtained from the ECM is compared with that obtained from (3.1).

The  $S_{21}^b$  includes the frequency response of the Tx and Rx antennas as well as the channel. Measurements of  $S_{21}^b$  between two antennas can be done inside an anechoic chamber using a network analyser. This measurement is conducted so that the free-space channel will not have a multipath. The reference plane is defined at the end of each cable using the through-open-short-match (TOSM) calibration technique. The  $S_{21}$  of Tx and Rx antennas is the  $S_{21}^b$  after de-embedding the free-space channel. The amplitude response of the two antennas is obtained based on the Friis transmission

equation, and the delay is de-embedded from the phase based on the delay due to the Tx-Rx distance. The phase shift in the free-space channel is calculated by:

$$\beta = -\omega d/v \quad (3.3)$$

where  $\omega$  is the angular frequency in rad/sec,  $v$  is the velocity in free space, and  $d$  is the distance between the two antennas in m.

For identical antennas, the amplitude and phase values of  $S_{21}$  for each antenna after de-embedding the free-space channel were then computed by taking the square root of the amplitude and by dividing the phase by two, respectively. The amplitude and phase of  $S_{21}$  can then be calculated by:

$$|S_{21}| = \sqrt{|S_{21}^b| d/\lambda} \quad (3.4)$$

$$\angle S_{21} = \frac{\angle S_{21}^b - \beta}{2} \quad (3.5)$$

where  $\lambda$  is the wavelength in m.

The Hilbert transform method provides the relationship between the real and imaginary part of a function  $\mathcal{F}(j\omega)$ , which is analytic in the RHS of the  $s$ -plane [33]:

$$\mathcal{F}(j\omega) = e^{-[\alpha(\omega)+j\phi(\omega)]} \quad (3.6)$$

where  $\alpha(\omega)$  and  $\phi(\omega)$  are the attenuation and phase of the function, respectively. The attenuation  $[\alpha(\omega)]$  can be calculated by taking the logarithms of (3.6), and the Hilbert transform is used to derive the phase  $[\phi(\omega)]$  [33]:

$$\alpha(\omega) = -\ell n|\mathcal{F}(j\omega)| \quad (3.7)$$

$$\phi(\omega) = -\frac{1}{\pi} \int_{-\infty}^{\infty} \frac{\alpha(\xi)d\xi}{\omega-\xi} \quad (3.8)$$

The Hilbert transform is applied to derive the minimum phase of  $S_{21}$  from the amplitude of  $S_{21}$  obtained from the  $S_{21}^b$ .

The impulse response of an antenna can be computed from the frequency response using IFFT. The result using a normal IFFT is a complex number, and the time-domain response can only be in real time. Among the many ways to obtain the

real time response from the complex  $S_{21}$  is the symmetric method, which provides accurate results in converting to and from the frequency response. In this method, a time scale is created from the frequency scale. The discrete points in the time domain should be double the frequency-discrete points. The purpose of this time scale is to create a time vector for symmetric IFFT. In the time domain, the mean group delay is the negative derivative of the transmission phase with respect to the frequency. The group delay characterises the dispersive nature of the antenna  $S_{21}$  and can be correlated to the spreading of the impulse response.

### 3.3 Vivaldi Antenna Design

#### 3.3.1 Antenna Design

The Vivaldi antenna is an aperiodic, continuously scaled travelling wave structure that Gibson invented in 1979 [48]-[51]. Vivaldi antennas are the most widely used type of tapered slot antennas, with a design that features an exponentially tapered slot line. Vivaldi antennas have a wide bandwidth and symmetric radiation – the beam width of the E and H planes is the same – with smaller sidelobes. The Vivaldi antenna has a non-resonant structure, linear polarisation, and significant gain across frequency performance with an endfire characteristic within a frequency range of 2–40 GHz.

Vivaldi antennas consist of three sections: the input feed line, the constant width slot line, and a radiating tapering flare at the end [49]. The strip line and the slot line are etched in two different sides of the substrate. The tapered slot line in a Vivaldi antenna has an exponential function. The transition in Vivaldi antennas from the strip line for coupling signals to the slot line is designed to exhibit low loss over the frequency band. This coupled transition is used to generate electromagnetic fields.

Figure 3.2 shows the three sections, as well as the parameters in these sections, that affect the Vivaldi antenna design. The width of the slot line is less than one-half the free-space wavelength, and the waves are bent along the exponential curve conductor.  $P_1(x_1, y_1)$  and  $P_2(x_2, y_2)$ , shown in Figure 3.2, describe the end points of the exponential, and the opening rate for the tapered section is described by  $R$ . The mouth opening in the tapered part yields the frequency range according to the points  $P_1$  and

$P_2$  in the exponential function: a lower cut-off frequency for the width of the top at point  $P_1$  and a higher frequency for the exponential function at point  $P_2$ . The exponential radiating tapering flare in the Vivaldi antenna is described in the following equations [52]:

$$x = c_1 e^{Ry} + c_2 \quad (3.9)$$

where the coefficients  $C_1$  and  $C_2$  can be obtained by:

$$c_1 = \frac{x_2 - x_1}{e^{Ry_2} - e^{Ry_1}} \quad (3.10)$$

$$c_2 = \frac{x_1 e^{Ry_2} - x_2 e^{Ry_1}}{e^{Ry_2} - e^{Ry_1}} \quad (3.11)$$

The width of the strip line can be calculated by a strip line characteristic impedance equation as [53]:

$$Z_0 = \frac{60}{\sqrt{\epsilon_r}} \ln\left(\frac{4H}{0.67\pi(T+0.8W)}\right) \quad (3.12)$$

where:

$Z_0$  is the characteristic impedance of the strip line in  $\Omega$

$\epsilon_r$  is the dielectric relative permittivity

$H$  is the thickness of the dielectric substrate

$T$  and  $W$  are the thickness and width of the strip line, respectively.

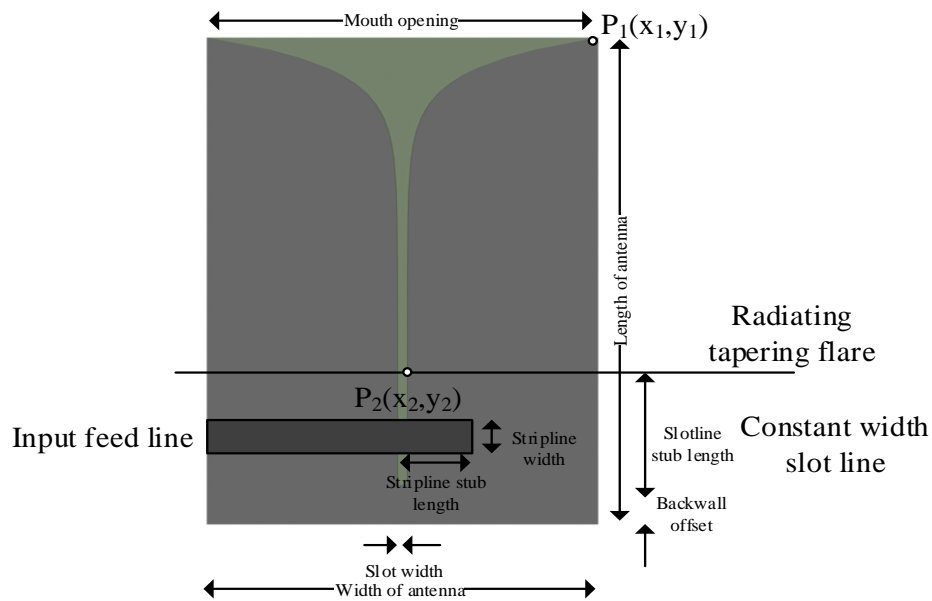


Figure 3.2. Vivaldi antenna parameters.

### 3.3.2 Antenna Simulation

The structure of the Vivaldi antenna used in this work, along with all dimensions (shown in mm), is illustrated in Figure 3.3. The antenna was designed on a Rogers RO4003C dielectric substrate with a thickness of 0.508 mm and a dielectric constant  $\epsilon_r = 3.38$ . The width and length of the feed line were 1.2 mm and 24.65 mm, respectively. The Vivaldi antenna was simulated in CST software to obtain the  $S_{11}$  value and the radiation patterns. Following the simulation, the antenna was fabricated, and  $S_{11}$  was measured using a network analyser. The response of  $S_{11}$  from the simulation and the measurement of the antenna was in agreement in operating over the frequency range 3.1–6.7 GHz, as shown in Figure 3.4.

The simulated radiation pattern gains are shown in Figure 3.5 for two different frequencies, 3.5 GHz and 6.3 GHz. In the figure, the sidelobes of the radiation pattern for each frequency show different directions and different power losses. The main beam of the radiation pattern, however, is in the same direction for both frequencies and displays endfire behaviour.

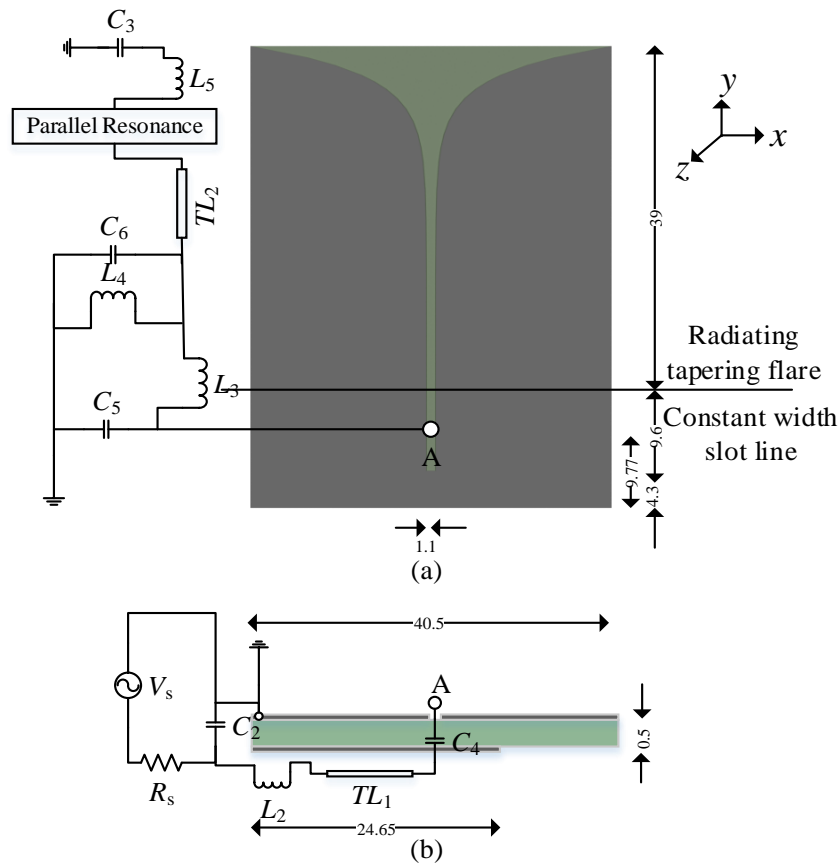


Figure 3.3. Vivaldi antenna geometry: (a) top view and (b) cross-sectional side view.

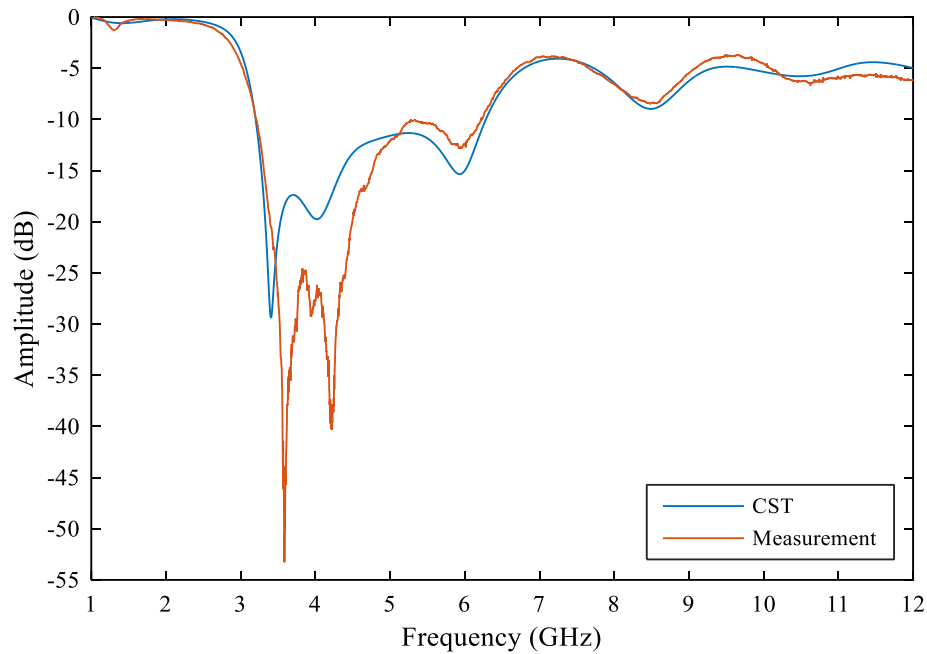


Figure 3.4. Comparison of  $S_{11}$  from CST and measurement.

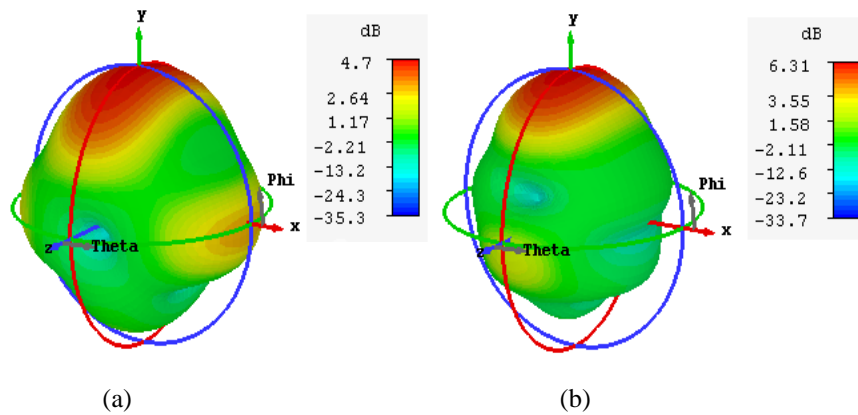


Figure 3.5. Radiation pattern gain at (a) 3.5 GHz and (b) 6.3 GHz.

### 3.4 ECM for Vivaldi Antennas

The ECM of the Vivaldi antenna was derived as a two-port network. The second port shows the radiation resistance, as shown in Figure 3.6. The ECM for the Vivaldi antenna was derived by identifying the circuit topology and then calculating the lumped and distributed element values. The topology for the ECM was identified for the antenna layout structure based on the method shown in Figure 3.3. In the figure, the feeding line is represented by the transmission line (TL1) and the inductor (L2). The slot line transition feeding line is represented by two capacitors, C4 and C5. The

lumped and distributed elements were computed using an iterative optimisation process, and the ECM was simulated and optimised using ADS software. The radiation resistance was found to be approximately  $68 \Omega$ .

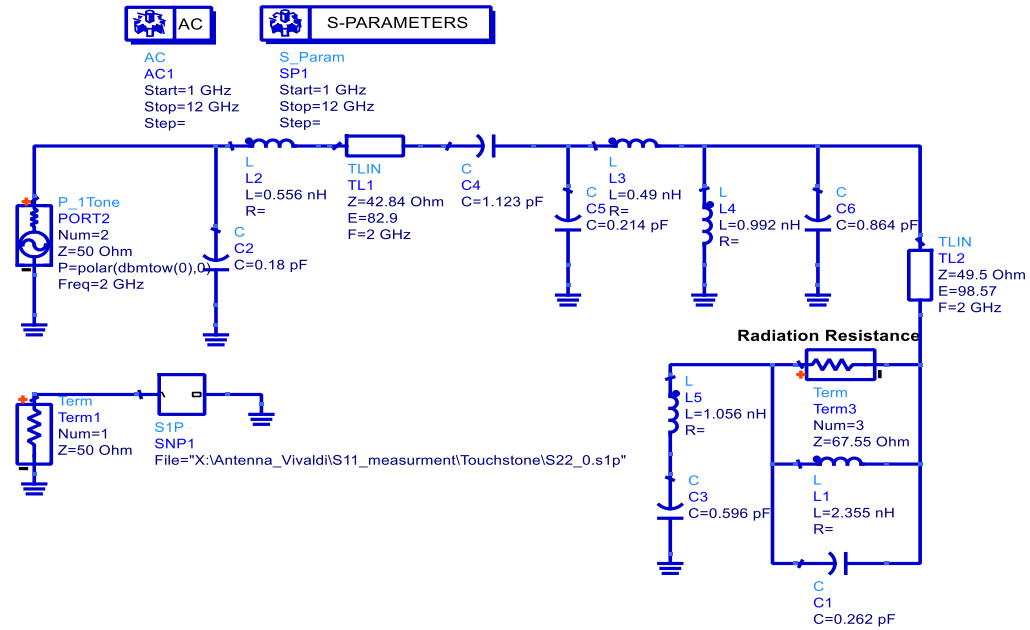


Figure 3.6. ECM for a Vivaldi antenna.

As Figure 3.7 indicates, the amplitude and the phase of  $S_{11}$  from the antenna measurement using the network analyser and the ECM simulated in ADS were in full agreement. Subsequently, the  $S_{21}$  value from the ECM was calculated using radiation resistance as the output load [18].

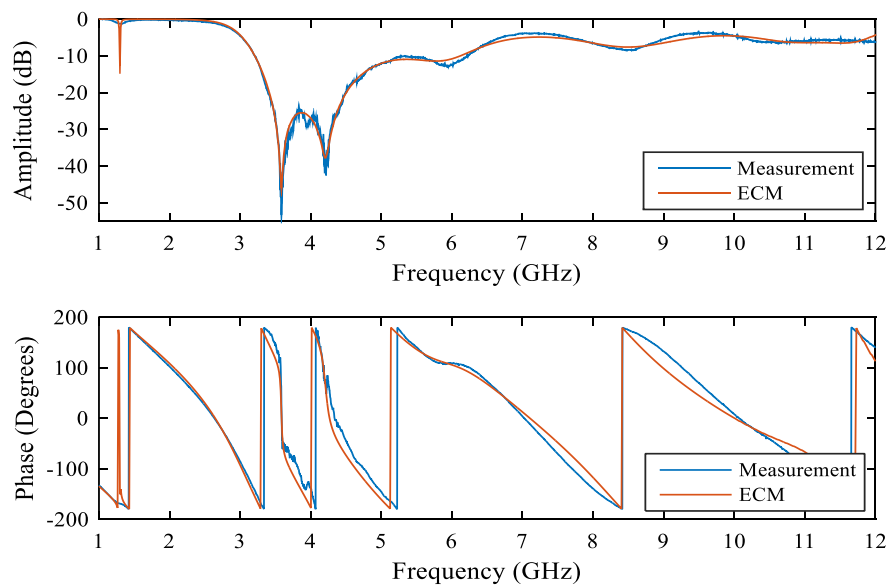


Figure 3.7.  $S_{11}$  of the Vivaldi antenna from measurement and ECM.

### 3.5 $S_{21}$ Measurement between Two Identical Antennas

Measurements of  $S_{21}^b$  were carried out in an anechoic chamber between two identical Vivaldi antennas 1 m apart, and the measurement setup along with the endfire direction of the antennas is shown in Figure 3.8. The result from the Measurements of  $S_{21}^b$  is shown in Figure 3.9. The delay was then de-embedded from the phase based on the distances, and the amplitude response was then obtained. The  $S_{21}$  for each antenna was then determined using (3.4) and (3.5) for the amplitude and phase, respectively.

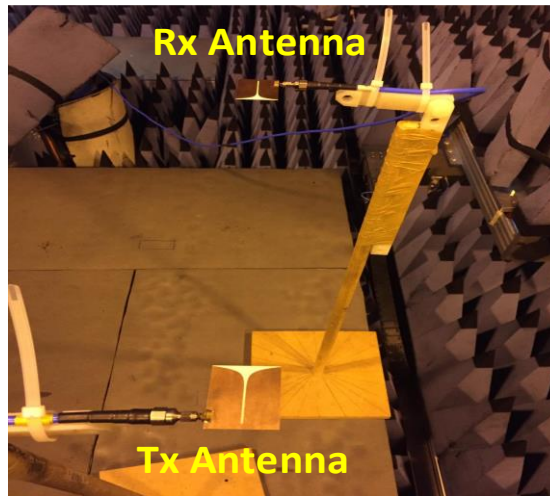


Figure 3.8. Photograph of the Vivaldi antenna measurement along with endfire direction in the anechoic chamber.

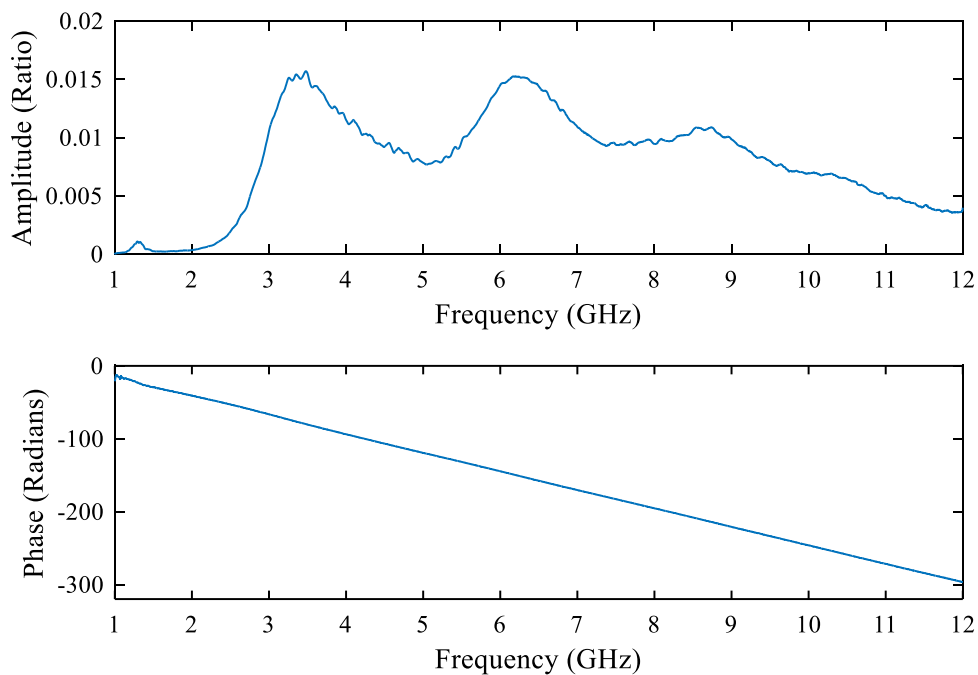


Figure 3.9. Measurement of  $S_{21}^b$  between two Vivaldi antennas in an anechoic chamber.

### 3.6 The Hilbert Transform

The Hilbert transform was applied to the amplitude of  $S_{21}$  to derive the minimum phase [33]. The amplitude of  $S_{21}$  was obtained from the  $S_{21}^b$  measurement in an anechoic chamber between two identical antennas after de-embedding the free-space channel. Because the Vivaldi antenna has a fixed-phase centre [34], an additional linear-phase component was computed after identifying the phase centre of the antenna. The phase centre can be identified from the phase of  $S_{21}$ : either from the  $S_{21}^b$  measurement or from the ECM. By adding the linear-phase component to the minimum phase obtained from the Hilbert transform, the phase of  $S_{21}$  could then be compared with that from the ECM and measurements.

### 3.7 Results and Discussion

The amplitude and phase of  $S_{21}$  were obtained from the  $S_{21}^b$  measured after de-embedding the free-space channel in order to compare the values with those from the ECM. The amplitude of  $S_{21}$  was obtained from the three different techniques and compared, as shown in Figure 3.10. The amplitude of  $S_{21}^a$  obtained from the ECM and from the  $S_{11}$  assuming a lossless antenna was well matched, as shown by the total radiated power of the antenna in all directions. In contrast, the amplitude of  $S_{21}$  obtained from the  $S_{21}^b$  measurement provided the radiated power in P2P communication along the endfire direction. The difference in  $S_{21}^a$  and  $S_{21}$  is due to the antenna radiation pattern gains shown in Figure 3.5 at two different frequencies.

With the addition of a linear-phase component to the minimum phase of  $S_{21}$  obtained from the Hilbert transform method, the phases of  $S_{21}$  obtained from the three techniques were in agreement, as shown in Figure 3.11. These results matched well with those obtained from the Hilbert transform because of the minimum-phase antenna. The phase of  $S_{21}$  obtained from the ECM matched the phase of  $S_{21}$  obtained from the  $S_{21}^b$  measurement in free space along the endfire direction. This matching occurred because the main beam of the fundamental radiation pattern was in the same direction as the measurement. The phase centre was calculated to be equivalent to an air-space distance of 0.1 m for each antenna from the antenna  $S_{21}$  phase, either from the measurement or from the ECM.

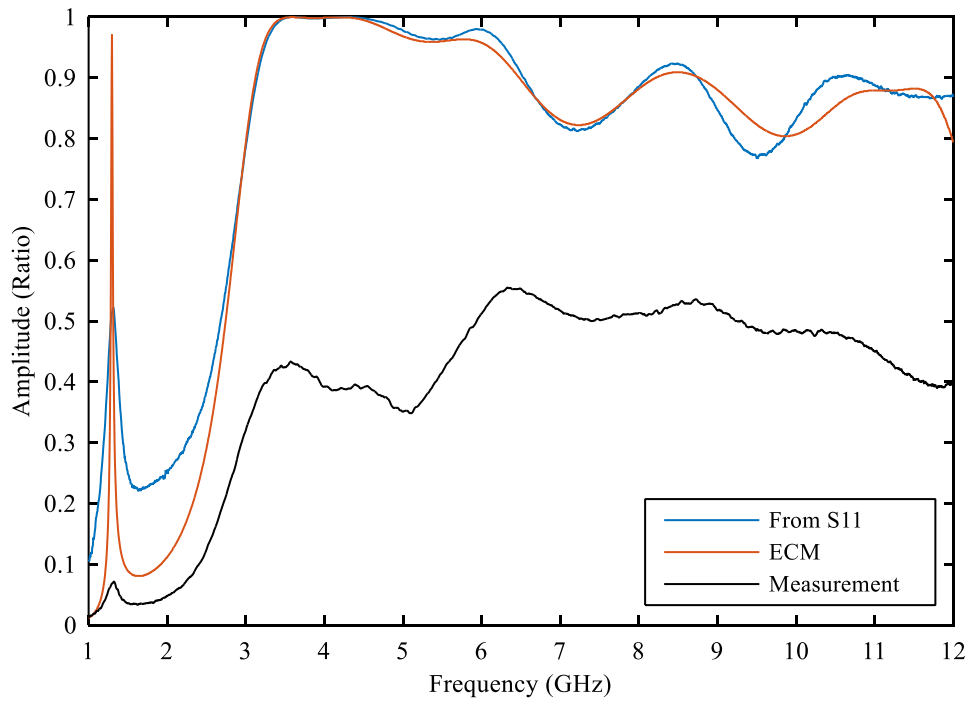


Figure 3.10. Comparison of the amplitude of  $S_{21}^a$  and  $S_{21}$  of the Vivaldi antenna.

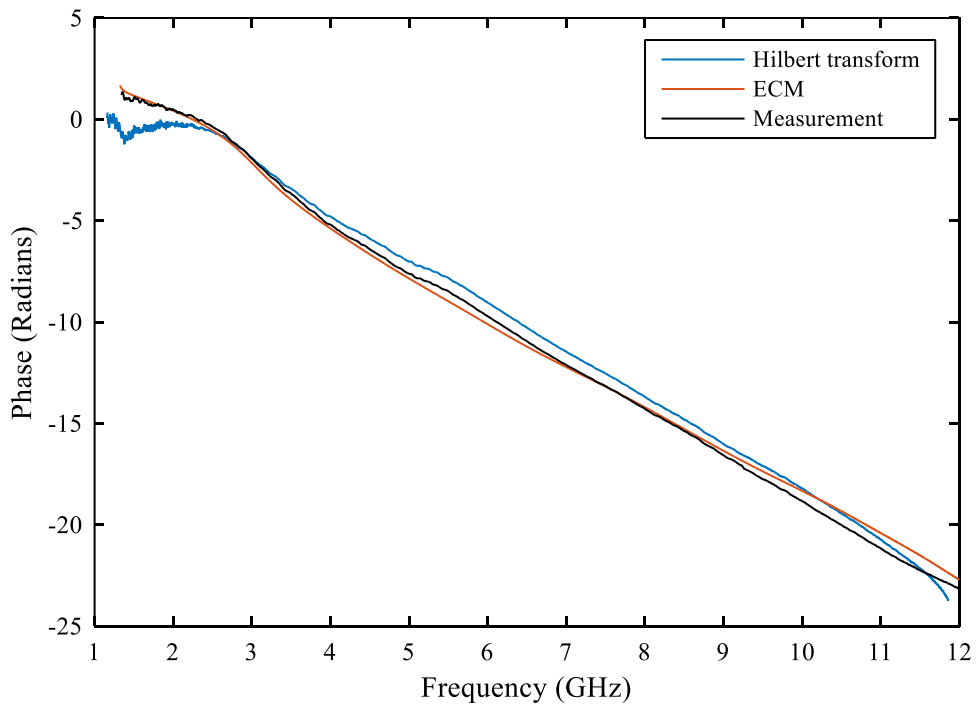


Figure 3.11. Comparison of the phase of  $S_{21}^a$  and  $S_{21}$  of the Vivaldi antenna.

Figure 3.12 illustrates a comparison of the group delay obtained from the Vivaldi antenna's  $S_{21}$  and its minimum phase from the Hilbert transform. From both group delays, a similar trend is visible in the frequency response. The difference between the two is equal along the frequency axis due to the linear-phase component. This finding also confirms that the Vivaldi antenna is minimum phase because of the constant difference delay in group delays between the antenna  $S_{21}$  and its minimum phase across the frequency axis.

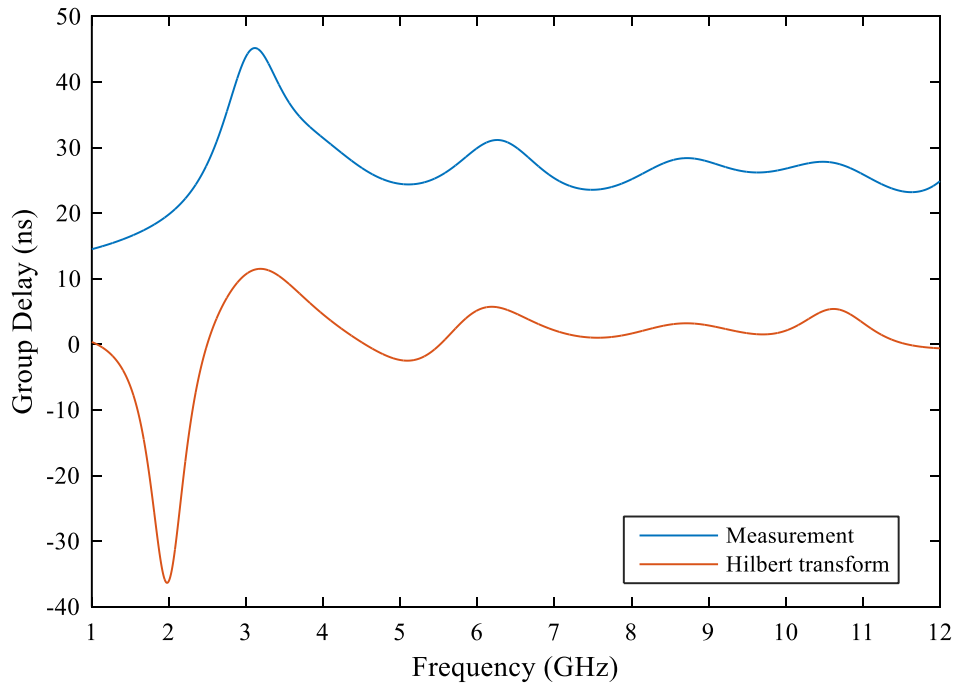


Figure 3.12. Comparison of group delay between the Vivaldi antenna  $S_{21}$  and the minimum phase from the Hilbert transform.

The impulse response of the Vivaldi antenna was then computed by applying IFFT to the  $S_{21}$  of the Vivaldi antenna, as shown in Figure 3.13. The antenna impulse response presented a delay due to the antenna, because the  $S_{21}$  phase had both linear-phase and minimum-phase components [2]. The linear-phase component causes a constant 0.33 ns delay, which is equivalent to that from an air-space distance of 0.1 m caused by the linear-phase component to the phase centre of the antenna.

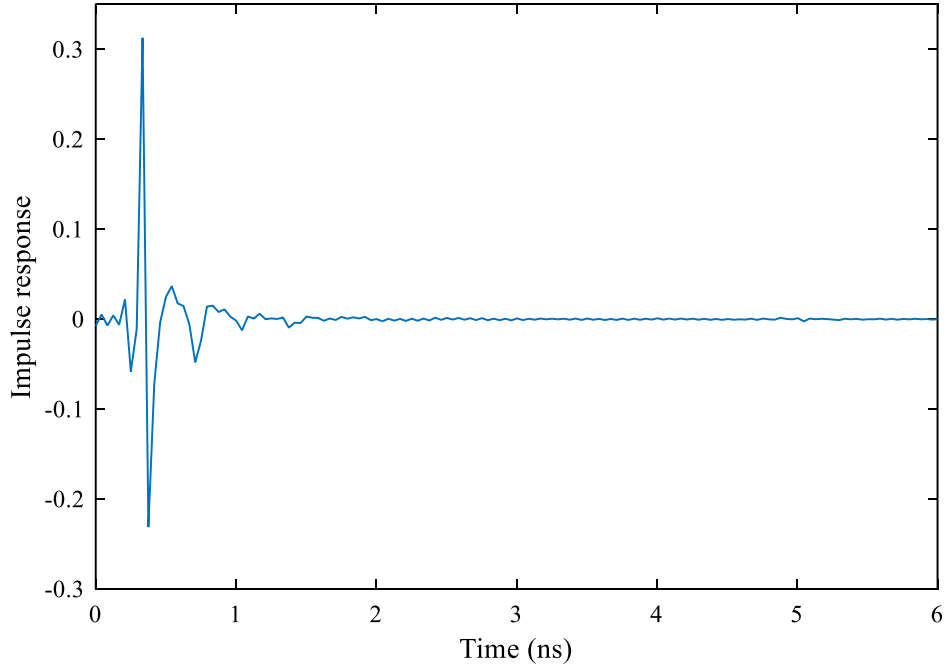


Figure 3.13. Impulse response of the Vivaldi antenna  $S_{21}$ .

### 3.7.1 Characterisation Procedure for Antennas in Multipath Channels

Measurements of  $S_{21}^b$  outside an anechoic chamber mix the antenna properties with the channel characteristics. The impulse response of the  $S_{21}^b$  measurement in a multipath channel will have many components, representing both the two antennas and the channel impulse responses. The channel characteristics depend on various phenomena, such as reflection, diffraction, and scattering. The impulse responses of both Tx and Rx antennas represent the impulse response of the direct path. This procedure enables designers to obtain the frequency response of an antenna without using an anechoic chamber based on measurements conducted in a multipath channel.

The characterisations of the antenna and channel were begun by measuring  $S_{21}^b$  between the Tx and Rx antennas in a multipath channel. Figure 3.14 illustrates a communication link with two antennas and a multipath channel.



Figure 3.14. Measurement of  $S_{21}^b$  between two antennas in a channel (communication link).

The  $S_{21}^b$  measurement of the system shown in Figure 3.14 includes the frequency response of the two antennas as well as the channel. The flowchart in Figure 3.15 shows the characterisation procedure for the antenna and the channel. The process begins by measuring the  $S_{21}^b$  between two identical antennas in a multipath channel and then de-embedding the direct path from the measurement. Then, by applying the IFFT to the complex  $S_{21}^b$  after de-embedding the free-space channel, the impulse response is obtained.

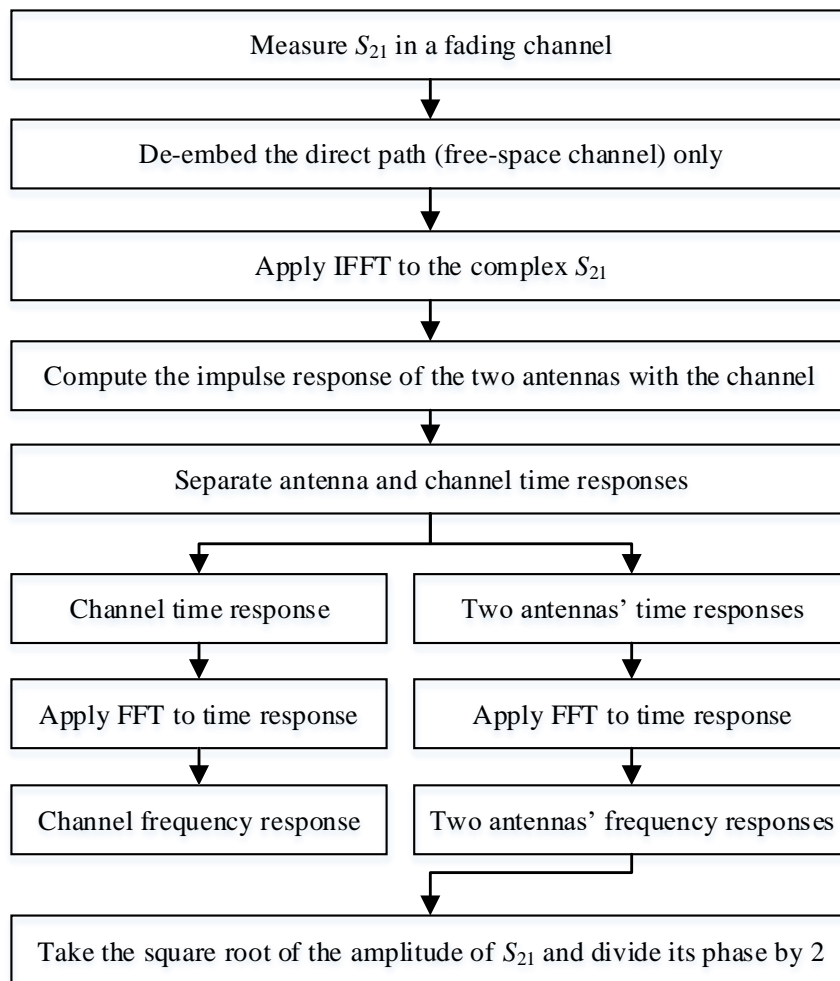


Figure 3.15. Antenna and channel characterisation flowchart.

The procedure characterises the antenna in an unknown channel. This characterisation can be achieved by splitting the time-domain response of the complex  $S_{21}^b$  into antenna and channel responses. The impulse response obtained represents the impulse response of the two antennas and the channel. The first ray found at the beginning of the time range until the end of the ringing represents the impulse response of the two

antennas, whereas the remaining rays represent the impulse response of the channel. By separating the two impulses, designers can ascertain the impulse response of the two antennas and the channel. The frequency response for the two antennas and channel can then be computed by applying the FFT to the corresponding time response. Finally, the  $S_{21}$  for each antenna can be obtained by taking the square root of the amplitude and dividing the phase by two.

### 3.7.2 Validation of Wideband Antenna and Channel Response

For this work, two identical Vivaldi antennas were measured with a distance of 1 m in a typical laboratory environment with three added reflectors. The orientations of the two antennas were in the endfire direction. Frequency measurements were taken at 4,001 points. Figure 3.16 presents a schematic of the environment of the Tx and Rx antennas in the channel. The  $S_{21}^b$  values of the two antennas with multipath channels in both amplitude and phase after de-embedding the direct path are shown in Figure 3.17. The impulse response of the  $S_{21}^b$  was then obtained and is shown in Figure 3.18. The figure shows the impulse response after separating the responses of the two antennas from the channel in the time domain. As shown in the figure, the main pulse (Ray 1) in the time domain, which represents the impulse response of the two Vivaldi antennas, occurs at 0.66 ns, and the width is 2.3 ns. The remaining time response was caused by the multipath channel. The channel time response has many rays, which represent the multipath through the reflectors in the environment. Rays 2, 3, and 5 occurred at 2.96 ns, 3.60 ns, and 6.46 ns, respectively. These rays arose from three multipaths through the three reflectors, as summarised in Table 3.1. Ray 4, which occurred at 5.13 ns, represents the path across Reflector 1 and Reflector 2.

Table 3.1: Impulse response from Vivaldi antenna and channels.

Impulse response	Component	Distance (cm)	Distance after de-embedding direct path (m)	Time delay (ns)
Ray 1	Two antennas	1.00	0	0.66
Ray 2	Reflector 1	1.69	0.69	2.96
Ray 3	Reflector 2	1.88	0.88	3.60
Ray 4	Reflectors 1 & 2	2.34	1.34	5.13
Ray 5	Reflector 3	2.74	1.74	6.46

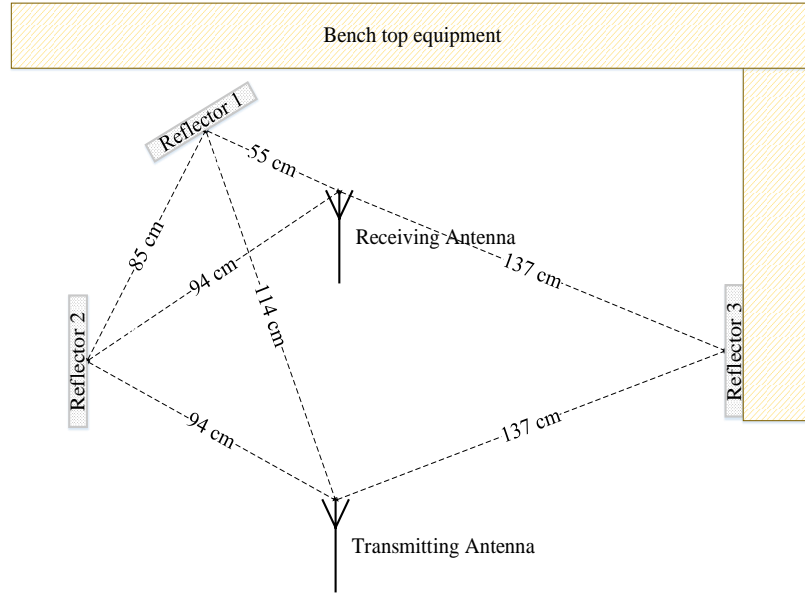


Figure 3.16. Schematic of a typical laboratory environment.

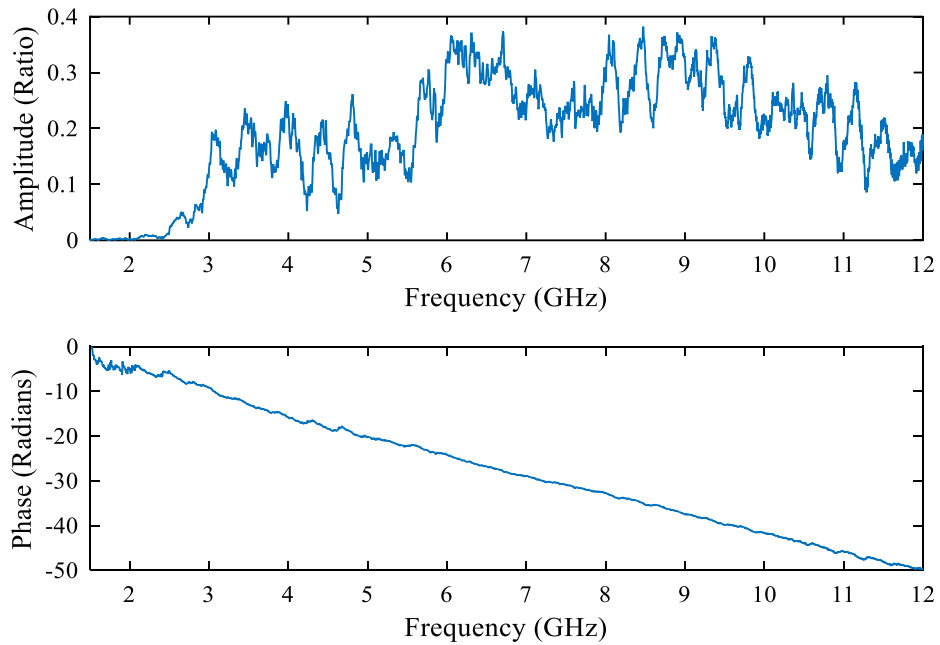


Figure 3.17.  $S_{21}^b$  measurement of the Vivaldi antenna in the laboratory environment after de-embedding the direct path.

From (2.1) and Table 3.1, the wideband channel to demonstrate the scattering effects with the NLOS path in the typical laboratory environment, was described mathematically as a discrete time response:

$$h(t) = 0.145(t - 0.66) + 0.018(t - 2.96) + 0.0135(t - 3.60) + 0.065(t - 5.13) + 0.05(t - 6.46) \quad (3.13)$$

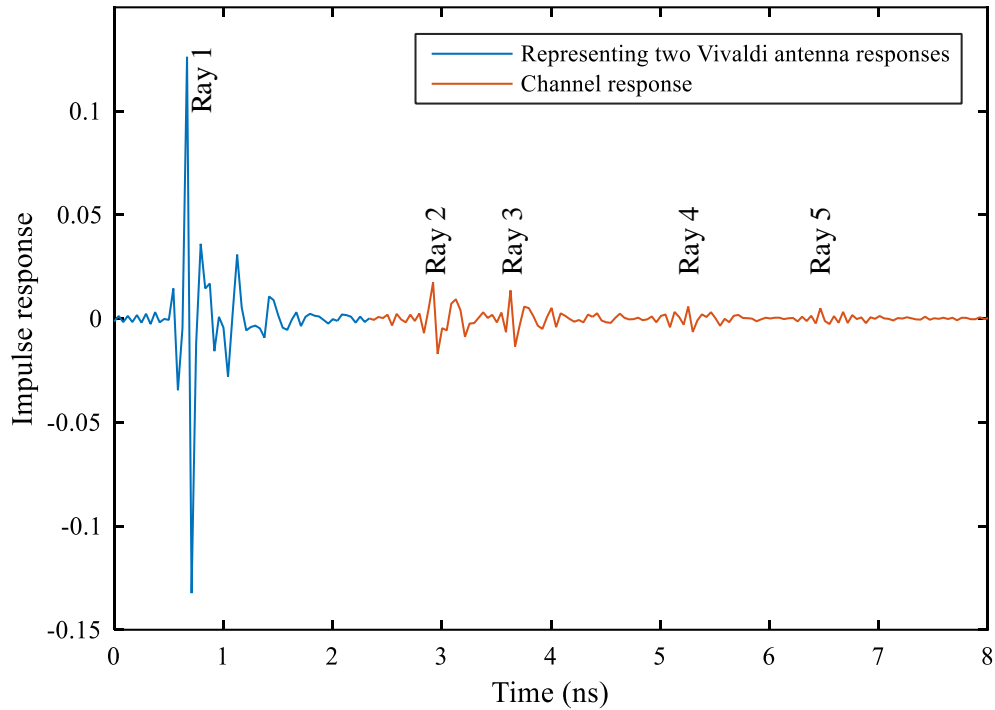


Figure 3.18. Impulse response of the  $S_{21}^b$  measurement of the Vivaldi antenna after de-embedding the direct path.

After the removal of the channel time response from the  $S_{21}^b$  measurement, the  $S_{21}$  of the antenna in the frequency domain was obtained by applying the FFT to the impulse response of the two antennas. Measurements of  $S_{21}^b$  were also conducted inside an anechoic chamber, with the same distance of 100 cm, and the free-space channel was then de-embedded from the  $S_{21}^b$  measurement. This step was done to compare the  $S_{21}$  of the antenna with that obtained from the procedure. The  $S_{21}$  of the antenna obtained from the  $S_{21}^b$  measurement in the anechoic chamber and from the procedure were in agreement, as shown in Figure 3.19.

The frequency response of the channel was then obtained by applying the FFT to the channel's time response, as illustrated in Figure 3.20. The figure shows the existence of a multipath caused by the multipath channel along the frequency axis, which was clear in the channel response in the time domain, as shown in Figure 3.18.

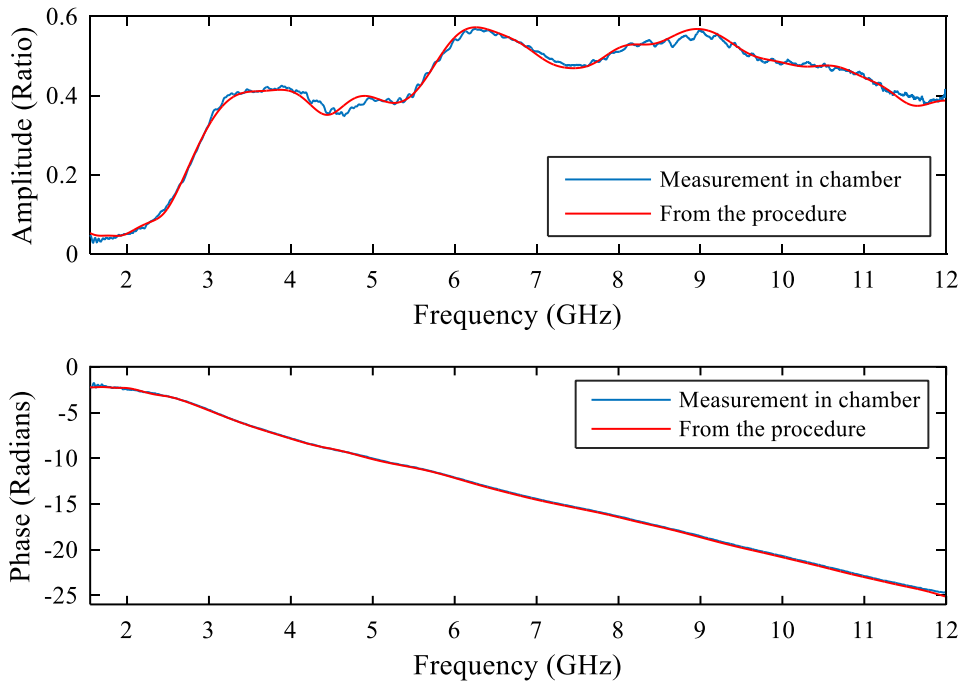


Figure 3.19.  $S_{21}$  of the Vivaldi antenna from the measurement in the anechoic chamber and the procedure.

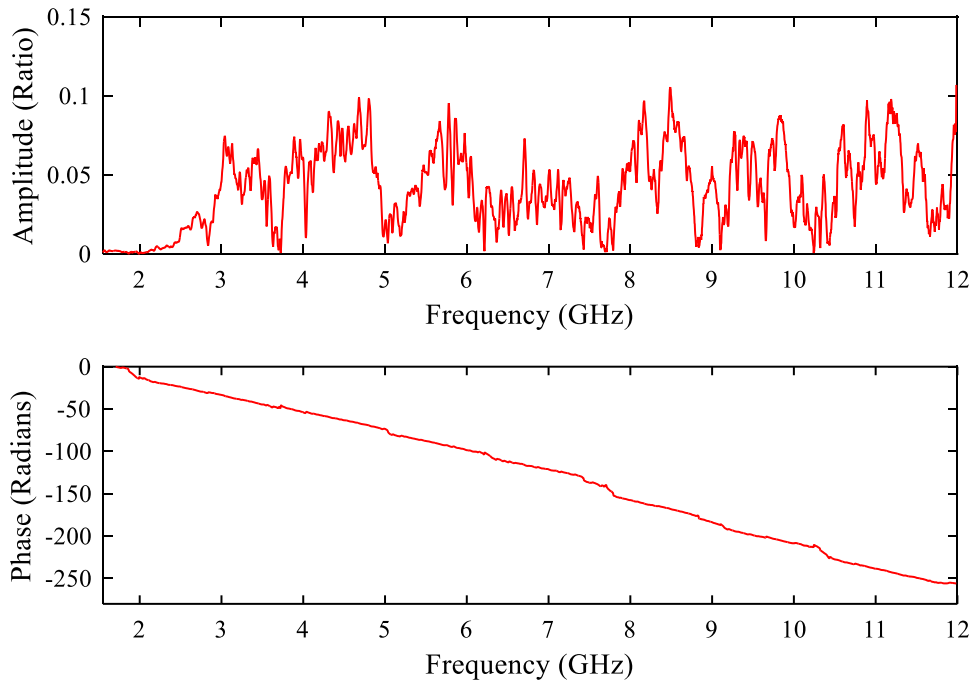


Figure 3.20. Frequency response of the multipath channel.

As discussed above, the  $S_{21}$  value of an antenna can be obtained accurately from the  $S_{21}^b$  measurement outside an anechoic chamber using two identical antennas. This

technique allows designers to obtain the  $S_{21}$  of an antenna if an anechoic chamber is not available. The procedure only requires a sufficiently large space, so that the Rx antenna will satisfy the condition of the far-field measurement.

### 3.7.3 Narrowband Antennas and Other Limitations

To establish the limits of the procedure, the technique was applied to a narrowband patch antenna. Figure 3.21 shows the geometry of the antenna, which was etched on a Rogers RT5880 dielectric substrate with a thickness of 1.575 mm and a dielectric constant  $\epsilon_r$  of 2.2. The antenna was simulated in CST and fabricated to be operated at a resonance frequency of 5.4 GHz. First, the three techniques were applied to characterise the patch antenna and to obtain  $S_{21}$  values. Two identical patch antennas were fabricated and tested in an anechoic chamber to obtain the  $S_{21}$ . An ECM was derived, which represents the antenna as a two-port network that matches the  $S_{11}$  measurement in amplitude and phase [17], [18]. The Hilbert transform was also applied to derive the minimum phase of  $S_{21}$  after obtaining the amplitude of  $S_{21}$  from the  $S_{21}^b$  measurement [33].

#### 3.7.3.1 ECM FOR PATCH ANTENNA

The ECM for the patch antenna was developed by identifying the topology and then calculating the element values by applying an iterative optimisation process, as shown in Figure 3.22. Thus, the desired response can be achieved that will match the  $S_{11}$  with the value from the measurement. ADS software was used for the simulation and optimisation of the ECM. Transmission lines were also a part of the ECM, because they represent the distributed elements of the antenna. The resistance values in the circuit were very low, which means the antenna was nearly lossless. As Figure 3.23 indicates, the amplitude and phase of  $S_{11}$  from the antenna structure simulated using CST, and the measurement and the ECM simulated in ADS, are in full agreement. The input resistance and the reactance from the layout simulation in CST and circuit simulation in ADS are also in full agreement, as illustrated in Figure 3.24.

The voltage-transfer function was calculated from the ADS simulator as the ratio of the voltage ( $V_r$ ) across the radiation resistance and the source voltage ( $V_s$ ), as shown in Figure 3.22. The  $S_{21}^a$  was then obtained from the voltage-transfer function [18].

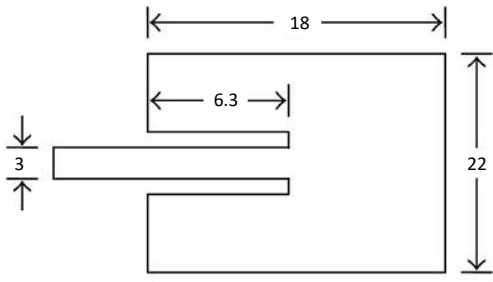


Figure 3.21. Patch antenna geometry (all dimensions in mm).

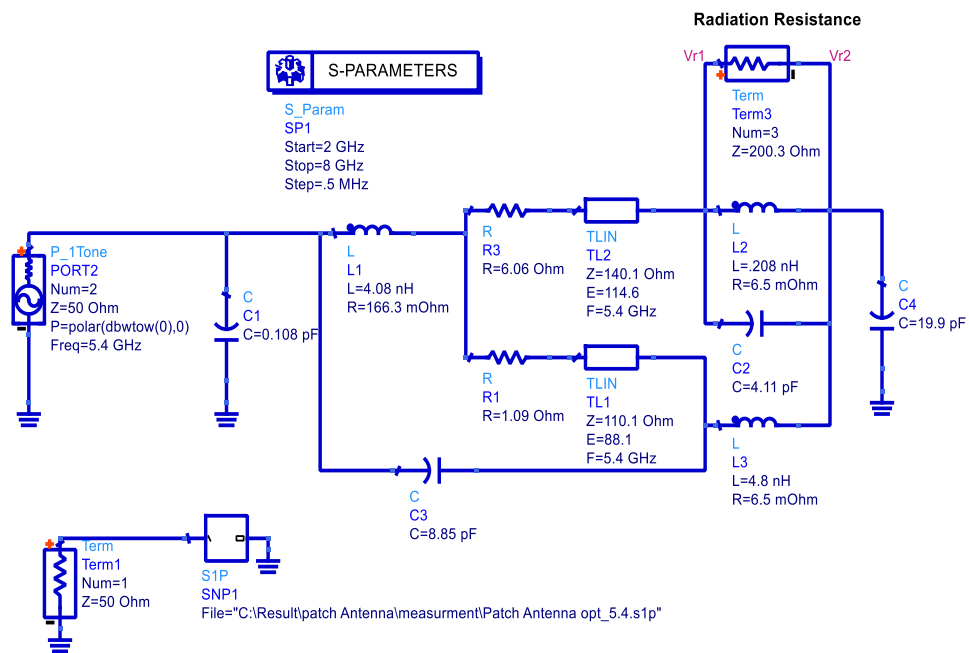


Figure 3.22. ECM for the patch antenna.

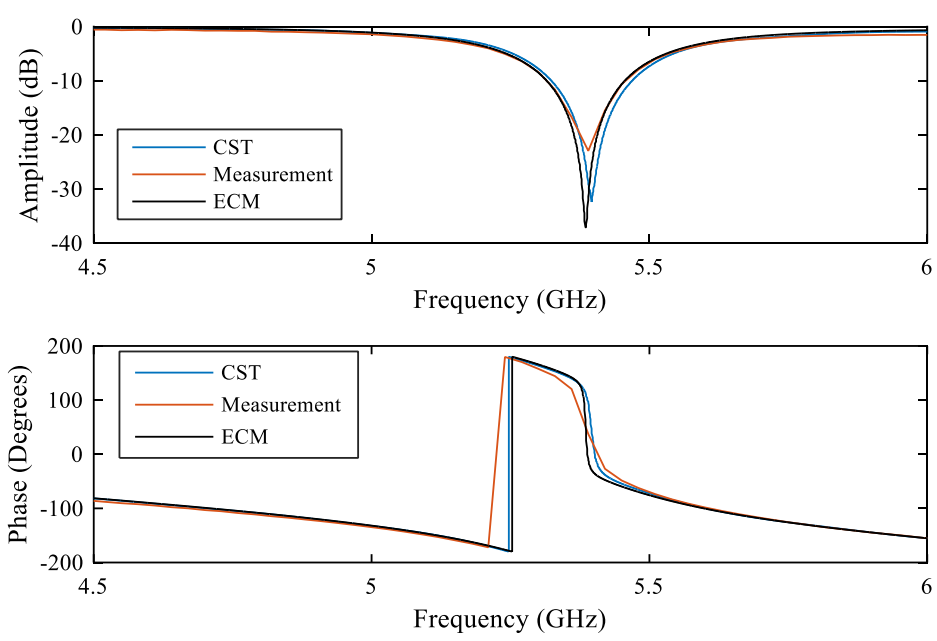


Figure 3.23.  $S_{11}$  of the patch antenna from EM simulation, measurement, and ECM.

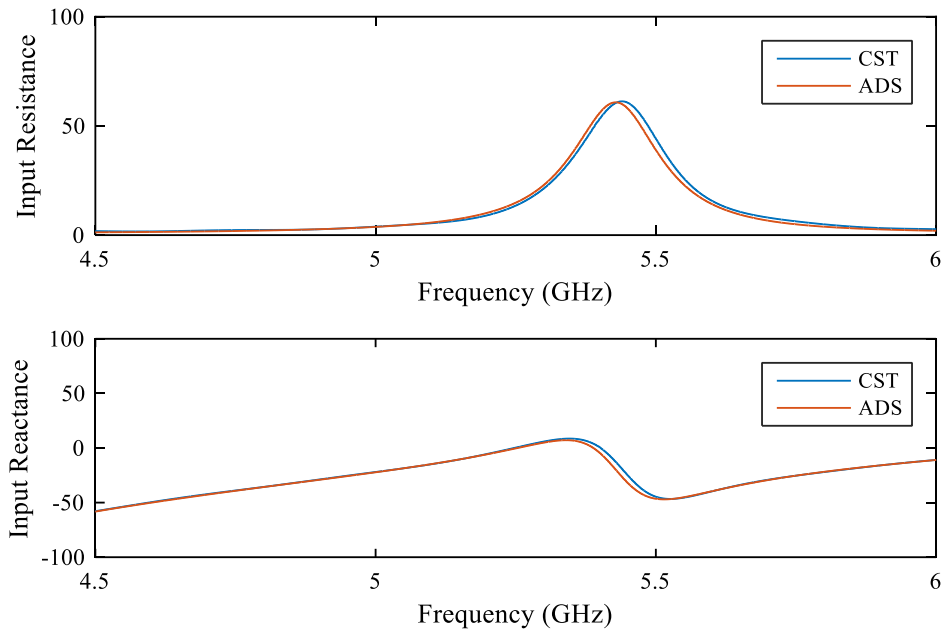


Figure 3.24. The input resistance and reactance of the patch antenna from EM simulation and ECM.

### 3.7.3.2 COMPARISON OF $S_{21}$

The amplitude of  $S_{21}^a$  obtained from the ECM and from  $S_{11}$  using (3.1), assuming the patch antenna is lossless, was matched, as shown in Figure 3.25. As the figure shows, the two values are quite well matched. The measured amplitude of  $S_{21}$  obtained from the  $S_{21}^b$  measurement provides the radiated power in the broadside direction, while the remaining power is radiated in other directions. By adding to the minimum phase of  $S_{21}$  obtained from the Hilbert transform method and a linear-phase component equivalent to the linear phase from either the measurement or the ECM, the phase of  $S_{21}$  obtained from the three techniques was compared and found to be well matched, as illustrated in Figure 3.26.

### 3.7.3.3 VALIDATION OF THE PATCH ANTENNA IN MULTIPATH CHANNELS

The  $S_{21}^b$  between two identical patch antennas in the broadside direction was measured in the same typical laboratory environment with the three reflectors shown in Figure 3.16. The analysis procedure was applied, and the time response of the  $S_{21}^b$  measurement after de-embedding the direct path is shown in Figure 3.27. The ringing of the impulse response of the two antennas (Ray 1) in the time domain ended at 4.65 ns, which made it difficult to distinguish between the impulse response of the antennas and the two rays in the channel response (Ray 2 and Ray 3). The  $S_{21}$  of the patch antenna was then obtained by applying the FFT to the impulse response of the

two antennas. Figure 3.28 shows the agreement in  $S_{21}$  of the patch antenna between the measurement in the anechoic chamber and the developed procedure. The  $S_{21}$  value obtained from this step was accurate: the amplitude of the impulse response of the antenna was high compared to the amplitude of Ray 2 and Ray 3.

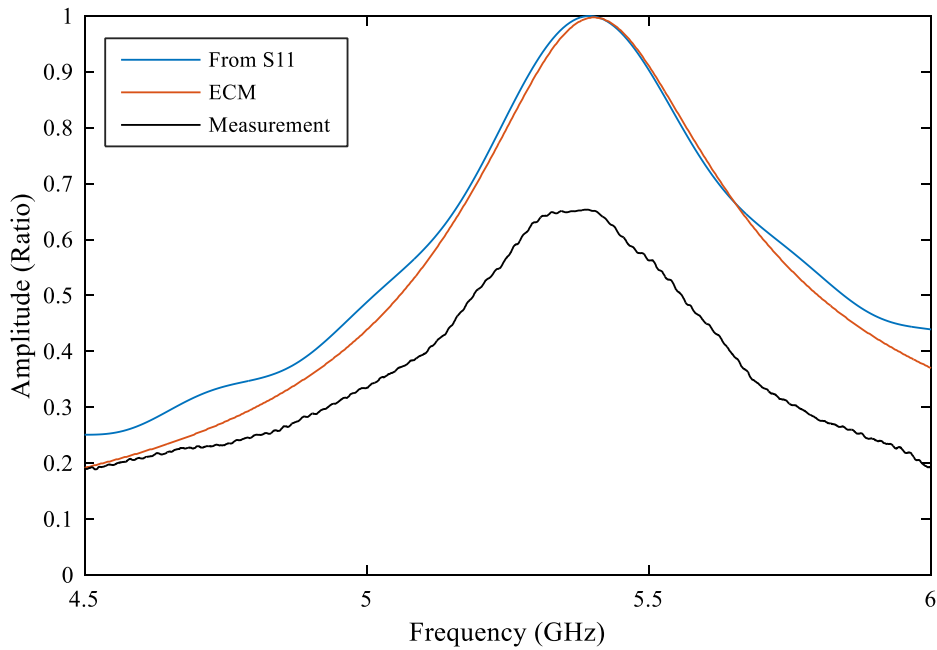


Figure 3.25. Comparison of the amplitude of  $S_{21}^a$  and  $S_{21}$  of the patch antenna.

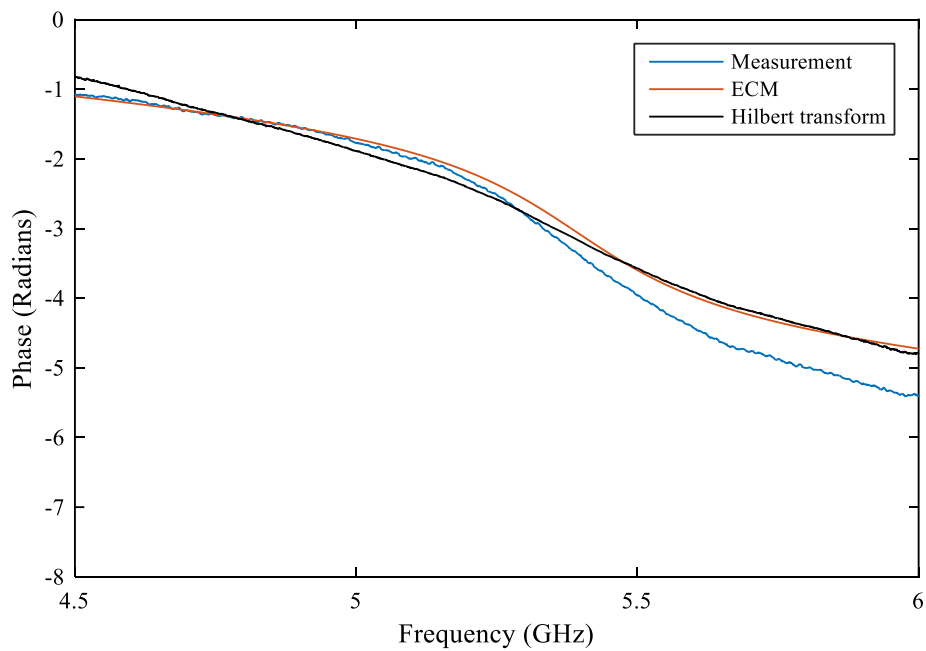


Figure 3.26. Comparison of the phase of  $S_{21}^a$  and  $S_{21}$  of the patch antenna.

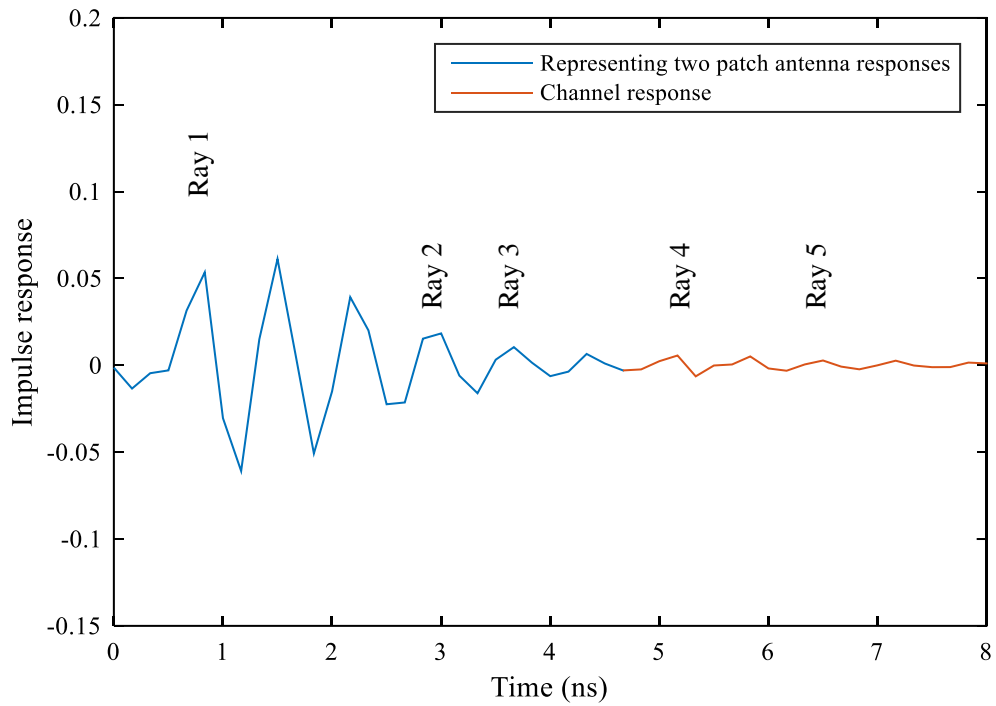


Figure 3.27. Impulse response of the  $S_{21}^b$  measurement of the patch antenna in the laboratory environment after de-embedding the direct path.

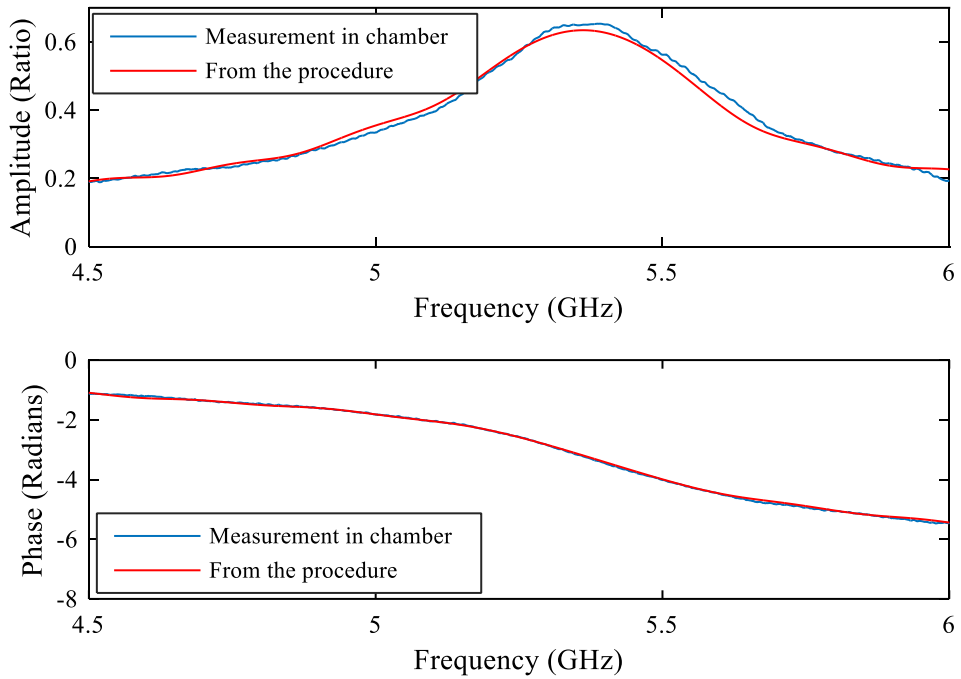


Figure 3.28.  $S_{21}$  of the patch antenna from measurements in the anechoic chamber and the procedure.

#### 3.7.3.4 OTHER LIMITATIONS

The width of the impulse response of an antenna and its ringing both depend on the bandwidth of the antenna. As discussed above, the far-field condition is required for this procedure. Another limitation related to the reflections to the channel is the long ringing of the impulse response of the antenna [19]. This ringing, in turn, results in a mixing of the antenna response with the channel response in the time domain. For instance, dipole and patch antennas both have a long ringing response in the time domain [4]. This ringing occurs because the narrowband transmission in the frequency domain will have a wide impulse response that will continue ringing in the long term. In such cases, the ray that represents the impulse response of the antenna will merge with the ray produced by the reflector. This property creates difficulties in distinguishing between the impulse responses of the antenna and the channel. To avoid this limitation, the shortest reflected path to the multipath channel has to occur after the end of the impulse response of the antenna. For the patch antenna, the shortest distance from the multipath channel needs to be at least 2.215 m and with a direct distance of 1 m to avoid mixing the ray representing the direct path with the rays representing the multipath channel in the time domain.

Figure 3.18 and Figure 3.27 show the differences in channel responses in the time domain, which represent the multipath components between the impulse responses of the Vivaldi and patch antenna measurements in the same typical laboratory environment. These differences occur because each ray manifests the antenna impulse response, which indicates that the channel still has the properties of the antenna used in the measurement [24], [26]. It thus is important to de-embed the antenna properties from the channel response in both the frequency and time domains to characterise the channel model, as will be discussed in Chapter 6.

### 3.8 Summary

In this chapter, the amplitude and phase values of the  $S_{21}$  of a wideband Vivaldi antenna were determined using three different techniques: ECM, measurement in an anechoic chamber, and the Hilbert transform method. The topology of the antenna's ECM was represented and mapped to the layout structure of the Vivaldi antenna. The

ECM was developed by combining lumped and distributed circuit elements. The second port in the ECM represents the radiation resistance. The amplitude of  $S_{21}$  obtained from the ECM shows the total radiated power from the antenna in all directions. The phase of  $S_{21}$  obtained from the ECM and the measurement was found to be well matched, because the direction of the main beam of the fundamental radiation pattern was in the same direction as the measurement.

This characterisation procedure using three techniques was also applied to a narrowband patch antenna. The ECM, the measurement, and the Hilbert transform confirmed this new approach to characterising an antenna. These techniques were used to characterise narrowband and wideband antennas to show the difference between the conventional approach of only realising a low  $S_{11}$  and the new approach of calculating the antenna response in a specific direction.

A procedure was also described to characterise wideband and narrowband antennas in multipath channels in the frequency and time domains using  $S_{21}^b$  measurements. The procedure was applied to Vivaldi and patch antennas in a typical laboratory environment to obtain the responses of the antenna and channel in the two domains. This technique allowed the separation of the impulse response of the antennas from that of the channel. Characterisation showed the impulse response from the direct path representing the impulse response of each antenna. The procedure therefore provides a method to predict the  $S_{21}$  of an antenna without requiring an anechoic chamber. The limitations of the procedure were also shown due to the long ringing caused by certain antennas in the time domain. Separating the channel response in the time domain becomes challenging with the existing multipaths that occur during the time of the impulse response of the antenna. The  $S_{21}$  of the patch antenna was accurately obtained, however, because the amplitude of the impulse response of the antenna was high compared to the mixing rays in the channel response. Obtaining accurate frequency- and time-domain responses of the antenna and channel allows for modelling both, which then provides the possibility of modelling them separately and including an antenna in DCS simulations. These steps will be described in the next chapter.

# CHAPTER 4: ANTENNA MODELLING TECHNIQUE FOR DIGITAL COMMUNICATION SYSTEMS

## 4.1 Introduction

The prediction of antenna effects is an important consideration for achieving good DCS performance. Antenna designers aim to have wideband non-dispersive antennas as well as minimal symbol scattering in order to minimise the circuit complexity at the receiver. Along with the multipath channel, non-linearity in the RF components also introduces symbol scattering at the receiver. The antenna can also cause signal distortion [18]. This distortion in the signal adversely affects DCS performance and increases the symbol scattering at the receiver.

In this chapter, a commercial dual-band antenna and the Vivaldi antenna that was characterised in Chapter 3 (as shown in Figure 4.1) were measured and modelled to predict antenna effects in a DCS. An ECM was derived for the commercial antenna to obtain the total radiated power and to characterise the antenna behaviour. The full set of  $S$ -parameters were measured in an anechoic chamber between two identical commercial antennas to compare the resulting  $S_{21}$  in amplitude and phase with the values obtained from the ECM, as described in Section 4.4. Section 4.5 presents the antenna modelling for both antenna types from the  $S_{21}^b$  measurements to be included in a DCS. An FIR model was derived for each  $S$ -parameter to represent a time-domain system model for the type of antenna. Section 4.6 presents the simulation of an antenna system model in a DCS using 16-QAM orthogonal frequency division multiplexing (OFDM) modulation to predict each antenna's effects in the DCS. Section 4.7 describes the experimental antenna setup in the DCS. The symbol-scattering experiments were conducted using 16-QAM OFDM transmission. The noise produced by the RF components was considered using a back-to-back (BTB) connection without antennas, and the same noise was added to the simulations based on the EVM values. The results were then compared between the simulations and experiments described in Section 4.8 to discuss each antenna's effect in the DCS.

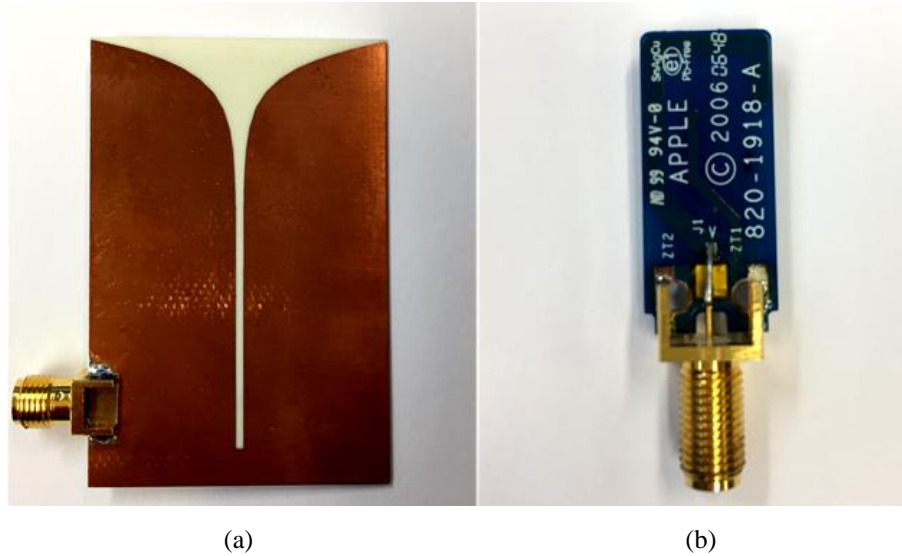


Figure 4.1. Photographs of two characterised antennas: (a) Vivaldi and (b) commercial dual-band.

## 4.2 Antenna Measurements

The  $S$ -parameter values in amplitude and phase can be measured in an anechoic chamber between two identical antennas [2]-[4]. Having the full set of  $S$ -parameter measurements enables designers to:

1. predict the correct frequency response in the direction of the channel;
2. derive a time-domain system model for inclusion in DCSs;
3. include the antenna in the simulation of a DCS and to calculate system performance, including symbol scattering due to dispersion and digital signal distortion;
4. optimise the antenna's design to improve antenna performance in DCSs.

Measuring  $S_{11}$ ,  $S_{21}$ ,  $S_{12}$ , and  $S_{22}$  in both amplitude and phase increases the accuracy when deriving antenna system models. For two identical antennas,  $S_{11}$  and  $S_{22}$  are similar, as are  $S_{12}$  and  $S_{21}$ . For the commercial and Vivaldi antennas used in the present study, the  $S$ -parameters were measured in P2P communications inside an anechoic chamber between two identical antennas. The distance for the free-space channel was 70 cm. The orientation for each antenna was on the antenna's principal axis. The commercial antenna was placed in the broadside direction, while the Vivaldi antenna was placed in the endfire direction.

### 4.3 ECM for the Commercial Antenna

A commercial dual-band antenna was printed on an FR-4 dielectric and had planar features. The first step was to define the topology, as mapped to the antenna structure shown in Figure 4.2. The antenna is represented by the transmission line TL1 and inductors L1, L2, and L4, whereas the capacitors represent the coupling to the ground. The ECM was simulated and optimised in ADS to match the complex  $S_{11}$  obtained from the measurement. The ECM for the antenna was then derived, as illustrated in Figure 4.3, and the radiation resistance of the antenna was found to be at  $63 \Omega$ . The one-Port  $S$ -Parameter (S1P) block shown in Figure 4.3 contains the  $S_{11}$  data-measurement result obtained using a network analyser. This block was then used to optimise the circuit to match the  $S_{11}$  measurement by using an iterative optimisation process in the ADS software. The ECM showed a single path for transferring energy through the ECM, which confirmed that the antenna is a minimum-phase antenna [4]. The  $S_{11}$  from the ECM was then compared with the measurement. Both values were found to match, as shown in Figure 4.4. The antenna had two radiating bands at the two resonance frequencies of 2 GHz and 6 GHz.

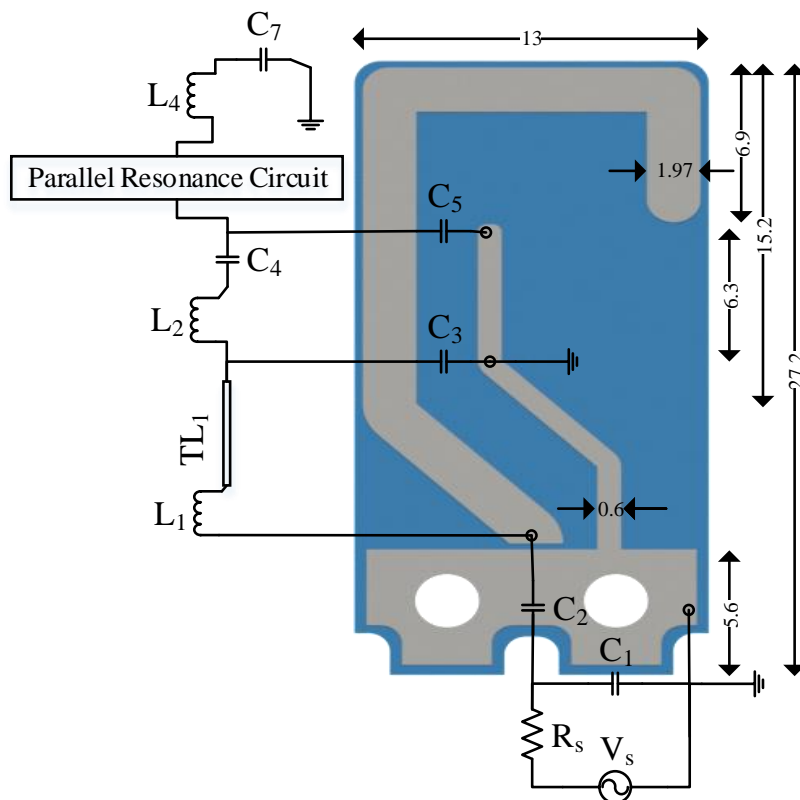


Figure 4.2. Commercial dual-band antenna structure and ECM topology (all dimensions in mm).

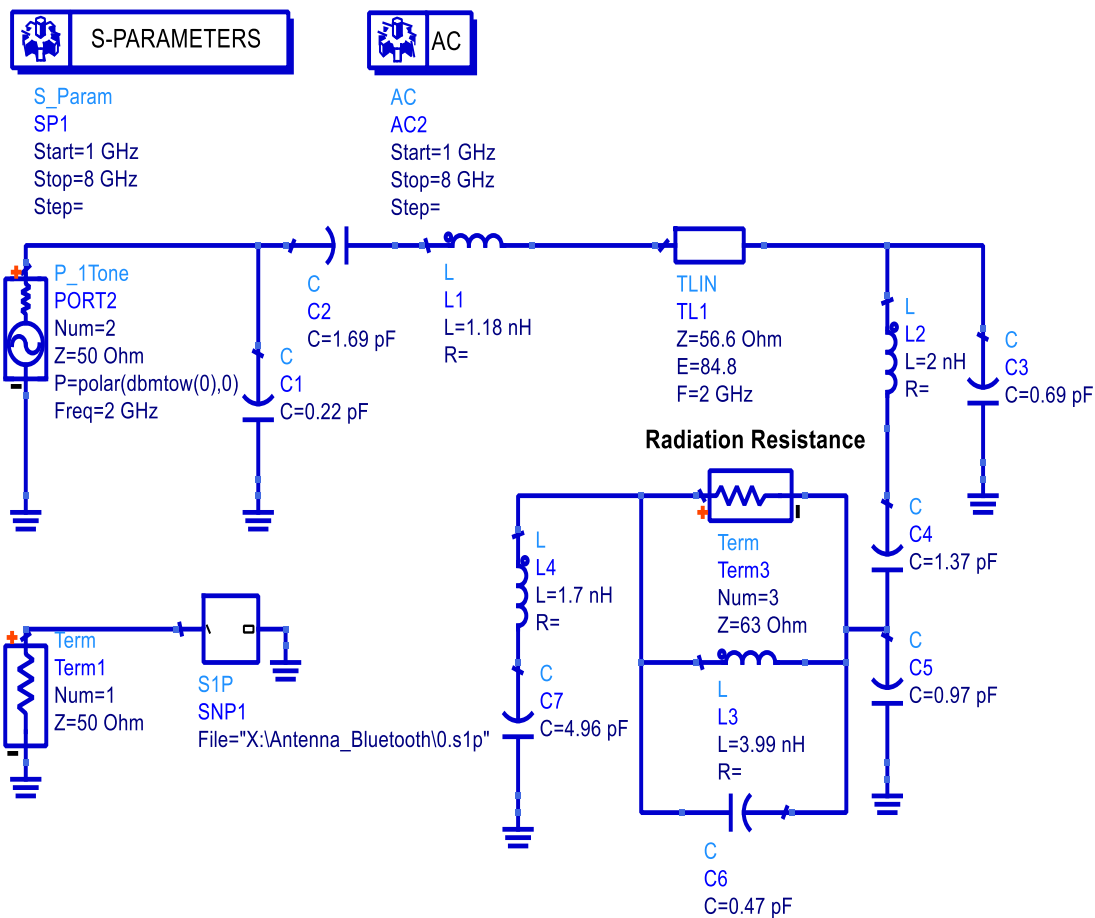


Figure 4.3. ECM for the commercial dual-band antenna.

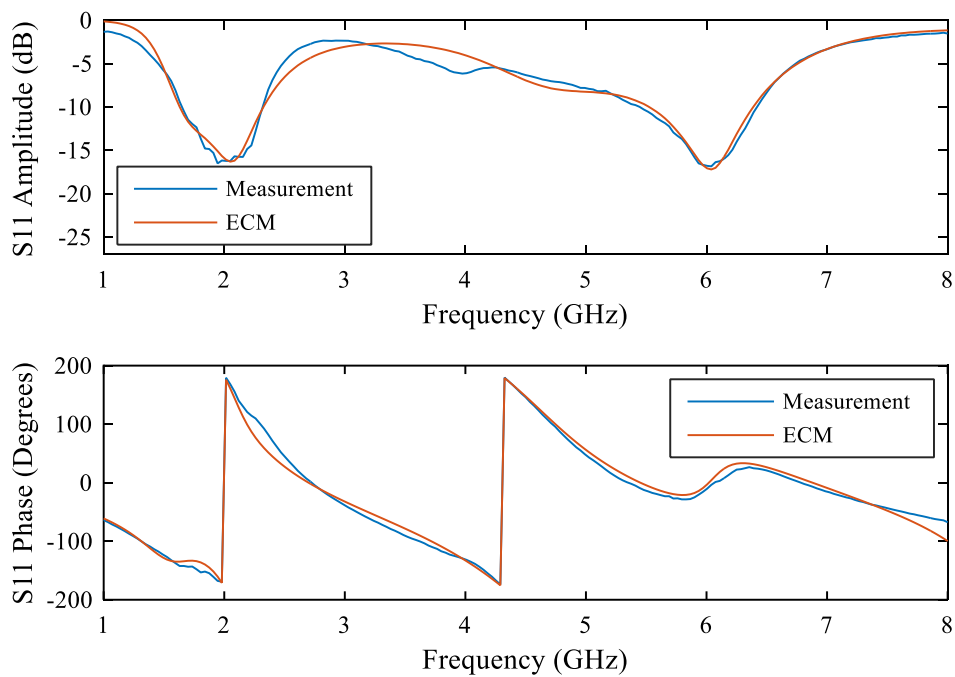


Figure 4.4. Comparison of  $S_{11}$  from measurements and from ECM: commercial antenna.

## 4.4 Characterisation of the Commercial Antenna

Measurements of  $S_{21}^b$  were conducted in an anechoic chamber between two identical antennas on their principal axes, with the free-space channel 0.7 m apart, using a network analyser. The TOSM calibration technique was used to define the reference plane at the end of each cable. The commercial antenna was placed in the broadside direction in the measurements, while the Vivaldi antenna was placed in the endfire direction. The amplitude and phase values of  $S_{21}$  for each antenna were obtained after de-embedding the free-space channel using (3.5) and (3.6), taking the square root of the amplitude, and dividing the phase by two. Assuming the antenna is lossless and that all observed power is radiated, the  $S_{21}^a$  value, which yields the total radiated power of each antenna, can be calculated from  $S_{11}$  using (3.1).

The  $S_{21}^a$  from the ECM matched that computed from  $S_{11}$ , assuming the antenna is lossless, as shown in Figure 4.5. This response shows the total radiated power by the antenna, which is the same as the power that has been accepted, or the total radiated power divided by the antenna efficiency.  $S_{11}$  provides the accepted power. Antenna losses due to inefficiency will be discussed in Chapter 7 to identify whether this antenna is lossless or has some losses. The  $S_{21}$  of the commercial antenna obtained from the  $S_{21}^b$  measurement after de-embedding the free-space channel is also shown in Figure 4.5. This value provides the radiated power from the antenna on the antenna's principal axis. The remaining power was radiated on the sidelobes.

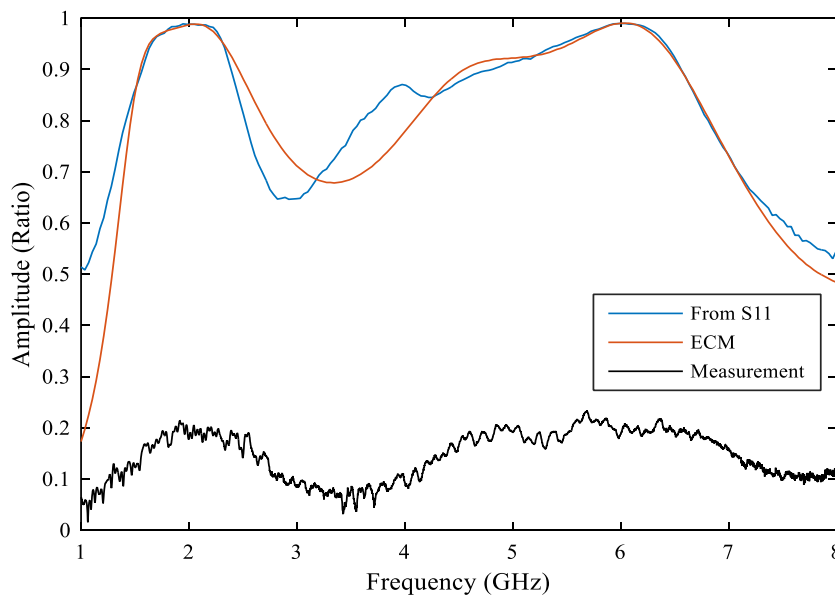


Figure 4.5. Amplitude of  $S_{21}^a$  and  $S_{21}$  of the commercial antenna.

As shown in Figure 4.6, the phase of  $S_{21}^a$  obtained from the ECM matched the  $S_{21}$  phase obtained from the  $S_{21}^b$  measurement, and both were found to be linear in phase. This situation indicates that only minimum-phase and linear-phase components were found in the  $S_{21}$  phase of the commercial antenna, which in turn confirms that the commercial antenna was a minimum phase and that its behaviour had a frequency-invariant radiation pattern [1].

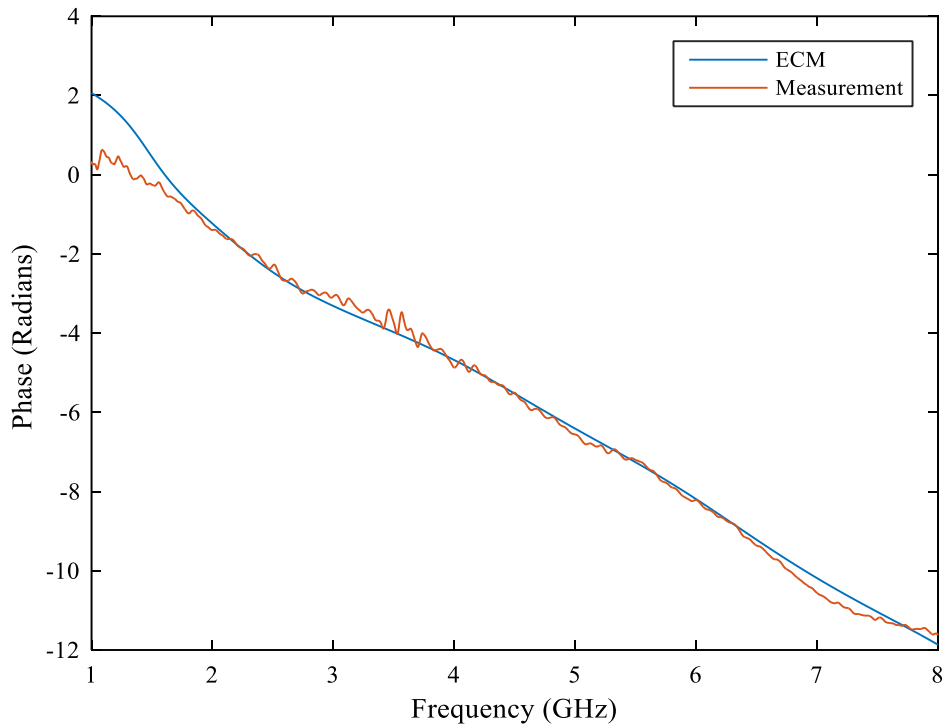


Figure 4.6.  $S_{21}$  and  $S_{21}^a$  phases from the measurement and the ECM.

## 4.5 Antenna System Model

Modelling an antenna as a time-domain system is often used to analyse the effects of an antenna in DCS software. Modelling is developed to determine the computability of the antenna in a DCS simulation.  $S$ -parameters can be measured between Tx and Rx antennas in an anechoic chamber [2]-[4]. The measurement of a full set of  $S$ -parameters enables designers to predict the correct frequency response in the direction of communication for P2P. The system model is derived by realising the complete  $S$ -parameters from the measurement between Tx and Rx antennas. This derivation also helps designers to model accurate system models with precise  $S_{11}$ ,  $S_{21}$ ,

$S_{12}$ , and  $S_{22}$  measurements. In the present study, the impulse response in the time domain was obtained by applying the IFFT to each complex  $S$ -parameter. In general, when using two identical antennas in the measurement, the  $S_{11}$  and  $S_{22}$  are the same, as are  $S_{12}$  and  $S_{21}$ . From the full set of  $S$ -parameters measured in an anechoic chamber, FIR models were then derived for each  $S$ -parameter with a 4,001-order to develop four models for the  $S$ -parameters.

The impulse responses of the  $S$ -parameters were computed using IFFT for each complex  $S$ -parameter obtained from the frequency-response measurement for each antenna type. The impulse responses of the  $S_{21}^b$  measurements for the commercial and Vivaldi antennas were then obtained. The impulse responses of the commercial antenna  $S_{21}^b$  FIR model and the Vivaldi antenna's  $S_{21}^b$  FIR model are shown in Figure 4.7a and Figure 4.7b, respectively. Note that the commercial antenna caused additional components due to multiple reflections in the antenna itself, which will cause symbol scattering in DCSs.

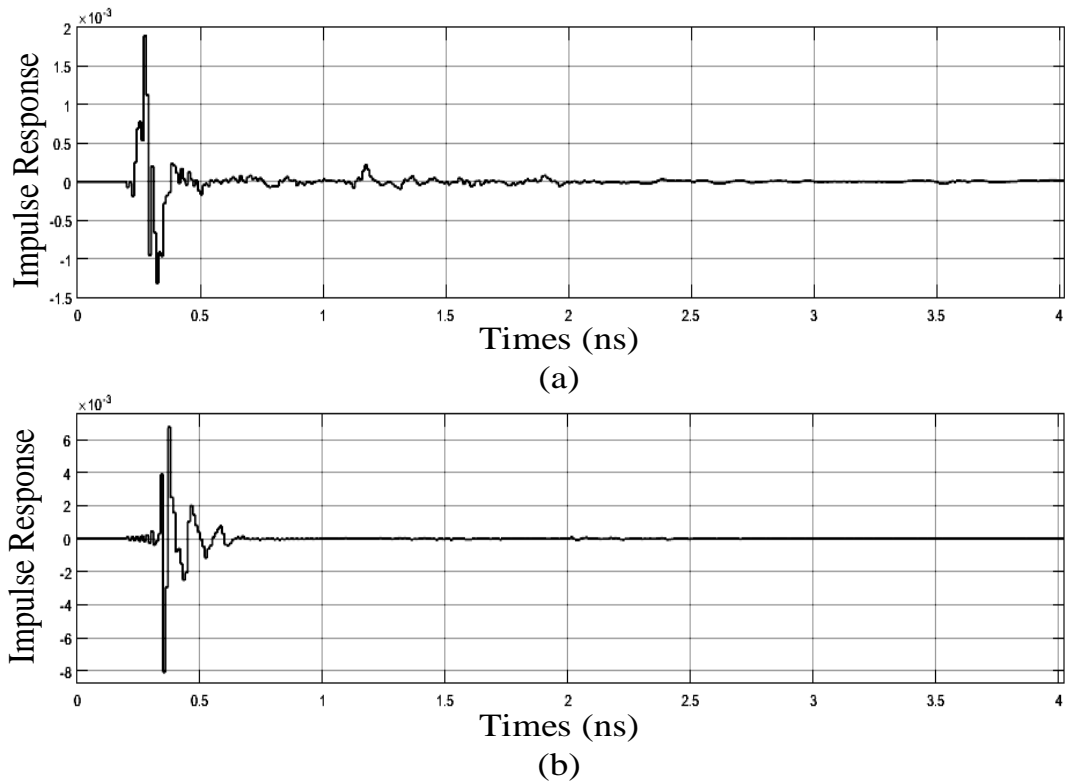


Figure 4.7. Impulse response of the  $S_{21}^b$  FIR model for (a) commercial and (b) Vivaldi antennas.

A complete system model with four FIR models derived for the full set of  $S$ -parameters was then developed in SIMULINK, as shown in Figure 4.8. The chirp signal in the input of the system is a frequency-swept source to predict the frequency response of the antenna system model, as shown in Figure 4.9a. This signal may be compared to the  $S_{21}^b$  measurement shown in Figure 4.9b, which contains the response of the two identical commercial antennas with a 0.7-m distance free-space channel.

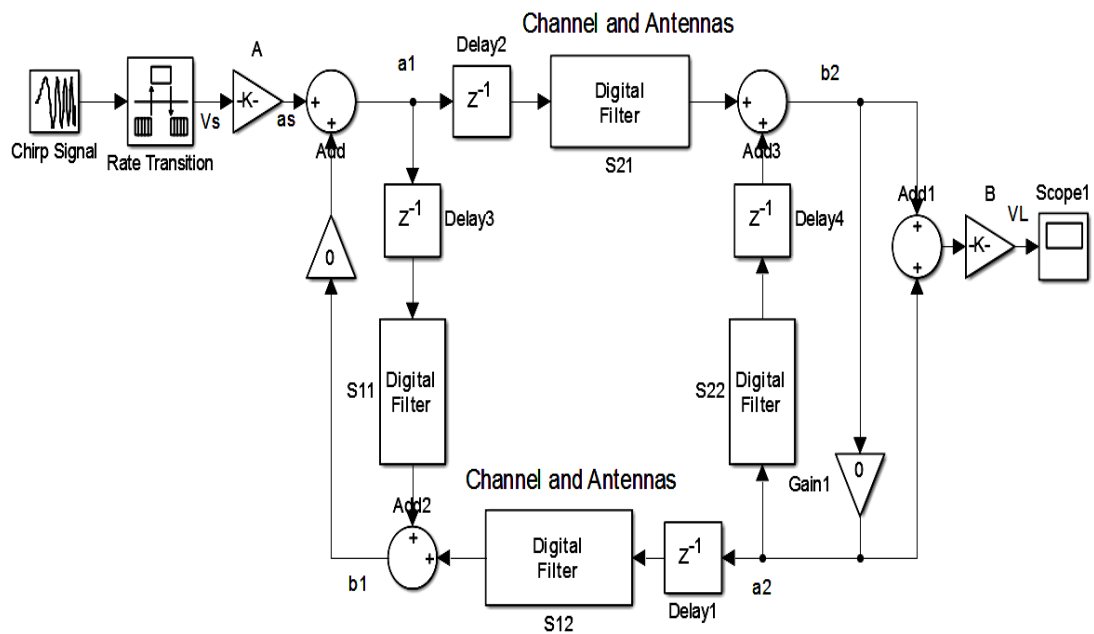


Figure 4.8. Complete antenna system model with four FIR models in SIMULINK.

The frequency response of the time-domain system model for the Vivaldi antenna is illustrated in Figure 4.10a. This response is similar to the antenna  $S_{21}^b$  measurements shown in Figure 4.10b, which shows the frequency responses of the two identical Vivaldi antennas, with the free-space channel 0.7 m apart. Antenna measurements were then modelled as a two-port network system to evaluate the performance of the antenna in a system simulation that could then be used directly in DCS software.

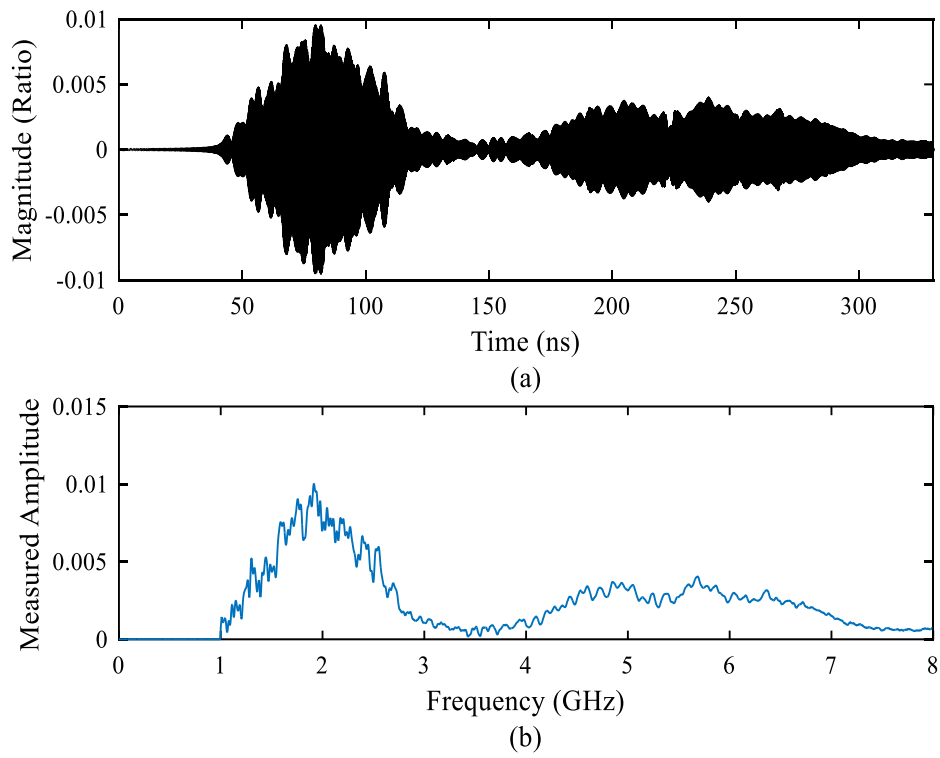


Figure 4.9. Frequency response of the commercial antenna: (a) system model and (b)  $S_{21}^b$  measurement.

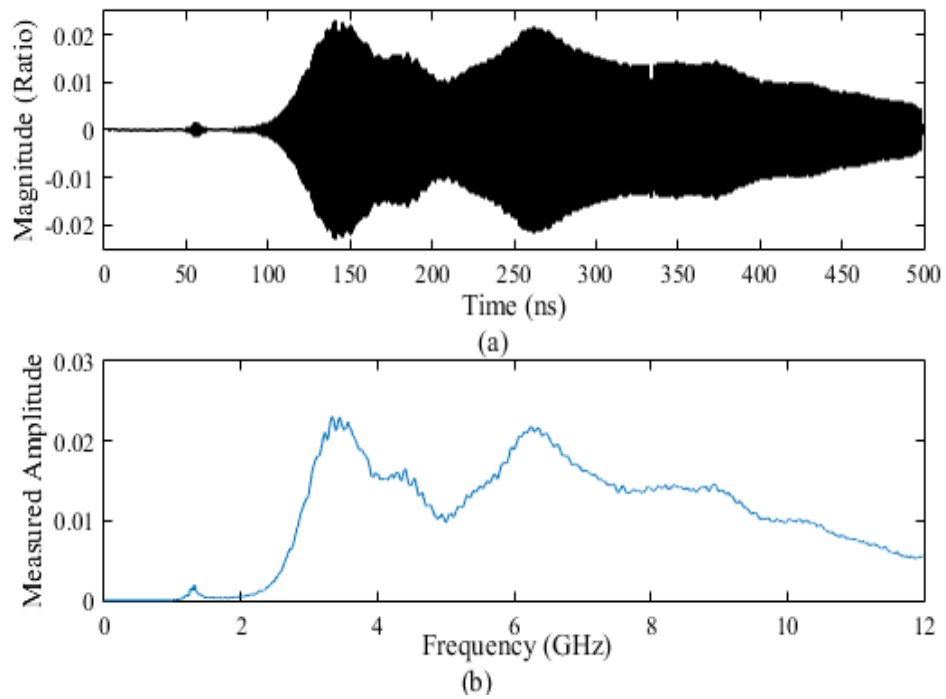


Figure 4.10. Frequency response of the Vivaldi antenna: (a) system model and (b)  $S_{21}^b$  measurement.

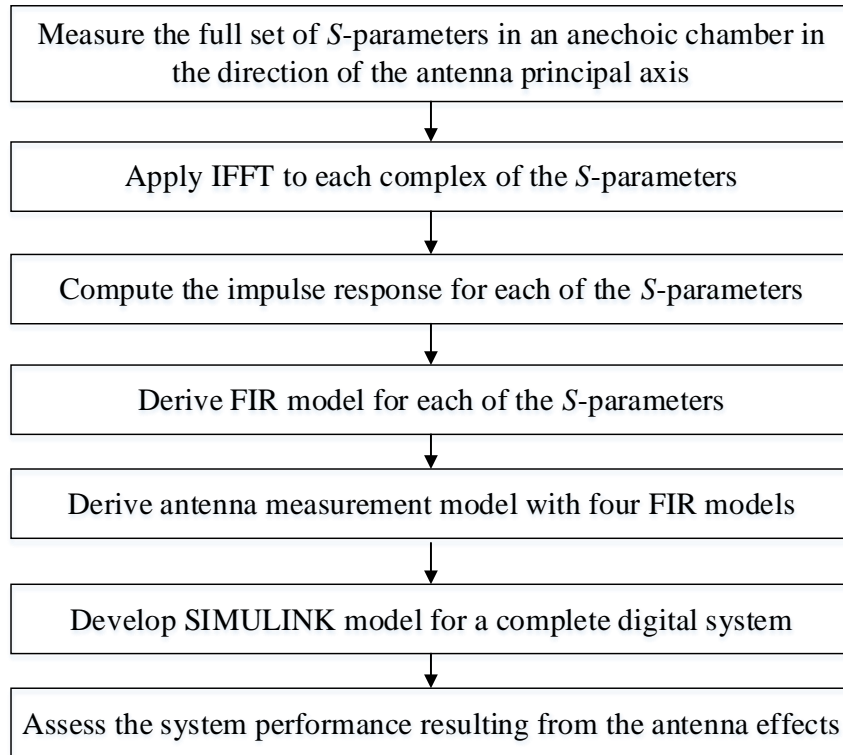


Figure 4.11. Flow chart to predict antenna effects in a DCS.

The system model shown in Figure 4.8 was then used to study the antenna effects on transmitted signals and to calculate the EVM as well as the resulting BER of a DCS [18]. This technique allows designers to assess the system performance that resulting from the antenna effects, such as symbol scattering that degrades system performance. Figure 4.11 shows the steps involved in predicting the effects of an antenna in a DCS, starting from the frequency-response antenna measurement.

#### 4.6 Antenna Simulation in a DCS

A complete DCS was then modelled in SIMULINK to simulate the two different antennas, as illustrated in Figure 4.12. The system model was derived to predict the effects of each antenna type and to obtain the EVM and BER for symbol-scattering characterisation. The DCS consists of a data generator that was then modulated by 16-QAM OFDM. An up-converter was used to send the data with a carrier frequency to convert the transmission data from the baseband to the passband, followed by the antenna system model. FIR models represented the full set of  $S$ -parameters of the antenna measurement from the two identical antennas with the free-space channel.

The signal was then passed through the down-converter to convert the signal back to the baseband-modulated signal. This step was performed without adding any noise so that the antenna effect in the DCS could be predicted.

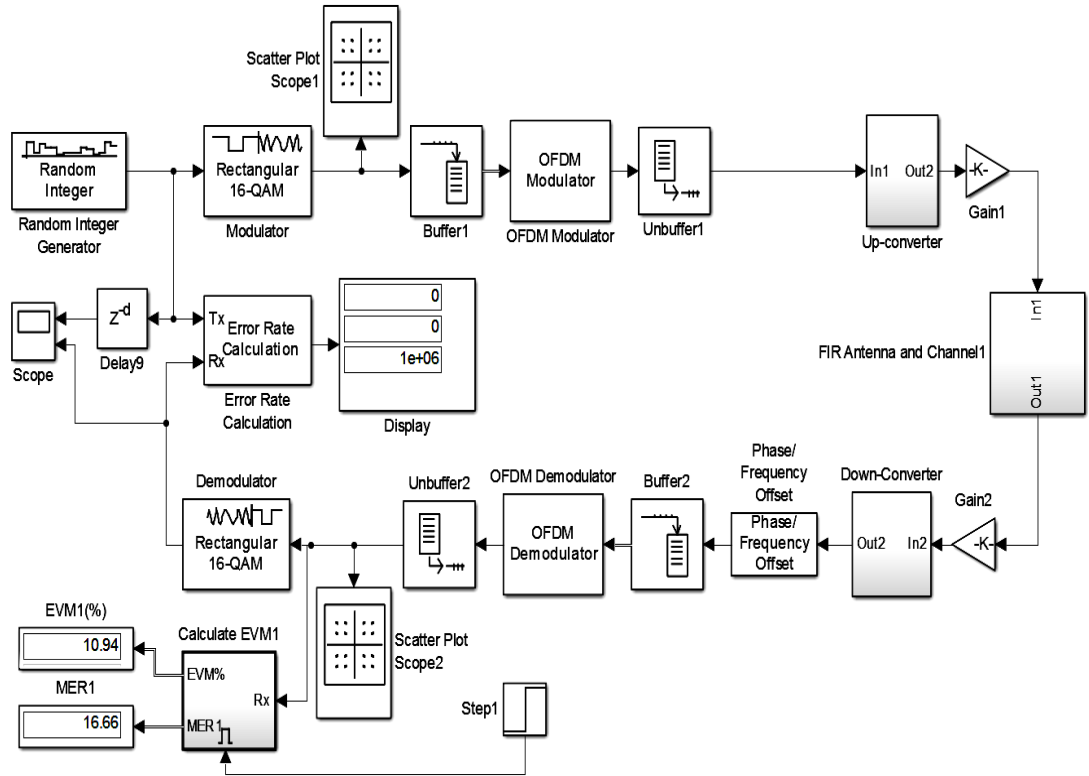


Figure 4.12. Antenna with free-space channel in a DCS.

#### 4.6.1 Commercial Antenna

In the DCS simulation, the commercial antenna was examined at two different carrier frequencies with  $10^6$  symbols. The effects of the antenna on the modulated signal were then investigated. The antenna effects with the free-space channel (from the measurement in the anechoic chamber) on DCS performance are shown in the constellation diagrams in Figure 4.13a and Figure 4.13b for the two carrier frequencies of 2 GHz and 6 GHz, respectively. The output constellation diagrams show that the antenna caused symbol scattering with varying EVM values. The EVM values were 10.94% and 7.68% in the carrier frequencies of 2 GHz and 6 GHz, respectively. The BER was zero because the receiver was able to recover the symbols despite the scattering that occurred. This scattering was the result of the antenna impulse response producing other components due to multiple reflections in the antenna itself, which

caused the symbol scattering shown in the constellation diagrams. Comparisons between the two carrier frequencies in the constellation diagrams and the EVM showed that the symbol scattering that occurred at 2 GHz was more severe than at 6 GHz. This comparison was helpful for estimating the antenna effects on the modulated symbol in the two bands. This technique is also useful for predicting the performance of the system in each band in multiband systems.

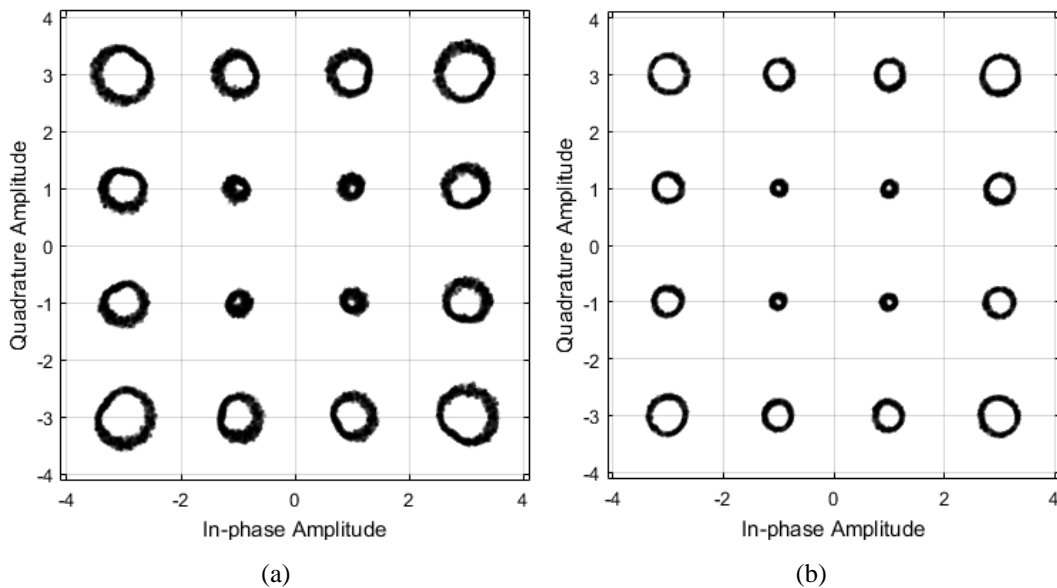


Figure 4.13. Output constellation diagrams based on the commercial antenna system model at carrier frequencies of (a) 2 GHz and (b) 6 GHz.

#### 4.6.2 Vivaldi Antenna

The Vivaldi antenna was also examined in the DCS at two carrier frequencies with  $10^6$  symbols with the free-space channel. The antenna effects on the modulated signal are shown in the constellation diagrams in Figure 4.14a and Figure 4.14b for the two carrier frequencies of 3.5 GHz and 6.3 GHz, respectively. The output constellation diagrams show that the antenna caused less symbol scattering with varying EVM values. The EVM values were 2.32% and 1.81% in the carrier frequencies of 3.5 GHz and 6.3 GHz, respectively.

The EVM changed with different carrier frequencies with the same antenna, as explained in the section on the commercial and Vivaldi antennas. Table 4.1 shows the EVM values with two different carrier frequencies for the two antenna types. The EVM and BER values can therefore be seen to be a function of frequency.

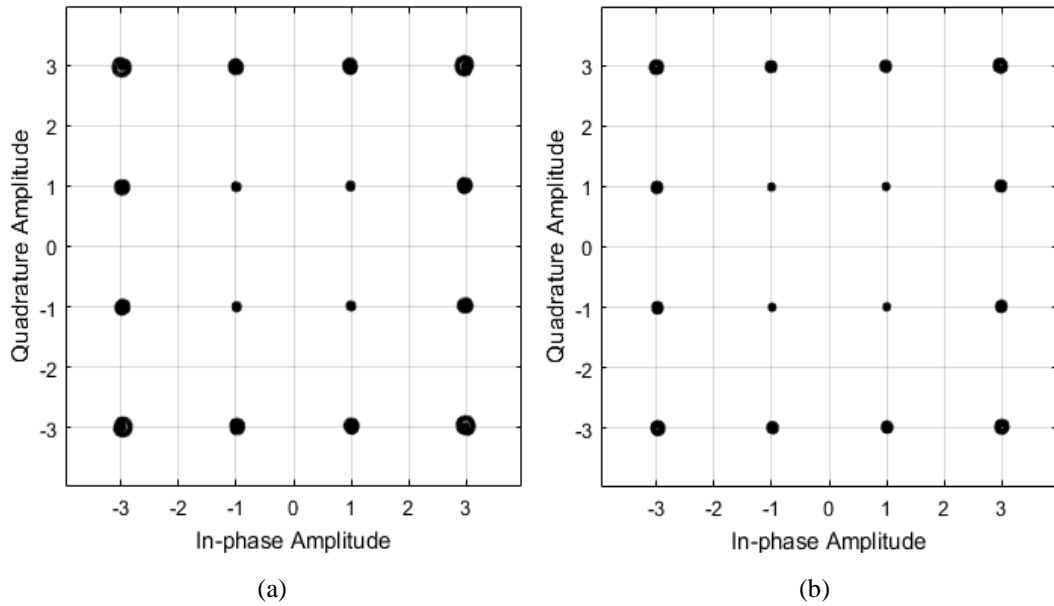


Figure 4.14. Output constellation diagrams based on the Vivaldi antenna system model at carrier frequencies of (a) 3.5 GHz and (b) 6.3 GHz.

Table 4.1: Comparison of EVM and BER with different carrier frequencies without adding noise.

Antenna type	Commercial		Vivaldi	
	2 GHz	6 GHz	3.5 GHz	6.3 GHz
RF frequency	2 GHz	6 GHz	3.5 GHz	6.3 GHz
EVM (%)	10.94	7.68	2.32	1.82
BER	0	0	0	0

The effects in a DCS depend on the antenna types employed. An antenna impulse response is an important parameter, especially if the antenna produces additional components due to multiple reflections in the antenna itself. Such reflections will increase the effects in a DCS's performance. This technique allows designers to simulate and predict the effects of antennas in a DCS. Doing so also allows them to modify and redesign antennas for robust DCS performance. Once antenna models are derived, the different antennas and channels can be used for a variety of applications. This is the case when, for example, a base station is transmitting and many users are receiving signals.

## 4.7 Experimental Setup for Antennas in a DCS

The signal distortion caused by the two different antennas was experimentally demonstrated in an anechoic chamber to avoid the symbol scattering caused by the

multipath channel. Experiments with data modulation were conducted with a BTB connection to identify the noise level caused by the RF components and to add an equivalent noise to the simulation. Experiments were conducted with the antennas in a DCS to compare the antennas' performance through constellation diagrams, and EVMs were examined by their performance to compare with that from the simulation. Figure 4.15a and Figure 4.15b show the experimental setup, including the equipment used with the BTB connection and with two identical antennas, respectively. The equipment included a Tektronix AWG7122C arbitrary waveform generator, a Tektronix DPO72304DX oscilloscope, two RF amplifiers, and various attenuators with different values. Figure 4.16 shows the actual experimental setup with along with the Vivaldi antenna orientation in the anechoic chamber. Data-modulation (16-QAM OFDM) experiments were then conducted with and without antennas to compare the performance of the DCS through the constellation diagrams and EVM. The data were generated with a 76 MHz bandwidth through a MATLAB block and the block's demodulation steps after being received at the other end. The input data for the experiment were derived from a SIMULINK model that had an integer generator with 16-QAM OFDM modulation. The output data from the experiment required processing in the SIMULINK model, which was used to plot the constellation diagram of the received signal from the experiment and to calculate the EVM. The parameters used in the experiments are shown in Table 4.2.

For the BTB connection, attenuators were used between the Tx and Rx amplifiers with different values. These values were based on the path loss and the gain of each antenna, as shown in Table 4.3. The two cables' losses at 6-m lengths were also considered, such as 1.8 dB at 2 GHz. The Tektronix AWG7122C had an up-converter function for the generation of data-modulated RF signals up to 6 GHz. At the other end, the Tektronix DPO72304DX (which has a spectrum analyser function) down-converted the RF signal to an intermediate frequency (IF). The signal was then captured at the IF.

Experiments were then conducted with the Vivaldi and commercial antennas with a free-space channel in an anechoic chamber with a 0.7-m distance between the two identical antennas for each type. Estimated times and phase offsets in the receiver were then adjusted, and the received symbols were demodulated into integers.

Table 4.2: Experimental parameters.

Parameter	Value
Bandwidth	76 MHz
Modulation	16-QAM OFDM
IFFT	512
Number of Data Subcarriers	392
Number of Pilots	8
Bandwidth of each subcarrier	180 KHz
Gain for RF amplifier	17 dB and 19 dB
Attenuators	31 dB to 35 dB
Signal level at AWG	0.6 V peak to peak
Sampling rate at AWG	12 G samples/sec.
Sampling rate at oscilloscope	25 G samples/sec.

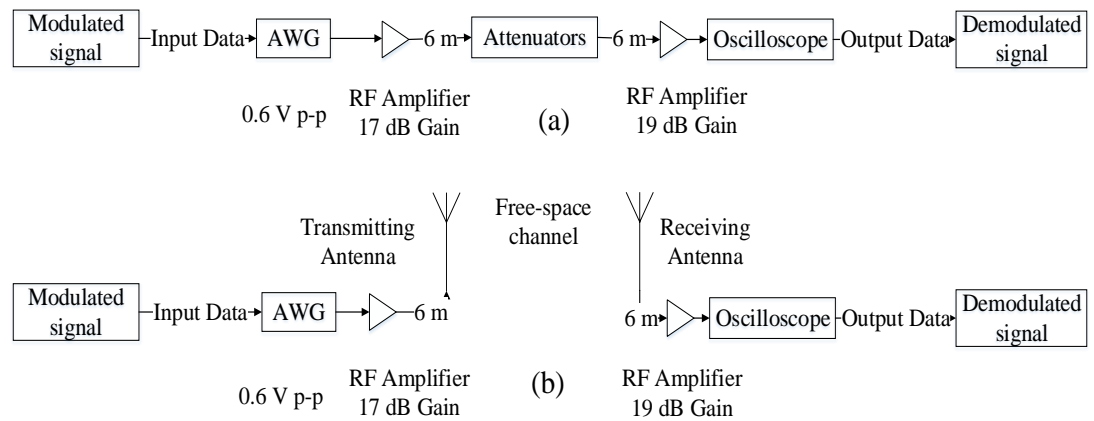


Figure 4.15. Experimental setup: (a) BTB connection and (b) antennas.



Figure 4.16. Photograph of the experiment setup.

Table 4.3: Values of the attenuators used in the experiments.

Antenna	RF (GHz)	Path loss (dB)	Gain (dB)	Attenuator (dB)
Commercial	2	35.36	0.6	33
Vivaldi	3.5	40.23	4.6	31

## 4.8 Experimental Verification of the Simulations

To compare the effects of the antennas from the simulation with the experiments, noise was added to the DCS simulation without the antennas to be equivalent to the symbol scattering obtained from the experimental BTB connection. The noise caused by the RF components was identified based on the EVM values from the performance of the DCS with a BTB connection. For instance, the constellation diagrams at a carrier frequency of 2 GHz from the simulation without an antenna and with noise added were quite similar to those obtained from the experiment, as shown in Figure 4.17a and Figure 4.17b (respectively), and the EVM values were the same, at 6.2%. The experiments were then conducted for the two antenna types using different carrier frequencies. The following sub-sections discuss and compare the output constellation diagrams and EVMs obtained from the experiments with the simulation using 16-QAM OFDM.

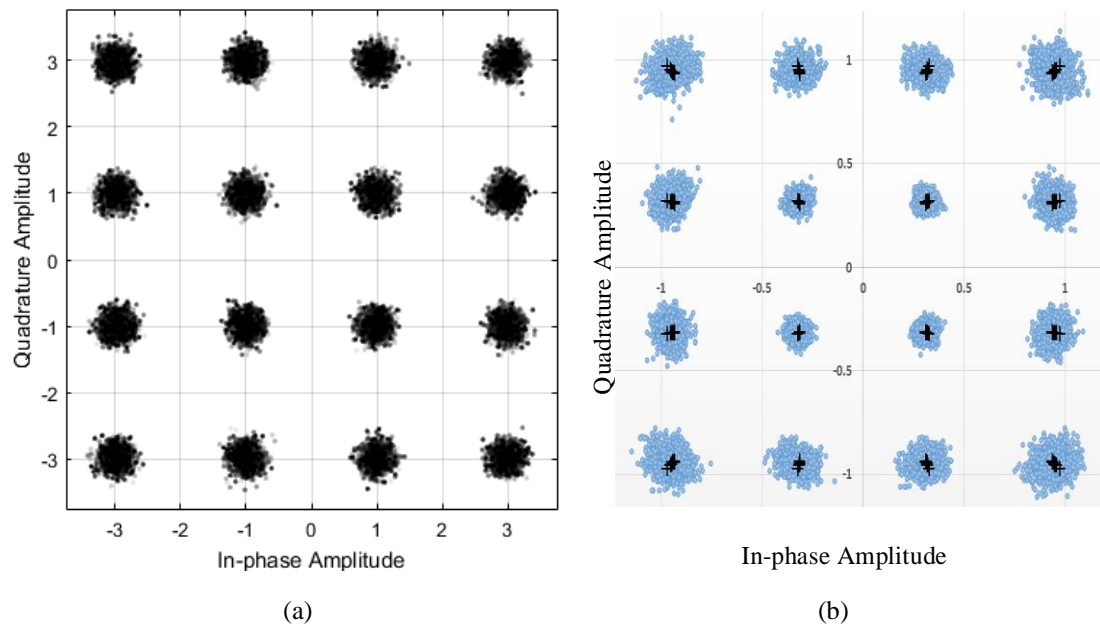


Figure 4.17. Output constellation at 2 GHz without antenna from (a) simulation and (b) experimentation.

### 4.8.1 Commercial Antenna

The effect of the commercial antenna in the DCS is shown in the constellation diagrams of Figure 4.18a and Figure 4.18b (respectively) from the simulation and the experiment. This antenna caused symbol scattering in the DCS. In general, a low signal-to-noise ratio (SNR) results in poorer performance. The signals captured in the oscilloscope from the experiments with the BTB connection and with a wireless channel showed the SNR, as illustrated in Figure 4.19a and Figure 4.19b, respectively. The SNR at the receiver with a wireless free-space channel is shown in Figure 4.19b, which indicates distortion in the transmitted signals. The corresponding distortion is notable in the constellation diagram shown in Figure 4.18b. A comparison between the simulation and experiment using the commercial antenna showed that the EVM had a near-agreement increase, as presented in Table 4.4.

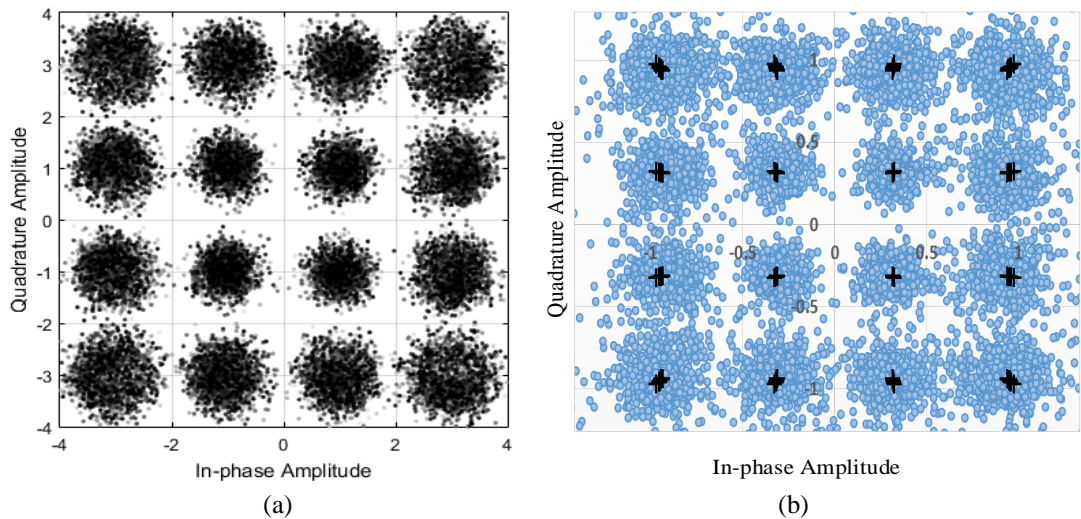


Figure 4.18. Output constellation at 2 GHz with the commercial antenna from (a) simulation and (b) experimentation.

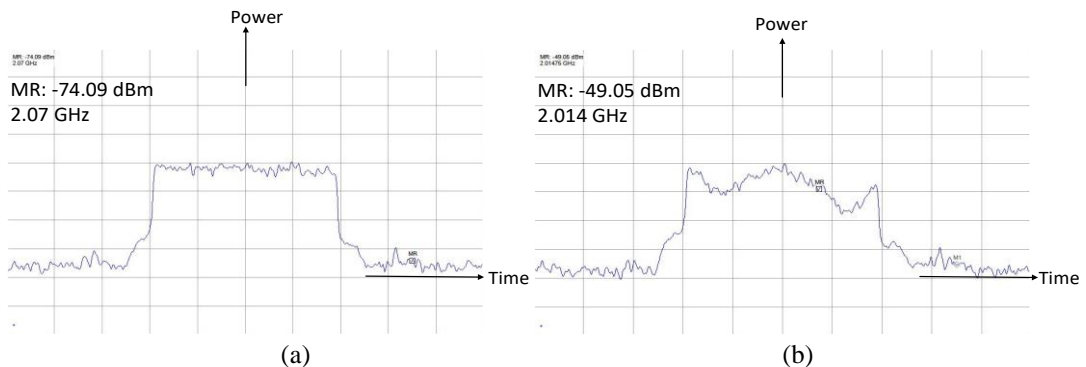


Figure 4.19. Signal captured in the oscilloscope at 2 GHz from (a) BTB connection and (b) wireless channel with commercial antenna.

#### 4.8.2 Vivaldi Antenna

Figure 4.20a and Figure 4.20b show constellation diagrams from the simulation and the experimentation, respectively. A comparison of the results from both the simulation and experimentation using the Vivaldi antenna showed an increase in the EVM that was similar in both the simulation and experimentation, as presented in Table 4.4. The simulation and experimentation results indicate that the Vivaldi antenna had few effects in the DCS. These minimal effects, which showed minimal symbol scattering, were observed when simulating without adding noise, as shown in Figure 4.14. The commercial antenna caused more symbol scattering in the transmitted signal and caused more distortion than the Vivaldi antenna.

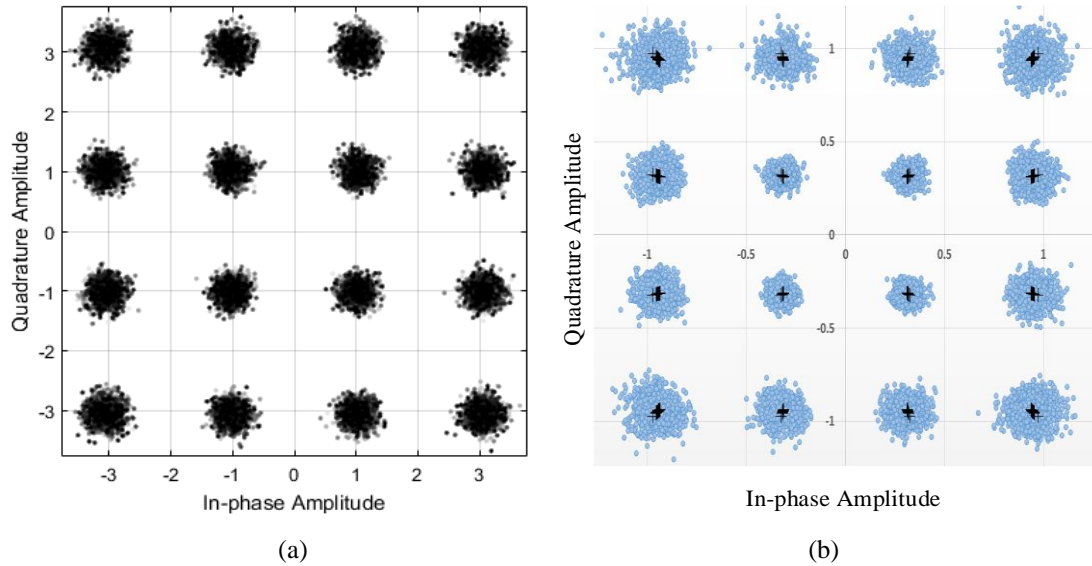


Figure 4.20. Output constellation at 3.5 GHz with the Vivaldi antenna from (a) simulation and (b) experimentation.

Table 4.4: Comparison of EVM (%) between simulation and measurement after adding noise.

Antenna	RF (GHz)	Simulation		Experiment	
		Without antenna	With antenna models	BTB	Wireless
Commercial	2	6.20	15.35	6.20	14.42
Vivaldi	3.5	5.43	7.40	5.43	7.65

The output constellation diagrams show that the two antennas caused different effects and that the EVM increased in both the simulations and the experiments. The increase

in EVM due to antenna type was found to have been similar between the simulations and experiments with and without antennas. The small changes in the constellation diagrams and the EVM between the simulations and experiments are attributable to the non-ideal measurement conditions caused by the non-linear amplifier used in the experiments.

In addition to the noise caused by the RF components, symbol scattering can also increase due to the antenna type that is employed. The impulse response of an antenna is an important consideration, especially if the antenna supports an additional component caused by multiple reflections in the antenna, which will influence the performance of the DCS. This technique enables designers to simulate an antenna in DCS simulation and to predict the closed effect of the antenna. The technique can also help designers to redesign antennas for optimal DCSs or to compare the effects of different wideband antennas in order to select the lowest effect in DCSs.

## 4.9 Summary

This chapter has described a technique to characterise and model an antenna to be included in DCS simulation. The chapter has also reported on the effect of the antenna on wireless links and DCSs. Different antennas were shown to have different effects in a DCS. The ECM for a commercial dual-band antenna was derived, and the  $S_{21}$  and  $S_{21}^a$  values were obtained in both amplitude and phase. The  $S_{21}^a$  provides the total radiated power, and the antenna behaviour was characterised from the transmission phase (the antenna  $S_{21}$  phase). FIR filter models were developed for all  $S$ -parameters for each type of antenna for inclusion in a DCS simulation. Different antennas showed varying impulse responses, and some antennas caused additional components due to multiple reflections in the antenna itself. These components were found to have introduced distortion and delay in the antenna impulse response.

The effects from each antenna type were first predicted in a DCS with 16-QAM OFDM, and the EVM and BER were calculated to characterise the symbol scattering. The results showed that the commercial antenna caused symbol scattering and that the EVM increased at the receiver for both bands at the two carrier frequencies. The commercial antenna's effects at 6 GHz were shown to have less of an effect compared

to the effects at 2 GHz, whereas the Vivaldi antenna showed minimal symbol scattering at the two different carrier frequencies over the operating frequency band. The resulting EVM was also different at the two carrier frequencies for the commercial and Vivaldi antennas, thus confirming that the EVM and BER are a function of frequency.

The experiments were then verified via simulation, which confirmed the effects from each antenna type in the DCS. The noise from the RF components was also considered in the simulation, based on the EVM values in the BTB connection in the experiments, whereas the noise from the multipath channel was eliminated by taking measurements in an anechoic chamber for both simulation and experimentation. The results from the comparison between the simulations and experiments showed increased symbol scattering in output constellation diagrams, and the increase in EVM was found to have been similar for each antenna type. This scattering, and the change in EVM, were both due to the antenna type that was employed. These effects reduced the order of the modulation scheme and the data-transmission rates.

This technique will enable designers to predict the performance of a multiband system in each band and will allow them to integrate antennas with multipath channels in DCS simulations for different applications. The commercial and Vivaldi antennas that were characterised in the current work had minimum transmission phases of  $S_{21}$ , which indicates that both antennas had frequency-invariant radiation patterns and could be used as directive antennas. A detailed analysis of the antenna-transmission phase for non-minimum-phase antennas will be addressed in the next chapter.

# CHAPTER 5: CHARACTERISATION OF NON-MINIMUM-PHASE WIDEBAND ANTENNAS FOR POINT-TO-POINT COMMUNICATIONS

## 5.1 Introduction

The frequency-dependent characteristics of a wideband antenna, such as its physical orientation and beam direction, are difficult to obtain using conventional design procedures. Knowing the  $S_{11}$  value alone allows the total radiated power to be determined but provides no insight into the beam direction or its frequency dependence. It is important to distinguish between the total radiated power and the radiated power in the direction of interest. Conventional procedures cannot provide information about the transmission-phase response, which is important for evaluating antenna behaviour as a resonant structure and the structure's frequency-variant radiation pattern. This step can be performed either from the antenna ECM or from measurements in an anechoic chamber in the antenna's principal axis direction.

UWB antennas have an operating bandwidth from 3.1 to 10.6 GHz [1]. They offer larger bandwidth compared to narrowband antennas, and can accommodate multiple RF Chains operating at different frequencies simultaneously. They are designed to achieve high data rates without errors. State-of-the-art UWB antennas have been characterised in [37]-[40]. For most UWB antennas in P2P communications, the frequency response of the physical channel between the Tx and Rx antennas depends on the orientation of the antennas [1]. The physical channel is usually selected based on the direction of the main beam of the fundamental radiation pattern (i.e. the principal axis). Knowing further parameters such as the frequency-variant radiation pattern and current distribution is also necessary for designing UWB antennas [37]-[40]. Although various techniques have been proposed by modifying the geometry of the UWB antenna in order to have a frequency-invariant radiation pattern [37]-[40], the radiation patterns are only represented at certain discrete frequencies, which does not allow for predicting the performance or the behaviour of the antenna over the entire operating bandwidth.

The antenna ECM can be derived from the amplitude and phase of  $S_{11}$ . Researchers have expressed interest in the development of an accurate circuit for UWB antennas. Researchers to date have primarily considered the amplitude response of  $S_{11}$  and have ignored the phase [7], [11], [54], which does not provide an accurate complex  $S_{21}$  of the antenna.

In a wideband communication system, the variation of group delay is critical, in that a large variation can distort the signal, and the group delay depends on the phase of  $S_{21}$  [36]. The modulated symbols emitted from a non-minimum-phase antenna on its principal axis can be distorted because different frequencies manifest different delays through the system. This distortion further increases the symbol scattering and leads to performance degradation. To avoid signal distortion, the group delay over the frequency range should be constant. Designing an antenna to be minimum phase can mitigate the symbol scattering as well as minimising the EVM and BER.

In Section 5.2 of this thesis, the Friis equation is modified in terms of total radiated power and radiated power in a certain direction. The effective aperture and gain are then derived for identical antennas with respect to the frequency axis. Section 5.3 then presents the design and EM simulation of a non-minimum-phase monopole UWB antenna. In Section 5.4, an ECM is derived to obtain the  $S_{21}^a$  from the radiation resistance and to study the antenna's behaviour. Section 5.5 presents an analysis of the amplitude and phase of the  $S_{21}$  obtained from the port-to-port transmission using CST, the ECM, and the measurements at two specific orientations in order to select the best antenna orientation. The variation of group delay for each orientation is then calculated and compared. Finally, two identical antennas with a free-space channel are modelled and simulated in a DCS to investigate the effect of the antenna in the two orientations.

## 5.2 Mathematical Formulation

The performance of the antenna in the free-space far-field region can be described by the Friis equation in terms of effective aperture [55]:

$$P_r = P_t A_t A_r \frac{1}{\lambda^2 d^2} \quad (5.1)$$

where  $P_t$  and  $P_r$  are the total transmitted and received power (respectively),  $A_t$  and  $A_r$  are the effective apertures in the direction of the link for the Tx and Rx antennas (respectively),  $\lambda$  is wavelength, and  $d$  is the distance of the physical channel. The effective aperture is given by [55]:

$$A_e = \frac{\lambda^2}{4\pi} G \quad (5.2)$$

where  $G$  is the gain of the antenna.

Section 3.2 considered two different transfer-scattering parameters,  $S_{21}^a$  and  $S_{21}^b$ , that act as a power ratio. These parameters yield the total radiated power and the measurement between the Tx-Rx antennas over distance  $d$ , respectively.  $|S_{21}^a|^2$  and  $|S_{21}^b|^2$  can then be represented mathematically as:

$$|S_{21}^a|^2 = \frac{P_t}{P_{av}} \quad (5.3)$$

$$|S_{21}^b|^2 = \frac{P_r}{P_{av}} \quad (5.4)$$

where  $P_{av}$  is the power available from the source.

From (5.3) and (5.4), (5.1) can be written in terms of  $S_{21}^a$  and  $S_{21}^b$ :

$$|S_{21}^b|^2 = |S_{21}^a|^2 A_t A_r \frac{1}{\lambda^2 d^2} \quad (5.5)$$

Note that the received power in the direction of the physical channel is a function of frequency, distance, and the effective apertures of the Tx and Rx antennas. (5.5) can then be applied for non-identical antennas. For identical antennas, the effective aperture and gain can be calculated respectively as:

$$A_e = \lambda d \frac{|S_{21}^b|}{|S_{21}^a|} \quad (5.6)$$

$$G = \frac{4\pi d}{\lambda} \frac{|S_{21}^b|}{|S_{21}^a|} \quad (5.7)$$

For a lossless network, the amplitude of the  $S_{21}^a$  can be calculated from the amplitude of  $S_{11}$  using (3.1).

As shown in Figure 5.1, the phase of  $S_{21}$  of each antenna can be separated into

three components: the minimum, linear, and all-pass phases. The linear-phase component represents a constant time delay due to the effective length to the phase centre [34], whereas the minimum-phase component represents the amplitude response of the antenna  $S_{21}$ . An all-pass component is an additional phase at certain frequencies in the band. This component arises due to the resonant structure, which affects the frequency-invariant radiation pattern. The all-pass component does not exist in the principal axes of minimum-phase antennas such as horn and Vivaldi antennas, or in the commercial antenna discussed in Chapter 4.

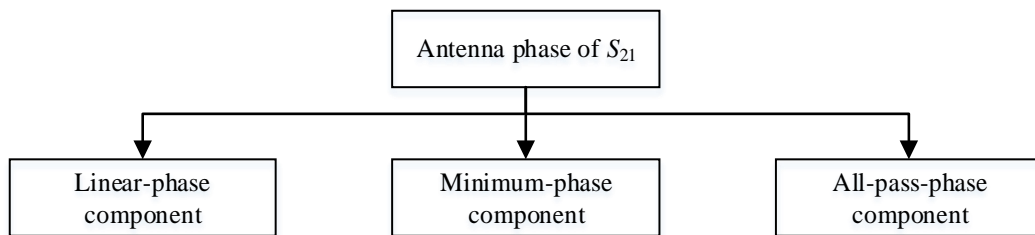


Figure 5.1. Phase components of  $S_{21}$ .

The Hilbert transform extracts a minimum-phase component without any associated linear or all-pass components and can be used to derive the minimum-phase component of the antenna  $S_{21}$  values obtained from the  $S_{21}^b$  measurements at different orientations.

### 5.3 Monopole UWB Antenna Design

A monopole UWB antenna with a coplanar waveguide (CPW) feed [56] was designed and simulated using CST Microwave Studio Suite®. Figure 5.2 shows the structure of the antenna, which was etched on a Rogers RT5880 dielectric substrate with a thickness of 1.575 mm and a dielectric constant  $\epsilon_r$  of 2.2. The  $S_{11}$  value was obtained from the simulator and compared with measurements obtained from a network analyser, as shown in Figure 5.2.

Figure 5.3a and Figure 5.3b present the simulated radiation pattern at 4 GHz and 7 GHz, respectively. The direction of the main beam of the radiation pattern at 4 GHz is broadside (principal axis), whereas at 7 GHz the direction of the main beam shifts to azimuth and elevation angles of  $90^\circ$  and  $45^\circ$ , respectively. Note that the

broadside gain is very low at 7 GHz, whereas the main beam gain at 7 GHz is slightly higher than at 4 GHz. The current distributions of the antenna were studied at 4 GHz and 7 GHz, as shown in Figure 5.4a and Figure 5.4b, respectively. As the figures show, the current intensity increases at the sharp edges of the structure, which causes delay paths in the antenna. It is also clear that the current at 7 GHz is predominantly on the ground plane, which indicates a narrowband resonant structure at this frequency.

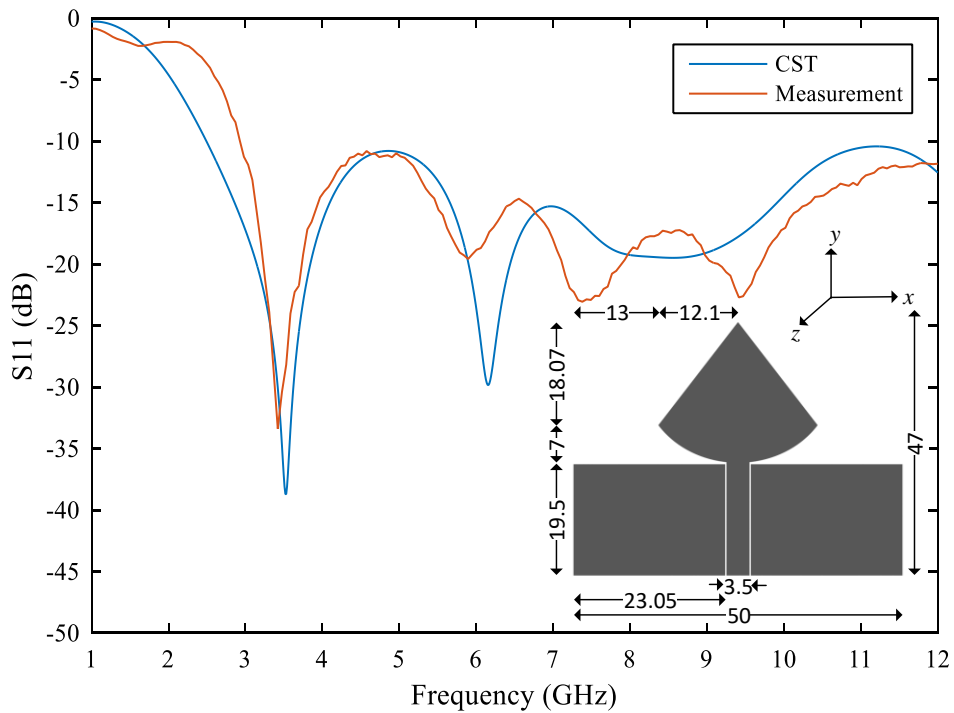


Figure 5.2.  $S_{11}$  from simulation and measurement, and inset antenna structure (all dimensions in mm).

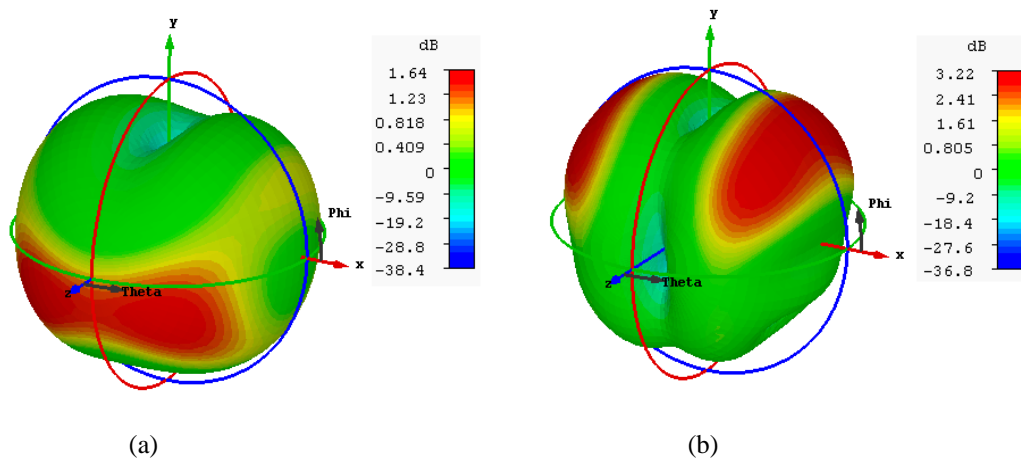


Figure 5.3. Radiation pattern gain at (a) 4 GHz and (b) 7 GHz.

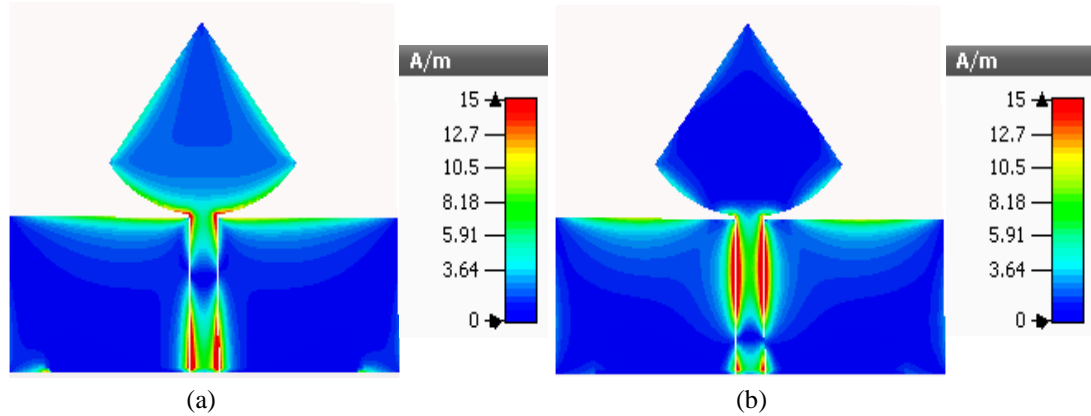


Figure 5.4. Current distribution at (a) 4 GHz and (b) 7 GHz.

The power simulated in CST was 0.5 W, and the accepted power was obtained from the antenna layout simulation to obtain  $|S_{21}^a|^2$ , which provides the total radiated power, assuming a lossless antenna. The  $S_{21}^b$  antenna-to-antenna transmission was also simulated in CST using open boundaries with a 0.5-m distance between two identical antennas in the broadside direction. The  $S_{21}^b$  simulation was then compared with the results from the ECM and from the anechoic chamber measurements, as will discuss in Section 5.5.

## 5.4 ECM for a Monopole UWB Antenna

In an antenna two-port ECM, the second port's impedance represents the radiation resistance. The ECM for the UWB antenna shown in Figure 5.5 was developed based on the flowchart illustrated in Figure 3.1 which shows the steps for identifying the topology and calculating the element values by applying an iterative optimisation process to match the  $S_{11}$  measurement. ADS software was used for the simulation and optimisation of the ECM. Transmission lines were included in the ECM to represent the distributed elements of the antenna.

As Figure 5.6 indicates, the amplitude and phase of  $S_{11}$  from the measurement and the ECM are in agreement. The radiation resistance of the UWB antenna was calculated at approximately  $90 \Omega$ . The voltage-transfer function was then computed from the simulator as the ratio of the voltage across the radiation resistance and the source voltage shown in Figure 5.5 in order to obtain  $S_{21}^a$ , which provides the total radiated power.

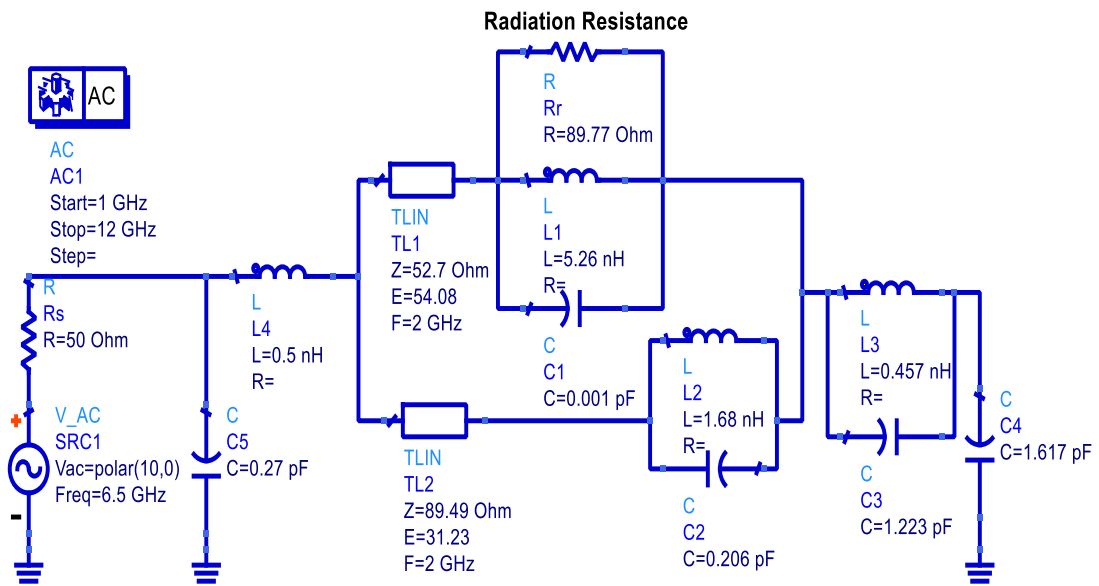


Figure 5.5. ECM for the monopole UWB antenna.

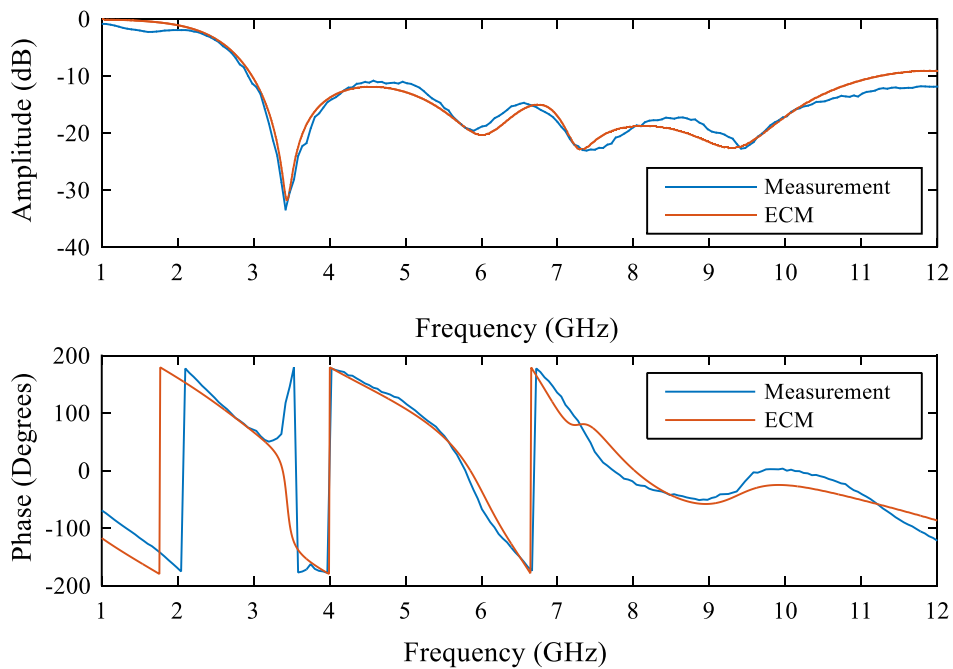


Figure 5.6.  $S_{11}$  of the UWB antenna from measurement and ECM.

## 5.5 Results and Discussion

Measurements of  $S_{21}^b$  were conducted in an anechoic chamber between two identical UWB antennas with the free-space channel 0.5 m apart, using a network analyser. The reference plane was defined at the end of each cable using the TOSM calibration

technique. As shown in Figure 5.7, this method was used to measure  $S_{21}^b$  at two orientations – the broadside and a second orientation – where the azimuth and elevation angles were  $90^\circ$  and  $45^\circ$ , respectively. Electrical length offset was adjusted to compensate for the connector and the feeding transmission line for each antenna.

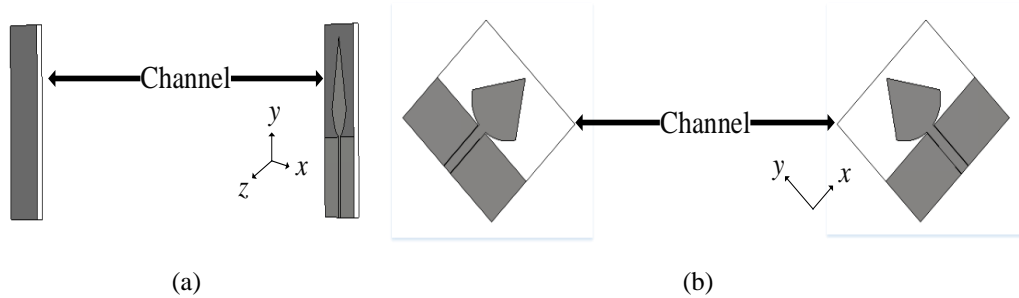


Figure 5.7. Antennas at (a) broadside and (b) second orientation (aligning the main beam at 7 GHz).

The measured  $S_{21}^b$  in the broadside orientation represents the frequency response of the two identical antennas with the free-space channel. The  $S_{21}^b$  measurement was compared to that obtained from the simulation in CST, as shown in Figure 5.8. A similar trend is visible in the  $S_{21}^b$  between simulation and measurement. The difference between the plots is the result of inaccurate meshing. Due to the electrically large simulation, domain-adaptive mesh refinement is not practical, and hence the discretisation of the antennas may not be sufficiently accurate to simulate full-wave antenna-to-antenna transmission.

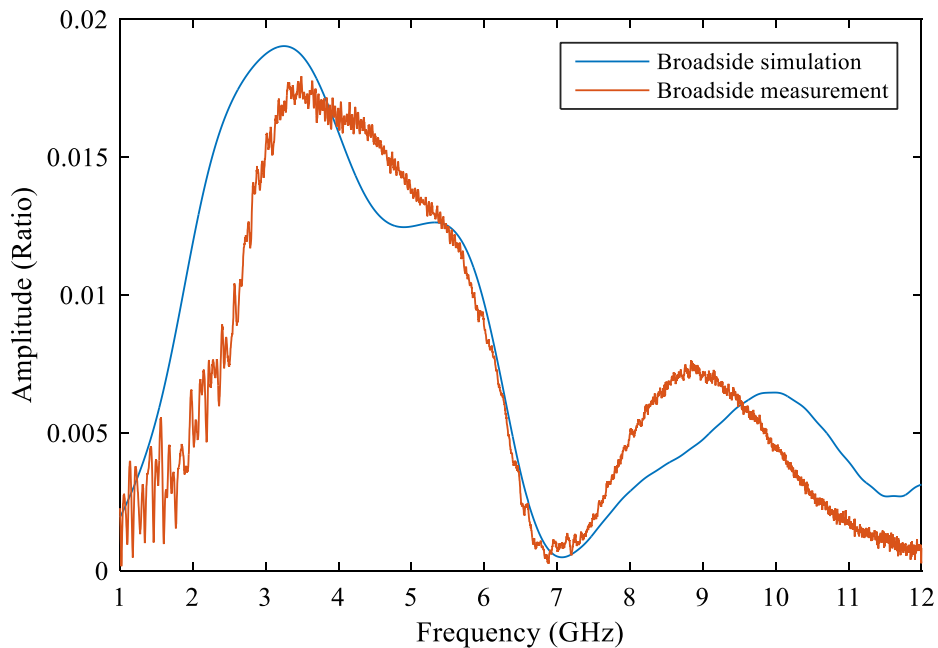


Figure 5.8. Comparison of  $S_{21}^b$  between simulation and measurement in the broadside direction.

The free-space channel was then de-embedded from the measured and simulated  $S_{21}^b$  based on the 0.5-m distance. The amplitude response was obtained based on the Friis transmission equation, and the delay was de-embedded from the phase. This step was taken to obtain the amplitude and phase of  $S_{21}$  for each antenna at the two orientations. The  $S_{21}$  of each antenna represents the directional dependency of  $S_{21}^a$ . The measurements were made within a frequency range of 1 GHz to 12 GHz. The data were then analysed and presented in a range from 2 GHz to 11 GHz to avoid band-edge effects.

The amplitude and phase of  $S_{21}^a$  were also obtained from the ECM. The antenna  $S_{21}^a$  and  $S_{21}$  values were then compared and analysed. The variation of group delay was obtained for the  $S_{21}$  of the antenna at the two orientations to identify the best orientation for the UWB antenna in P2P communications. Finally, the  $S_{21}^b$  measurement (from two identical antennas with a free-space channel) for the two orientations was modelled and simulated in a DCS to observe the antenna effects at the two orientations in the DCS, as discussed in the following sub-sections.

### 5.5.1 $S_{21}$ Amplitude Response

Figure 5.9 shows agreement between  $S_{21}^a$  (which provides the total radiated power) obtained from the antenna simulation, the ECM, and the calculation from the  $S_{11}$  measurement using (3.1). This agreement confirms the validity of the proposed method in obtaining the total radiated power from the antenna ECM shown in Figure 3.1. The agreement also confirms that the antenna is effectively lossless.

Figure 5.9 also shows agreement in the  $S_{21}$  of the antenna obtained from the  $S_{21}^b$  between the anechoic chamber measurement and simulation in CST in the broadside direction. Figure 5.9 also illustrates the  $S_{21}$  of the antenna obtained from the  $S_{21}^b$  measurement in the two orientations: broadside and the 7-GHz beam orientation (the second orientation). These values show the radiated power from the Tx antenna in both directions at the same time versus the frequency. The remaining power is radiated in other directions and is eventually dissipated in the sidelobes of the radiation pattern. As expected at 7 GHz, the transmitted power did not steadily radiate in the broadside direction (the principal axis). The variation between the  $S_{21}^a$  and  $S_{21}$  values

of the antenna was due to the angular direction of the radiation patterns at each frequency.

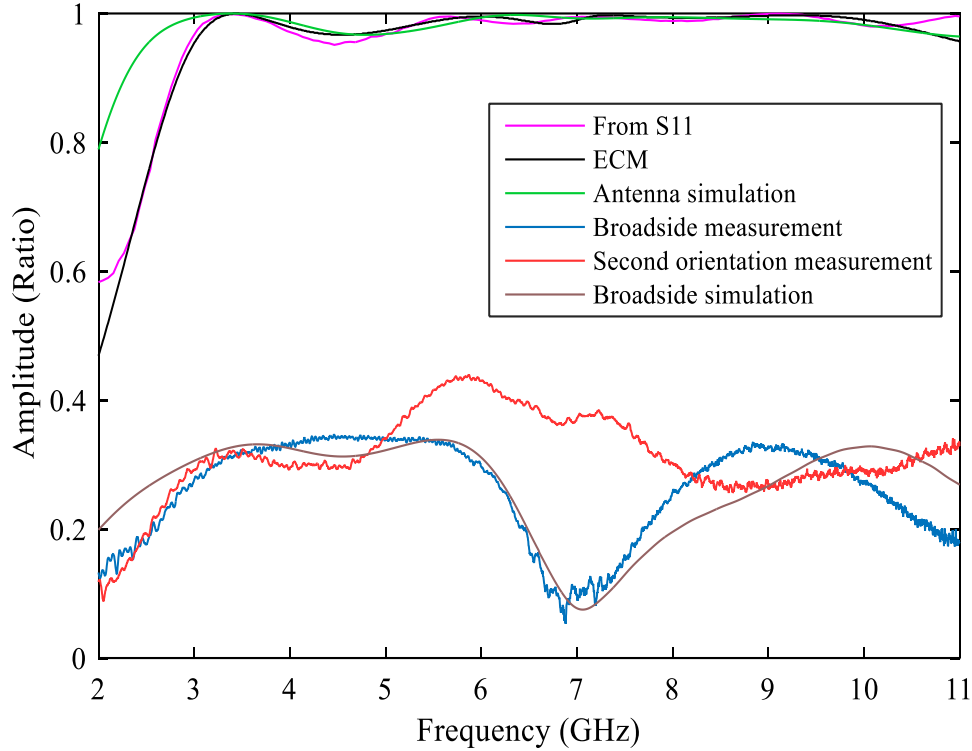


Figure 5.9. Comparison of  $S_{21}^a$  and  $S_{21}$  at two orientations.

Next, (5.6) and (5.7) were applied to calculate the effective aperture and gain values, which were then compared with the results from the radiation pattern gain simulation and gain measurements. Figure 5.10 illustrates the variation of the effective aperture for the broadside and the second orientation. Figure 5.11 depicts the difference in the gain of the antenna at the two orientations. The effective aperture at 7 GHz at the broadside was very low, and the gain was around  $-10$  dB, whereas the gain in the second orientation generally was more acceptable over the whole frequency band. This scenario indicates that the antenna performance was acceptable for P2P communications when both antennas were positioned in the second orientation.

The gain was also measured in the broadside orientation using a calibrated reference antenna in an anechoic chamber from 4 GHz to 7 GHz. The gain was then compared with that obtained from the proposed process and EM simulation. The measured gain values at discrete frequencies were approximately the same as those obtained from the proposed process and the EM simulator, as shown in Table 5.1.

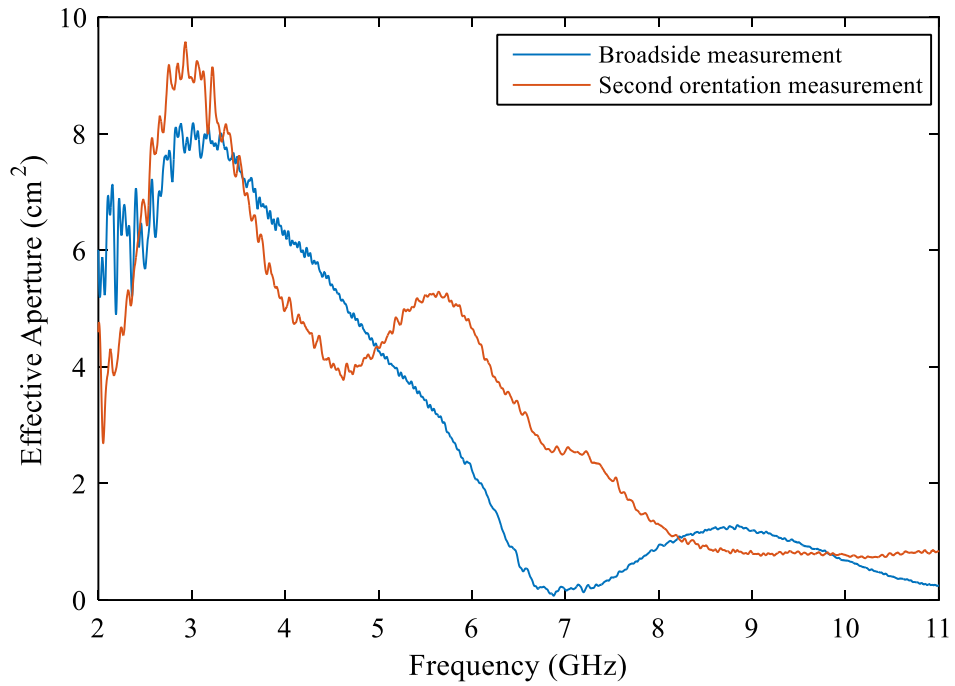


Figure 5.10. Effective aperture of the UWB antenna at two orientations.

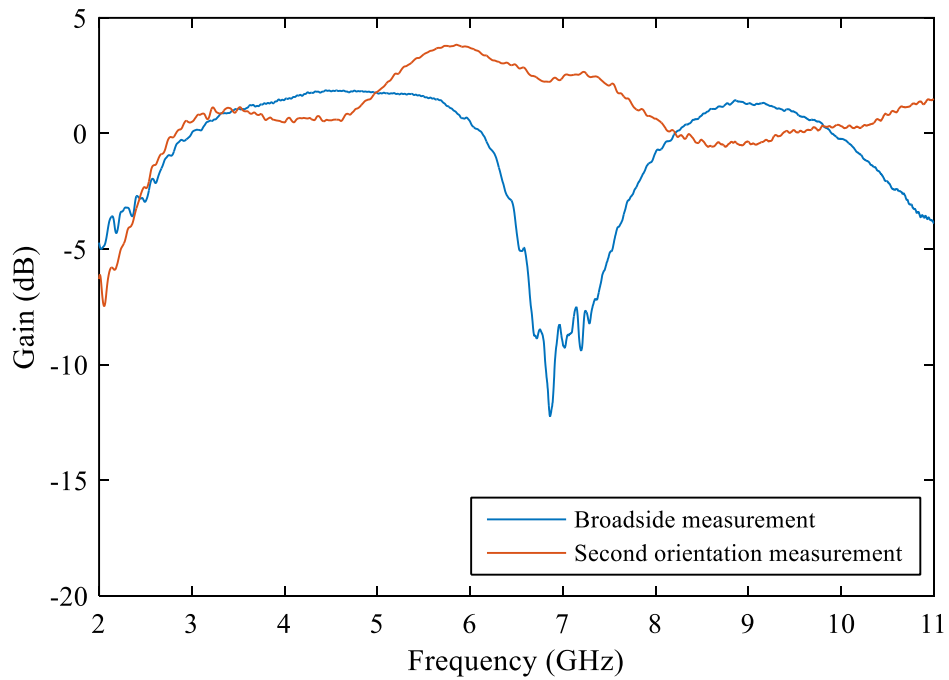


Figure 5.11. Gain of the antenna at two orientations from the proposed process.

Table 5.1: Gain in dB (broadside orientation).

Frequency	4 GHz	5 GHz	6 GHz	7 GHz
EM simulation	0.96	0.5	-0.16	-13.9
Gain measurement	0.92	1.63	0.51	-10.1
Proposed process	1.5	1.75	0.5	-9.5

It should also be noted that the current distributions on the antenna were mostly concentrated around the edges, as shown in Figure 5.4a and Figure 5.4b. This distribution caused a delay in the antenna phase response, represented by a pair of transmission lines, as shown in the antenna ECM (Figure 5.5). The two different paths in the ECM indicate that the antenna is non-minimum phase in at least some rotations.

### 5.5.2 $S_{21}$ Phase Components

Figure 5.12 illustrates the  $S_{21}$  phase of each antenna in the two orientations and the phase of  $S_{21}^a$  obtained from the antenna ECM. The phase obtained from the ECM matches the phase of the broadside  $S_{21}$ , because the broadside measurement was taken in the principal-axis direction. As a result, the radiation pattern of the antenna is variant with respect to the frequency due to the non-linearity in the phase of the broadside  $S_{21}$  [1], whereas the  $S_{21}$  phase in the second orientation is similar to a linear phase.

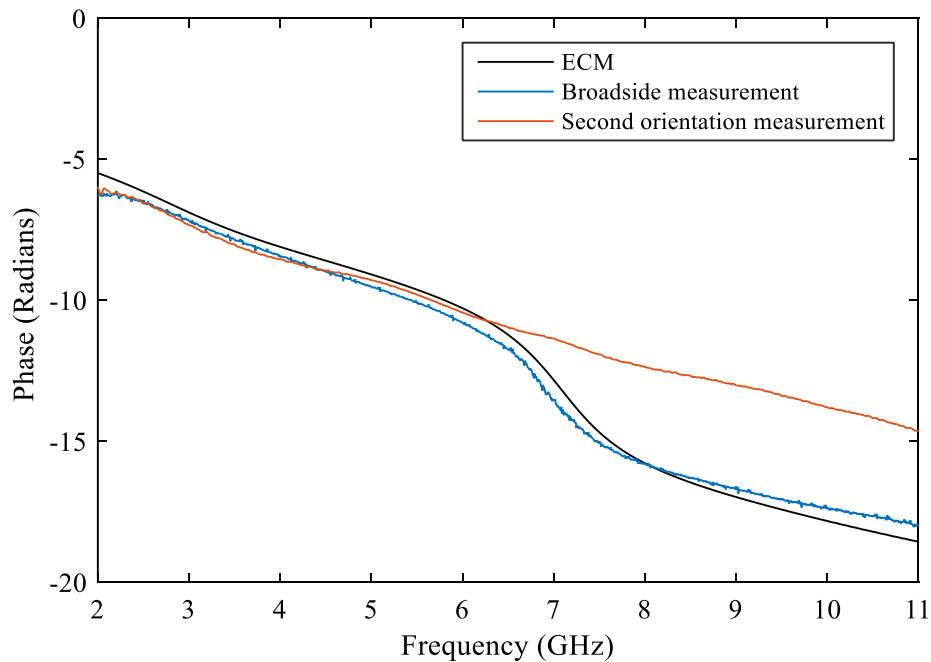


Figure 5.12. Phase of  $S_{21}$  from ECM and measurements with two orientations.

The second orientation's phase indicated that no additional phase component in  $S_{21}$  existed over the frequency band. The  $S_{21}$  phase was almost linear, because the minimum-phase component was insignificant compared to the linear-phase component. Recalling that the antenna  $S_{21}$  phase consists of three components – minimum, linear, and all-pass phases [19] – the phase of  $S_{21}$  with the two orientations was then analysed from the frequency response to study the antenna's behaviour.

The minimum-phase component was computed by applying the Hilbert transform method to the  $S_{21}$  amplitude, whereas the linear-phase component was calculated with respect to the antenna's phase centre [34]. By identifying the phase centre for each orientation, the linear-phase component could then be isolated. The all-pass-phase component was obtained after removing the linear-phase and minimum-phase components from the total  $S_{21}$  phase obtained from the  $S_{21}^b$  measurement. The phase components were then characterised for the two orientations as follows.

- 1) *Broadside*  $S_{21}$ . Figure 5.13 shows a comparison between the measured phase after removing the linear- and minimum-phase components. Note the differences in phase because of the existing all-pass component within the frequency range of 6 GHz to 8 GHz. The large variation of the antenna gain in this direction, as shown in Figure 5.11, can only be attributed to the all-pass component of  $S_{21}$ , and not to the minimum- or linear-phase components. This variation is also clear from the antenna ECM because of the existence of more than one path across the ECM for the energy transferred through the circuit, which again confirms that the antenna is non-minimum phase on the principal axis due to the resonant structure at certain frequencies.

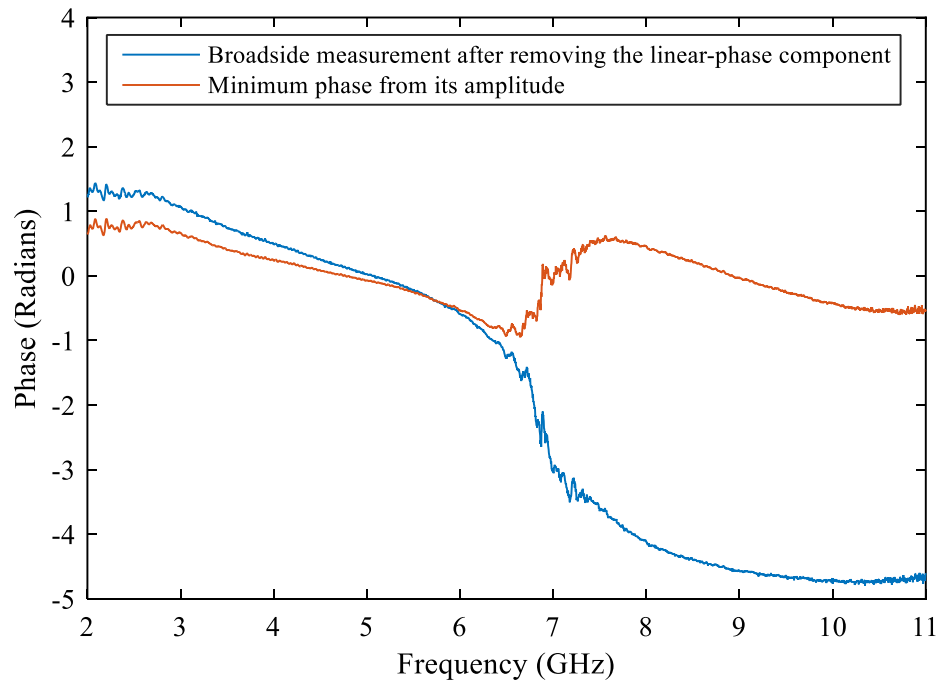


Figure 5.13. Minimum-phase component and antenna  $S_{21}$  phase after removing the linear component in the broadside orientation.

2) *Second Orientation  $S_{21}$* . Figure 5.14 illustrates a comparable trend between the phases of  $S_{21}$  with the linear-phase component removed as well as  $S_{21}$ 's minimum phase. The antenna is nearly minimum phase in this orientation, because the deviation of the calculated gain versus frequency was minor, as illustrated in Figure 5.11, meaning that the radiated power in this direction continued to radiate over the entire band, with little variation.

This scenario confirms that the antenna is non-minimum phase in the principal axis because of the existing all-pass component. But because there is no all-pass component in the  $S_{21}$  phase in the second orientation, the antenna is minimum-phase in this particular angular direction (the second orientation) when the antenna continues to radiate the power over the entire band with little variation, thus indicating that the radiation patterns can provide acceptable gain in this direction over the frequency band.

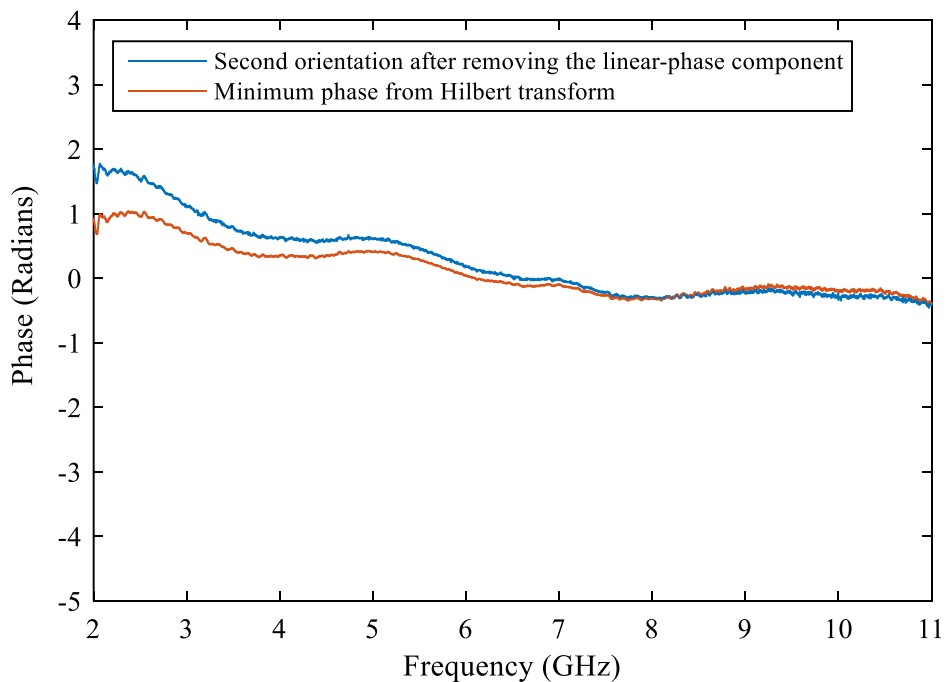


Figure 5.14. Minimum-phase component and antenna  $S_{21}$  phase after removing the linear component in the second orientation.

### 5.5.3 Group Delay

The group delay was obtained for the UWB antenna from the  $S_{21}$  as a function of frequency with the two orientations. Figure 5.15 shows the group delays from  $S_{21}$  in

the broadside and second orientation. The positive large peak within the frequency range 6 GHz to 8 GHz of the group delay was obtained from the broadside measurement, which then had a negative impact on symbol scattering and the resulting BER at the receiver. This setup also means that the attenuation at the broadside direction was extremely high and that the gain dropped sharply in this range, as shown in Figure 5.11. In contrast, the group delay obtained from the second orientation  $S_{21}$  showed little variation over the UWB frequency band, which introduced a low level of symbol scattering and BER. The second orientation is thus the best choice for P2P communications for this antenna.

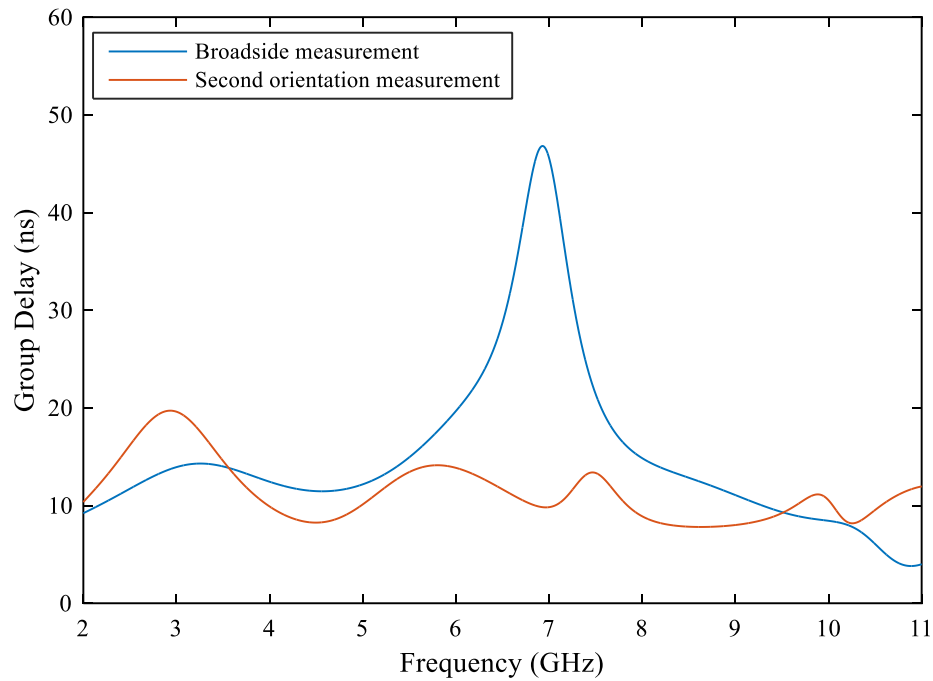


Figure 5.15. Group delay of antenna  $S_{21}$  from broadside and second orientation measurements.

#### 5.5.4 DCS Simulation with Two Orientations

FIR filter models were then derived for all  $S$ -parameters obtained from the measurements for each orientation, the  $S_{21}^b$  having been measured in the anechoic chamber between two identical UWB antennas with a distance of 0.5 m. The antenna  $S$ -parameter measurements were modelled as a system model, as discussed in Section 4.5 (Figure 4.8), so that each orientation would be compatible with a DCS. The impulse responses of the monopole UWB antenna's  $S_{21}^b$  FIR model at the broadside and the second orientation are shown in Figure 5.16a and Figure 5.16b, respectively.

Note that the impulse responses of the antenna vary at the different directions in P2P communications.

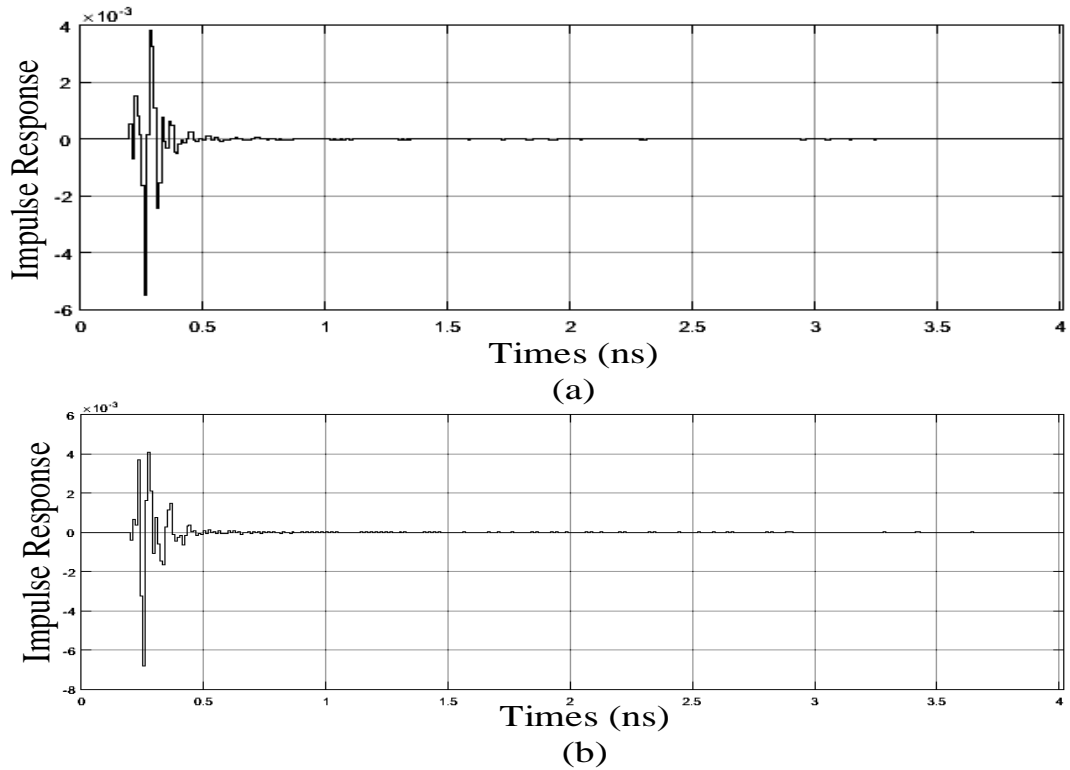


Figure 5.16. Impulse responses of the  $S_{21}^b$  FIR model for monopole at (a) broadside and (b) second orientation.

The frequency response of the time-domain system model for the broadside  $S_{21}^b$  measurement is illustrated in Figure 5.17a. This response is similar to the antenna  $S_{21}^b$  measurement shown in Figure 5.17b, which shows the frequency response of the two identical antennas at the broadside direction, with the free-space channel 0.5 m apart. Figure 5.18a and Figure 5.18b also show the results for the second orientation from the system model and the  $S_{21}^b$  measurement, respectively.

The complete system models from the measurements at the two orientations were included in a DCS, as shown in Figure 5.19. This step was done to predict the effect of the antenna on the DCS and to calculate the EVM and the BER in order to characterise the symbol scattering caused by the antenna. The effects of the antenna on the 64-QAM-modulated signal for the two orientations were then studied for the two carrier frequencies of 3.5 GHz and 6 GHz.

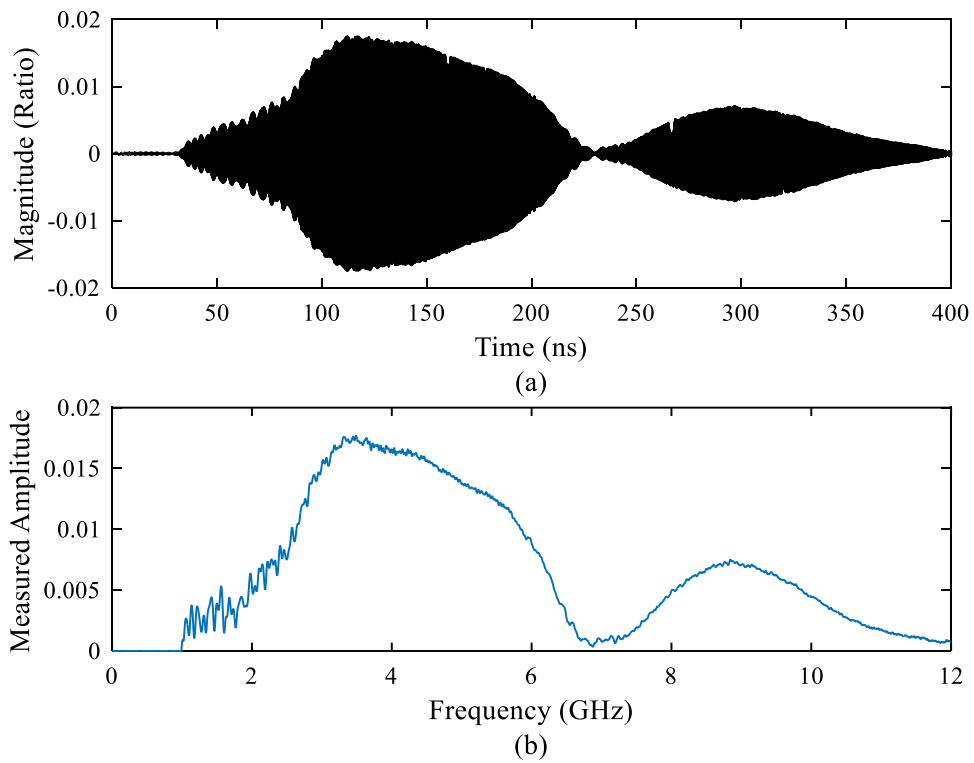


Figure 5.17. Frequency response in broadside: (a) antenna system and (b)  $S_{21}^b$  measurement.

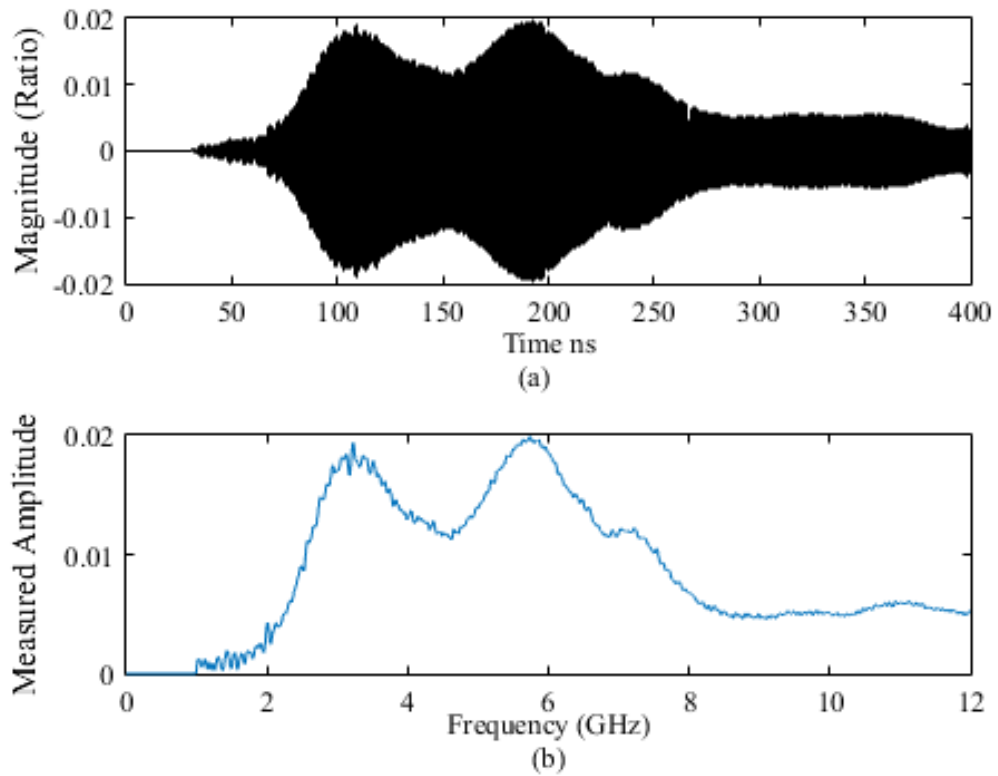


Figure 5.18. Frequency response in second orientation: (a) antenna system and (b)  $S_{21}^b$  measurement.

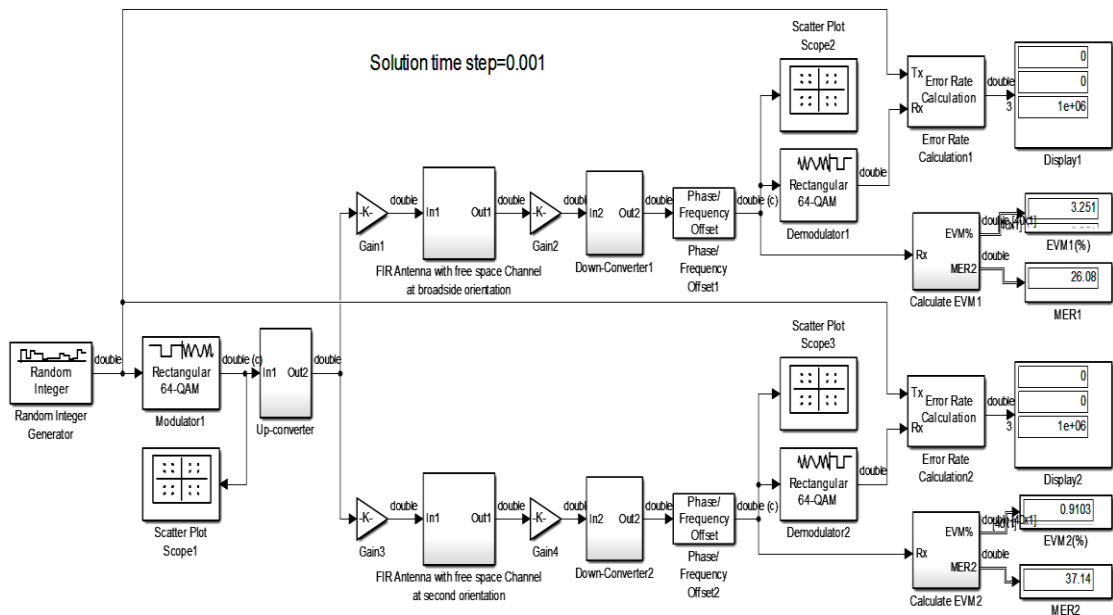


Figure 5.19. DCS with antennas at two orientations.

The simulation was done in SIMULINK for  $10^6$  symbols, with the complete DCS having a 64-QAM modulation when a carrier frequency was selected at 3.5 GHz and 6 GHz, respectively. The antenna effects on the 64-QAM-modulated signal for the two orientations were examined for each carrier frequency. Figure 5.20a and Figure 5.20b show constellation diagrams for the broadside and second orientation, respectively, at the receiver with a carrier frequency of 3.5 GHz. The constellation diagrams at 6 GHz are shown in Figure 5.21a and Figure 5.21b for the same orientations.

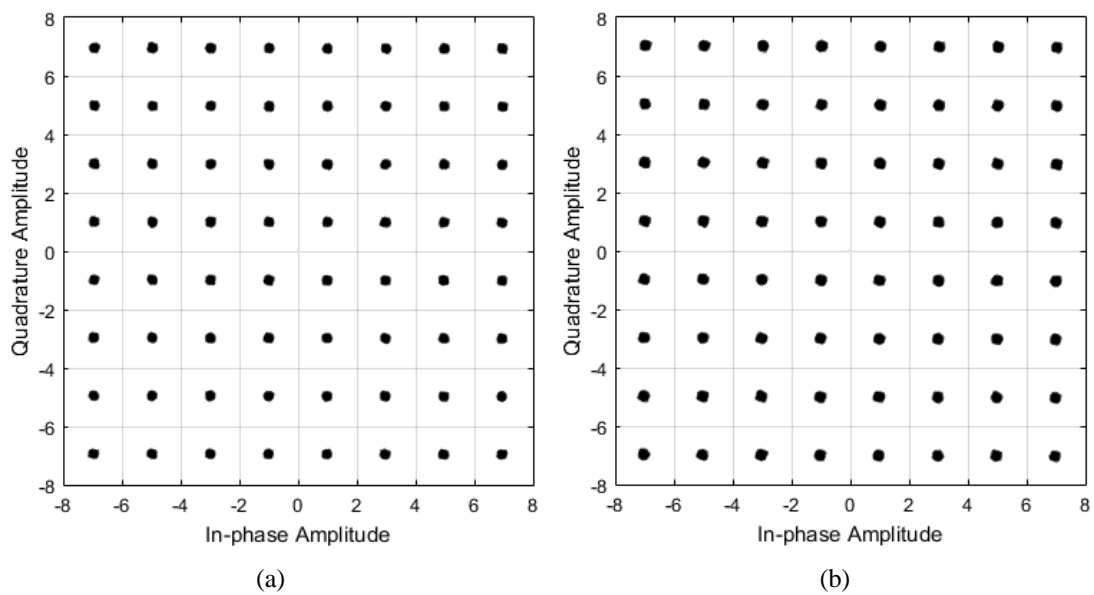


Figure 5.20. Constellation diagram at 3.5 GHz for (a) broadside and (b) second orientation.

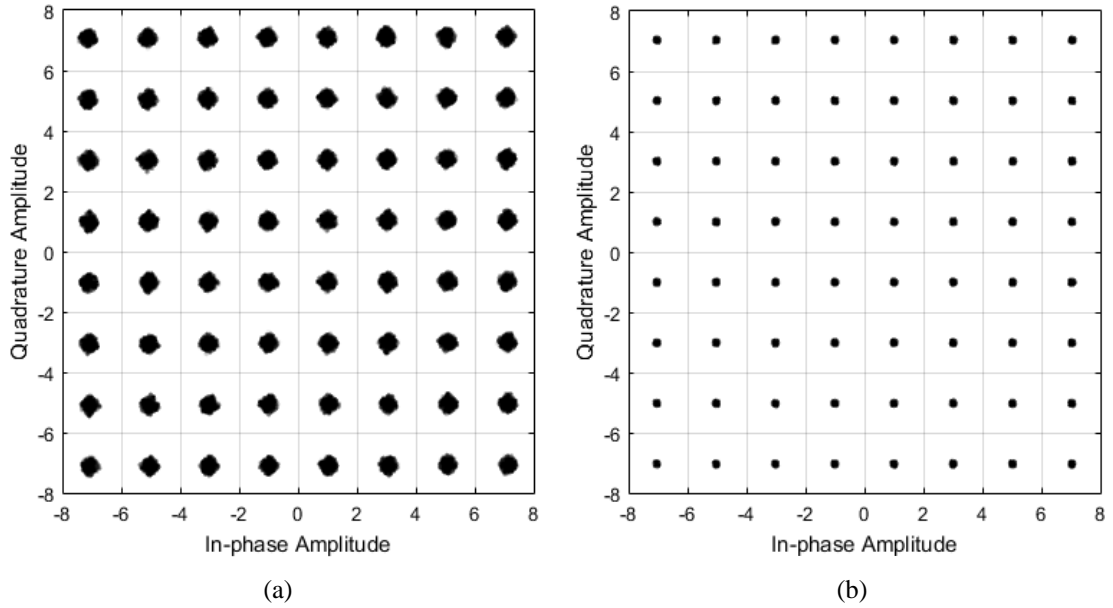


Figure 5.21. Constellation diagram at 6 GHz for (a) broadside and (b) second orientation.

The communication properties as well as the EVM and BER results for the two carrier frequencies at the two orientations are summarised in Table 5.2. The EVM values for the DCS at 6 GHz were found to be 3.25% and 0.91% for the broadside and second orientation, respectively. The receiver was able to recover the symbols for both carrier frequencies at the two orientations, and the BER was found to be zero. The reason for the symbol scattering in the broadside was the poor transmission at 6 GHz caused by the large variation of antenna gain within the frequency range 6 GHz to 8 GHz in this direction. The second orientation was found to have a higher UWB than the broadside. The EVM could be further improved by applying equalisation at the receiver. These simulations thus confirm that the second orientation is preferable for the whole UWB in DCSs because of the low symbol scattering at 6 GHz.

Although an antenna itself is wideband in terms of total radiated power ( $S_{21}^a$ ) for P2P communications, antennas provide varying frequency-response patterns for different orientations. A system that was operated at 3.5 GHz showed no difference in EVM values between the two orientations. At 6 GHz, however, the second orientation performed better than the broadside orientation, where symbol scattering could be observed. P2P communication thus primarily depends not only on the bandwidth or the carrier frequency of the system but also on antenna orientation. This situation enables P2P communication system designers to choose the proper operating frequency according to antenna orientation.

Table 5.2: DCS parameters.

Antenna orientation	Broadside		Second orientation	
Modulation scheme	64-QAM		64-QAM	
Samples per symbol	1		1	
RF frequency	3.5 GHz	6 GHz	3.5 GHz	6 GHz
EVM (%)	1.40%	3.25%	1.42%	0.91%
BER	0	0	0	0

Symbol scattering is caused by an antenna when the transmission phase is non-linear, which indicates the existence of an all-pass component. This scattering was shown in the broadside characterisation of the UWB antenna (Figure 5.21a). The amplitude was smooth, but the transmission phase was non-linear. These factors produced additional components in the antenna time-domain response.

## 5.6 Summary

In this chapter, a process was developed to characterise the frequency response of UWB antennas for P2P communications. The Friis equation was modified in terms of total radiated power and measured radiated power in the physical channel to calculate the effective aperture and gain. This process will provide antenna designers with useful insights into the variation of radiation patterns across the frequency band in certain directions. The frequency response of the non-minimum-phase UWB antenna was also investigated in two orientations. A frequency-dependent ECM was derived from only measuring  $S_{11}$  in amplitude and phase. The total radiated power calculated from the ECM was shown to provide radiated power in all directions from the antenna, assuming a lossless antenna. In addition, designers can use the phase of  $S_{21}^a$  obtained from the ECM to predict the behaviour of the antenna over the frequency band.

The phase of  $S_{21}$  for each orientation was separated into three components in this work: linear, minimum, and all-pass phases. Having an all-pass component means that there is resonant structure in the frequency band, resulting in a variant radiation pattern with respect to the frequency. A minimum-phase antenna will have a frequency-invariant radiation pattern and non-resonant structure over the band on its principal axis. The existence of constant gain means that the group delay of  $S_{21}$  is

constant and that there is no all-pass component. The frequency response – in terms of the effective aperture, the gain, the phase of  $S_{21}$ , and the group delay – confirmed that the antenna performance was acceptable for P2P communications in the second orientation, where the azimuth and elevation angles were  $90^\circ$  and  $45^\circ$ , respectively. The effects of the antenna on digital modulation were also observed for the two orientations. This observation demonstrated that the effects of the antenna in the second orientation were acceptable compared to the broadside. More symbol scattering was caused by the antenna when the transmission phase was non-linear, which indicated an all-pass component in the phase. P2P communication depends on the bandwidth, the carrier frequency of the system, and the antenna orientation.

# CHAPTER 6: INVERSE ANTENNA SYSTEMS AND THEIR APPLICATIONS IN DIGITAL COMMUNICATION

## 6.1 Introduction

Statistical channel models that describe the impulse response of an ultra-wideband (UWB) channel are typically represented by Dirac impulses, such as in Saleh-Valenzuela's [25] popular model. These statistical models are derived from measurements between antennas in multipath channels and assume that the antennas do not cause signal distortion. The Saleh-Valenzuela model uses many independent multipath components to describe the impulse response of the UWB channel [25]. Several multipath components represent one cluster, and each multipath component within a cluster repeats the waveform of the antenna impulse response [24], [26]. This representation indicates that the antenna response is embedded within the UWB channel's time response. If de-embedding the antenna is required, then the inverse system must be derived. Both the antenna system and its inverse must be stable, because the cascading of both systems is necessary to achieve a stable convolution [57].

Minimum-phase systems will realise the required amplitude response with minimal phase shift, which can be realised mathematically by ensuring that all the zeros are in the LHS of the  $s$ -plane. Minimum-phase antennas exhibit frequency-invariant radiation patterns and are suitable for P2P communications, as they can be used as directive antennas. In the current study, a stationary multipath channel-transfer function was extracted by de-embedding the antennas from the global transfer function of a radio link in a desired channel for P2P communication. This step enables the transfer function of multipath channels to be independent of the antenna that is used.

Antenna models may be derived in several ways [18]. An LTI IIR model is derived to represent the antenna's  $S_{21}$ , which is represented as the ratio of two polynomials in the  $s$ -domain [33]. A stable system requires all poles to be in the LHS of the  $s$ -plane. Minimum-phase antennas have both minimum-phase and linear-phase

components, as discussed in Section 3.7. The minimum-phase component represents the amplitude response of  $S_{21}$ , whereas the linear-phase component has a constant time delay due to the effective length of the antenna phase centre [34]. Non-minimum-phase antennas have an additional all-pass-phase component at certain frequencies in the band, which results in a frequency-variant radiation pattern, as discussed in Section 5.5.2. The  $S_{21}$  of a minimum-phase antenna is typically computed using the Hilbert transform [33]. Minimum-phase antennas include horn and Vivaldi antennas [2], [3], [19]. Using a minimum-phase antenna simplifies the equalisation of  $S_{21}$ , thus resulting in minimal effects in DCSs.

Modelling antennas and channels in the time domain with FIR improves the accuracy of modulated transmission simulations and provides compatibility with DCS simulations. This modelling is done to include the antennas and channels separately in DCS simulations to predict their individual effects. Previous chapters have examined different antenna effects in DCSs. These chapters have shown that different antennas have varying effects in DCSs and that the antennas' impulse responses differ. Some antennas show additional components in the antenna time response, which often introduces distortion and delay. For example, the commercial dual-band antenna examined in Section 4.6.1 was found to have caused symbol scattering in DCSs. Deriving an inverse antenna system is then required to compensate for these effects.

This chapter presents a new approach to modelling an inverse antenna system either in the frequency or the time domain for different applications in DCSs for P2P communications. These applications are done to characterise multipath channels and to compensate for the antenna effects in a DCS. Section 6.2 describes the methodology used to characterise channels and to improve antenna performance in DCSs. Section 6.3 presents an IIR system model for a Vivaldi antenna's  $S_{21}$  derived from the  $S_{21}^b$  measurement of two identical antennas in an anechoic chamber. The inverse system for the antenna is then derived from a minimum-phase  $S_{21}$  model. In Section 6.4, stationary multipath channel-transfer functions are derived for two indoor office environments with two different distances using the derived inverse system. In Section 6.5, the two channels with and without antennas are simulated in a DCS to predict the channel effects in the system. Finally, the technique is applied to a commercial antenna

to reduce the symbol scattering that occurs in the DCS and to improve system performance.

## 6.2 Methodology for Deriving Inverse Antenna Systems

To utilise this methodology, a suitable antenna must be chosen for which an inverse system will be derived. The chosen antenna is then characterised and modelled in the frequency and time domains. As discussed in Chapter 4, two different antennas are characterised in this study: a Vivaldi antenna, which has minimal effects in DCSs, and an inexpensive commercial antenna, which causes symbol scattering in DCSs. Both antennas have a minimum transmission phase, which indicates that they exhibit frequency-invariant radiation patterns and can be used for P2P communications. The inverse system is used in two different applications in DCSs: characterising the multipath channels and compensating for antenna effects in DCSs. The methodology consists of three procedures, as follows.

### 6.2.1 *Measuring and Modelling the Antenna*

The  $S_{21}^b$  between the Tx and Rx antennas is measured in the far field using a network analyser [2], [4]. The measurement of  $S_{21}^b$  in an anechoic chamber includes a determination of the frequency response of the two antennas along with the free-space channel. The TOSM calibration technique is applied to define the reference plane at the end of each cable to measure the  $S_{21}^b$  between the two antennas in their principal axes. The free-space channel is then de-embedded from the  $S_{21}^b$  measurement. For two identical antennas,  $S_{21}$  and  $S_{12}$  are similar, as are  $S_{11}$  and  $S_{22}$ . The  $S_{21}$  for each antenna is obtained using (3.4) and (3.5) for the amplitude and phase, respectively. The characterisation of an antenna is summarised in the following steps:

- 1) Measure the  $S_{21}^b$  between two identical antennas in an anechoic chamber.
- 2) To characterise each antenna in the frequency domain, compute the antenna  $S_{21}$  from the  $S_{21}^b$  measurement after de-embedding the free-space channel.
- 3) Compute the time-domain response using the IFFT.
- 4) Develop a system model for the antenna, either as an IIR or FIR model.
- 5) Develop an inverse system for the antenna, or an inverse antenna effect in

DCSs, in both domains.

Once inverse antenna systems are derived for different antennas, this technique can be used to combine different types of Tx and Rx antennas.

### 6.2.2 *Measuring and Modelling the Channel*

The  $S_{21}^b$  measurement between the two antennas in a channel incorporates the frequency responses of both, along with the response of the channel. Three steps are then involved in characterising and modelling the channel:

- 1) Measure the  $S_{21}^b$  in a desired channel without changing the positions of the Tx and Rx antennas.
- 2) De-embed the Tx and the Rx antenna responses from the  $S_{21}^b$  measurement.
- 3) Obtain the deconvolved channel-transfer function.

### 6.2.3 *Improving Antenna Performance in DCSs*

The antenna and channel can be included in the DCS simulation as an FIR system. This step is included to predict the individual antenna and channel effects separately in the system. An inverse antenna system is then derived to enable designers to characterise the multipath channel and to compensate for the antenna effects in DCSs, according to the following steps.

- 1) Predict the antenna effects in a DCS, and calculate the BER.
- 2) Predict the stationary channel effects in a DCS after de-embedding the Tx and Rx antennas from the  $S_{21}^b$  measurement in the channel.
- 3) Use the time-inverse antenna effects to improve the BER in the DCS by compensating for the antenna effects.

## **6.3 Measuring and Modelling the Vivaldi Antenna**

Vivaldi antennas are minimum-phase antennas with a frequency-invariant radiation pattern [49], [50]. The dominant direct path of a Vivaldi antenna is in the endfire direction. The Vivaldi antenna that was designed in Section 3.3.2 was characterised on a Rogers RO4003C dielectric substrate with a dielectric constant of 3.38 and a thickness of 0.5 mm. Figure 6.1 shows the antenna geometry. As the figure shows, the

$S_{11}$  was measured and compared with the simulation, and the results were found to agree. The radiation pattern gain at 6.3 GHz had only one main lobe in the endfire direction, as shown in Figure 6.1, and it displayed low sidelobe values.

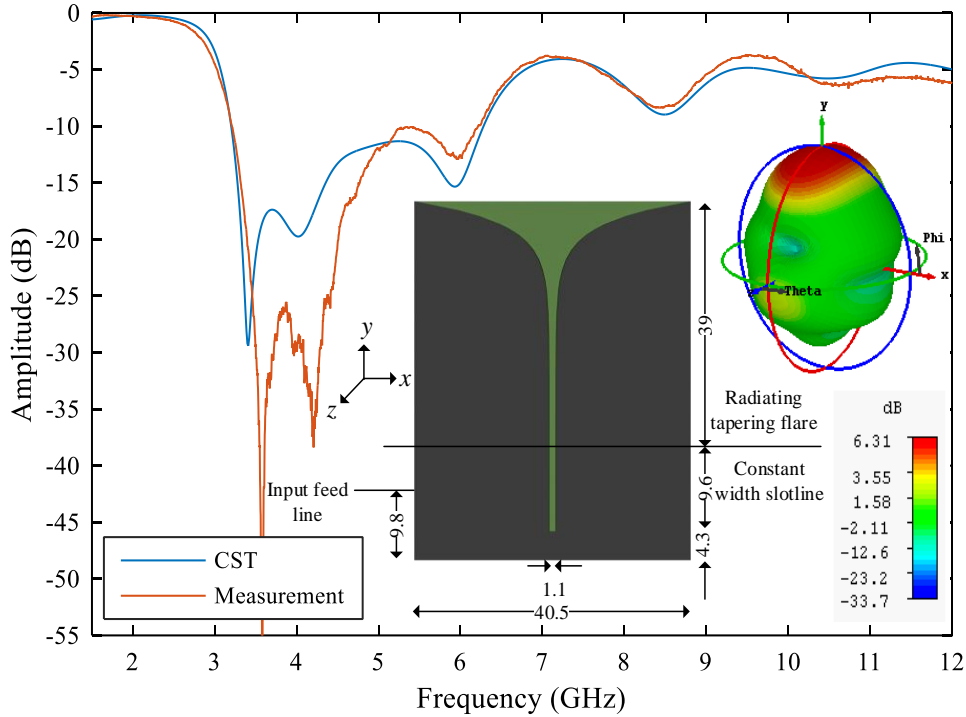


Figure 6.1. Antenna structure and  $S_{11}$  from simulation and measurement (all dimensions in mm).

The  $S_{21}^b$  between the two identical Vivaldi antennas was measured in an anechoic chamber in the endfire orientation. The  $S_{21}^b$ , which includes the responses of the Tx and Rx antennas along with the free-space channel (100 cm), was shown in Figure 3.9. The  $S_{21}$  of each antenna was then obtained from the  $S_{21}^b$  measurement in an anechoic chamber, as shown in Figure 6.2. The  $S_{21}$  phase was quite linear, since the linear-phase component was significantly higher than the minimum-phase component. Measurements were carried out within the frequency range of 1–12 GHz, while data analyses were conducted in the frequency range of 2–11 GHz.

### 6.3.1 Antenna System Model

The  $S_{21}$  of the antenna can then be represented by an IIR model as the ratio of two polynomials in the  $s$ -domain [18]:

$$F(S) = \frac{a_0s^{n-m} + a_1s^{n-m-1} + a_2s^{n-m-2} + \dots + a_ns^{-m}}{b_0 + b_1s^{-1} + b_2s^{-2} + \dots + b_ms^{-m}} \quad (6.1)$$

The coefficients  $a_0 \dots a_n$  and  $b_0 \dots b_m$  were all computed by an optimisation procedure in MATLAB to match the antenna's  $S_{21}$  [18]. The optimisation was applied to immunise any errors with low orders using iterations, and the optimisation was constrained to be approximately stable within the system. An IIR model was derived in the  $s$ -domain for the  $S_{21}$  of the Vivaldi antenna, with an order of 14 for both numerator and denominator. Figure 6.2 shows a comparison between the  $S_{21}$  of the antenna and the derived IIR model. As the figure shows, the values are well matched. Figure 6.3a shows the zeros and poles of the model, with a number of zeros in the RHS of the  $s$ -plane. For the inverse system to be stable, the antenna system model must be minimum phase, which requires all zeros to be in the LHS of the  $s$ -plane [33]. By shifting the zeros located in the RHS of the  $s$ -plane across the real axis to the LHS (Method I), the model is now minimum phase without affecting the amplitude response, and the change in the phase is linear, which causes a constant time delay. Figure 6.3a and Figure 6.3b show the situation before and after shifting the zeros, respectively. Please note that in the figures two poles are close to each other.

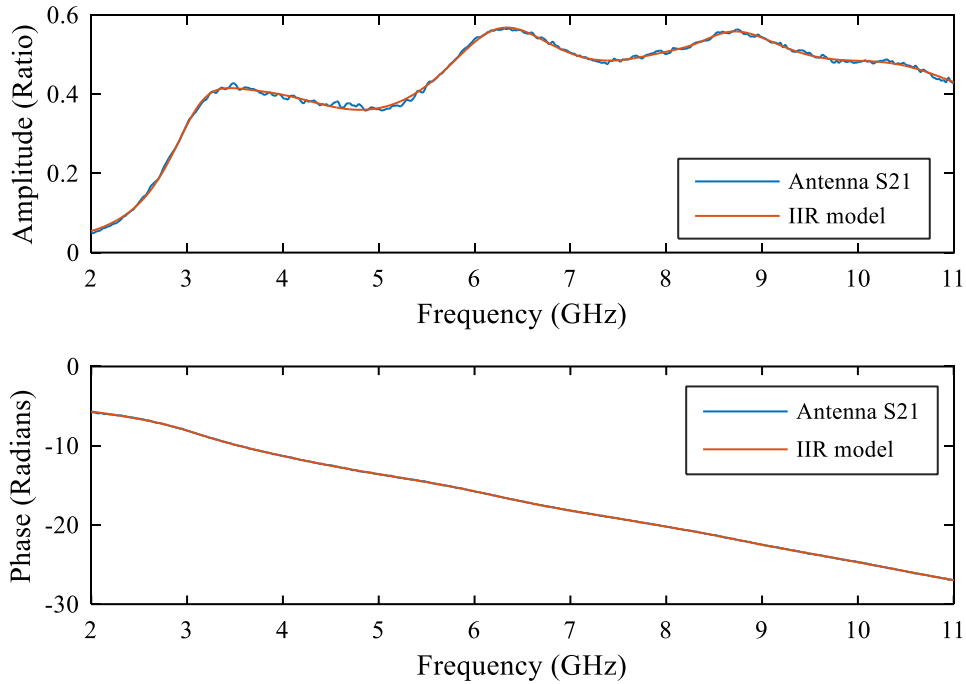


Figure 6.2.  $S_{21}$  of the Vivaldi antenna and the antenna's IIR model.

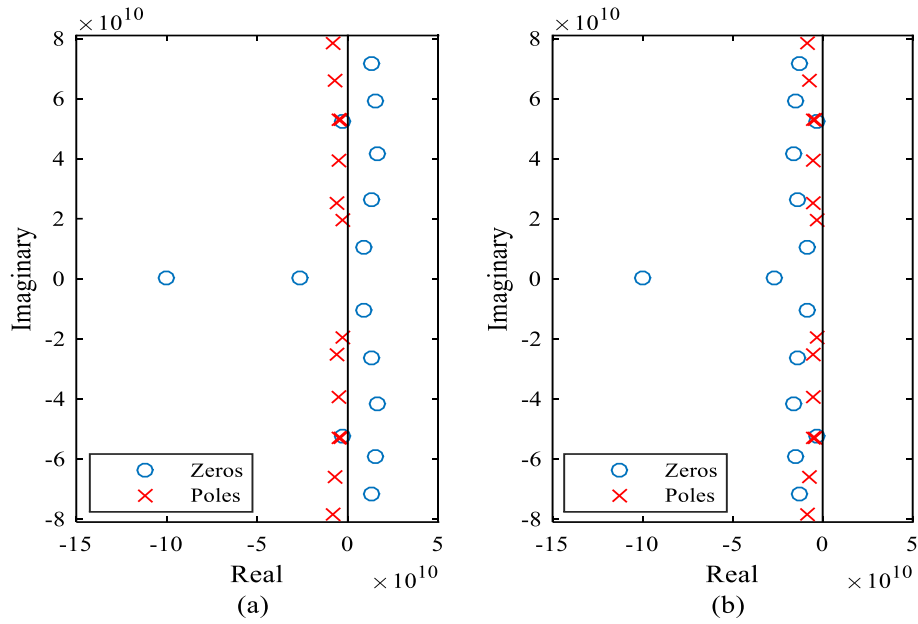


Figure 6.3. Poles and zeros of the IIR model in the  $s$ -domain using Method I for (a) antenna  $S_{21}$  and (b) minimum-phase model.

Another method for obtaining a minimum-phase model involves the Hilbert transform (Method II), which yields the relationship between the real and imaginary part of a function that is analytic in the RHS of the  $s$ -plane [33]. The Hilbert transform can be used to extract the minimum-phase component without any associated components. The minimum-phase  $S_{21}$  was obtained using Method II, and an IIR model was derived with an order of 12 for both numerator and denominator. All zeros and poles of the model were located in the LHS. Figure 6.4 shows a comparison of the minimum-phase model from the two methods. The difference between the two methods is a constant phase shift and a small linear-phase component remaining in the model obtained from Method I. These two methods were applied to obtain a minimum-phase model in order to generate a stable inverse model. Either method may be chosen for deriving a standard minimum-phase model for an antenna.

The group delay, which indicates the rate of change of the phase with frequency, was obtained from the two minimum-phase models and was found to nearly match and show the same trend, as shown in Figure 6.5. The difference in the group delay between the two minimum-phase models and the Vivaldi antenna was found to be constant, although Method I was more accurate. Notably, the group delay also showed minimal variation across the frequency axis, which indicates that the antenna had minimal effects in DCSs.

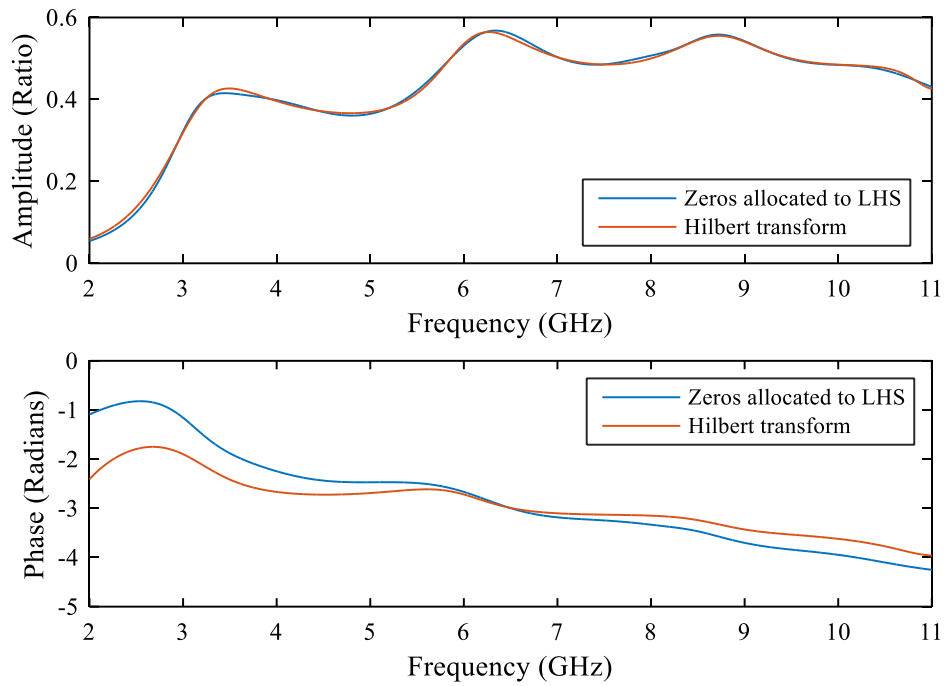


Figure 6.4. Minimum-phase  $S_{21}$  IIR model from the two methods.

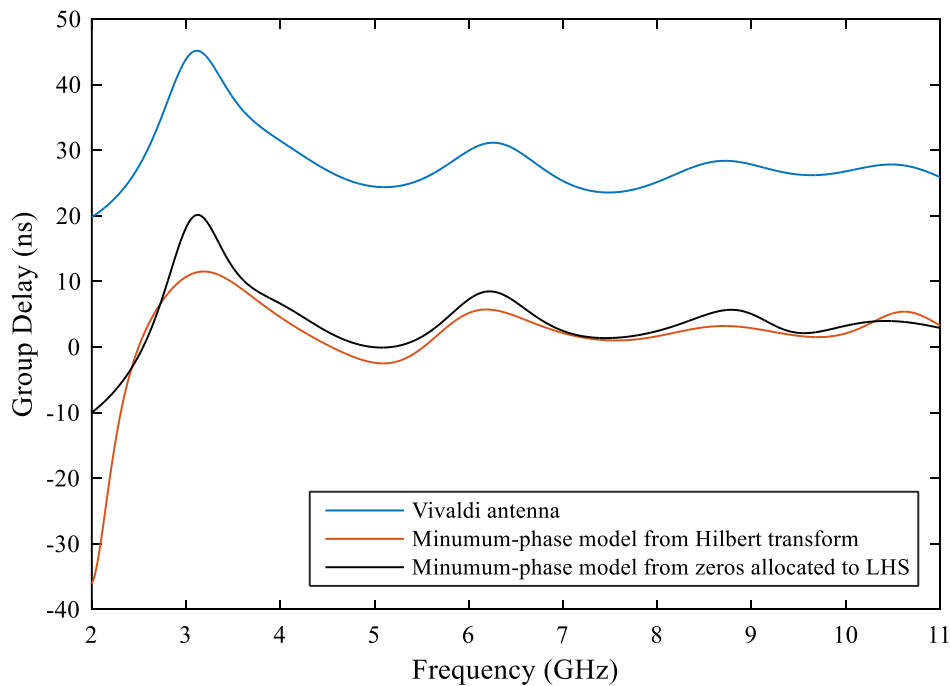


Figure 6.5. Difference in group delay between the antenna  $S_{21}$  and the two minimum-phase models.

As discussed above, two methods were used to obtain the minimum  $S_{21}$  phase of the Vivaldi antenna. This technique can only be used for minimum-phase antennas. For non-minimum-phase antennas, an additional phase component in the  $S_{21}$  phase is created due to the resonant structure of the antenna and can cause frequency-variant

radiation patterns. As discussed in Section 5.5.2, the transmission phase of a non-minimum-phase antenna has three phase components: linear, minimum, and all pass. The all-pass component causes different delays in the frequency response, which necessitates the derivation of an additional inverse system for the all-pass component using the cascading method.

### 6.3.2 Inverse Antenna System

In inverse antenna systems, the antenna responses are extracted from the global transfer function of a radio link in order to characterise a channel with multipath components. In this study, a channel-transfer function for P2P communications was derived by applying an inverse system for both Tx and Rx antennas in the  $S_{21}^b$  measurement between the two antennas that includes a multipath channel, as illustrated in Figure 6.6. If the Tx and Rx antenna models are minimum phase, then the inverse system can be obtained by taking the inverse ratio of the polynomial function in (6.1). The inverse systems for the Vivaldi antenna were derived from the two methods and compared, as shown in Figure 6.7. The only difference between the inverse minimum-phase models was a constant phase shift of 2 radians, as well as a small linear-phase component that remained in the model from Method I, since the Hilbert transform (Method I) extracts the minimum-phase component only.

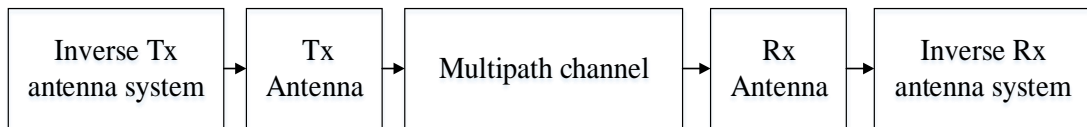


Figure 6.6. Derivation of a channel-transfer function for P2P using an inverse antenna system.

The validity of the inverse system model obtained from Method I was then verified by convolution with the minimum-phase model and the antenna  $S_{21}$  model, as shown in Figure 6.8 and Figure 6.9, respectively. The result from the convolution shown in Figure 6.8 provided unity in amplitude and the zero phase in the frequency axis, whereas in Figure 6.9, the convolution phase was linear, similarly to the linear-phase component in the antenna  $S_{21}$  phase. The linear-phase component was computed with reference to the phase centre of the antenna [34]. This component was derived from the particular effective distance, which typically causes a constant time delay. The effective distance to the phase centre of the Vivaldi antenna was computed

equivalently to a free-space distance of 0.1 m. The linear-phase component was then removed by including the equivalent effective distance in the delay in the channel.

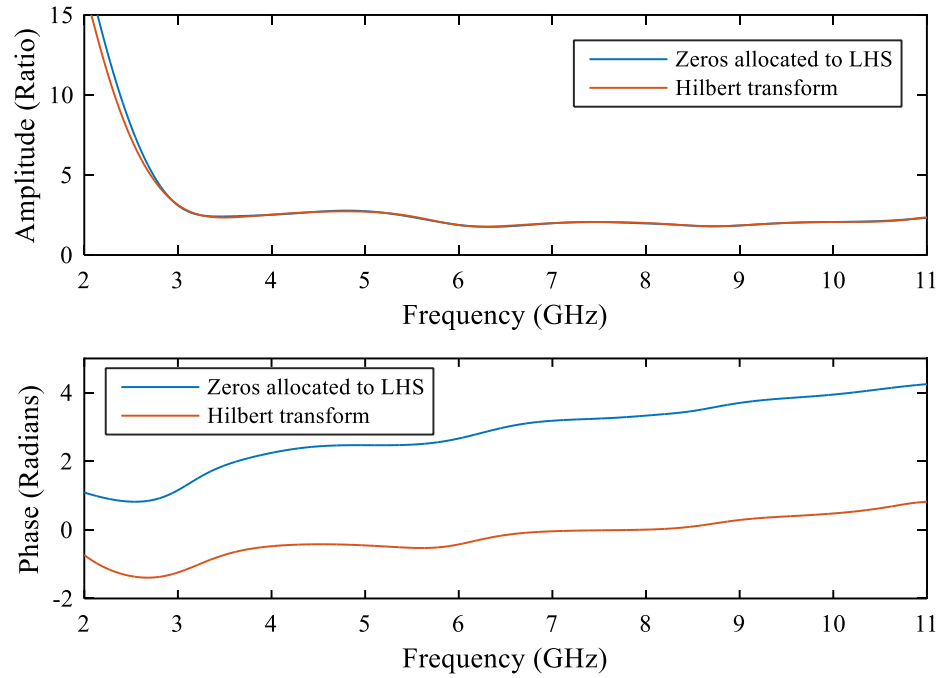


Figure 6.7. Stable inverse system of the Vivaldi antenna from the two methods.

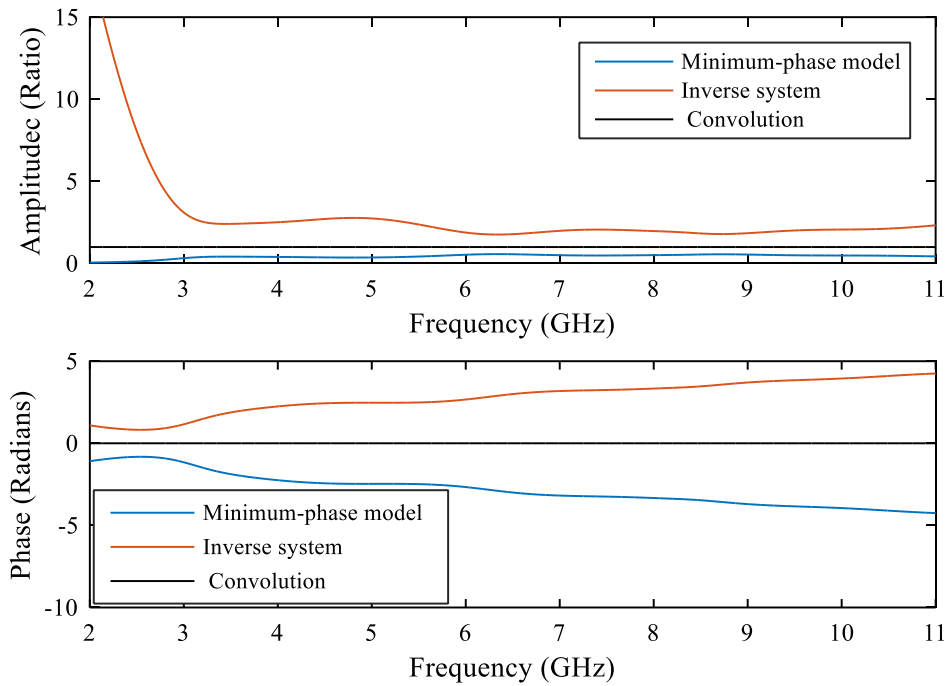


Figure 6.8. IIR model from Method I and the model's inverse system, with both models' convolutions.

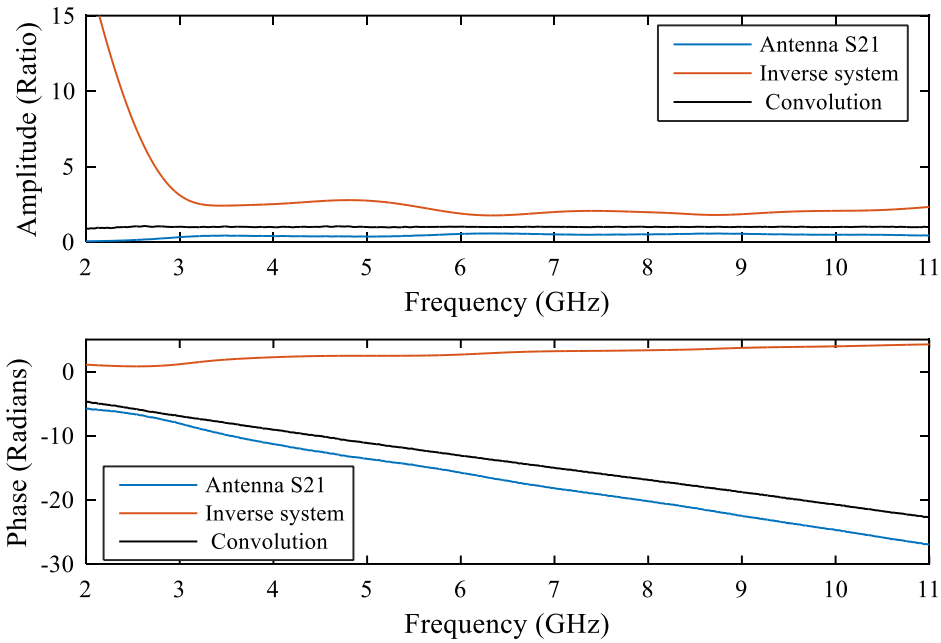


Figure 6.9. Vivaldi antenna  $S_{21}$  and the inverse system, with the systems' convolutions.

## 6.4 Measuring and Modelling the Channel

The coefficients of the IIR inverse system were then obtained to characterise the multipath components in the channels. From the antenna  $S_{21}^b$  measurements and the inverse antenna system model for the Tx and Rx antennas, the stationary channel-transfer functions were derived. The next step was to obtain a wideband channel-transfer function in an office environment from the known inverse system models of the Tx and Rx antennas. This step was taken to predict the frequency responses of the different channels by de-embedding the two antennas from the  $S_{21}^b$  measurements. The  $S_{21}^b$  values between the two identical Vivaldi antennas were measured to obtain the global transfer function of a radio link in two different indoor office environments (Office1 and Office2) with 1 m and 3 m distances, respectively. Figure 6.10a and Figure 6.10b show the setups along with the endfire orientations of the two Vivaldi antennas and their environments for Office1 and Office2, respectively. Figure 6.11a and Figure 6.11b show the  $S_{21}^b$  between the two identical antennas 1 m apart in Office1 and Office2, respectively. The rippling in the amplitude of the channel is higher in Office2 because that office has more computers and desks, which results in varying channel conditions caused by different multipaths.

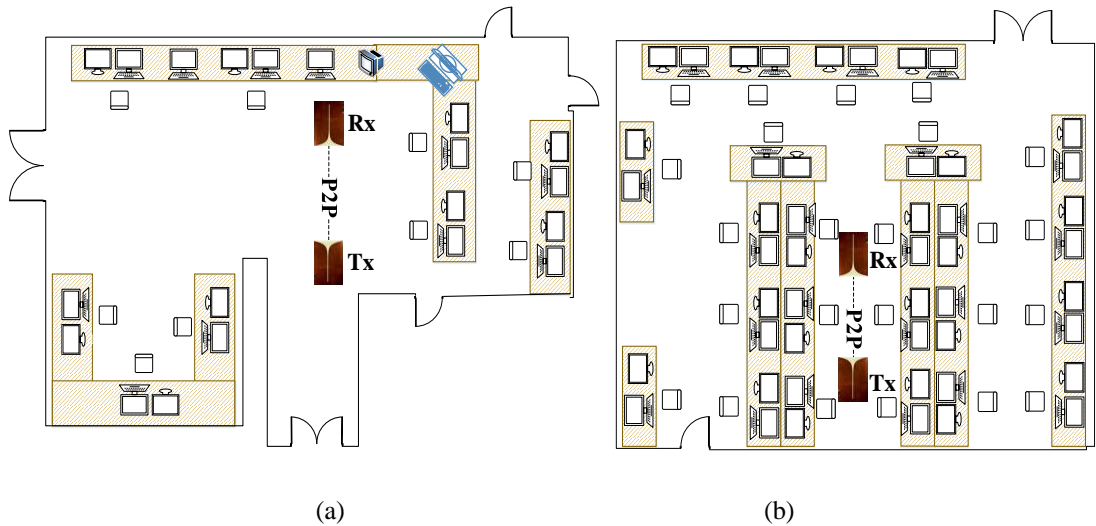


Figure 6.10. Schematic of the environment in (a) Office1 and (b) Office2.

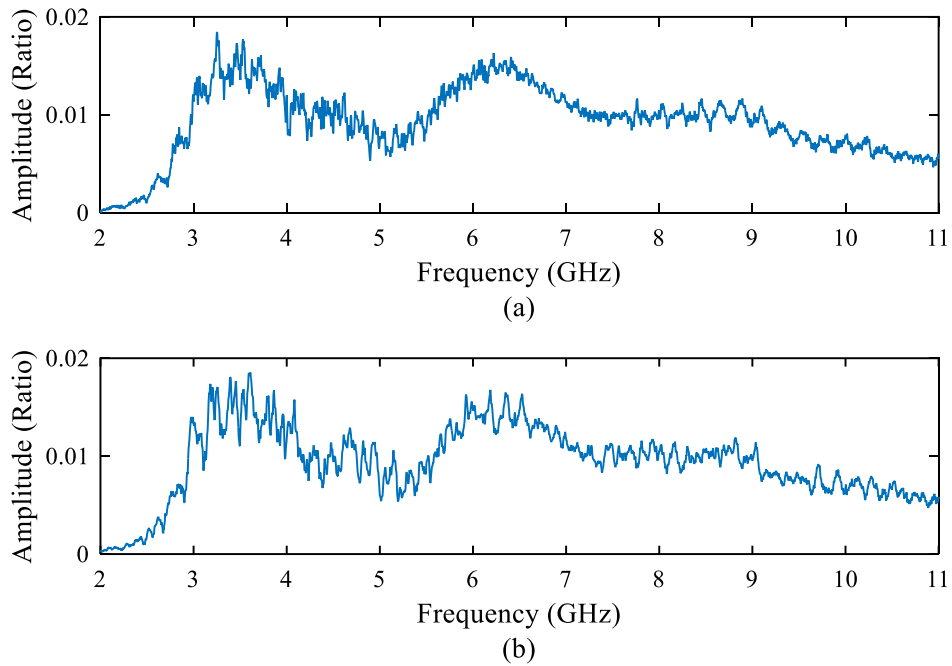


Figure 6.11. Measurements of  $S_{21}^b$  between the two Vivaldi antennas at 100-cm distance in (a) Office1 and (b) Office2.

#### 6.4.1 Office1 Channel

Figure 6.12 shows the deconvolved channel-transfer function for Office1 after de-embedding the two antennas from the  $S_{21}^b$  measurement with the two different distances. The amplitude of the channel-transfer function illustrates the path loss with multipath components in radio propagation at each distance in the frequency axis. The Tx and Rx antennas compensate for the path loss in the channel due to their directivity,

which can be observed in the difference in scale between Figure 6.11 and Figure 6.12. The Vivaldi antenna does affect the transfer function of the channel but with minimal effects in DCSs. The increase in signal attenuation and multipath components is also noticeable between the distances of 1 m and 3 m. The phase shown in Figure 6.12 estimates the delay as a function of frequency due to the distances of 1 m and 3 m.

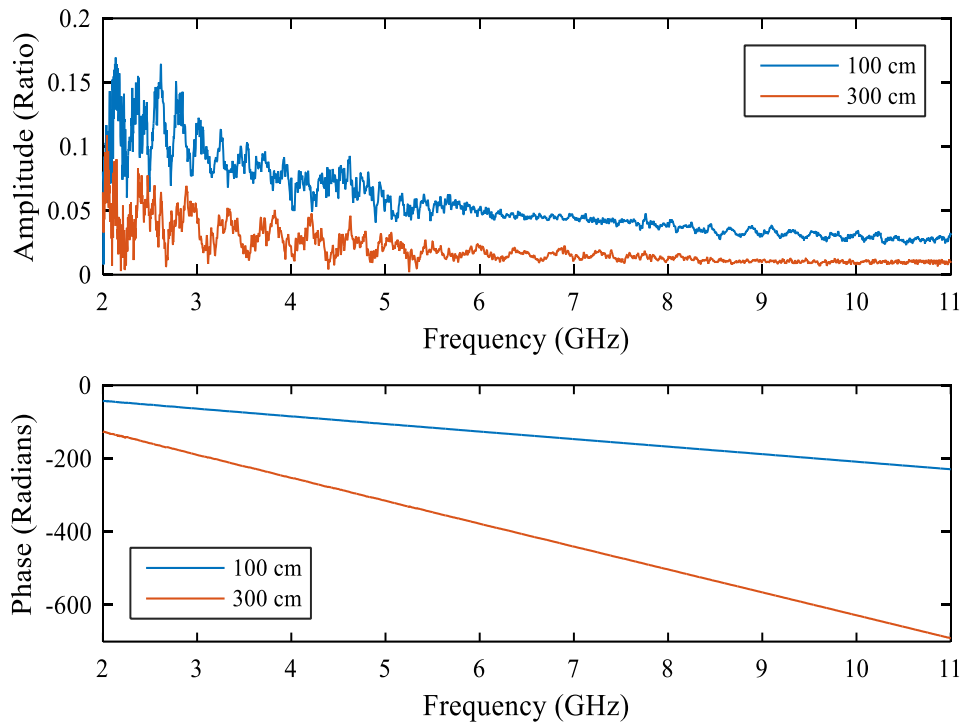


Figure 6.12. Deconvolved channel-transfer function of Office1 at two distances.

#### 6.4.2 Office2 Channel

Figure 6.13 shows the deconvolved channel-transfer function for Office2 after de-embedding the antenna for the two different distances. This channel showed more rippling compared to Office1, which resulted in a varying channel model caused by different multipaths. The phase in Office2 was the same as Office1 for the two distances.

Even though the antennas are directive, the channel consists of multipath components due to reflections from nearby surfaces. As long as these surfaces (i.e. the environment) remain stable, the multipath components in the channel will remain stationary. The derived channel-transfer functions can be used with antennas that have

a frequency-invariant radiation pattern with low sidelobe values. Using an inverse antenna system thus enables designers to characterise the channels in P2P communications for different applications in a variety of environments. Once system models and their inverse models are derived for different antennas, various types of Tx and Rx antennas can be combined with a variety of channels in order to simulate an end-to-end wireless system for numerous applications.

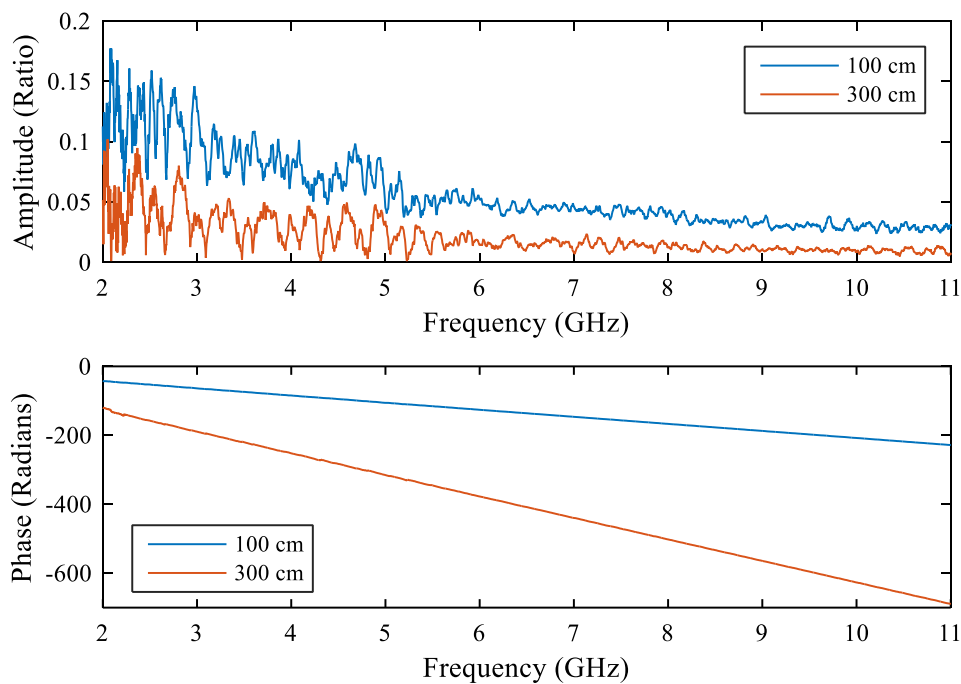


Figure 6.13. Deconvolved channel-transfer function of Office2 at two distances.

## 6.5 Antenna and Channel Performance in a DCS

In the next step, a complete DCS was developed in SIMULINK, as shown in Figure 6.14. The DCS was used to simulate and predict the channel effects of Office1 and Office2 and to characterise the symbol scattering by calculating the EVM and BER for  $10^6$  symbols. Data were generated for the system, and 64-QAM modulation was used. The DCS was simulated without equalisation at the receiver to analyse the individual effects caused by the antenna and channel, and to compensate for the antenna effects to reduce the BER in the system.

### 6.5.1 DCS Simulation with Different Channels

Because Vivaldi antennas are minimum phase and have minimal effects in DCSs, the different channel effects were predicted in two different ways: (1) by modelling the antenna and channel as FIR models from  $S$ -parameter measurements in a channel and (2) by modelling only the channel after de-embedding the Tx and Rx antennas from the  $S_{21}^b$  measurement. The carrier frequency was 6.3 GHz.

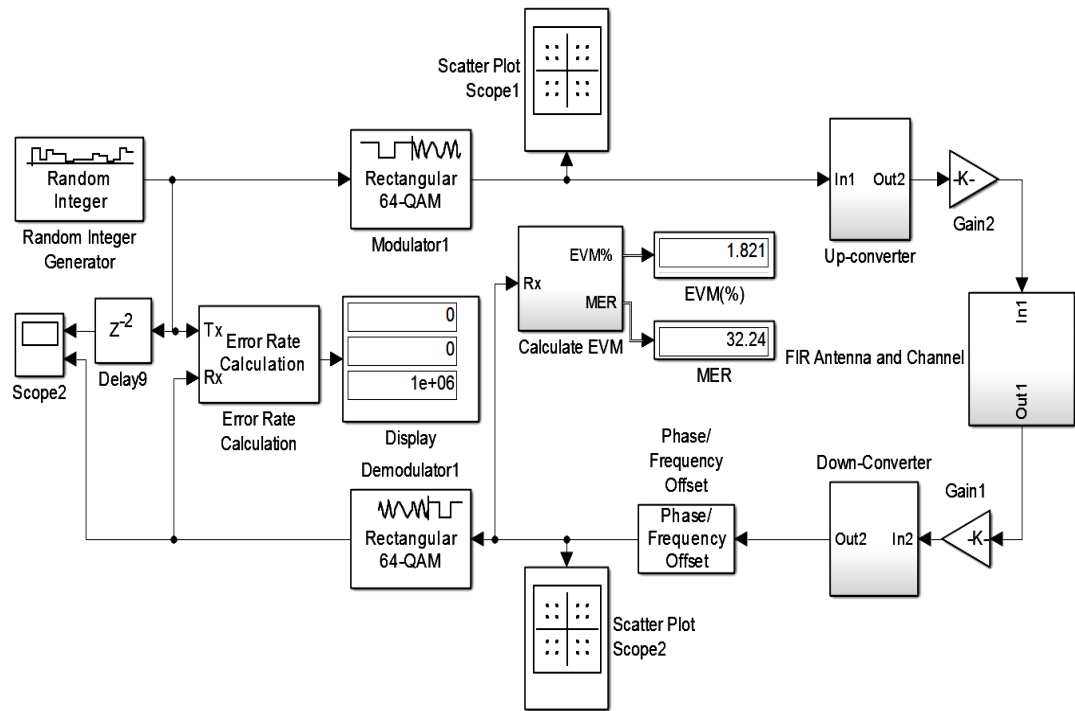


Figure 6.14. DCS with Vivaldi antenna and channel.

#### 6.5.1.1 ANTENNA AND CHANNEL SIMULATION IN THE DCS

From the  $S_{21}^b$  measurements of the Vivaldi antenna in the free-space channel, the antenna measurement was modelled for two different distances: 1 m and 3 m. These models were based on the  $S$ -parameter measurements in an anechoic chamber to predict the antenna effects in the DCS. The EVM values at the receiver were found to be low, at 1.8% and 2.8% for the distances of 1 m and 3 m, respectively. The constellation diagrams in Figure 6.15a and Figure 6.15b show the symbol scattering for the two different distances. Determining the symbol scattering caused by the antenna with the free-space channel yields the antenna effects in the DCS. This step confirmed that the antenna had minimal symbol scattering and that the Vivaldi antennas had minimal effects in DCSs.

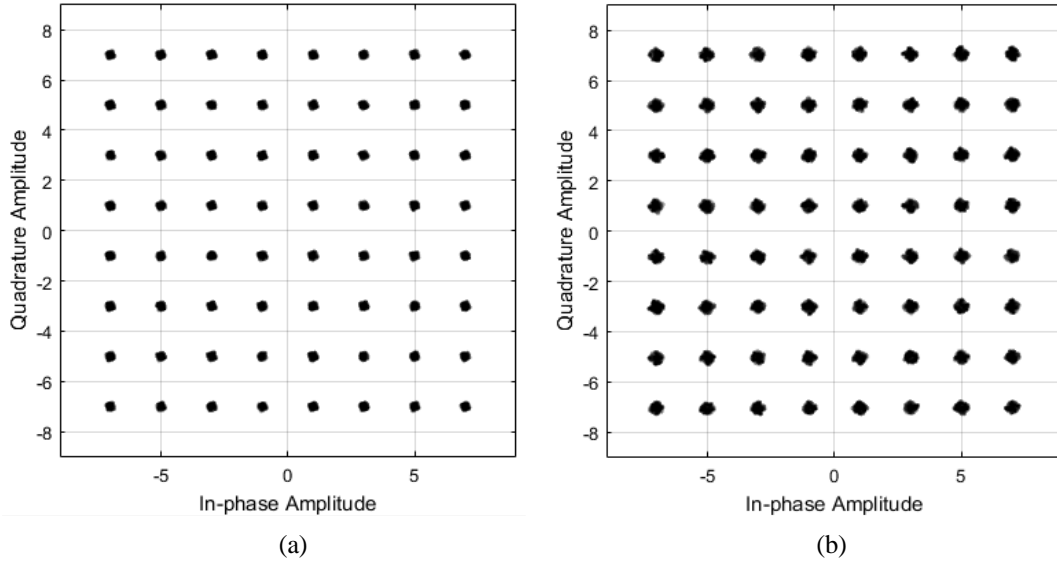


Figure 6.15. Constellation diagram from Vivaldi antenna measurements in an anechoic chamber with distances of (a) 1 m and (b) 3 m.

The  $S_{21}^b$  measurements of the Vivaldi antenna in two different channels for Office1 and Office2 were modelled to predict the channel effects. The symbol scattering for the antenna modelling in Office1 and Office2 with a 1-m distance was found to be different, as shown in Figure 6.16a and Figure 6.16b, respectively. This difference occurred because the channel in Office2 had more reflections. The EVM values were found to be 4.3% and 12.9%, respectively, as shown in Table 6.1. The BER in Office2 was 0.037, whereas in Office1 the value was zero because the receiver was able to recover the symbols.

#### 6.5.1.2 CHANNEL SIMULATION IN THE DCS

The two different channel-transfer functions for the Office1 and Office2 models with a distance of 1 m after de-embedding the Tx and Rx antennas were then simulated in the DCS. These models were included as FIR models in the DCS to predict the channel effects on system performance and to compare those effects with the results obtained from modelling the antennas in Office1 and Office2. Figure 6.17a and Figure 6.17b show the symbol scattering caused by the channel without the antenna's effects for Office1 and Office2, respectively. Table 6.1 shows the resulting EVM and BER values. These results for Office1 and Office2 are quite similar to those obtained from modelling the antennas and the two offices, since Vivaldi antennas have minimal effects in DCSs.

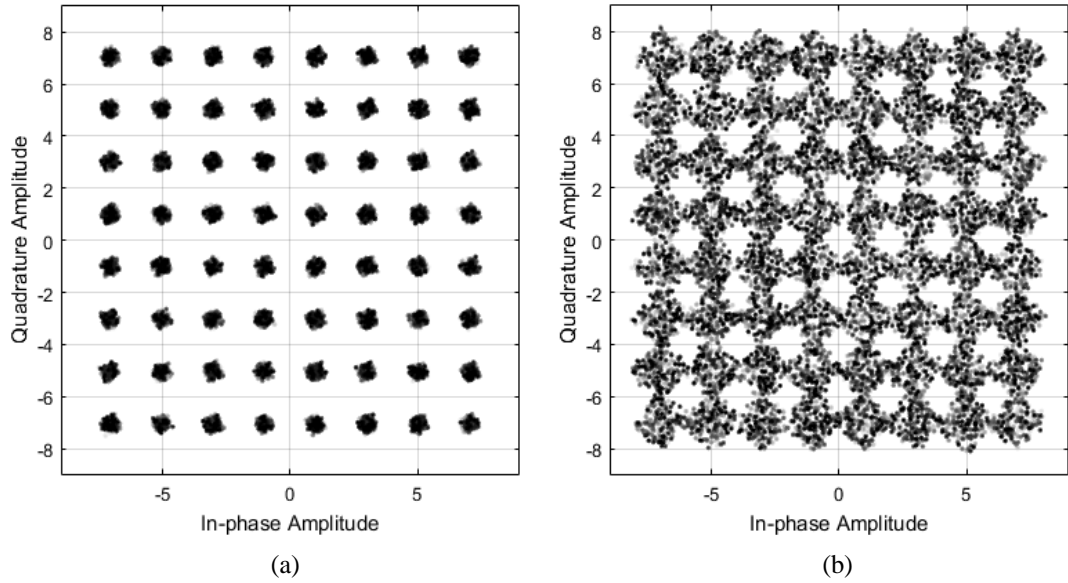


Figure 6.16. Constellation diagram with a 1-m distance based on a Vivaldi antenna and a channel model in (a) Office1 and (b) Office2.

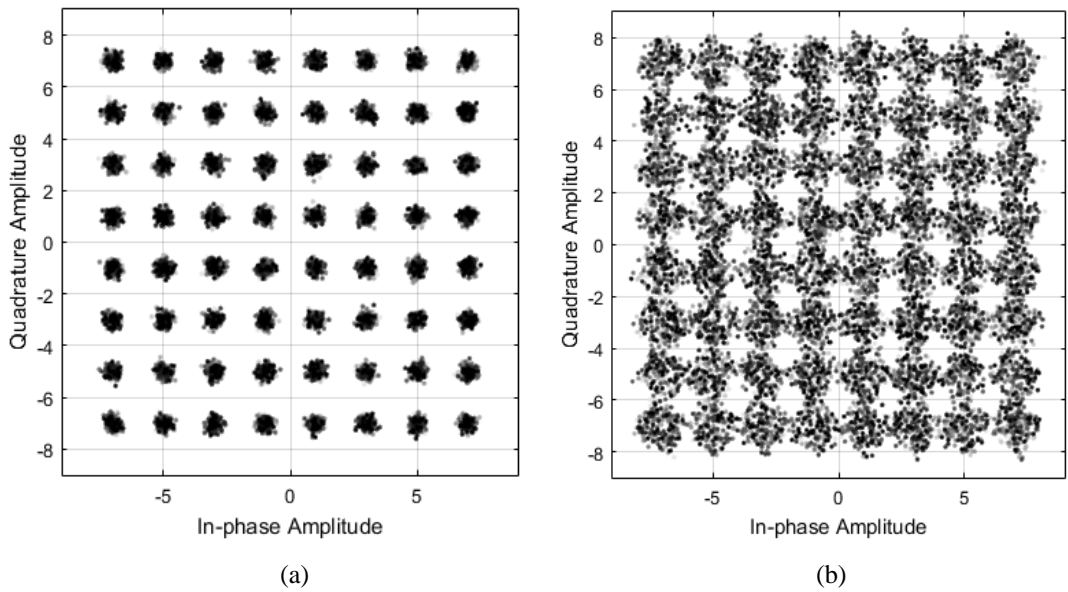


Figure 6.17. Constellation diagram with 1-m distance based on the channel model after de-embedding the antenna in (a) Office1 and (b) Office2.

In general, multipath channels and antennas cause symbol scattering in DCSs. These effects will degrade the performance of the system. De-embedding the Tx and Rx antenna responses from the  $S_{21}^b$  measurements in a channel yields an accurate stationary channel-transfer function for P2P applications. This derivation also helps to include the channel-transfer function with different types of antenna models in DCS simulations when the channels are controlled for P2P.

Table 6.1. EVM and BER in different channels with a 1-m distance.

<b>Modelling</b>	<b>Channel with antennas</b>		<b>Channel only</b>	
<b>Modulation scheme</b>	64-QAM		64-QAM	
<b>Carrier frequency</b>	6.3 GHz		6.3 GHz	
<b>Channel</b>	Office1	Office2	Office1	Office2
<b>EVM (%)</b>	4.3	12.9	4.3	12.6
<b>BER</b>	0	0.037	0	0.034

### 6.5.2 Reducing the BER in the DCS

Antennas cause symbol scattering and BER in DCSs. This scattering depends on the antenna design as well as the carrier frequency. The sets of measured  $S$ -parameters of such a commercial dual-band antenna in an anechoic chamber in the broadside direction are presented in Section 4.4. The antenna has two bands at the two carrier frequencies of 2 GHz and 6 GHz. In this study, the  $S_{21}$  of the commercial antenna was obtained from the  $S_{21}^b$  measurement between two identical commercial antennas in an anechoic chamber to eliminate the multipath components. The antenna had a minimum transmission phase, but the amplitude showed rippling, which introduced additional components into the time domain. The time-domain response for each antenna's  $S_{21}$  was then computed using the IFFT, as shown in Figure 6.18a. This commercial antenna generally causes symbol scattering, which occurs because the time-domain response of the antenna has additional components, as shown in Figure 6.18a. These components are caused by multiple reflections in the antenna itself.

The previously described methods for deriving an IIR inverse system model could not be applied in this case, as the amplitude response showed rippling, which would require a very high-order system. Another method that can be used to remove the antenna effects in DCSs is to derive a time-inverse antenna system. Such systems are derived by inverting the time response after the end of the antenna impulse response to achieve cascading with the antenna response, as shown in Figure 6.18b. This step compensates for the multipath components caused by the antenna itself.

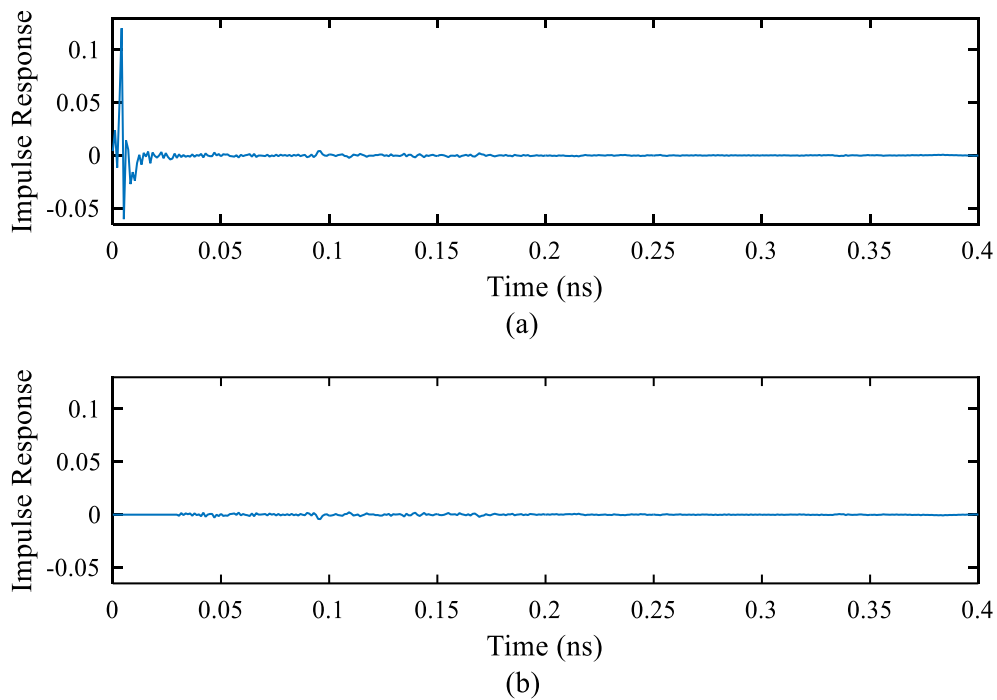


Figure 6.18. Impulse response of the antenna  $S_{21}$  in (a) commercial antenna and (b) inverse antenna effects.

The commercial antenna  $S_{21}$  was modelled and then simulated in the DCS for both bands at the two carrier frequencies. This step was done to compare the symbol scattering that occurred before and after compensating for the additional components caused by the antenna itself. Figure 6.19a and Figure 6.20a show output constellation diagrams of the antenna system at carrier frequencies of 2 GHz and 6 GHz, respectively. These effects were caused by the existence of additional components in the time domain of the commercial antenna.

The current study also found increases in BER and EVM to be a function of frequency. Figure 6.19b and Figure 6.20b show the output constellation diagrams after applying the inverse system, which compensated for the antenna effects for the two bands. The inverse antenna system minimised the BER and EVM for the two bands. Table 6.2 shows the resulting EVM and BER values before and after applying the inverse antenna system. The absence of rippling in the antenna frequency response and the linear phase produced a low level of symbol scattering and lowered the EVM and BER values.

Table 6.2. EVM and BER values in a DCS with an inverse antenna in the broadside orientation.

Modelling	Commercial antenna		With inverse antenna	
Modulation scheme	64-QAM		64-QAM	
Carrier frequency	2 GHz	6 GHz	2 GHz	6 GHz
EVM (%)	6.9	3.1	0.6	0.4
BER	0	0	0	0

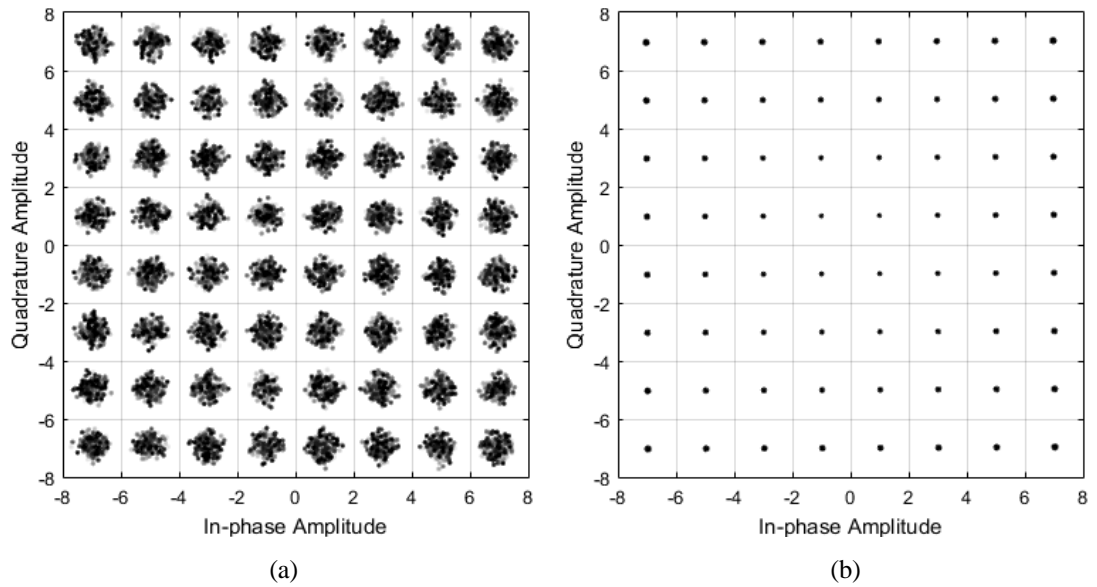


Figure 6.19. Constellation diagram at carrier frequency of 2 GHz (a) after commercial antenna system and (b) with inverse time response system.

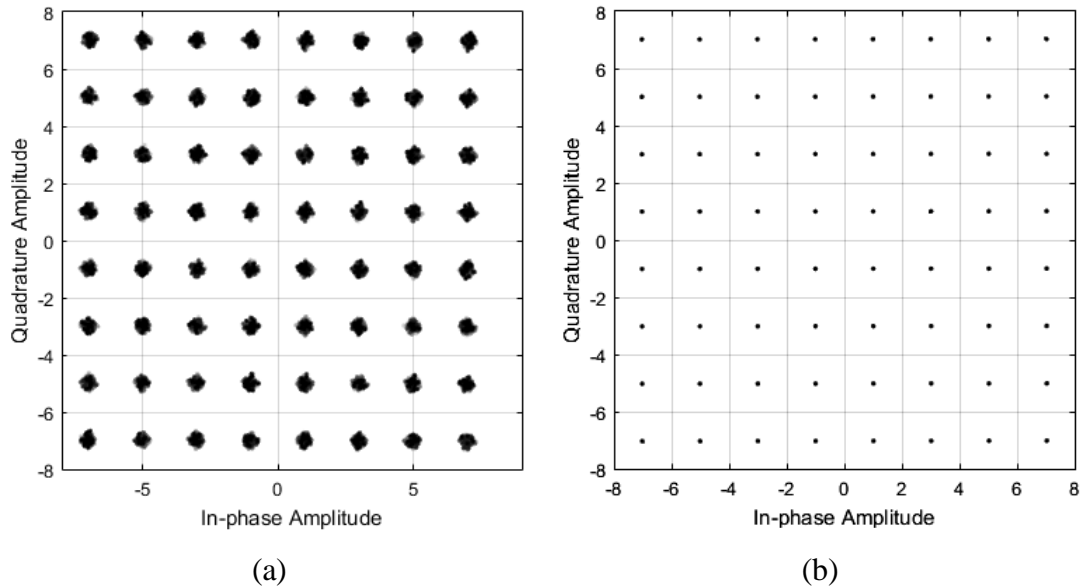


Figure 6.20. Constellation diagram at carrier frequency of 6 GHz (a) after commercial antenna system and (b) with inverse time response system.

The use of this technique enables designers to eliminate the antenna effects in DCSs and allows for the use of inexpensive antennas (which are generally highly dispersive) in order to improve their performance in DCSs. The equalisation can then be used to determine the channel effects separately. To compensate for the antenna effects, the implementation of the algorithm must be conducted using either hardware or software. The hardware can be implemented in the RF or IF, whereas software must be in IF, as RF would require very fast digital circuitry.

## 6.6 Summary

This chapter has presented an approach to modelling an inverse antenna system for characterising multipath channels and compensating for the antenna effects in DCSs for P2P communications. The chapter has also presented the characterisation and modelling of a Vivaldi antenna, which had minimal effects in DCSs, as well as an inexpensive commercial antenna, which caused symbol scattering in the system. An inverse antenna system for the Vivaldi antenna was derived to de-embed the antenna response from the  $S_{21}^b$  measurement in a channel. This technique allowed for characterising channel-transfer functions.

A system model was derived for the antenna  $S_{21}$  obtained from the  $S_{21}^b$  measurements in an anechoic chamber after de-embedding the free-space channel. A minimum-phase model was derived using two methods: by shifting the zeros to the LHS and by using the Hilbert transform. An inverse system model was then generated from the two derived minimum-phase models. This technique can be applied for minimum-phase antennas that have frequency-invariant radiation patterns. The sidelobes should have minimal values, and the antenna frequency response should not show rippling.

Two office channels were then characterised and modelled from the inverse system and the  $S_{21}^b$  measurement in the desired channel. This technique provided separate models for the antenna and channel so that their effects in DCSs could then be analysed separately.

The Vivaldi antenna with a free-space channel was modelled as a time domain

at two different distances to show that Vivaldi antennas have minimal effects in DCSs. Two office environments were modelled, both with and without antennas, in order to perform a complete analysis of the channel conditions and to predict different channel effects in a DCS. This modelling will enable designers to show the limitations of higher-order modulation schemes and to find the maximum distance of signal transmission to determine the coverage area. In general, the accurate modelling of antennas and channels enables designers to achieve robust designs of complete DCSs.

Another application of an inverse antenna system was applied to a commercial antenna to reduce the BER and to eliminate the antenna effects in DCSs. This step will enable designers to compensate for the antenna effects and to use low-cost, highly dispersive antennas in DCSs.

Because the transmission phase has three components – linear, minimum, and all pass, as discussed in Section 5.5.2 – a non-minimum-phase antenna that exhibits frequency-variant radiation patterns will be required for future research to derive an additional inverse system for an all-pass component. Such a setup will allow for considering the total radiated power by an antenna as a function of frequency and will include the frequency-variant radiation patterns in the antenna system model. An antenna's total radiated power can be obtained from measurements conducted in a reverberation chamber. Doing so will require further research to calculate the reverberation chamber cavity loss, as will be discussed in the next chapter.

# CHAPTER 7: DETERMINING TOTAL RADIATED ANTENNA POWER FROM REVERBERATION CHAMBER MEASUREMENTS

## 7.1 Introduction

The Wheeler-Cap method, introduced in the late 1950s, was originally used for small narrowband antennas to measure the antenna's total efficiency and loss [58]. Rosengren used reverberation chambers to measure the total efficiency of non-small wideband antennas to compute the total radiated power by an antenna from the measurements inside the reverberation chamber. The total efficiency is the power ratio of the radiated power to the available power from the source, while the radiation efficiency is the ratio of power radiated to the power accepted by the antenna port [5]. Anechoic chamber measurements are used for P2P communications, whereas reverberation chamber measurements provide the total radiated power [6]. The difference between the two environmental measurements is in the directivity of the Tx and Rx antennas [6]. Hence anechoic chamber measurements require alignment of the TX and Rx antennas, whereas reverberation chamber measurements provide isotropic fields within the chamber and can include antennas placed randomly or with any orientation without affecting the results [58], [59].

Obtaining  $S_{21}^a$  which provides the total radiated power by an antenna helps to derive a comprehensive antenna system model as a function of frequency and includes the frequency-variant radiation patterns. An antenna's total radiated power can be obtained from measurements conducted in a reverberation chamber [58], [59]. The quality factor due to the skin depth of the walls of a cavity and antenna losses are the two factors that affect reverberation chamber measurements [5] while computing the total radiated power by an antenna. In the literature, the quality factor is usually attained by measuring the S-parameters inside the cavity, but this measurement mixes the losses due to the skin depth of the walls with the losses due to the antenna itself [5], which indicates that the antenna efficiencies used in the measurement have been inadvertently included in the quality factor. The quality factor must include the losses

of the cavity without including the effects of the antenna, which means that the quality factor must be computed based on the cavity properties only.

This chapter presents the computation of an antenna's total radiated power and losses from measurements in a reverberation chamber that was built from a medium-size aluminium cavity. This computation was achieved by compensating for the cavity losses due to the walls without the antenna effects, which was done by using an empirical equation to compute the total radiated power by an antenna from the measurement in the cavity. The chapter introduces reverberation chamber measurements of the three antennas characterised in the previous chapters: Vivaldi, commercial, and monopole UWB antennas.

The remainder of this chapter is organised as follows. Section 7.2 presents a mathematical formulation for studying the relationship between the total radiated power of an antenna and the quality factor of the cavity. A medium-size cavity was built from aluminium walls, based on the reverberation chamber measurements described in Section 7.3. Section 7.4 presents the measurements of the three characterised antennas with different orientations and distances to show that antenna measurements are not a function of distance and do not depend on radiation patterns. An empirical equation is then derived from the Vivaldi antenna measurements in the cavity described in Section 7.5 (since the Vivaldi antenna is a lossless antenna) in order to apply this equation to the measurements of the commercial and monopole UWB antennas to compute the  $S_{21}^a$  value, which yields the total radiated power from each antenna type.

## 7.2 Mathematical Formulation

In general, reverberation chambers are built in the form of metallic enclosures for waveguide resonators. Electric and magnetic energy is stored inside the cavity, and the power dissipation is due to the skin depth of the wall material.

From the theory of the measurements in well-performing reverberation chambers, the total radiated power of a Tx antenna is defined as [60]:

$$P_{TX} = \langle P_{RX} \rangle \frac{C_{RC}}{Q} \quad (7.1)$$

where  $P_{TX}$  and  $\langle P_{RX} \rangle$  are transmitted and averaged received power, respectively, and  $C_{RC}$  is the reverberation chamber constant of the cavity that is used. This constant is defined from the literature as [59]:

$$C_{RC} = \frac{16\pi^2 V}{\lambda^3} \quad (7.2)$$

where  $V$  is the volume of the chamber (i.e. the cavity) in  $\text{m}^3$ .

The quality factor of a resonator is defined as the ratio of stored energy in the cavity and the dissipated power per cycle through the walls of the cavity. The quality factor  $Q$  of a lossy cavity can be computed by [5], [61]:

$$Q = \omega \frac{U}{P_d} \quad (7.3)$$

where  $U$  is the stored energy in the cavity and  $P_d$  is the dissipated power through the walls. The walls are built from metal, and an air dielectric exists between the walls. Because of the assumption of steady-state conditions in reverberation chambers, the dissipated power is the same as the antenna's transmitted power.

The rectangular cavity is a rectangular waveguide with thin-faced (i.e. side) plates or walls. The walls have infinite conductivity. A cavity with the dimensions  $a$ ,  $b$ , and  $h$ , all in m, is shown in Figure 7.1.

For a rectangular cavity with dimensions  $a$ ,  $b$ , and  $h$ , a theoretical expression for the stored energy and the dissipated power in the cavity was derived in [62], as follows:

$$U = E_0^2 \frac{\epsilon abh}{8} \quad (7.4)$$

$$W_L = \frac{R_s \lambda^2}{8\eta^2} E_0^2 \left[ \frac{ab}{h^2} + \frac{bh}{a^2} + \frac{1}{2} \left( \frac{a}{h} + \frac{h}{a} \right) \right] \quad (7.5)$$

where  $a$ ,  $b$ , and  $h$  are the dimensions inside the cavity in the x-, y-, and z-axes, respectively;  $E_0$  is the magnitude of the electric field;  $\epsilon$  is the permittivity of the dielectric (for free space,  $\epsilon_0 = 8.854 * 10^{-12} \text{ F/m}$ ); and  $R_s$  is the surface resistivity of the walls of the cavity in  $\Omega$ .

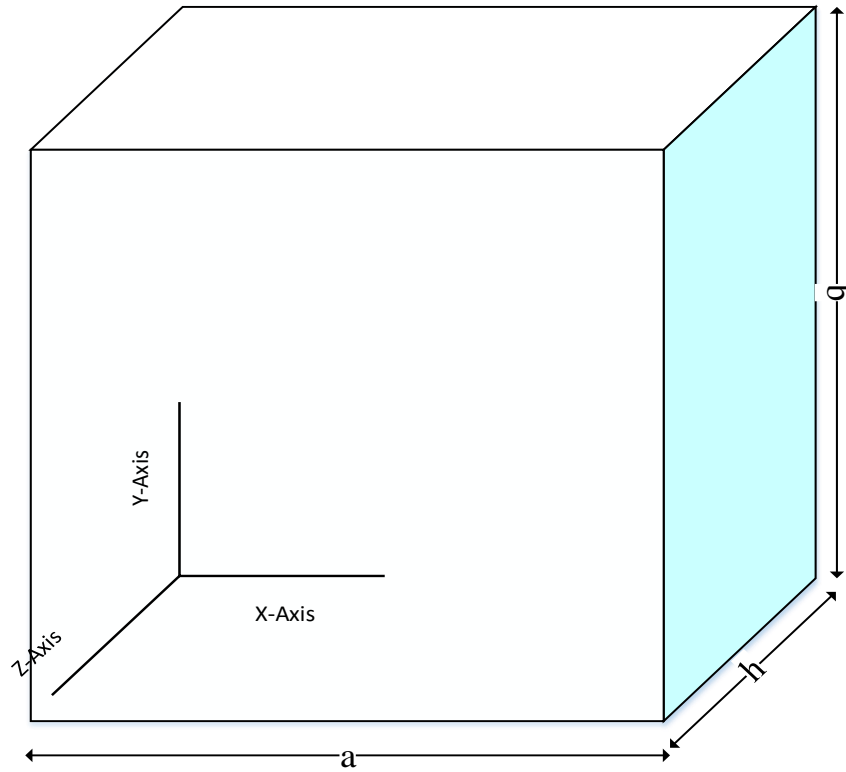


Figure 7.1. Rectangular cavity design as a function of the reverberation chamber.

From (7.3), (7.4), and (7.5), the quality factor of a cavity can be computed as follows [62]:

$$Q = \frac{\pi\eta}{4R_s} \left[ \frac{2b(a^2+h^2)^{\frac{3}{2}}}{ah(a^2+h^2)+2b(a^3+h^3)} \right] \quad (7.6)$$

where  $\eta$  is the intrinsic impedance (for an air dielectric,  $\eta_0 = 120\pi$ ). The surface resistivity of the walls [62] is calculated by the following:

$$R_s = \frac{1}{\sigma\delta} \quad (7.7)$$

where  $\sigma$  is the conductivity of the walls and  $\delta$  is the skin depth of a conductor if the walls have  $R_s$ . The skin depth is provided by:

$$\delta = \sqrt{\frac{2}{\sigma\omega\mu}} \quad (7.8)$$

where  $\mu$  is the permeability of the dielectric (for free space,  $\mu_0 = 4\pi * 10^{-7} H/m$ ).

For a cube  $a = b = h$ , the quality factor can be calculated by:

$$Q_{cube} = 0.742 \frac{\eta}{R_s} \quad (7.9)$$

In terms of two-port  $S$ -parameter reverberation chamber measurements,  $|S_{21}^a|^2$  and  $\langle |S_{21}^{RC}|^2 \rangle$  can be represented mathematically as follows:

$$|S_{21}^a|^2 = \frac{P_{TX}}{P_{av}} \quad (7.10)$$

$$\langle |S_{21}^{RC}|^2 \rangle = \frac{\langle P_{RX} \rangle}{P_{av}} \quad (7.11)$$

where  $P_{av}$  is the power available from the source.

The reverberation chamber measurements between two identical antennas provide two  $S_{21}^{RC}$  values, as the reverberation chamber depends on the transmissions from both the Tx and Rx antennas, which means that the amplitude of the  $S_{21}^{RC}$  measurement in the reverberation chamber has the frequency responses of the Tx and Rx antennas along with the quality factor due to the skin depth of the aluminium walls.

From (7.10) and (7.11), (7.1) can be written in terms of  $S_{21}^a$  and  $S_{21}^{RC}$  as follows:

$$|S_{21}^a|^2 = \langle |S_{21}^{RC}|^2 \rangle \frac{C_{RC}}{Q} \quad (7.12)$$

where  $S_{11}^{RC}$  and  $S_{21}^{RC}$  represent the measurement of  $S$ -parameters in a reverberation chamber between two identical antennas using a network analyser.

Equation (7.12) by itself is not the complete equation, however. Particular scaling coefficients need to be incorporated into the equation to compensate for the cavity losses due to the skin depth of the walls. The empirical equation will be derived in Section 7.5.

### 7.3 Reverberation Chamber Cavity

A rectangular cavity was built from metal walls in this work as a reverberation chamber in order to conduct measurements inside the cavity. For this purpose, a medium-size cavity was built with aluminium walls. As shown in Figure 7.2, all dimensions,  $a$ ,  $b$ , and  $h$ , are 1 m. Table 7.1 [62] shows the skin-effect properties of aluminium from the literature, with the cube-cavity properties of aluminium walls. As

the table shows, the skin depth, the surface resistivity, and the quality factor are all a function of frequency only. Figure 7.3 and Figure 7.4 show the skin depth and the surface resistivity, respectively, of the aluminium as a function of frequency.

Table 7.1. Cube-cavity properties of aluminium walls.

Aluminium Parameters	Value
Conductivity ( $1/(\Omega m)$ )	$\sigma = 3.72 * 10^7$
Depth of penetration ( $m$ )	$\delta = \frac{0.0826}{\sqrt{f}}$
Surface resistivity ( $\Omega$ )	$R_s = 3.26\sqrt{f} * 10^{-7}$
Quality factor	$Q = \frac{8.58 * 10^8}{\sqrt{f}}$

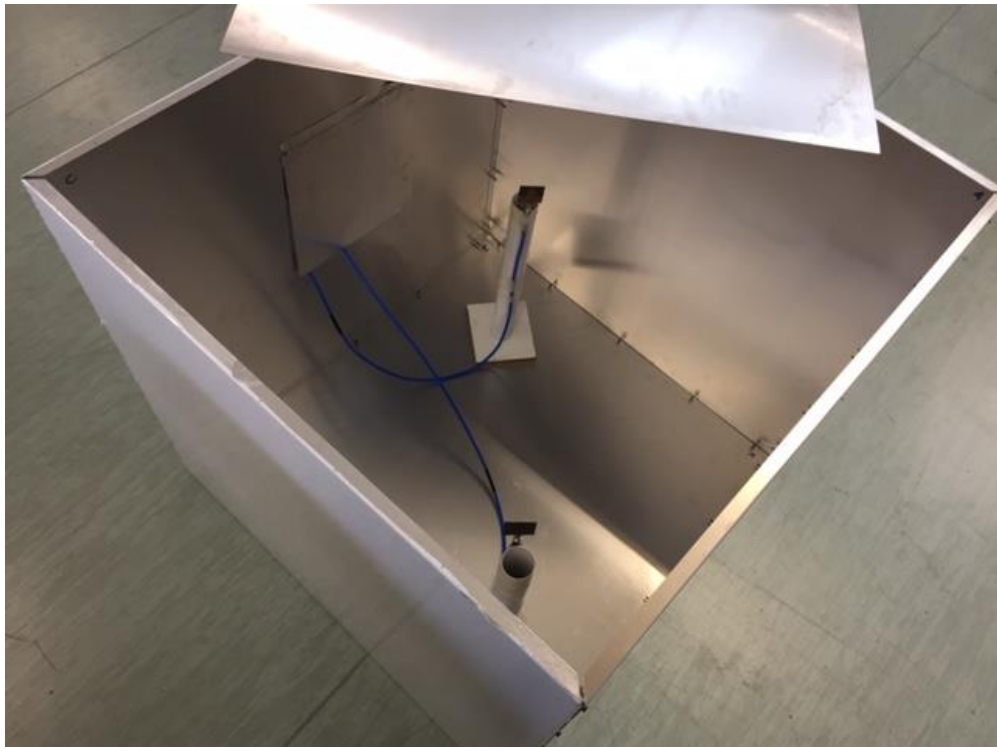


Figure 7.2. Photograph of the cube cavity used as a reverberation chamber.

For an aluminium wall cavity where  $a = b = d$ , the quality factor values were computed using (7.9) as follows:

$$Q = \frac{8.58 * 10^8}{\sqrt{f}} = 4.954\sqrt{\lambda} * 10^4 \quad (7.13)$$

The reverberation chamber constant for the cavity was also calculated using (7.2) as follows:

$$C_{RC} = \frac{157.914}{\lambda^3} \quad (7.14)$$

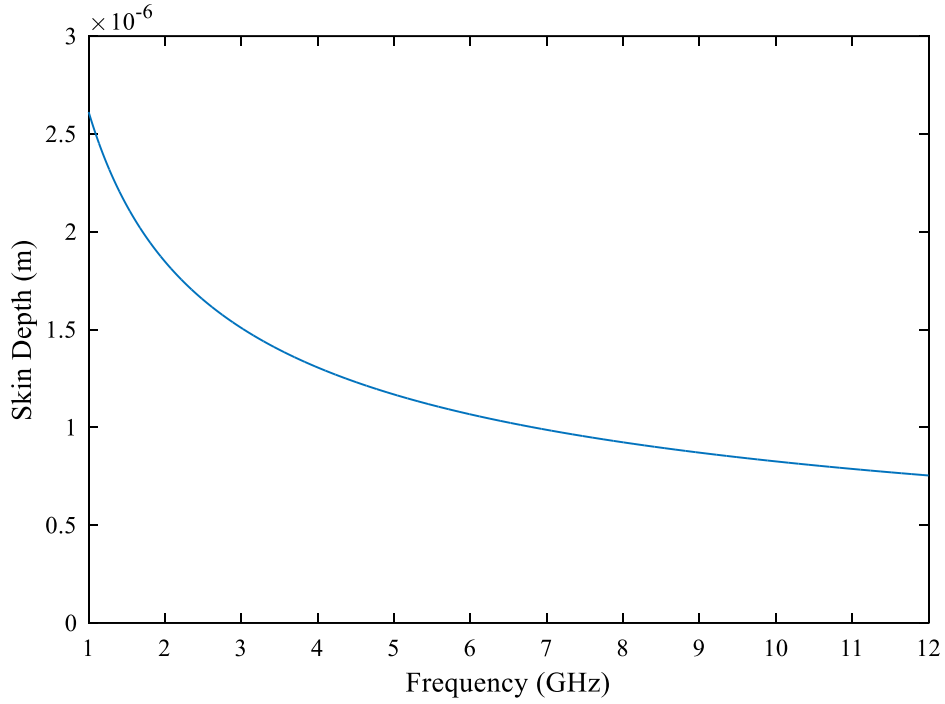


Figure 7.3. Skin depth of the aluminium.

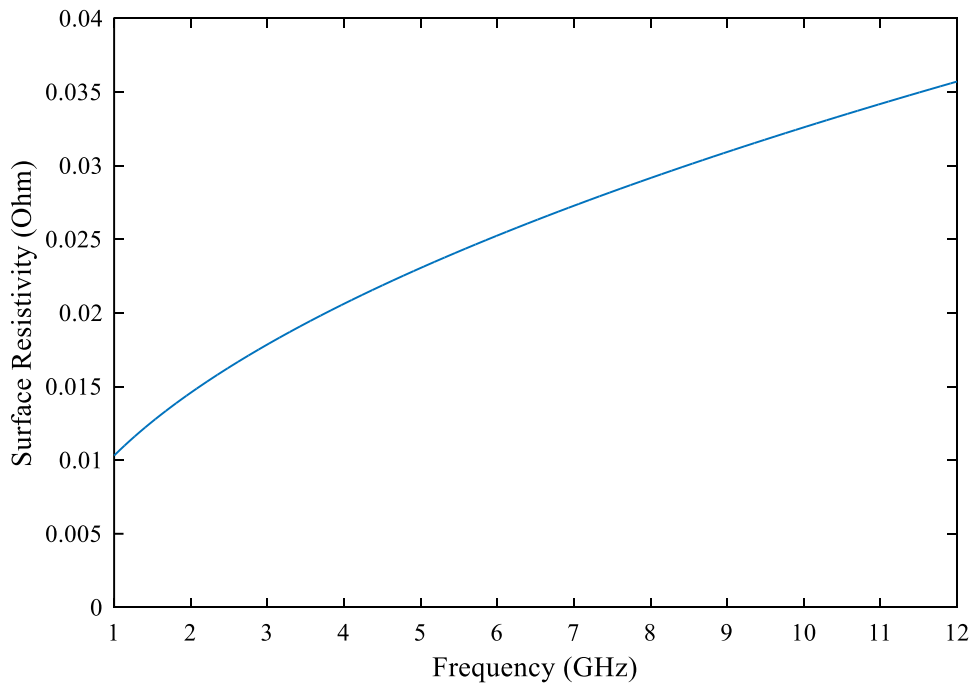


Figure 7.4. Surface resistivity of the aluminium.

The quality factor of the designed cavity was computed for the aluminium from the surface resistivity, as shown in Figure 7.5. The reverberation chamber constant of the cube cavity is presented in Figure 7.6.

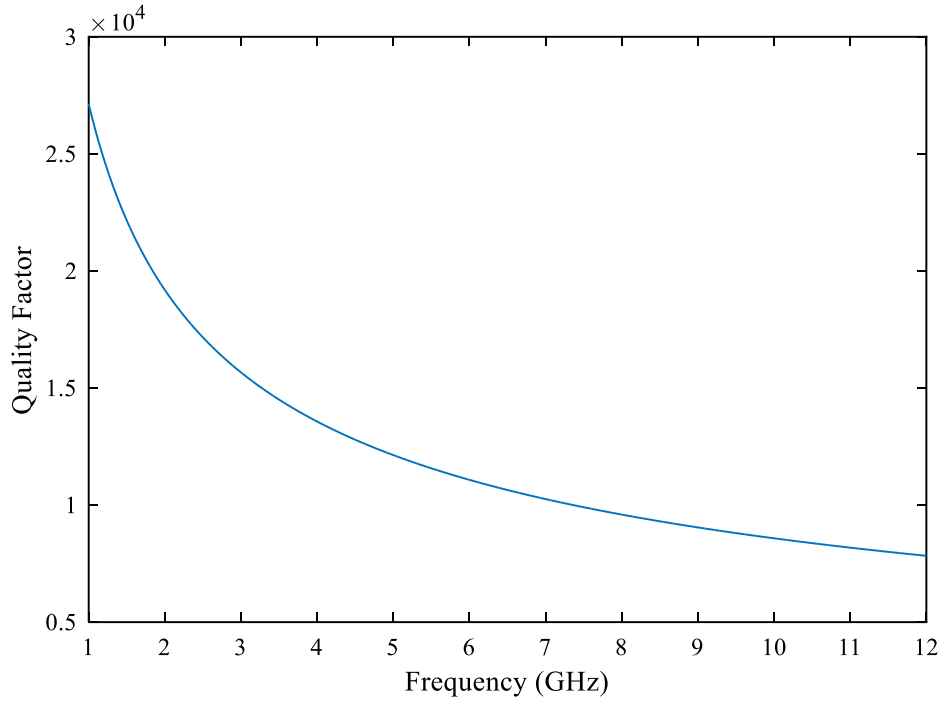


Figure 7.5. Quality factor of the cube cavity from the aluminium walls.

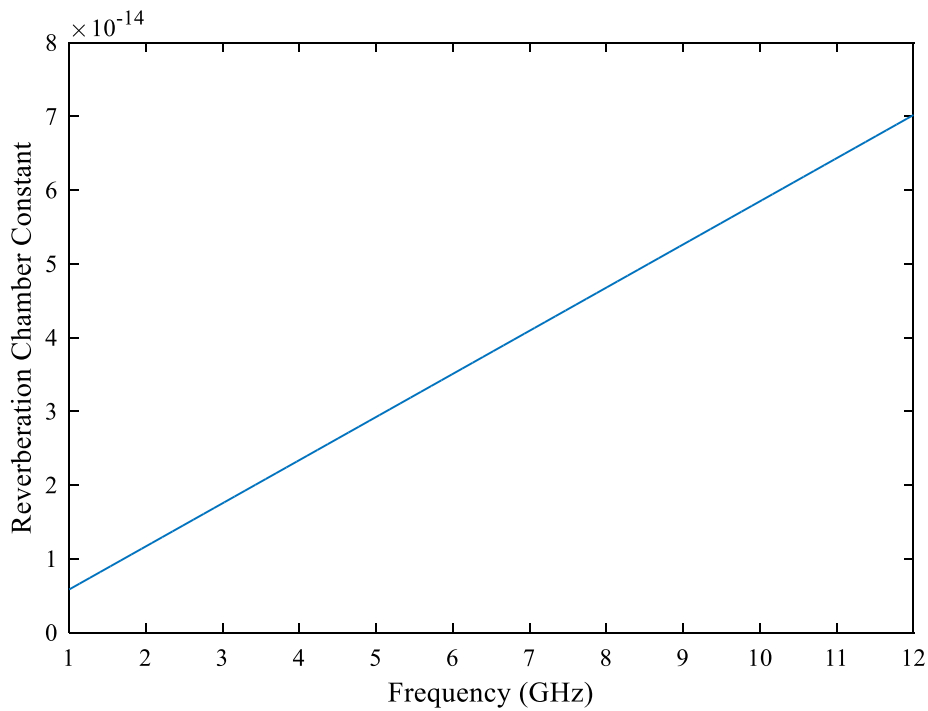


Figure 7.6. Reverberation chamber constant of the cube cavity.

## 7.4 Measuring Antennas in the Cavity

The  $S$ -parameters of the antenna measurement in the reverberation chamber were then determined between two identical antennas. Standard calibration techniques were applied to remove losses due to the cables connecting ports 1 and 2 using a network analyser. These measurements were conducted to show that neither the distances between the Tx and Rx antennas nor the antenna orientation affected the measurements. These results indicate that the measurements taken in a reverberation chamber yield the total radiated power by the antenna. The measurements were carried out for the three different types of antennas used in this work (Vivaldi, commercial, and monopole UWB), all of which were characterised in previous chapters.

### 7.4.1 Vivaldi Antenna

The  $S$ -parameters between two identical Vivaldi antennas were measured in the cube cavity with different orientations and varying distances. These measurements were taken to show that the reverberation chamber would yield the same results with different orientations or with two different distances, 0.5 m and 0.6 m. The  $S_{11}^{RC}$  measurement of the Vivaldi antenna in the cavity is shown in Figure 7.7, where high levels of reflections are notable in the amplitude due to the metal walls.

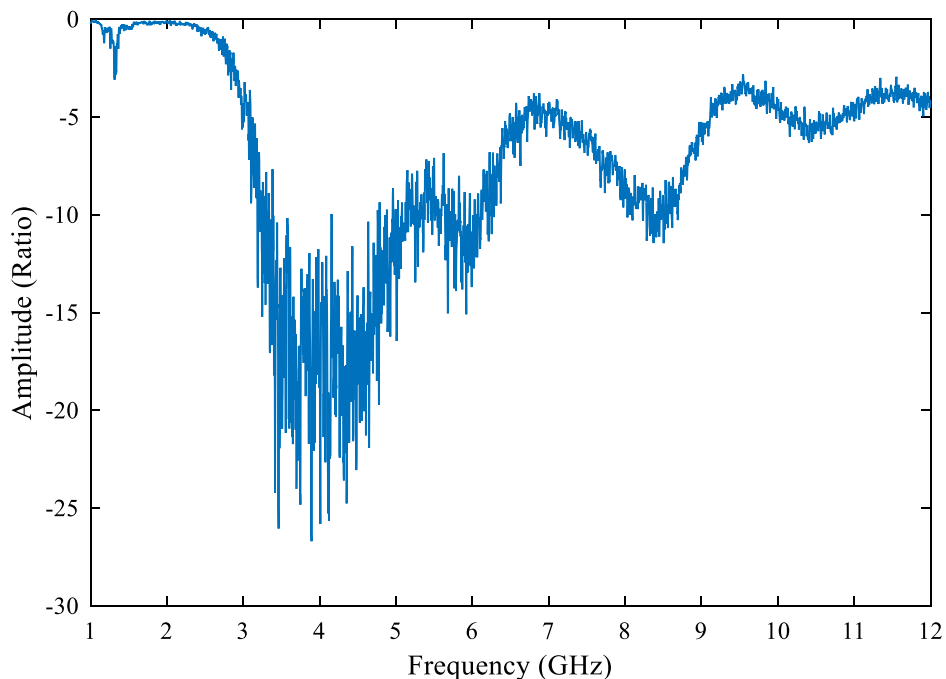


Figure 7.7. Measurement of  $S_{11}^{RC}$  in the reverberation chamber.

The  $S_{21}^{RC}$  measurements between the two Vivaldi antennas with two different orientations and two different distances are shown in Figure 7.8. The measurements derived from using either different orientations or different distances yielded the same results with varying reflections, which indicates that neither the radiation patterns nor the distance affected the measurements in the reverberation chambers and that the measurements are a function of frequency and the constant scaling factor.

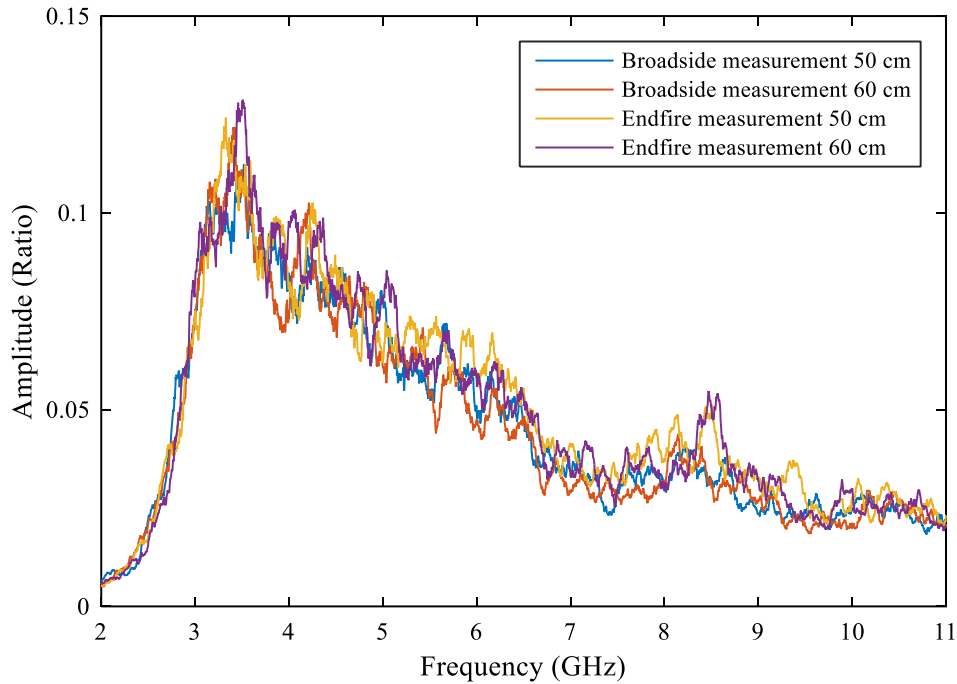


Figure 7.8. Vivaldi antenna  $S_{21}^{RC}$  measurements in the reverberation chamber with different orientations.

#### 7.4.2 Commercial Antenna

The two identical commercial antennas were measured in the cavity to obtain their  $S$ -parameter values. The  $S_{21}^{RC}$  measurement is shown in Figure 7.9 with two different orientations – the broadside and endfire directions – and with different distances: 0.5 m and 0.6 m. As the figure shows, the results from the different distances and orientations were almost the same with varying reflections.

#### 7.4.3 Monopole UWB Antenna

A monopole UWB antenna was also measured in the cavity to show that antenna measurements conducted in a reverberation chamber do not depend on distance or orientation, as shown in Figure 7.10. The measurements in the cavity were carried out

in two orientations – broadside and a second orientation, as characterised in Section 5.5 – as this antenna displayed different frequency responses in the two different orientations based on the measurements taken in the anechoic chamber, as shown in Figure 5.9. This difference occurred because the P2P communications for the two orientations showed different frequency responses (as explained in Section 5.5.1), which indicates that in general, measurements conducted in a reverberation chamber provide the total radiated power of an antenna.

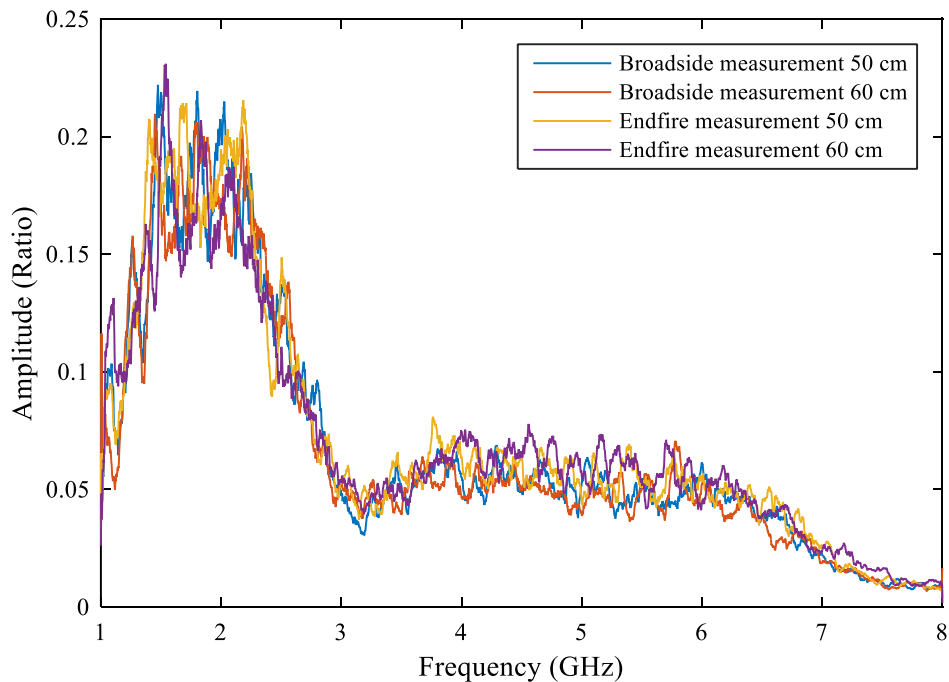


Figure 7.9. Commercial antenna  $S_{21}^{RC}$  measurement in the reverberation chamber with different orientations.

The above results derived from the measurements in the cavity for the three types of antennas indicate that the results do not depend on the distances between the two antennas, nor on the antenna orientation, which indicates that reverberation chamber measurements provide the total radiated power. As discussed previously, however, two factors that do affect these measurements are losses due to the cavity and losses from the antenna itself. The measurements in the reverberation chamber are a function of exponential of the free-space wavelength with a constant scaling factor. The exponential and the scaling factor can be derived using an empirical equation for lossless antennas.

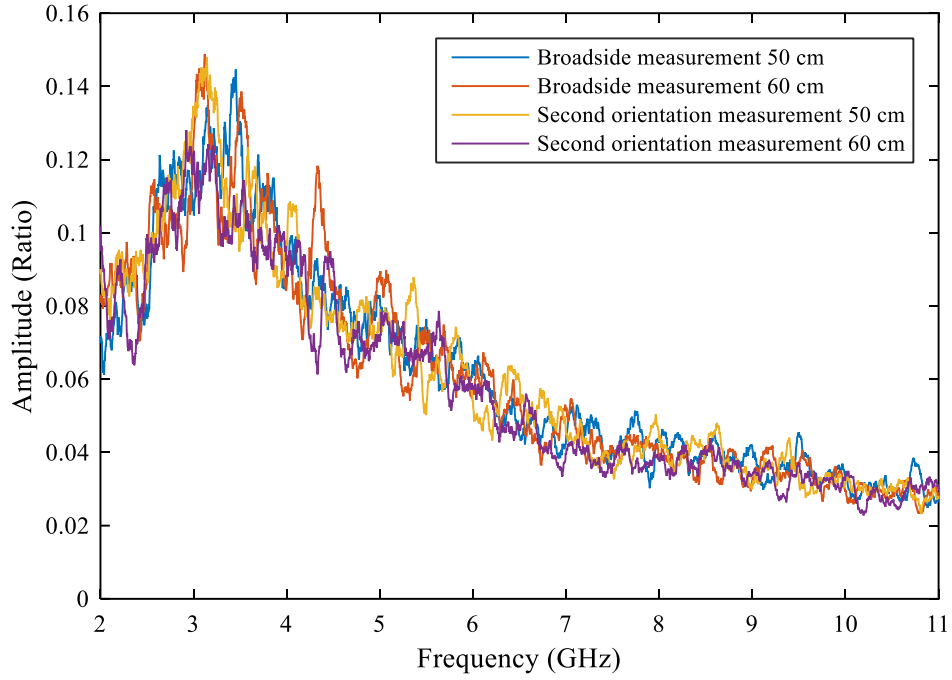


Figure 7.10. UWB antenna  $S_{21}^{RC}$  measurement in the reverberation chamber with different orientations.

## 7.5 Empirically Modelling Cavity Losses in Reverberation Chambers

The mathematical relationship presented in (7.12) between the  $S_{21}^a$ , which provides the total radiated power, and the  $S_{21}^{RC}$ , which provides the measurement in the reverberation chamber, must be related using an empirical equation. Hence the designed cavity shown in Figure 7.2 can be used to compute the total radiated power of an antenna. The exponential of  $\lambda$  can be derived with a constant multiplication factor. (7.12) thus can be represented mathematically as:

$$|S_{21}^a|^2 = \langle |S_{21}^{RC}|^2 \rangle \frac{\text{ampscal}^2}{\lambda^2 * \text{lamexp}} \quad (7.15)$$

where *ampscal* is the amplitude scale, and *lamexp* is the exponential of  $\lambda$ . These parameters are unknown values and can be obtained using an optimisation MATLAB programme to obtain the  $S_{21}^a$ , which provides the total radiated power by an antenna, assuming the antenna is lossless.

Because the reverberation chamber measurement yields the total radiated power from the antenna in all directions, the  $S_{21}^a$  value from the frequency response obtained from the  $S_{11}^{RC}$  using (3.1) was used to compensate for reverberation chamber

losses using MATLAB optimisation. This step was taken to compute the exponential of the free-space wavelength and the constant scaling factor to match the  $S_{21}^{RC}$  measurement in the reverberation chamber with the antenna  $S_{21}^a$  value obtained from the  $S_{11}^{RC}$ . This MATLAB optimisation was applied to immunise the errors using iterations and to compute the constant scaling factor and the exponential factor of the wavelength. This process was applied to the Vivaldi antenna, as it is a lossless antenna.

The *ampscal* and *lamexp* values were obtained using the optimisation programme as follows:

$$ampscal = 0.38$$

$$lamexp = 1.25$$

After using the Vivaldi antenna measurement in the cavity for the optimisation, (7.15) was used to compute the  $S_{21}^a$  for the commercial and monopole UWB antenna measurements in the cavity. The compensation values for the cavity loss in the measurements inside the cavity for the three antennas are presented in the following sub-sections.

### 7.5.1 Vivaldi Antenna

Figure 7.11 shows the optimisation result after compensating for cavity loss due to the walls compared to the  $S_{21}^a$  values obtained from the  $S_{11}$ . Despite the reflections caused by the aluminium walls from the reflections obtained from the measurement in the cavity, the amplitude of  $S_{21}^a$  obtained from the  $S_{11}$  and  $S_{21}^{RC}$  values showed agreement.

### 7.5.2 Commercial Antenna

Figure 7.12 shows a comparison in the amplitude of  $S_{21}^a$  in the frequency response between the value obtained from the  $S_{11}$  and from the  $S_{21}^{RC}$  measurement in the cavity using empirical equation (7.15). The figure shows that the antenna is not lossless, as the  $S_{21}^a$  from the average  $S_{21}^{RC}$  measurement in the cavity after compensating for the cavity loss does not agree with that from the measurement from the  $S_{11}$ . This situation occurs because the  $S_{21}^{RC}$  measurement provides the total radiated power, whereas the  $S_{11}$  measurement provides the accepted power, which is the total radiated power divided by the antenna efficiency.

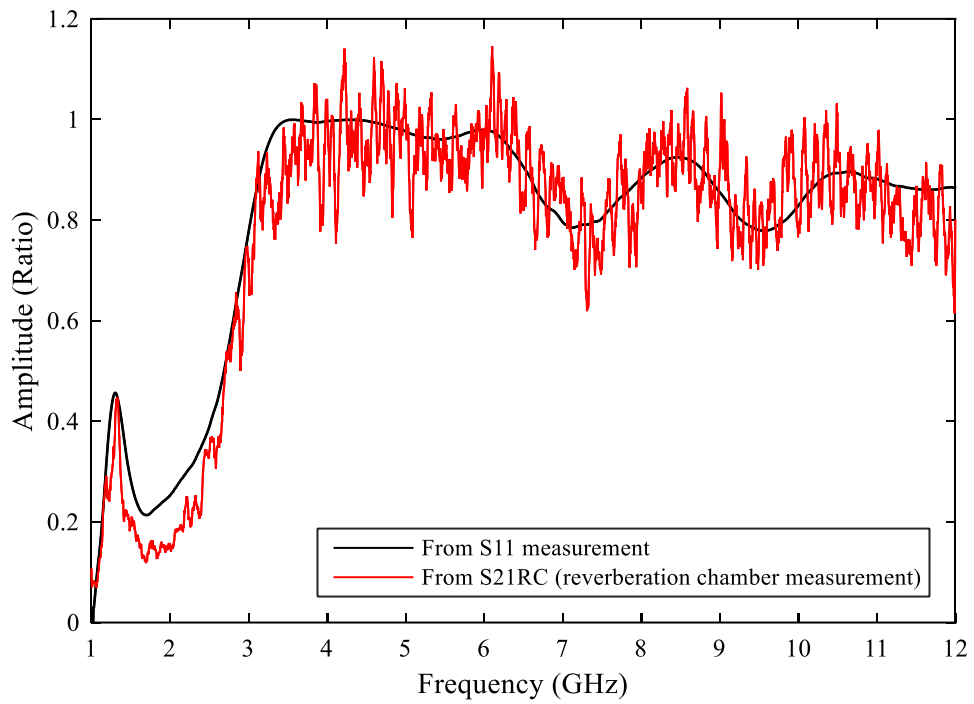


Figure 7.11. Vivaldi antenna  $S_{21}^a$  obtained from (a)  $S_{11}$  and (b)  $S_{21}^{RC}$  measurement in the reverberation chamber.

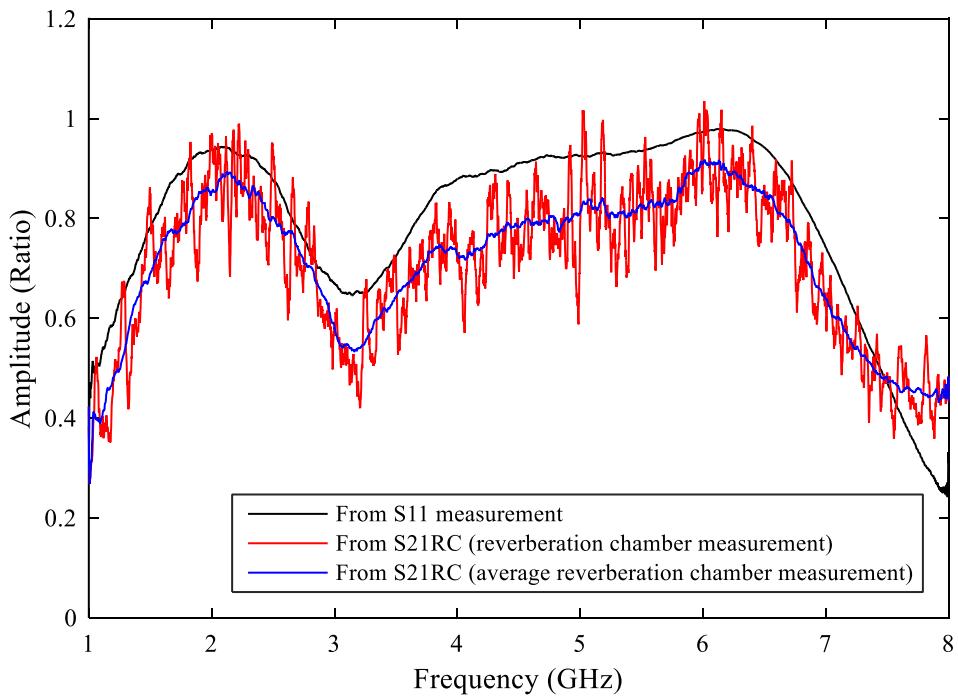


Figure 7.12. Commercial antenna  $S_{21}^a$  obtained from (a)  $S_{11}$  and (b)  $S_{21}^{RC}$  measurement in the reverberation chamber.

### 7.5.3 Monopole UWB Antenna

Figure 7.13 shows a comparison in the amplitude of  $S_{21}^a$  of the monopole UWB antenna between the values obtained from the  $S_{11}$  and from the average  $S_{21}^{RC}$  measurement in the cavity using (7.15). Despite the reflection in the value obtained from the  $S_{21}^{RC}$ , the results display the same trend. As the figure shows, the UWB antenna exhibits low losses, as the values agree.

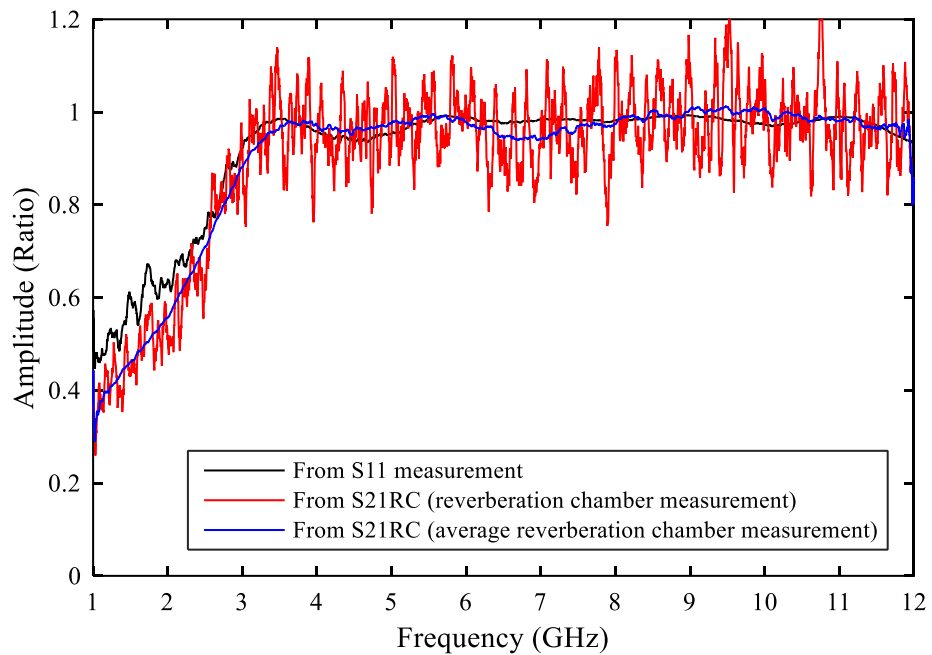


Figure 7.13. Monopole UWB antenna  $S_{21}^a$  obtained from (a)  $S_{11}$  and (b)  $S_{21}^{RC}$  measurement in the reverberation chamber.

The commercial antenna is not a lossless antenna compared with the other two antennas (Vivaldi and monopole UWB), since the  $S_{21}^a$  value obtained from the  $S_{21}^{RC}$  measurement was lower than the value obtained from the  $S_{11}$  measurement. Reverberation chamber measurements provide the total radiated power, which is an important consideration for antenna characterisation in domestic applications. The empirical equation can be used for measurements inside a  $1 \text{ m}^3$  cube cavity built from aluminium walls to compute the total radiated power by an antenna to predict antenna losses.

## 7.6 Summary

This chapter has presented an approach to obtaining the  $S_{21}^a$  value (which provides the total radiated power by an antenna), derived from the measurements in a reverberation chamber. Anechoic chamber measurements yield the power radiated at a specific direction, whereas reverberation chamber measurements do not depend on the radiation pattern and provide the total radiated power. Two factors affect reverberation chamber measurements: losses from the antenna itself and losses due to the skin depth of the walls of the cavity. The proposed approach will enable designers to identify antenna losses based on the total radiated power obtained from reverberation chamber measurements, which will then allow for measuring the antennas to compute the total radiated power in terms of  $S_{21}^a$  before the product is manufactured. The losses due to the walls may be defined by computing the quality factor of the cavity. Reverberation chamber measurements do not depend on antenna orientation, nor on the distance between the Tx and Rx antennas, because the measurements provide the total radiated power of the antenna.

In this work, a medium-size cube cavity of  $1 \text{ m}^3$  with aluminium walls was built for use as a reverberation chamber. The cavity was then used for different antenna measurements. Three different antennas were measured in the cavity using different orientations and varying distances between the Tx and Rx antennas for each type. The results from each antenna type with different orientations and distances were the same despite the reflections due to the walls, which indicates that reverberation chamber measurements provide the total radiated power in all directions and can be used to characterise antennas for domestic applications.

An empirical equation was derived for the cavity, which was built from aluminium walls in the shape of a  $1 \text{ m}^3$  cube, to compute the  $S_{21}^a$  value, which shows the total radiated power of an antenna. MATLAB optimisation was then used to obtain the exponential of the free-space wavelength and the constant scaling factor for use in the empirical equation using the Vivaldi antenna, as such antennas are lossless. The results showed that the commercial antenna was not lossless compared with the Vivaldi and monopole UWB antennas. A mathematical formulation for defining the quality factor of a cavity was defined based on the metal walls' properties. The

empirical equation derived using MATLAB optimisation requires justification, as the equation is related to the quality factor of the cavity and the reverberation chamber constant. Future work will identify the mathematical relationships between  $S_{21}^{RC}$  measurements conducted in a reverberation chamber and the  $S_{21}^a$  value, which provides the total radiated power.

## CHAPTER 8: CONCLUSIONS AND FUTURE WORK

### 8.1 Conclusions

This thesis has explained how an ECM and a system model for an antenna can be derived as well as how these models can be used to calculate the resulting BER in a digital P2P communication system. Different antenna types were characterised to clearly demonstrate the difference in design approaches between realising a low  $S_{11}$  value and the new approach of calculating the antenna response in the desired direction. In general, antennas may be represented by both circuit and system models as two-port networks. The ECM is derived by measuring only the  $S_{11}$  value. The use of an antenna time-domain system model derived from frequency-domain measurements allows for the integration of the antenna into communication system simulations.

Four types of antennas have been characterised in this thesis: a narrowband patch antenna, a wideband Vivaldi antenna, and commercial dual-band and monopole UWB antennas. The thesis has presented practical measurements, theoretical results, and simulations. The key conclusions from the research are presented below.

(1) The thesis has included a proposal for a new approach to calculating the antenna frequency response in the channel direction. Three techniques were applied to characterise a wideband Vivaldi antenna and a narrowband patch antenna. These techniques were used by deriving an ECM, processing the  $S_{21}^b$  measurements between the two identical antennas in an anechoic chamber, and applying the Hilbert transform to the amplitude of  $S_{21}$ . The ECM was derived by inspecting the physical structure and matching the measured  $S_{11}$ . In general, this inspection requires an educated guess at what the order and topology of the ECM should be. This step requires skill on the part of the designer, because not everything is done by computation. The derived ECMs contain both lumped and distributed elements. A lumped/distributed circuit is a circuit that contains inductors, capacitors, and transmission lines (i.e. delay elements). A purely lumped circuit cannot represent the antenna.

The ECM was then optimised using an iterative optimisation process in ADS to match the measured  $S_{11}$  in both amplitude and phase. The second port in the ECM provided the radiation resistance value. Determining this value allowed for obtaining the  $S_{21}^a$  value that would provide the total radiated power from the antenna in all directions, whereas the  $S_{21}$  value that yielded the radiated power in a certain direction was obtained by processing the  $S_{21}^b$  measurement between two identical antennas in an anechoic chamber. The use of the ECM allows designers to determine the transmission phase of the antenna in the principal axis. The phase can also be obtained from the  $S_{21}^b$  measurement in the antenna's principal axis direction. This phase is typically used to characterise antenna behaviour, such as the antenna's resonant structure and frequency-invariant radiation patterns.

(2) A new procedure was proposed for characterising the antenna in multipath channels as a two-port network. This procedure characterises the antenna and channel in both the frequency and time domains to separate the impulse response of the antenna from that of the channel. The direct path represents the impulse response of Tx and Rx antennas. This procedure was applied to a wideband Vivaldi antenna and a narrowband patch antenna to establish the limitations due to the long ringing in the time domain caused by certain antennas. The technique provides a method to obtain the frequency response of an antenna from the measurements in the multipath channels if an anechoic chamber is not available. The method only requires a sufficiently large space in the far field, as well as a network analyser. Obtaining the frequency response of an antenna allows designers to obtain the gain and the group delay of the antenna.

(3) The Friis equation was revised as a function of total radiated power and measured radiated power in the channel direction. This modification was done to calculate the gain and the effective aperture for identical antennas. The gain and effective aperture values were derived as a function of frequency, distance, total radiated power, and measured radiated power in the channel direction. The transmission phase of a non-minimum-phase antenna was also examined based on the linear, minimum, and all-pass phase components to study antenna performance. Minimum-phase antennas

such as Vivaldi, horn, and commercial dual-band antennas lack an all-pass phase component. The existence of an all-pass component in the antenna-transmission phase indicates that the frequency band has a resonant structure, which then results in varying frequency-radiation patterns. A constant gain indicates that the group delay of the antenna is constant and that the transmission phase does not have an all-pass component. This proposed process will provide designers with useful insights into the variation of radiation patterns along the frequency axis in certain directions.

(4) The proposed process described above was then applied to a non-minimum-phase monopole UWB antenna for P2P communications to select the best orientation. A frequency-dependent ECM was derived from  $S_{11}$  measurements only. The phase of the  $S_{21}^a$  value obtained from the ECM confirmed that the antenna had a resonant structure and a frequency-variant radiation pattern over the band on its principal axis (i.e. the broadside direction). This behaviour was caused by an all-pass component in the transmission phase within the frequency range 6–8 GHz. The gain and the group delay also showed large variations across the frequency band. The frequency response (in terms of the effective aperture, gain,  $S_{21}$  phase, and group delay) confirmed that the monopole UWB antenna had a frequency-variant radiation pattern and a resonant structure over the band on the broadside direction. The antenna performance for P2P communications was acceptable in the second orientation, however, where the azimuth and elevation angles were  $90^\circ$  and  $45^\circ$ , respectively. This situation occurred because there was no all-pass component and because the transmission phase was quite linear in the second orientation, as the minimum-phase component is insufficient with the linear-phase component. An antenna's frequency response is often sensitive to antenna orientation, so measurement of the full set of  $S$ -parameters enables designers to predict the correct frequency response in the direction of communication.

(5) The thesis has also shown how to predict antenna effects within DCSs by modelling an antenna for inclusion in system software. The effects caused by each antenna type were analysed in a DCS without adding noise. Different antennas were shown to have varying effects in DCSs. The impulse responses of the various antennas

were shown to differ. For example, some antennas showed an additional component in the antenna response in the time domain. These components often introduce distortion and delay in the antenna's time response. The system model derived for an antenna contains all measured  $S$ -parameters in the direction of communication as an FIR filter model. These models were then used in DCS software. This technique was applied to model and characterise different antennas to be included in DCS software. These steps also helped to identify sophisticated antenna structures that would minimise the effect of the antenna in the DCS. The existence of ripples, and the additional components in the frequency and time domains, typically cause symbol scattering due to multiple reflections by the antenna itself. Another common cause of symbol scattering is the transmission phase when the phase is non-linear, which indicates the existence of an all-pass component.

Commercial dual-band, monopole UWB, and Vivaldi antennas were then characterised, and their complete system models were derived. The system model was derived from all  $S$ -parameters from the frequency-response antenna measurement in the direction of communication to be able to include the antenna in a DCS simulation. These measurements were carried out in an anechoic chamber to eliminate any multipath components. The effects from the different antennas were first predicted in a DCS at two different carrier frequencies. The symbol scattering was then characterised by calculating the EVM and BER. Symbol-scattering experiments were performed in an anechoic chamber using a Tektronix AWG7122C arbitrary waveform generator and a Tektronix DPO72304DX oscilloscope. The equivalent noise caused by the RF components was added in the simulation. The increase in EVM due to the antennas was found to be similar between the simulation and experiments, and the symbol scattering and changes in EVM were found to be dependent on the antenna type that was employed.

The commercial antenna used in this study had a ripple in the frequency response, which affected its impulse response and resulted in the existence of an additional component due to the multiple reflections caused by the antenna itself. The commercial antenna's effects caused symbol scattering, and the EVM increased at the receiver for both bands at the two carrier frequencies. The effects at 6 GHz were less pronounced compared to the effects at 2 GHz. These effects occurred because the

antenna frequency and time responses showed ripple and additional components, respectively.

A monopole UWB antenna was also modelled to predict the antenna effects in a DCS for the broadside direction (i.e. the antenna's principal axis) at two carrier frequencies: 3.5 GHz and 6 GHz. The UWB antenna had a smooth frequency response, but the transmission phase in the broadside direction was found to be non-linear due to the existence of the all-pass component. This non-linear transmission phase occurred because two paths for energy transfer were defined in the antenna ECM. The symbol scattering, and the resulting EVM caused by the UWB antenna's effects in the broadside direction at 6 GHz, were found to be high compared to those at 3.5 GHz. This scattering occurred because the low transmission at 6 GHz was caused by the non-linear transmission phase within the 6–8 GHz frequency range in this direction (the broadside direction).

The effects of the UWB antenna at the second orientation in the DCS were also investigated. Minimal symbol scattering was found to have occurred at the two carrier frequencies of 3.5 GHz and 6 GHz. This low level of scattering was caused because of the smooth frequency response and the linear transmission phase in the second orientation, resulting in low variation gain over the frequency band in order to have acceptable antenna performance over the UWB frequency bandwidth. In contrast, the Vivaldi antenna's effects were investigated over two carrier frequencies: 3.5 GHz and 6.3 GHz. Minimal symbol scattering was again found, and the EVM showed low values for both carrier frequencies because the frequency response of Vivaldi antennas in general is smooth, and the phase is quite linear (minimum- and linear-phase components only exist). This linear transmission phase makes the ECM simpler, and it only has a single path for energy transfer. The monopole UWB antenna was found to have performed better than the commercial antenna, but the Vivaldi was the best performer. The UWB antenna showed minor rippling in the time response and the non-linear transmission phase in the frequency response.

(6) In general, antennas cause symbol scattering and bit errors in DCSs. This scattering depends on the antenna design as well as carrier frequency. This symbol scattering is

only caused by the antenna, and recent studies have found increases in BER and EVM to be a function of frequency. The absence of rippling in the antenna frequency response and in the linear phase produce low-level symbol scattering and the lowest EVM and BER values. The technique will enable communication system designers to choose the antenna and carrier frequency that will best minimise the BER. The channel response depends on the antenna time response and the transmission phase, which in turn depend on the antenna structure and the frequency-variant radiation pattern. Measurements within the multipath channels showed that the multipath components manifested the antenna impulse response. This characterisation, which was applied to a narrowband patch antenna and a wideband Vivaldi antenna, confirmed that the antenna properties were found in the multipath component. An inverse antenna system hence is required to de-embed the antenna from the antenna measurement in a given channel.

(7) An inverse antenna system was derived in P2P communications for Vivaldi and commercial antennas. Vivaldi antennas generally have minimal effects in DCSs, while commercial antennas typically cause symbol scattering in the system. This modelling was done to de-embed the Vivaldi antenna's properties from the antenna's *S*-parameter measurements in the multipath channels. Two methods were explained to eliminate the linear-phase component in order to derive a minimum system model: by allocating the zeros to the LHS and by using the Hilbert transform. Both techniques were used to derive a stable inverse antenna system and were used only for minimum-phase antennas that had frequency-invariant radiation patterns.

The inverse system was cascaded to the antenna measurements with two different office environments at two different distances: 1 m and 3 m. This cascading was done to characterise the two office multipath channels in P2P communications in the frequency domain. This technique, which provides separate antenna and channel models whose effects can be examined separately in DCSs, will enable designers to use these systems to reduce the complexity found at the receiver.

In general, Vivaldi antennas have minimal effects in DCSs. This thesis has shown that the modelling of antenna measurements in an anechoic chamber with two

different distances in a DCS had minimal effects. Different office multipath channels were also modelled with and without the Vivaldi antenna to be included in a DCS, and the channel effects were found to be the same as the Vivaldi antennas: they both had minimal effects in the system. This derivation allowed for predicting the channel effects in a DCS. The use of an inverse system model will also enable designers to derive accurate channel-transfer functions after de-embedding the antenna response from the  $S$ -parameter measurements in the multipath channels to be independent of the antenna that is used.

(8) Another application of an inverse antenna system was derived for a commercial antenna to mitigate the antenna effects in a DCS. This step will enable designers to use low-cost, highly dispersive antennas by compensating for the antenna effects to reduce the BER in the DCS. This application was achieved theoretically. The implementation of the algorithm must be conducted either with hardware or with software. Software implementation must be done in either the intermediate frequency (IF) or radio frequency (RF), and RF implementation requires rapid digital circuitry.

(9) As investigated in this thesis, measuring an antenna in an anechoic chamber yields the power radiated in a specific direction (which is useful for P2P communications), whereas measurements conducted in a reverberation chamber do not depend on the radiation pattern and provide the total radiated power and thus are helpful for domestic applications. The difference between the two environmental measurements is found in the directivity of the antennas.

(10) An approach was presented for obtaining the total radiated power by an antenna from measurements conducted in a reverberation chamber. This approach will enable designers to identify antenna losses from measurements taken in a reverberation chamber. For this work, a reverberation chamber was built as a medium-size cube cavity of  $1 \text{ m}^3$  with aluminium walls. Three different antennas were measured using different orientations and varying distances. The results were the same for each

antenna type for the different orientations or distances between the two identical antennas. These measurements are not a function of distance and do not depend on the radiation patterns. Instead, they provide the total radiated power by the antenna.

Both the quality factor of the reverberation chamber and antenna losses affect reverberation chamber measurements. An empirical equation for a cube cavity was derived for compensating the cavity loss. This step allowed for computing the total radiated power by an antenna in order to identify the antenna losses. This equation was derived using MATLAB optimisation to obtain the exponential of the free-space wavelength and the constant scaling factor using Vivaldi antenna measurements, as such antennas are lossless. The results showed that the commercial antenna exhibited some losses compared with the Vivaldi and monopole UWB antennas. This approach will enable designers to predict antenna losses and to characterise antennas for domestic applications.

(11) Finally, several methods for deriving circuit and system models were developed. Details were also provided to explain how the system model can be included in a complete communication system. An inverse antenna system model was derived as the standard to de-embed the antenna response from the multipath channel. This step then allowed for characterising and modelling the channel. Different environments in an anechoic chamber, a reverberation chamber, and different multipath offices were all utilised for conducting measurements between two identical antennas. One recommendation for designers is that an ECM, antenna system model and an inverse antenna system model should be derived for every an antenna.

## **8.2 Future Work**

Future work will develop various methods for modelling and cancelling the undesirable effects of antennas in DCSs. These methods include further research in the following areas.

- (a) A method will be developed to derive an inverse system for non-minimum-phase antennas with an all-pass component, which will require research to

model the delay caused by the all-pass component and to use cascading with an inverse minimum-phase model. The inverse system will then be used to reverse any antenna distortion that occurs.

- (b) Time-domain filters or a time-inverse antenna system will be designed to eliminate the ringing that occurs in the impulse response. This design can already be implemented theoretically in simulation, but the main difficulty is the implementation of an inverse antenna system within IF components using additional hardware or software. This difficulty will be addressed in future work to compensate for the antenna effects in DCSs and to characterise the multipath channel.
- (c) Carrier and digital data will be synchronised to eliminate any discontinuities in amplitude and phase.
- (d) The empirical equation that was derived in this work using MATLAB optimisation will be justified to compute the  $S_{21}^a$  value, which provides the total radiated power by the antenna based on measurements conducted in a reverberation chamber. This derivation will enable designers to predict antenna losses and to characterise the antenna for domestic applications. This work will be done to identify the mathematical relationships between measurements conducted in a reverberation chamber and the antenna's total radiated power.
- (e) The radiation pattern with the antenna  $S_{21}^a$ , which provides an antenna's total radiated power, will be described to derive a complete antenna system model as a function of frequency and elevation and azimuth angles.

## REFERENCES

- [1] D. Panaitopol *et al.*, ‘Impact of the design of an UWB antenna on the maximum achievable rate of the communication in presence of multi user interferences’, in *2008 Asia-Pacific Microwave Conference*.
- [2] H. Foltz *et al.*, ‘UWB antenna transfer functions using minimum phase functions’, in *2007 IEEE Antennas and Propagation Society International Symposium*.
- [3] J. S. McLean, H. Foltz, and R. Sutton, ‘Differential time delay patterns for UWB antennas’, in *2008 IEEE International Conference on Ultra-Wideband*.
- [4] J. S. McLean, H. Foltz, and R. Sutton, ‘Directional dependence of the minimum phase property of antenna transfer functions’, in *2009 Loughborough Antennas & Propagation Conference (LAPC 2009)*.
- [5] C. L. Holloway *et al.*, ‘Reverberation chamber techniques for determining the radiation and total efficiency of antennas’, *IEEE Transactions on Antennas and Propagation*, vol. 60, no. 4, pp. 1758-1770, 2012.
- [6] H. Zhao, J. Hu, and Z. Chen, ‘Study of monopole antenna’s received power in reverberation and anechoic chambers’, in *2017 Asia-Pacific International Symposium on Electromagnetic Compatibility (APEMC)*.
- [7] Y. Wang, T. Jiang, and Y. Li, ‘Equivalent circuit model of a triple frequency rejection band UWB antenna’, in *2017 International Applied Computational Electromagnetics Society Symposium – Italy (ACES)*.
- [8] A. Moradikordalivand *et al.*, ‘An equivalent circuit model for broadband modified rectangular microstrip-fed monopole antenna’, *Wireless Personal Communications*, vol. 77, no. 2, pp. 1363-1375, 2014.
- [9] C. K. Lin and S. J. Chung, ‘A compact filtering microstrip antenna with quasi-elliptic broadside antenna gain response’, *IEEE Antennas and Wireless Propagation Letters*, vol. 10, pp. 381-384, 2011.
- [10] M. Kufa, Z. Raida, and J. Mateu, ‘Equivalent circuits of planar filtering antennas fed by apertures’, in *2014 Microwaves, Radar, and Wireless Communication (MIKON), 20th International Conference on*.
- [11] O. K. Heong, C. K. Chakrabarty, and G. C. Hock, ‘Circuit modeling for rectangular printed disc monopole antenna with slot for UWB system’, in *2012 3rd International Conference on Intelligent Systems Modelling and Simulation*.
- [12] Y. Guo *et al.*, ‘Equivalent circuit modeling of UWB antennas for system co-design’, in *2010 IEEE Antennas and Propagation Society International Symposium*.

- [13] N. Li *et al.*, ‘Gauss filter circuit equivalent model of antenna with characteristic modes approach’, in *2015 IEEE International Conference on Communication Problem-Solving (ICCP)*.
- [14] L. Yue and W. Zhennan, ‘A new approach to parameter extraction for equivalent circuit model of terahertz antenna’, in *Signal Processing, Communications and Computing (ICSPCC), 2015 IEEE International Conference on*.
- [15] M. Moulay, M. Abri, and H. Abri Badaoui, ‘Quad-band bowtie antenna design for wireless communication system using an accurate equivalent circuit model’, *International Journal of Microwave Science and Technology*, vol. 2015, 2015.
- [16] T. Prakoso *et al.*, ‘Antenna representation in two-port network scattering parameter’, *Microwave and Optical Technology Letters*, vol. 53, no. 6, pp. 1404-1409, 2011.
- [17] M. I. Sobhy, B. Sanz-Izquierdo, and J. C. Batchelor, ‘System and circuit models for microwave antennas’, in *2006 European Conference on Wireless Technology*.
- [18] M. I. Sobhy, B. Sanz-Izquierdo, and J. C. Batchelor, ‘System and circuit models for microwave antennas’, *IEEE Transactions on Microwave Theory and Techniques*, vol. 55, no. 4, pp. 729-735, 2007.
- [19] J. S. McLean, R. Sutton, and H. Foltz, ‘Minimum phase / all-pass decomposition of LPDA transfer functions’, in *2009 IEEE International Conference on Ultra-Wideband*.
- [20] H. D. Foltz *et al.*, ‘Non-minimum phase behavior due to fractional Hilbert transform in broadband circular polarization antennas’, in *Electromagnetic Theory (EMTS), 2010 URSI International Symposium on*.
- [21] T. Hirano, J. Hirokawa, and M. Ando, ‘Measurement technique for gain and distance and numerical simulation with a dipole antenna’, in *2014 IEEE Antennas and Propagation Society International Symposium (APSURSI)*.
- [22] K. Harima, ‘Calibration of broadband double-ridged guide horn antenna by considering phase center’, in *2009 European Microwave Conference (EuMC)*.
- [23] V. Sipal, B. Allen, and D. Edwards, ‘Analysis and mitigation of antenna effects on wideband wireless channel’, *Electronics Letters*, vol. 46, no. 16, pp. 1159-1160, 2010.
- [24] V. Sipal, B. Allen, and D. Edwards, ‘Effects of antenna impulse response on wideband wireless channel’, in *2010 Loughborough Antennas & Propagation Conference (LAPC 2010)*.
- [25] A. F. Molisch, J. R. Foerster, and M. Pendergrass, ‘Channel models for ultrawideband personal area networks’, *IEEE Wireless Communications*, vol. 10, no. 6, pp. 14-21, 2003.

- [26] H. Ferchichi *et al.*, ‘The measurement impulse response of UWB antennas in the time-domain’, in *2010 IEEE 11th Annual Wireless and Microwave Technology Conference (WAMICON)*.
- [27] L. Ophir, Y. Bitran, and I. Sherman, ‘Wi-Fi (IEEE 802.11) and Bluetooth coexistence: Issues and solutions’, in *2004 IEEE 15th International Symposium on Personal, Indoor and Mobile Radio Communications. IEEE cat. no.04TH8754*.
- [28] S. D. Rogers, J. T. Aberle, and D. T. Auckland, ‘Two-port model of an antenna for use in characterizing wireless communications systems, obtained using efficiency measurements’, *IEEE Antennas and Propagation Magazine*, vol. 45, no. 3, pp. 115-118, 2003.
- [29] W.-J. Tseng and S.-J. Chung, ‘Analysis and application of a two-port aperture-coupled microstrip antenna’, *IEEE Transactions on Microwave Theory and Techniques*, vol. 46, no. 5, pp. 530-535, 1998.
- [30] D. Piazza, D. Michele, and K. R. Dandekar, ‘Two port reconfigurable CRLH leaky wave antenna with improved impedance matching and beam tuning’, in *2009 3rd European Conference on Antennas and Propagation*.
- [31] S. Caizzone, E. DiGiampaolo, and G. Marrocco, ‘Constrained pole-zero synthesis of phase-oriented RFID sensor antennas’, *IEEE Transactions on Antennas and Propagation*, vol. 64, no. 2, pp. 496-503, 2016.
- [32] J. T. Aberle, ‘Two-port representation of an antenna with application to non-Foster matching networks’, *IEEE Transactions on Antennas and Propagation*, vol. 56, no. 5, pp. 1218-1222, 2008.
- [33] H. Y. Lam, ‘Properties of network functions’, in *Analog and Digital Filters: Design and Realization*, L. O. Chua, Ed. Upper Saddle River, NJ: Prentice-Hall, 1979, pp. 55-61.
- [34] H. Aumann, T. Schmitt, and D. Mooradd, ‘A modification of the two-antenna method to determine the phase center location as well as the gain of a wideband antenna’, in *2015 IEEE International Symposium on Antennas and Propagation & USNC/URSI National Radio Science Meeting*.
- [35] Anonymous, ‘IEEE standard for definitions of terms for antennas’, *IEEE Standard 145-2013 (revision of IEEE Standard 145-1993)*, pp. 1-50, 2014.
- [36] P. Bahramzy and G. F. Pedersen, ‘Group delay of high Q antennas’, in *2013 IEEE Antennas and Propagation Society International Symposium (APSURSI)*.
- [37] G. S. Reddy, S. Kharche, and J. Mukherjee, ‘Ultra wideband printed monopole antenna with curve shaped extended asymmetric CPW ground plane for stable unidirectional radiation pattern’, in *2014 IEEE Antennas and Propagation Society International Symposium (APSURSI)*.

- [38] F. Fereidoony, S. Chamaani, and S. A. Mirtaheri, 'Systematic design of UWB monopole antennas with stable omnidirectional radiation pattern', *IEEE Antennas and Wireless Propagation Letters*, vol. 11, pp. 752-755, 2012.
- [39] S. K. Ghosh and R. K. Badhai, 'Printed monopole antenna for UWB and SWB with directional radiation characteristics and high F/B ratio', in *2016 International Conference on Wireless Communications, Signal Processing and Networking (WiSPNET)*.
- [40] T. Dissanayake and K. P. Esselle, 'UWB performance of compact L-shaped wide slot antennas', *IEEE Transactions on Antennas and Propagation*, vol. 56, no. 4, pp. 1183-1187, 2008.
- [41] A. M. Hayar and G. M. Vitetta, 'Channel models for ultra-wideband communications: An overview', *15th Mobile and Communications Summit*, 2005, pp. 1-5.
- [42] M. A. Matin *et al.*, 'Statistical model for UWB channel in an industrial environment', in *2008 International Conference on Microwave and Millimeter Wave Technology*.
- [43] Keysight Technologies, *Defining a channel sounding measurement system for characterising of 5G air interfaces*, December 2017.
- [44] J. T. Quimby *et al.*, *NIST channel sounder overview and channel measurements in manufacturing facilities*, 2017.
- [45] Y. Duroc *et al.*, 'On the characterization of UWB antennas', *International Journal of RF and Microwave Computer-Aided Engineering*, vol. 19, no. 2, pp. 258-269, 2009.
- [46] Y. Duroc *et al.*, 'UWB antennas: Systems with transfer function and impulse response', *IEEE Transactions on Antennas and Propagation*, vol. 55, no. 5, pp. 1449-1451, 2007.
- [47] D. M. Pozar, 'The scattering matrix in microwave network analyzer', in *Microwave Engineering*, 4<sup>th</sup> ed. New Jersey: John Wiley & Sons, 2012, pp. 177-183.
- [48] P. J. Gibson, 'The Vivaldi aerial', in *1979 9th European Microwave Conference (EuMC)*, pp. 101-105.
- [49] Z. Liu, Y. Zhu, and J. Zhou, 'Improved design of Vivaldi antenna with loading resistance for wideband applications', in *2016 IEEE International Conference on Microwave and Millimeter Wave Technology (ICMMT)*.
- [50] N. Hamzah and K. A. Othman, 'Designing Vivaldi antenna with various sizes using CST software', in *Proceedings of the World Congress on Engineering 2011*.

- [51] Y. Erdogan, 'Parametric study and design of Vivaldi antennas and arrays', *Middle East Technical University, Ankara, Turkey*, 2009.
- [52] J. Shin and D. H. Schaubert, 'A parameter study of stripline-fed Vivaldi notch-antenna arrays', *IEEE Transactions on Antennas and Propagation*, vol. 47, no. 5, pp. 879-886, 1999.
- [53] Anonymous, 'High-speed board layout guidelines', Altera Corp., May 2007. [http://www.altera.com/literature/hb/stx2/stx2\\_sii52012.pdf](http://www.altera.com/literature/hb/stx2/stx2_sii52012.pdf).
- [54] S. J. Wu *et al.*, 'Study of an ultrawideband monopole antenna with a band-notched open-looped resonator', *IEEE Transactions on Antennas and Propagation*, vol. 58, no. 6, pp. 1890-1897, 2010.
- [55] C. A. Balanis, 'Antenna vector effective length and equivalent areas', in *Antenna Theory: Analysis and Design*, 3<sup>rd</sup> ed. New Delhi: Beekam Print & Pack, 2015, pp. 89-96.
- [56] H. Schantz, 'A taxonomy of UWB antennas', in *The Art and Science of Ultrawideband Antennas*, London: Artech House, 2005, pp. 214-227.
- [57] Y. Jung and M. Enqvist, 'Estimating models of inverse systems', in *52nd IEEE Conference on Decision and Control*, 2013.
- [58] H. G. Krauthäuser and M. Herbrig, 'Yet another antenna efficiency measurement method in reverberation chambers', in *2010 IEEE International Symposium on Electromagnetic Compatibility*.
- [59] C. Li *et al.*, 'A comparison of antenna efficiency measurements performed in two reverberation chambers using non-reference antenna methods', in *2015 Loughborough Antennas & Propagation Conference (LAPC 2015)*.
- [60] D. A. Hill, 'Electromagnetic theory of reverberation chambers', *NIST Technical Note*, vol. 1506, 1998.
- [61] H. G. Krauthäuser, 'On the measurement of total radiated power in uncalibrated reverberation chambers', *IEEE Transactions on Electromagnetic Compatibility*, vol. 49, no. 2, pp. 270-279, 2007.
- [62] S. Ramo, J. R. Whinnery, and T. Van Duzer, Eds., 'Resonator cavities', in *Fields and Waves in Communication Electronics*, 3<sup>rd</sup> ed. New Jersey: John Wiley & Sons, 1984, pp. 490-494.